Chemical structure and properties of functional polyolefins

‘Deep characterization leading to cutting-edge applications’

Jakub Kruszyński

CHAPTER I - Introduction

CHAPTER II

CHAPTER III

1.1 Historical overview of the major milestones in the polyolefin industry

Over the centuries, many materials, mainly made of leather, wood, natural rubber, and metal alloys, have been developed and tested in various applications. Subsequent breakthroughs in material science have been significantly transforming the world around us ever since. However, the real revolution began with the discovery of vulcanization of natural rubber in 1844 by Charles Goodyear. Subsequently, in 1907, Leo Baekeland introduced phenol-formaldehyde resin—the first fully synthetic polymer.[1–6] Disruptive milestone in the polymer industry occurred in 1933 with the discovery of the first polyolefin: low-density polyethylene (LDPE), with its full-scale production beginning in 1939. [7] Long-chain branches, present in LDPE, provide high melt strength under relatively low viscosity, which is required in the film-blowing production of items such as shrink wrap, vapor barriers, agricultural covers, and trash bags.[8–10] Additionally, numerous short-chain branches decrease the density and degree of crystallinity which translates into improved flexibility and a lower melting point of the polyolefins. Despite the cost-inefficiency and limited controllability of LDPE radical polymerization process, the material is widely used in various applications. [10,11]

After the next 20 years of extensive polymer research, a new era began in 1953 at the Max Planck Institute in Germany. Professor Karl Ziegler discovered a heterogeneous catalytic system able to polymerize ethylene into linear, high molecular weight polyethylene.[12] Compared to the LDPE this new product, called high-density polyethylene (HDPE), exhibited notably improved properties such as increased melting temperature, elevated density, and crystallinity. Distinctly cheaper and well-controlled polymerization of ethylene using Ziegler catalyst immediately attracted attention of many researchers. Thus, in 1954, the Italian professor Giulio Natta proposed the use of the Ziegler catalyst to polymerize propene into isotactic polypropylene (*i*PP).[13] The obtained *i*PP exhibited a well-packed crystal structure, which translates into excellent mechanical and thermal properties.[14–16] It is worth mentioning that in the 1950s, parallel to the discoveries of Ziegler and Natta, Phillips Petroleum Company has been conducting extensive research on polyolefin catalytic polymerization. In 1951 John Hogan and Robert Banks successfully polymerized ethylene using chromium oxide supported on silica, which later became known as

the Phillips catalyst.[17] The resulting high-density polyethylene (HDPE) exhibited superior mechanical properties and the polymerization method was significantly simpler and more cost-effective compared to the radical process.[18] Comparing the polymerization mechanisms, Ziegler-Natta catalysts operate via a coordination-insertion mechanism, where an incoming monomer coordinates with the metal active center and inserts into the growing polymer chain. This mechanism allows to produce highly stereospecific isotactic and syndiotactic polymers. In contrast, the mechanism of the Phillips catalyst involves the reduction of chromium and the formation of active sites on the silica surface. This coordination mechanism is less stereospecific and is limited to the polymerization of ethylene. Consequently, Ziegler-Natta catalysts gained a larger share of the market due to their versatility in polymerizing propylene and other α-olefins.[19–21]

In the 1970s, Kaminsky and Sinn disclosed a successful polymerization of ethylene using isospecific single site catalyst (SSCs) activated with methylaluminoxane (MAO).[22] A new generation of SSCs revealed high activity, enabling production of novel high molecular weight engineering polyolefins with enhanced mechanical properties. The SSCs provided better insight into the polymerization mechanism of stereoselective incorporation of α-olefins into growing polyolefin chains.[23] This development opens a window to a new range of materials within the polyolefin family ranging from Polyolefin Elastomers (POEs) and Thermoplastic Polyolefins (TPOs). POEs are elastomeric materials made by copolymerizing ethylene or propylene with other α-olefins like 1-butene, 1-hexene, or 1-octene, whereas TPOs are blends or alloys typically consisting of a polypropylene (PP) matrix combined with an elastomeric polymers like ethylene-propylene rubber (EPR) or ethylene-propylene-diene-based rubber (EPDM).

In the 1970s, Yves Chauvin created the first description of the metathesis reaction.[24] Based on that fundament, Richard R. Schrock in 1991, described in Accounts of Chemical Research the potential of molybdenum and tungsten-based catalysts in living ring opening methathesis polymerization.[25] Subsequently Robert Grubbs and his co-workers discovered ruthenium-based olefin metathesis catalysts exhibiting higher tolerance to oxygen and water, allowing for the introduction of a wider range of functional moieties. [26] The discovery of metathesis enabled the polymerization of linear alpha olefins and cycling olefins by a new approach namely: ADMET (Acyclic Diene Methathesis) and ROMP (Ring Opening Metathesis

Polymerization).[27–29] The contributions of professors Chauvin, Schrock and Grubbs were awarded the Nobel Prize in Chemistry in 2005.

In summary, polyolefins can be produced through various ways, using either radical or catalytic processes. It is remarkable that such a wide range of polymers can be derived from a simple olefinic structure. Depending on the degree of chain branching, molecular weight, and crystallinity, polyolefins find applications in packaging, automotive, building and construction, as well as in previously unavailable engineering applications, such as membranes, sensors, and compatibilizers.[30] In 2024, the global polyolefin market reached enormous size around 264.8 billion USD. Interestingly, that value refers to a 42.4% of the entire plastics market![31,32] The ongoing development of polymerization and copolymerization techniques for olefins remains highly relevant. Each year, chemical companies supported by academic communities introduce new types of functionalized polyolefins that are increasingly tailored to customer needs and the growing demands of the circular economy.

1.2 Ways to prepare polyolefins

1.2.1 Free radical polymerization

Free radical polymerization of ethylene is performed at extremely high pressure (ranging from 100 to 400 MPa) and elevated temperature (140 – 300 ºC). The process begins with the initiation step when highly active, free radicals are generated through thermolysis, photolysis, radiolysis, or redox decomposition of the initiator, which is typically based on organic peroxides or azo compounds. Driving force of radical process is based on exothermic conversion of π-bonds in the monomer into more stable, σ-bonds. The formed free radicals react with consecutive monomers which leads to growing polymer chain. The propagation step continues until the monomers are available. Afterwards radicals at the end of the chain either recombine or undergo disproportionation—a process involving the transfer of a hydrogen atom what create two distinct polymer chain (Figure 1). The radical process is primarily employed for the synthesis of LDPE because rapid, uncontrolled termination step handicap the polymerization of α-olefins such as propene and 1-butene.[33–35]

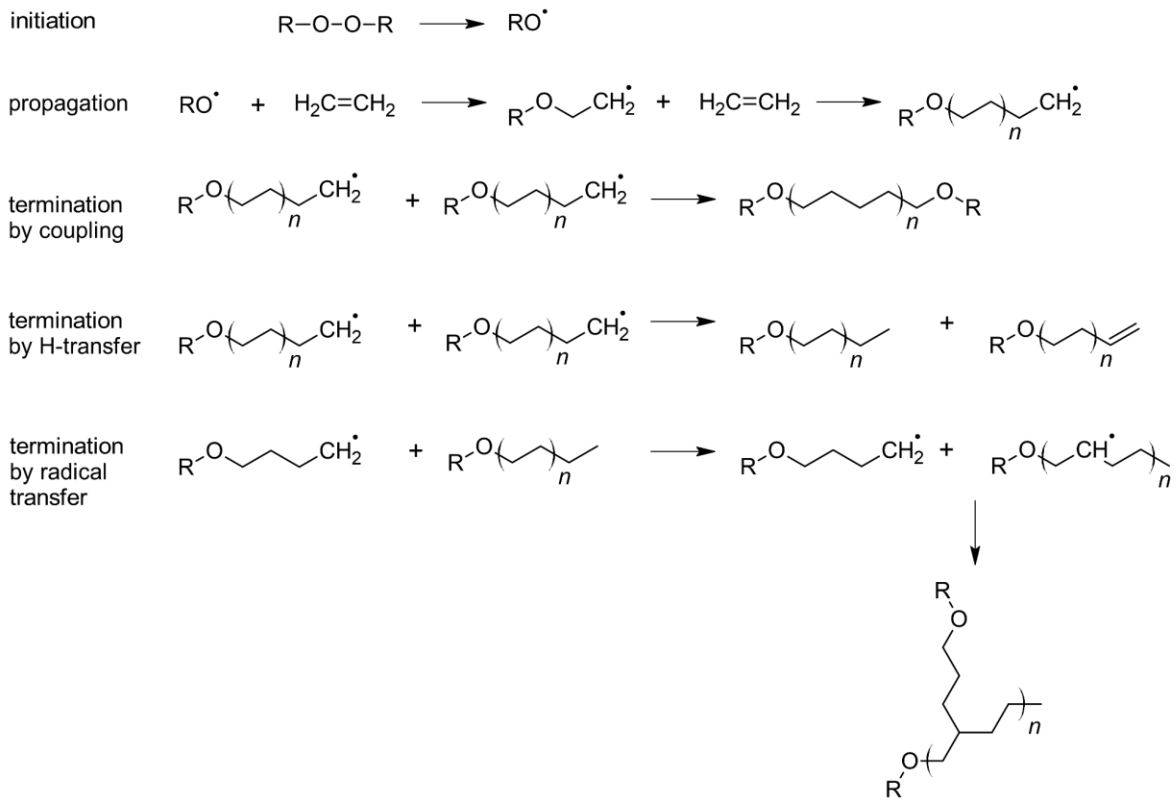

Figure 1. General pathway for LDPE polymerization via radical process.

1.2.2 Metathesis polymerization

Ring-Opening Metathesis Polymerization (ROMP) is a catalytic process based on the metathesis of cyclic olefins, such as cyclobutene, cyclopentene, or norbornene (bicyclo[2.2.1]hept-2-ene). The process exhibits a chain-growth mechanism and involves a metal-mediated exchange of alkene fragments through the breaking and reforming of carbon–carbon (C=C) double bonds. Transition metals with organic ligands are preferred as catalysts due to their homogeneous nature, which translates to easier process control. Catalytic activity can be tuned through proper ligand design. Ruthenium-based complexes, known as Grubbs catalysts, have gained the more popularity in olefin metathesis than molybdenum or tungsten-based complexes (Schrock catalyst) due to their higher activity, improved reaction control, and better resistance to air and functional groups (Figure 4). [36–40]

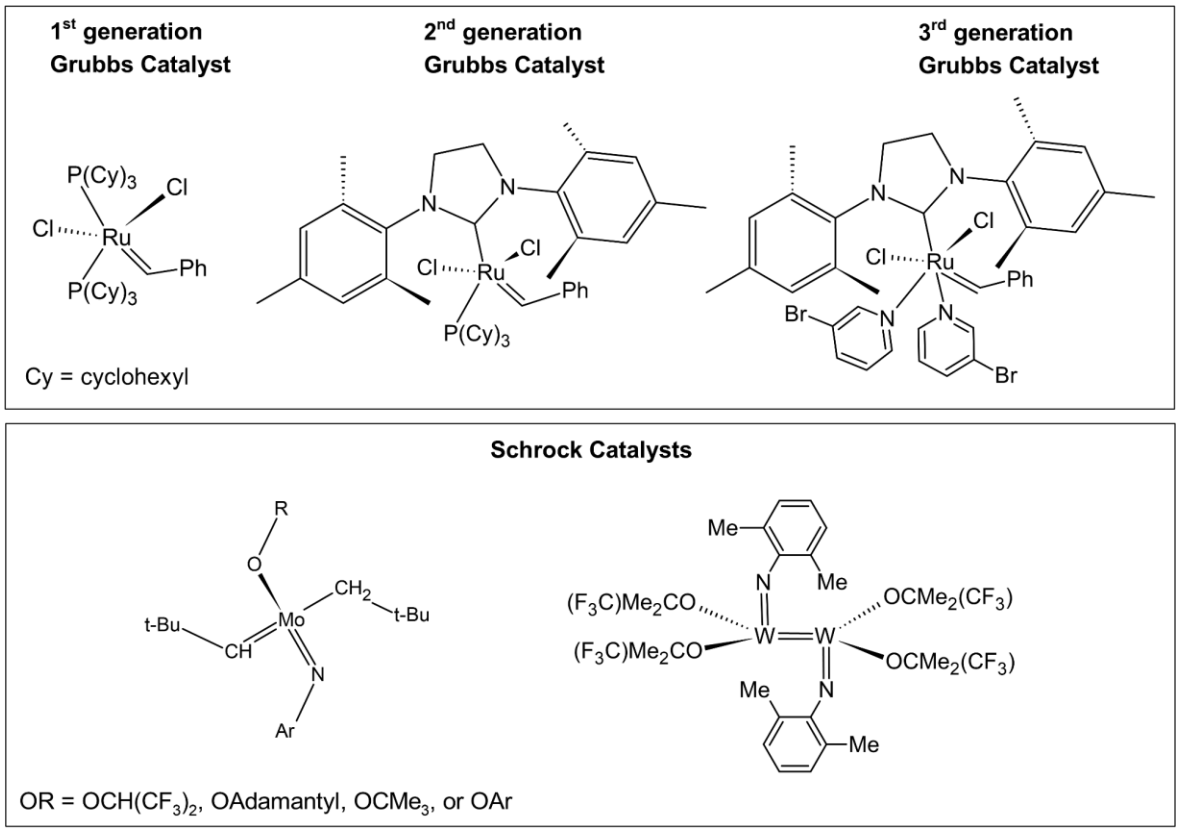

Figure 4. Ruthenium–carbene complexes (Grubbs catalyst) and molybdenum and tungsten-based complexes (Schrock catalyst) complexes.[36–40]

The initiation step of ROMP involves the coordination of a cyclic monomer by a transition metal complex.[41–43] As depicted in Figure 5, ROMP process is driven by the release of ring strain in cyclic olefins, which ultimately decreases entropy. This approach enables the synthesis of unique bio-based, degradable, and regioselective polymers, including amphiphilic block copolymers that form self-assembling micelles depending on the solvent used,[43–45] as well as disulfide-containing polyolefins, which facilitate degradation.[46,47]

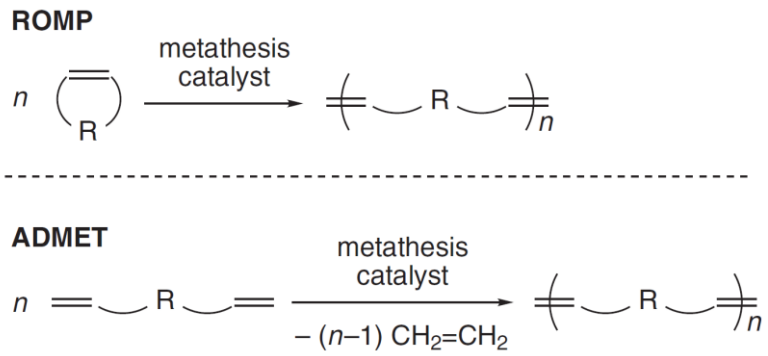

Figure 5. General schemes of metathesis–based polymerizations. [48] *Reproduced with permission from Springer Nature.*

Contrary to ROMP, Acyclic Diene Metathesis (ADMET) is a step-growth catalytic process involving the acyclic metathesis of α,ω-dienes.[48–51] The reaction can be catalyzed by either Grubbs or Schrock catalysts (Figure 4). However, the use of molybdenum- or tungsten-based complexes is limited due to their extreme sensitivity to water, air, and functional groups. Among the generations of Grubbs catalysts, the first generation remains the most useful in ADMET, as it has been shown that later generations induce side reactions, including intramolecular cyclization and isomerization of double bonds.[50] As presented in Figure 6, the ADMET process begins with the reaction of terminal olefins with a catalyst containing a metal–methylidene group. The resulting metal alkylidene complex then reacts with another terminal olefin, leading to polymer chain formation and the release of the catalyst. Since ADMET is a step-growth process, high conversion is required to achieve a high molecular weight polymer. Importantly, the polycondensation mechanism is driven by the continuous removal of volatile olefins.[52] One of the key advantages of ADMET is its ability to precisely incorporate functional branches along the polyethylene chain. Since the discovery of olefin metathesis by Professors Chauvin, Grubbs, and Schrock, the technology has been rapidly adopted in the polyolefin industry. In addition to polymerizations based on ROMP and ADMET, Olefin Conversion Technology (OCT), developed by Phillips Petroleum Company, provides a straightforward method for producing propylene from other olefins such as ethylene and but-2-ene.[53,54] Currently, ongoing academic research has focused on improvement of metathesis catalysis by using more sustainable and cost-efficient complexes mostly using first-row transition metals such as manganese and iron. Researchers are looking for a catalyst enable to introduce polar monomers and revealing better selectivity to minimize chain transfer, isomerization and cross-linking side reactions. Additionally, a metal-free approach using hydrazine for the ROMP of cyclobutenes, appears to be a promising strategy to enhance the efficiency of the chain transfer mechanism.[48,55,56]

1.2.3 Coordination polymerization

Coordination polymerization is a specific type of polymerization catalysed by transition metal salts and their complexes. The catalytic system relies on a wide range of heterogeneous supported catalysts (Ziegler-Natta catalysts) or

homogenous systems based on organometallic complexes (Single Site catalysts). Evolution of coordination polymerization has undergone significant transformation over the years.[57] The next generations of catalysts reveal improved selectivity, polymerization control and process efficiency.[58] For example, in 2011, Dow announced the implementation of the 6th generation of Ziegler-Natta (Z-N) catalysts, named CONSISTA™, where phthalate internal donors were replaced with non-phthalate alternatives to comply with new regulations in plastics processing. [59] Most of the commercially available polypropylene is produced using conventional Ziegler-Natta catalysts. Nevertheless, polypropylene-based products prepared using Single Site Catalysts (SSC) are gaining popularity year by year.[59]

1.2.3.1 Conventional Ziegler-Natta polymerization

Z-N catalysis is based on heterogeneous system that combines a transition metal, usually titanium tetrachloride ($TiCl_4$) or vanadium oxytrichloride ($VOCl_3$) supported on $TiCl_3$ (Figure 7, 1st generation Z-N catalyst), $MgCl_2$ or SiO_2.[60–62] Before the polymerization starts, the catalyst must be activated by a co-catalyst such as triethylaluminum ($Al(C_2H_5)_3$).

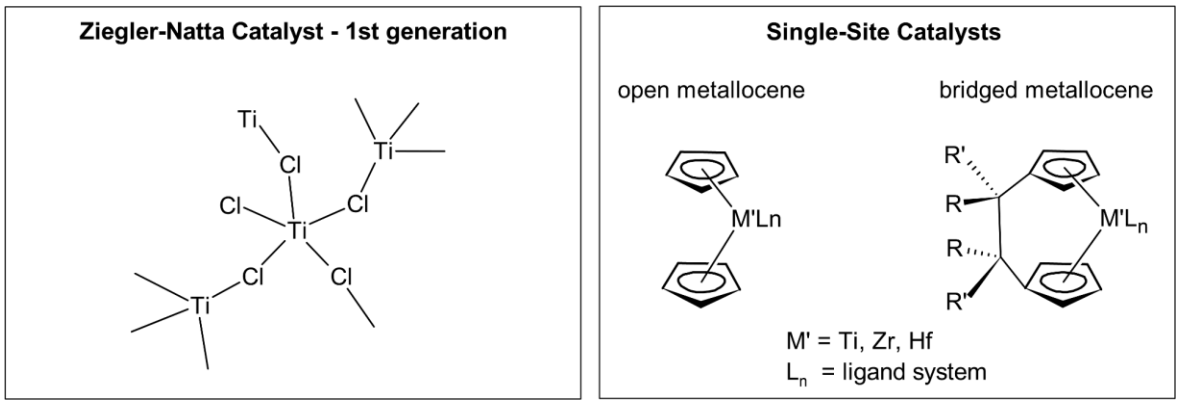

Figure 7. General structures for olefin polymerization catalysts: 1st generation Ziegler-Natta catalyst, open and bridged metallocene catalysts.[15,58]

As depicted in Figure 8, the polymerization process starts with a complexation step, during which the incoming olefin forms a π-complex with the active center of the catalyst. The interaction is enhanced by the co-catalyst, which creates a vacant coordination site on the metal. Next, the coordinated olefin undergoes stereospecific insertion into the carbon chain what determines the

tacticity of the growing polymer. The olefin's C=C bond interact with the metal center, forming a stable σ-bond between the metal and the terminal carbon. Interestingly, each second 40.000 monomer molecules are attached at a single metal center. The release of the polymer chain from the catalyst may occur through spontaneous β-H transfer / elimination or via the addition of a chain transfer agent (CTA), such as alkyl aluminum compounds, hydrogen, metal alkyls, or chlorinated hydrocarbons, which leads to the termination of the polymerization process.[63]

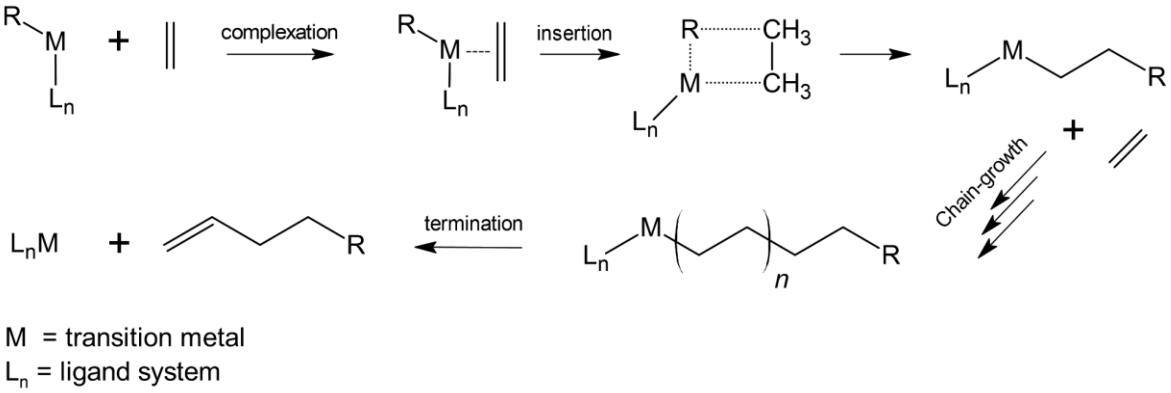

Figure 8. General mechanism of Ziegler Natta catalyzed polymerization of olefins.[58,64]

Migratory-insertion mechanism allows to obtain high molecular weight polymers, precisely control the branching, and stereoregularity of the polymer chain.[14] However, polyolefins produced by Z-N catalysts exhibit several drawbacks that limit their applications. For example, the broad molecular weight distribution (PDI > 2) of Z-N polyolefins significantly affects processability and mechanical strength. The catalytic system is extremely sensitive to moisture or oxygen residue, which leads to deactivation of the active site. Moreover, in Z-N catalysis, the incorporation of polar comonomers into the backbone is severely limited by the high affinity of polar groups for the active site, leading to catalyst deactivation. Z-N catalysts demonstrate lower activity and productivity compared to single-site catalysts.[14,65]

1.2.3.2 Single-site catalyst polymerization

Single-Site Catalysts (SSCs) are a group of homogenous systems based on open or bridged metallocene structures with well-defined and uniform active sites (Figure 7).[23,66] Thus, SSCs provide better control over polymer chain growth, higher

catalytic efficiency, and improved selectivity compared to Ziegler-Natta (Z-N) catalysts.[67] In the polymerization of alpha-olefins, SSCs are employed in a specific structure where a transition metal atom, usually titanium (Ti), zirconium (Zr), or hafnium (Hf), is sandwiched between two cyclopentadienyl (Cp) ligands. Similar to Z-N catalysts, metallocene complexes must first be activated by a co-catalyst. Importantly, in the case of single-site catalysts (SSCs), the catalyst is typically treated with methylaluminoxane (MAO), triethylaluminum (TEA), boranes, or (trityl or ammonium) borates. While the transition metal in SSCs is cationic in nature, the polymerization proceeds via a coordination–migratory insertion mechanism.[68] Similar to Z-N catalysis, after the initial activation of the catalyst, the positively charged metal centre exhibits a high affinity for olefin molecules. The process begins with the coordination of the olefin's π-electrons to the metal centre, facilitating its insertion into the metal-carbon bond. Subsequent olefin molecules are inserted in the same migratory-insertion manner. The spatial structure of the ligands determines the tacticity of the growing polymer chain. Polymerization termination can occur through β-hydride elimination, chain transfer to aluminum, or chain transfer to a monomer.

In 2006, researchers from Dow Chemical Company reported in *Science* a catalytic approach for producing unprecedented olefin block copolymers (OBCs).[69] Ariolla and co-workers proposed a single-reactor polymerization system based on two single-site catalysts (Figure 9) and diethylzinc (Et_2Zn) as a chain shuttling agent (CSA).

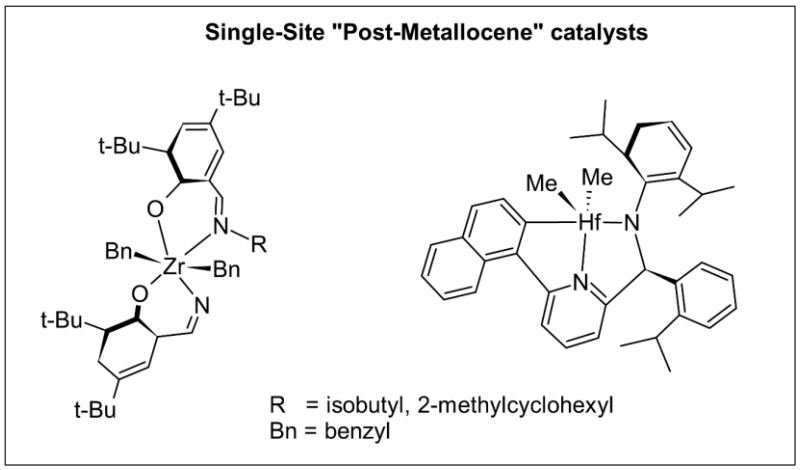

Figure 9. Examples of metal complexes employed for Chain Shuttling Polymerization (CSP).[69]

In contrast to traditional single-site catalysts (SSC), this “post-metallocenes” contain pyridylamido chelating ligands instead of a metallocene structure, which enables to obtain low and high selectivity toward different monomers. The application of a CSA facilitates the exchange of the growing polymer chain between the two catalysts. This powerful method (Figure 10), known as Chain Shuttling Polymerization (CSP), enables the production of olefin block copolymers like InFuse™, which combine semicrystalline and amorphous segments in a predetermined order. By varying the concentration of hard and soft blocks, it is possible to maintain a high melting point while tuning the glass transition temperature (T_g), thereby improving elasticity of the polyolefins.[70–72]

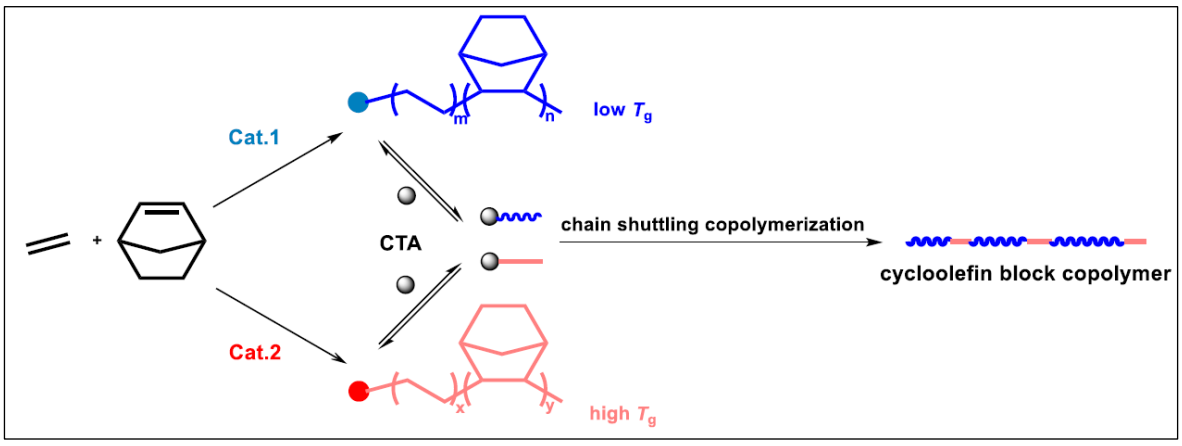

Figure 10. Copolymerization of ethene and bicyclo[2.2.1]hept-2-ene via Chain Shuttling Polymerization.[72] *Reprinted with permission from Macromolecules. Copyright © 2024, American Chemical Society.*

1.3 Worldwide production of polypropylene

1.3.1 Industrial classification of propylene based polymers.

The classification of polypropylene observed in the industry is directly related to the effects of its structure—such as chain branching, crystallinity, density, and molecular weight distribution—which translate into key properties like melt flow ratio (MFR) and stiffness/impact balance (Figure 11). Hence, producers categorize polypropylene (PP) grades into specific groups such as homopolymers, random copolymers, and impact polypropylene.[73,74]

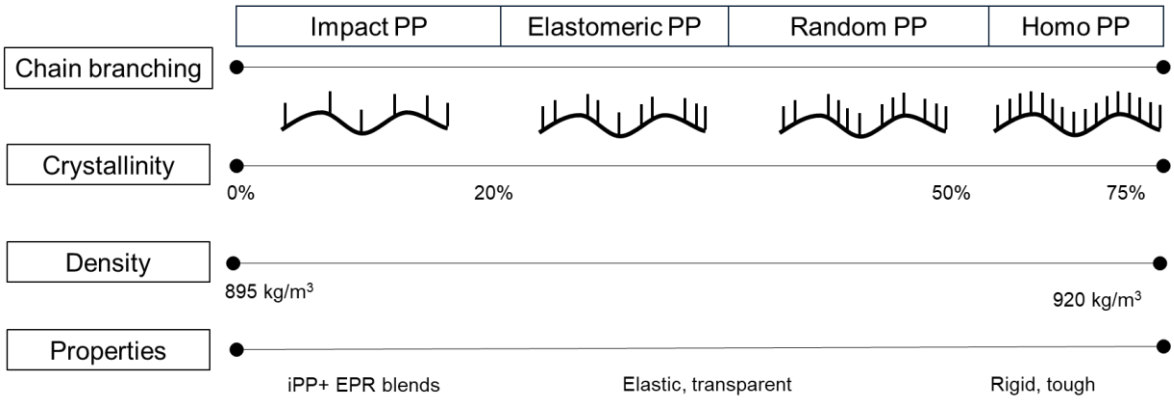

Figure 11. Schematic illustration of propylene-based copolymers.

Polypropylene homopolymers are characterized by excellent tensile strength, stiffness, and temperature resistance among all types of polypropylene-derived products, which makes them one of the most widely consumed single-grade plastic to date.[75]Nevertheless, their poor toughness, low-temperature impact resistance, and lack of functional groups limit their use in applications where elasticity at lower temperatures is required.[76] The compounding of homogeneous, semi-crystalline isotactic polypropylene (*i*PP) with elastomers such as ethylene-propylene-diene monomer (EPDM) or ethylene-propylene rubber (EPR) is commonly used in the production of thermoplastic polyolefins (TPOs). The resulting blends can be readily processed by injection molding, extrusion, or thermoforming, and are widely used in the automotive industry and household products.[77,78]

Polypropylene random copolymers are an important class of materials produced through the direct copolymerization of propylene with small amount of ethene, butene or higher alpha-olefins as comonomers. The level of randomly distributed alpha-olefin branches depends on the involved catalyst, reaching up to

7.3 mol% with Ziegler–Natta (Z-N) catalysts and as high as 20.8 mol% with single-site catalysts (SSC). Increasing the incorporation of branches along the polypropylene chain reduces the crystallization ratio and lamellar thickness, which enables the production of softer, more elastic, and more transparent PP-based materials[59,79]

Impact PPs are class of polymer materials with significantly enhanced impact strength. In contrast to random copolymers, impact PPs exhibit a heterophasic structure, in which a rubber phase (e.g., ethylene–propylene rubber, EPR) is dispersed within a semi-crystalline PP homopolymer matrix. Most commercially available impact PPs contain up to 30% rubber phase, while researchers are developing high-impact polypropylenes (HIPPs) with rubber contents reaching as high as 70%.[80–84]

1.3.2 Processes applied in the industry to produce polypropylene homopolymer and copolymers.

Polypropylene is primarily produced as semi-crystalline isotactic polypropylene (*i*PP), which contains less than 5 wt% of atactic polypropylene (*a*PP) as a by-product.[85] The majority of commercially available *i*PPs are synthesized through coordination polymerization using heterogeneous Ziegler–Natta (Z-N) catalysts, with aluminum alkyl compounds as co-catalysts and organic esters to control stereoselectivity.[86–88] The consolidation of global chemical corporations—such as ExxonMobil, Chevron-Phillips, Braskem, and LyondellBasell—has significantly accelerated research on novel strategies employing technologies based on single-site catalysts (SSCs).[89]

Polypropylene is primarily characterized by its density, which is controlled through stereoregularity of the polymer chain. Traditionally, most industrially available PP grades exhibit an isotactic index of approximately 94.5–97.5%. Notably, advances in organometallic chemistry have significantly improved control over stereoselectivity, enabling the production of highly isotactic polymers with tacticity reaching up to 99.5%.[14] Some manufacturers intentionally produce grades with elevated levels of *a*PP for specialized applications such as adhesives, self-healing materials, and viscosity modifiers.[90] *i*PP and their copolymers can be produced via gas-phase, slurry, solution, or combined gas-solution technologies, typically without any by-product formation.[30]

The gas-phase polymerization of propene occurs in fluidized bed reactor (FBR) in a moderate temperature around 85 °C and pressures up to 40 atm involving chromium, Z-N or metallocene catalyst. Historically, the first gas-phase process was introduced by BASF in the late 1960s, initially producing only homopolymer polypropylene in a single reactor. Subsequent developments in catalysis enabled the application of gas-phase technology for producing bimodal isotactic polypropylene (*i*PP) copolymers.[91] Today, gas-phase technologies account for approximately 48.5% of global polypropylene production capacity and are dominated by three major processes: Novolen (Lummus), Unipol (W.R. Grace), and Innovene (INEOS).[75,92] As shown in Figure 12, gas-phase polymerization can be operated in single, parallel, or cascade modes, depending on the desired morphology of the polypropylene. In each reactor, a chain transfer agent (CTA) is added to control the molecular weight. The obtained polypropylene is continuously collected and directed to the first-stage degassing vessel, where unreacted monomer is recovered and pumped back into the feed line. Subsequently, the homopolymer iPP obtained in the first stage is transferred to a second gas-phase fluidized or stirred-bed reactor where additional ethylene-propylene copolymerization occurs within the pores of the semi-crystalline iPP, enhancing its impact resistance.[83]

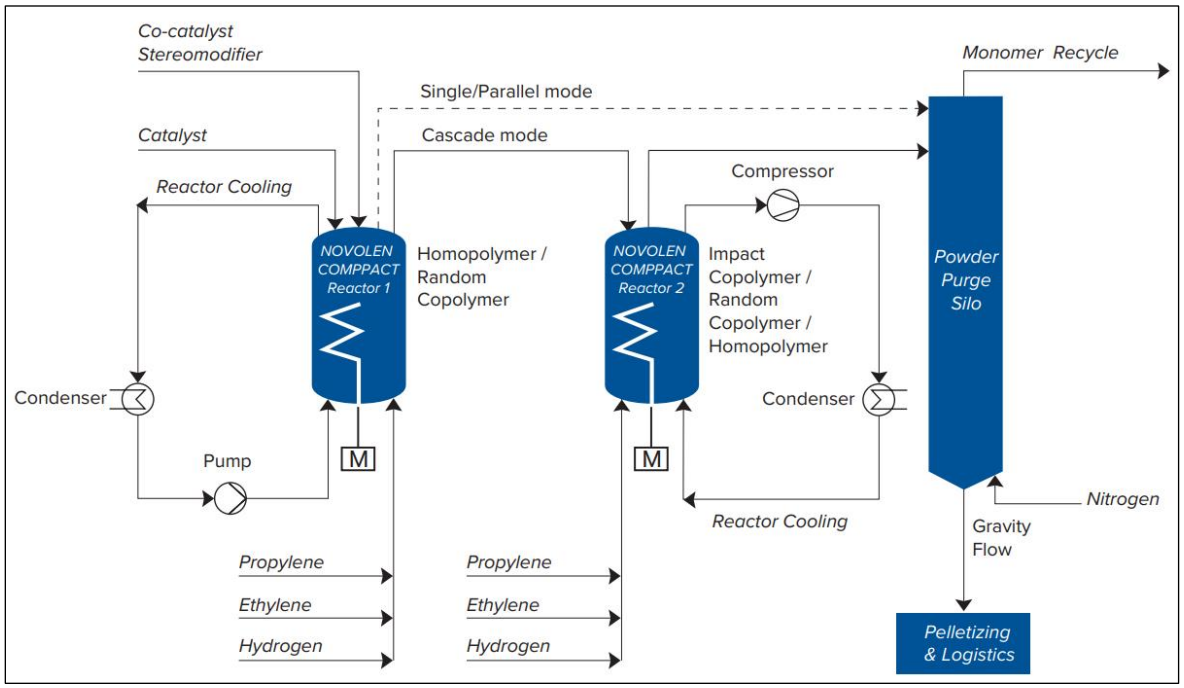

Figure 12. Flow diagram of polypropylene gas-phase process based on Lummus Novolen Technology.[93]

Slurry process involves a liquid olefin (polymerization in bulk) or additional inert diluent, as a carrier for the suspension of the solid catalyst.[94] Slurry mixture is precisely fed into reactor system, where polymerization typically takes place under below 75 °C. Production of polypropylene copolymers via slurry process consisting of but-1-ene, hex-1-ene, or oct-1-ene takes place in a cascade continuous stirred-tank reactor (CSTR) or cascade loop system involving either Z-N or metallocene catalyst.[95] Depending on the type of medium used, solid polymer particles suspended in the diluent can be directly flushed from the reactor under reduced pressure or removed by a centrifugal pump. In some cases, post-polymerization de-ashing may be necessary to remove catalyst residues and by-products. Importantly, polyolefins from the slurry process reveal a narrower PDI than those from the gas-phase process. Grades produced via this process are generally limited to a melt index of up to 150 g/min.[94] Technologies based on combined gas-phase and slurry polymerization, where supercritical propene is employed, are provided by major players such as Borealis (Borstar® - cascade loop reactor), Chevron Phillips (MarTECH™ Loop Slurry Process), LyondellBasell (Spheripol®, loop reactor), and Mitsui (CX technology, stirred tank reactor system).

Solution polymerization, similar to the slurry process, occurs in a homogenous liquid phase.[96] However, polymer formed during the solution process remains dissolved in the diluent used. This process is gaining popularity year by year due to the simplicity of the reactor system, the uniform and well-defined structures of produced polymers, and better control over the generated heat, which is removed via a reflux system. Examples of novel polyolefins produced via solution polymerization include Fortify™ (provided by Sabic SK Nexlene Co.), Vistamaxx™ (ExxonMobil), and Tafmer™ (Mitsui Chemicals).

1.3.3 Forecast and analysis of the polypropylene market [31,32,75]

Since the first industrial implementation of *i*PP in the early 1960s, polypropylene has gained popularity in both everyday and niche applications.[31,75] The consumption of *i*PP is primarily driven by the packaging, automotive, and construction sectors. Polypropylene plays a crucial role in modern, lightweight, and durable packaging solutions. According to the S&P Global Commodity (former IHS Markit), over the last decade, global *i*PP production has continued to grow dynamically at an average rate of around 5 % per year, reaching 108. 7 million metric

tons (MMt) in 2023, which constitutes 23.3 % of all produced plastics.[75] Figure 13 provides insight into the scale of production and consumption of virgin and recycled polypropylene around the world. Interestingly, China is responsible for 51.5% of worldwide PP production, while Europe covers only 10.6%. Although the supply-demand balance in the PP market is relatively even across all continents, European consumption—especially in Eastern Europe—is supported by imports.

Growing social awareness and legislative emphasis on the circular economy have translated into an increasing demand for recycled materials, which accounted for 6.2% of total production capacity in 2023. The production of recycled PP is still niche, so the produced PP is almost completely consumed within particular regions. It is estimated that European market will compete with China to be a leader in the production of recycled PP.

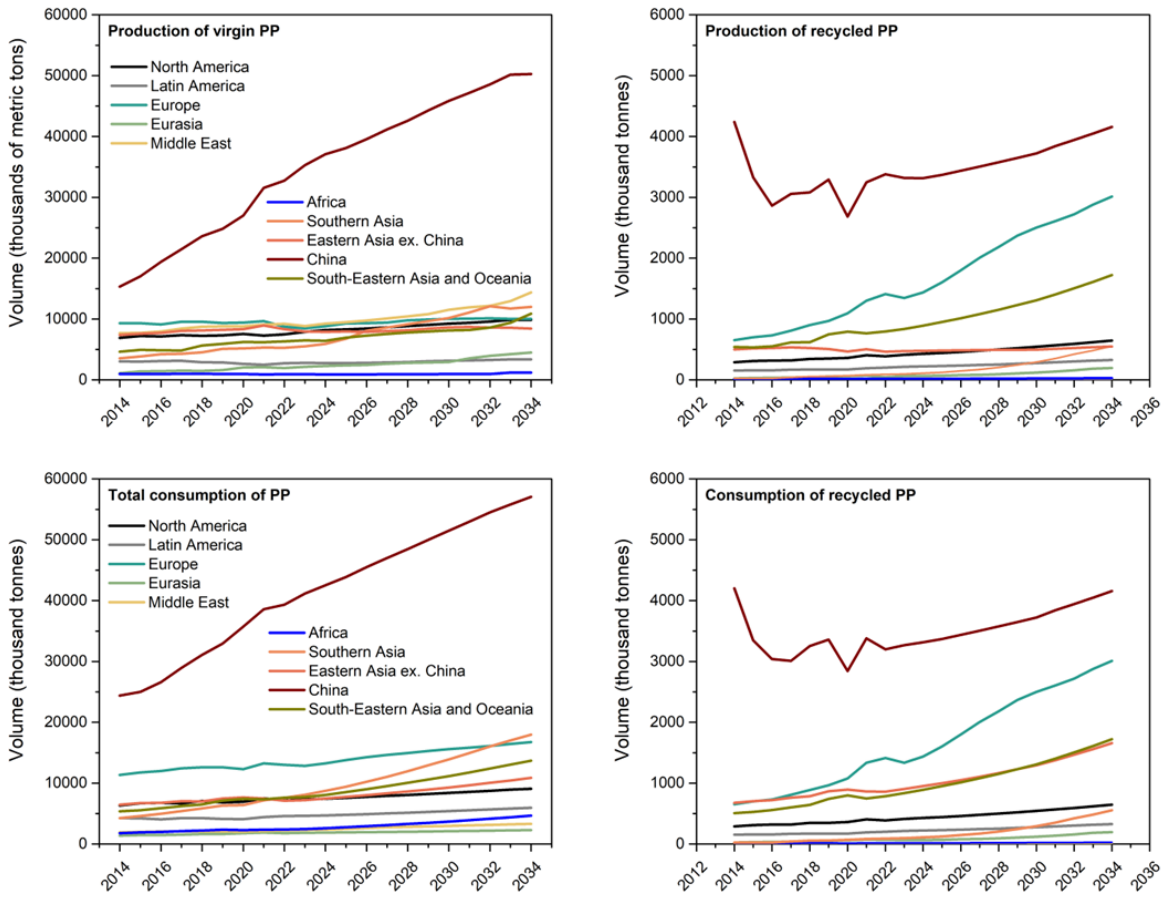

Figure 13. World supply / demand for virgin and recycled polypropylene.

1.4 Advances in polypropylene resins

Despite fantastic properties of polypropylene, which makes it's the most suitable material for circular economy, lack of functionality limits its application in some areas. Over the last 20 years, extensive research into the catalytic activation of the C(sp^3)-H bond in polyolefins has led to several strategies for introducing of polar moieties into the carbon chain. The introduction of functional groups seems to be an interesting improvement of polyolefin properties with special reference to adhesion to metals, compatibilization of polymer waste streams, and its use as viscosity modifiers. Considering morphology, four categories of functional polyolefins can be distinguished: randomly functionalized copolymers with linear or branched morphology, chain-end functionalized copolymers, block and graft copolymers. Functionality can be introduced into polyolefins by different methods, ranging from surface pretreatment, post-polymerization or in-reactor functionalization. For example, the high-pressure radical copolymerization process of ethylene and vinyl comonomers enables the synthesis of products such as EVA and ethylene–acrylate copolymers with a wide range of functionality levels. However, this strategy requires harsh conditions and is restricted to LDPE-like products. Another proven route toward functionalized polypropylene is peroxide-initiated grafting of functionalized substrates such as maleic anhydride and acrylates via reactive extrusion (REX). Yet, competitive side reactions such as crosslinking or β-scission typically result in ill-defined products. Considering REX, the main problem with this approach for producing functionalized polyolefin materials is that the amount of functionality and the overall molecular structure of the polymers are difficult to control. Furthermore, the higher upper limit for the processing temperature excludes functional polyolefins from many potential applications. There remains a need for a process that provides well-controlled polymer functionalization and allows for the accurate tuning of the final, highly performant functionalized material with desired properties. Whereas randomly functionalized polyethylene can be produced by the high-pressure radical process, functionalized propylene-based copolymers with a well-defined polymer microstructure and sufficient incorporation of functionality can only be prepared by catalytic copolymerization of propylene and functionalized comonomers. Despite relevant progress in the (co)polymerization of ethylene and higher α-olefins, synthesis with propylene remains challenging.

In-reactor functionalization (IRF) can enable the production of well-defined and scalable products that will greatly expand the application window of polyolefins and help penetrate application areas traditionally dominated by high-performance, expensive copolymers. Hydroxyl-functionalized propylene-based terpolymers obtained via IRF belong to the group of promising products that can mitigate the above-mentioned limitations of functionalized materials. The unusual properties of hydroxyl-functionalized *i*PP terpolymers suggest that the precise formulation of these polymers could provide solutions to common problems in many industrial fields.

1.5 Outline of this thesis

The objectives of this PhD thesis are focused on the characterization of the chemical structure and properties of functionalized polyolefins (FPOs) obtained via IRF, with a special emphasis on randomly OH-functionalized polypropylene, as well as amphiphilic block and graft copolymers thereof. The major purpose of executing investigation is to propose novel applications for FPO-based products, which cannot be fulfilled by standard polyolefins like polyethylene or polypropylene.

Chapter 2 focuses on the synthesis and characterization of FPOs that can be applied as hot melt adhesives, with the main emphasis on adhering glass-filled *i*PP to aluminum or steel—an application particularly relevant in the automotive sector. In recent years, the rapid development of high-performance lightweight materials has demanded excellent adhesion to a vast range of individual components. Polyolefins account for over 65% of all polymers, and due to the aforementioned advantages, are a major component of lightweight constructions. Hybrid systems, employing, for example, metal and polymer surfaces, are commonly used in a wide range of applications such as automotive, encapsulation of electronic devices, furniture, and construction. Although various adhesive solutions are available for polar polymers, it is extremely difficult to bond polar substrates to polyolefins due to their low surface free energy, chemical inertness, and absence of functional groups. The presented research includes an investigation of FPOs as hot melt adhesives, whose amphiphilic character allows adhesion to polar substrates (viz. aluminum, steel) as well as apolar materials like standard polyolefins.[97] Importantly, the research also presents a novel approach to adjusting adhesive performance by blending functionalized propylene copolymers with non-functionalized counterparts,

offering a promising, cost-saving alternative for tuning adhesive strength at an industrial scale.[98]

Chapter 3 focuses on in-house synthesized FPO-based amphiphilic copolymers and polyolefin-like polyesters as compatibilizers for polyolefin blends. The research involves a meticulous examination through the preparation of a series of two- and three-component PP/polycarbonate (PC) and PP/polyethylene (PE) blends to determine the inherent potential of the synthesized compatibilizers. Among all polymers, polyolefins play by far the most prominent role in our daily life. It is remarkable that, based on only a handful of monomeric building blocks, such a wide range of polymers with different chemical composition and topologies has been produced. With applications in packaging, automotive, building, and construction, polyolefins are ubiquitous and are progressively taking over positions originally reserved for engineering plastics. However, especially as packaging materials, the lifetime of polyolefins is unsettlingly short before disposal. There is increasing societal awareness of the need to recycle plastics. The mechanical recycling of plastics represents a rational approach to repurposing abandoned polymer products; however, numerous challenges must be overcome. One significant challenge is the differentiation of polymer waste stream. Despite availability of advanced sorting technologies to isolate mixed plastic waste, the separation of distinct polyolefin types is hindered. Despite their structural similarities, different polyolefins exhibit a limited miscibility, and mixtures of these materials generally display inferior optical and mechanical characteristics. Therefore, it is essential to identify strategies that enhance the mechanical properties of polyolefin blends to yield high-performance materials from recycled polymers by their compatibilization.

1.6 References

(1) Goodyear, C. Improvement in the Process of Divesting Caoutchouc, Gum-Elastic, or India-Rubber of Its Adhesive Properties, and Also of Bleaching the Same, and Thereby Adapting It to Various Useful Purposes. US240A, **1837**.

(2) Lunn, R. W. CHARLES GOODYEAR, 1800–1860. *Ind. Eng. Chem.* **1939**, 31 (10), 1190–1192.

(3) Sebrell, L. B. Charles Goodyear Memorial Lecture. The Second Mile. *Ind. Eng. Chem*. **1943**, 35 (7), 735–750.

(4) Calzonetti, J. A.; Laursen, C. J. PATENTS OF CHARLES GOODYEAR: HIS INTERNATIONAL CONTRIBUTIONS TO THE RUBBER INDUSTRY. *Rubber Chemistry and Technology* **2010**, 83 (3), 303–321.

(5) Wagner, B. E. Leo Baekeland's Legacy – 100 Years of Plastics. In 100+ Years of Plastics. Leo Baekeland and Beyond; *ACS Symposium Series* **2011**, 1080, pp 31–67.

(6) Baekeland, L. H. Impress of Chemistry upon Industry Bakelite, an Example. *Ind. Eng. Chem*. **1935**, 27 (5), 538–543.

(7) Malpass, D. B., Free Radical Polymerization of Ethylene. *In Introduction to Industrial Polyethylene*; John Wiley & Sons, Inc.: Hoboken, NJ, **2010**; pp 23−32.

(8) Froese, R. D.; Arriola, D. J.; den Doelder, J.; Hou, J.; Kashyap, T.; Lu, K.; Martinetti, L.; Stubbert, B. D. A Commercially Viable Solution Process to Control Long-Chain Branching in Polyethylene. *Science* **2024**, 383 (6688), 1223–1228.

(9) Peacock, A. Handbook of Polyethylene: Structures: Properties, and Applications (1st edition) **2000**; CRC press.

(10) Platzer, N. Branched Polyethylene. LDPE and LLDPE. *Industrial & Engineering Chemistry Product Research and Development* **1983**, 22 (1), 158–160.

(11) S&P Global, IHS Markit. Polyethylene Resins, Low-Density (LDPE) *Chemical Economy Handbook* **2024**.

(12) Ziegler, K.; Holzkamp, E.; Breil, H.; Martin, H. Das Mülheimer Normaldruck-polyäthylen-verfahren. *Angewandte Chemie* **1955**, 67 (19-20), 541–547.

(13) Natta, G. Stereospezifische Katalysen Und Isotaktische Polymere. *Angewandte Chemie* **1956**, 68 (12), 393–403.

(14) Kaminsky, W. Polyolefins: 50 Years after Ziegler and Natta II. Advances in Polymer Science, Polyolefins by Metallocenes and Other Single-Site Catalysts, Advances in Polymer Science **2013**, vol 258. Springer

(15) Eisch, J. J. Fifty Years of Ziegler–Natta Polymerization: From Serendipity to Science. A Personal Account. *Organometallics* **2012**, 31 (14), 4917–4932.

(16) Haenel, M. W. Historical Landmarks of Chemistry: Karl Ziegler. Max-Planck-Institut für Kohlenforschung, **2008**.

(17) McGuinness, D. S.; Davies, N. W.; Horne, J.; Ivanov, I. Unraveling the Mechanism of Polymerization with the Phillips Catalyst. *Organometallics* **2010**, 29 (22), 6111–6116.

(18) Hogan, J. P.; Banks, R. Polymers and Production Thereof, US2825721A, **1958**.

(19) Groppo, E.; Martino, G. A.; Piovano, A.; Barzan, C. The Active Sites in the Phillips Catalysts: Origins of a Lively Debate and a Vision for the Future. *ACS Catal.* **2018**, 8 (11), 10846–10863.

(20) MacAdams, L. A.; Buffone, G. P.; Incarvito, C. D.; Rheingold, A. L.; Theopold, K. H. A Chromium Catalyst for the Polymerization of Ethylene as a Homogeneous Model for the Phillips Catalyst. *J. Am. Chem. Soc*. **2005**, 127 (4), 1082–1083.

(21) Brown, C.; Lita, A.; Tao, Y.; Peek, N.; Crosswhite, M.; Mileham, M.; Krzystek, J.; Achey, R.; Fu, R.; Bindra, J. K.; Polinski, M.; Wang, Y.; van de Burgt, L. J.; Jeffcoat, D.; Profeta, S. Jr.; Stiegman, A. E.; Scott, S. L. Mechanism of Initiation in the Phillips Ethylene Polymerization Catalyst: Ethylene Activation by Cr(II) and the Structure of the Resulting Active Site. *ACS Catal*. **2017**, 7 (11), 7442–7455.

(22) Sinn, H.; Kaminsky, W.; Vollmer, H.-J.; Woldt, R. “Living Polymers” on Polymerization with Extremely Productive Ziegler Catalysts. *Angew. Chem., Int. Ed.* **1980**, 19 (5), 390–392.
(23) De Rosa, C.; Auriemma, F.; Spera, C.; Talarico, G.; Tarallo, O. Comparison between Polymorphic Behaviors of Ziegler−Natta and Metallocene-Made Isotactic Polypropylene: The Role of the Distribution of Defects in the Polymer Chains. *Macromolecules* **2004**, 37 (4), 1441–1454.
(24) Astruc, D. *In Olefin Metathesis: Theory and Practice*; John Wiley & Sons, Inc.: Hoboken, **2014**; pp 1−36.
(25) Schrock, R. R. Living Ring-Opening Metathesis Polymerization Catalyzed by Well-Characterized Transition-Metal Alkylidene Complexes. *Acc. Chem. Res.* **1990**, 23 (5), 158–165.
(26) Nguyen, S. T.; Grubbs, R. H.; Ziller, J. W. Syntheses and Activities of New Single-Component, Ruthenium-Based Olefin Metathesis Catalysts. *J. Am. Chem. Soc.* **1993**, 115 (21), 9858–9859.
(27) Sun, Z.; Liu, B.; Ma, M.; Alexander-Katz, A.; Ross, C. A.; Johnson, J. A. ROMP of Macromonomers Prepared by ROMP: Expanding Access to Complex, Functional Bottlebrush Polymers. *J. Am. Chem. Soc*. **2025**, 147 (4), 3855–3865.
(28) Gitter, S. R.; Li, R.; Boydston, A. J. Access to Functionalized Materials by Metal-Free Ring-Opening Metathesis Polymerization of Active Esters and Divergent Postpolymerization Modification. *ACS Macro Lett*. **2024**, 13 (2), 144–150.
(29) Lee, H.-K.; Choi, T.-L. Unusual Superior Activity of the First Generation Grubbs Catalyst in Cascade Olefin Metathesis Polymerization. *ACS Macro Lett*. **2018**, 7 (5), 531–535.
(30) Jasinska-Walc, L.; Bouyahyi, M.; Duchateau, R. Potential of Functionalized Polyolefins in a Sustainable Polymer Economy: Synthetic Strategies and Applications. *Acc. Chem. Res.* **2022**, 55 (15), 1985–1996.
(31) Grand View Research. Polyolefin Market Size, Share & Trends Analysis Report; **2023**.
(32) Grand View Research. Plastic Market Size, Share & Trends Analysis Report. **2023**.
(33) Häußler, M.; Eck, M.; Rothauer, D.; Mecking, S. Closed-Loop Recycling of Polyethylene-like Materials. *Nature* **2021**, 590 (7846), 423–427.
(34) Burdett, I. D.; Eisinger, R. S. Ethylene Polymerization Processes and Manufacture of Polyethylene. *In Handbook of Industrial Polyethylene and Technology*; *2017*; pp 61–103.
(35) Wang, X.; Wang, S.; Song, S.; Chen, Y.; Sun, H.; Zhu, C. Group Transfer Radical Polymerization for the Preparation of Carbon-Chain Poly(α-Olefins). *Sci. Adv.* **2025**, 10 (39), eadp7385.
(36) Schrock, R. Multiple Metal-Carbon Bonds for Catalytic Metathesis Reactions. Nobel Lecture. **2005**.
(37) Gulyás, H.; Hayano, S.; Madarász, Á.; Pápai, I.; Szabó, M.; Bucsai, Á.; Martin, E.; Benet-Buchholz, J. Air-Stable 18-Electron Adducts of Schrock Catalysts with Tuned Stability Constants for Spontaneous Release of the Active Species. Commun. Chem. **2021**, 4 (1), 71.
(38) Schrock, R. R.; Murdzek, J. S.; Bazan, G. C.; Robbins, J.; DiMare, M.; O’Regan, M. Synthesis of Molybdenum Imido Alkylidene Complexes and Some Reactions Involving Acyclic Olefins. J. Am. Chem. Soc. **1990**, 112 (10), 3875–3886.

(39) Blencowe, A.; Qiao, G. G. Ring-Opening Metathesis Polymerization with the Second Generation Hoveyda–Grubbs Catalyst: An Efficient Approach toward High-Purity Functionalized Macrocyclic Oligo(Cyclooctene)s. J. Am. Chem. Soc. **2013**, 135 (15), 5717–5725.

(40) Kang, E.-H.; Yu, S. Y.; Lee, I. S.; Park, S. E.; Choi, T.-L. Strategies to Enhance Cyclopolymerization Using Third-Generation Grubbs Catalyst. J. Am. Chem. Soc. **2014**, 136 (29), 10508–10514.

(41) Hayano, S.; Nakama, Y. Iso- and Syndio-Selective ROMP of Norbornene and Tetracyclododecene: Effects of Tacticity Control on the Hydrogenated Ring-Opened Poly(Cycloolefin)s. *Macromolecules* **2014**, 47 (22), 7797–7811.

(42) Mandal, I.; Mandal, A.; Rahman, M. A.; Kilbinger, A. F. M. Chain Transfer Agents for the Catalytic Ring Opening Metathesis Polymerization of Norbornenes. Chem. Sci. **2022**, 13 (42), 12469–12478.

(43) Gaucher, G.; Dufresne, M.-H.; Sant, V. P.; Kang, N.; Maysinger, D.; Leroux, J.-C. Block Copolymer Micelles: Preparation, Characterization and Application in Drug Delivery. *Journal of Controlled Release* **2005**, 109 (1), 169–188.

(44) Förster, S.; Plantenberg, T. From Self-Organizing Polymers to Nanohybrid and Biomaterials. *Angew. Chem., Int. Ed* **2002**, 41 (5), 688–714.

(45) Rodríguez-Hernández, J.; Chécot, F.; Gnanou, Y.; Lecommandoux, S. Toward 'Smart' Nano-Objects by Self-Assembly of Block Copolymers in Solution. *Prog. Polym. Sci.* **2005**, 30 (7), 691–724.

(46) Chang, C.-C.; Emrick, T. Functional Polyolefins Containing Disulfide and Phosphoester Groups: Synthesis and Orthogonal Degradation. *Macromolecules* **2014**, 47 (4), 1344–1350.

(47) Seong, H. G.; Russell, T. P.; Emrick, T. Degradable Polyolefins Prepared by Integration of Disulfides into Metathesis Polymerizations with 3,6-Dihydro-1,2-Dithiine. *Chemical Science* **2024**, 15, 17084−17091.

(48) Sutthasupa, S.; Shiotsuki, M.; Sanda, F. Recent Advances in Ring-Opening Metathesis Polymerization, and Application to Synthesis of Functional Materials. *Polym. J*. **2010**, 42 (12), 905–915.

(49) Kempel, S. J.; Hsu, T.-W.; Nicholson, J. L.; Michaudel, Q. Cis-Selective Acyclic Diene Metathesis Polymerization of α,ω-Dienes. *J. Am. Chem. Soc*. **2023**, 145 (23), 12459–12464.

(50) Liu, S.; Yan, J.; Zhang, Q.; Yan, Y. Acyclic Diene Metathesis (ADMET) as Powerful Tool for Functional Polymers with Versatile Architectures. *J. Inorg. Organomet. Polym. Mater*. **2022**, 32 (9), 3368–3394.

(51) Caire da Silva, L.; Rojas, G.; Schulz, M. D.; Wagener, K. B. Acyclic Diene Metathesis Polymerization: History, Methods and Applications. *Prog. Polym. Sci*. **2017**, 69, 79–107.

(52) Pribyl, J.; Wagener, K. B.; Rojas, G. ADMET Polymers: Synthesis, Structure Elucidation, and Function. *Mater. Chem. Front*. **2021**, 5 (1), 14–43.

(53) Banks, R. L.; Bailey, G. C. Olefin Disproportionation. A New Catalytic Process. *Industrial & Engineering Chemistry Product Research and Development* **1964**, 3 (3), 170–173.

(54) Freeman, J.W.; Buster J.L.; Knudsen, R.D.; Olefin production. US5856257A, **1997**.

(55) Ogawa, K. A.; Goetz, A. E.; Boydston, A. J. Metal-Free Ring-Opening Metathesis Polymerization. *J. Am. Chem. Soc.* **2015**, 137 (4), 1400–1403.

(56) Leguizamon, S. C.; Lyons, K.; Monk, N. T.; Hochrein, M. T.; Jones, B. H.; Foster, J. C. Additive Manufacturing of Degradable Materials via Ring-Opening Metathesis Polymerization (ROMP). *ACS Appl. Mater. Interfaces* **2022**, 14 (45), 51301–51306.
(57) Baier, M. C.; Zuideveld, M. A.; Mecking, S. Post-metallocenes in the industrial production of polyolefins. *Angew. Chem., Int. Ed*. **2014**,53 (37), 9722−9744.
(58) Paghadar, B. R.; Sainani, J. B.; M., S. K.; Bhagavath, P. Internal Donors on Supported Ziegler Natta Catalysts for Isotactic Polypropylene: A Brief Tutorial Review. *Journal of Polymer Research* **2021**, 28 (10), 402.
(59) Paulik, C.; Tranninger, C.; Wang, J.; Shutov, P.; Mileva, D.; Gahleitner, M. Catalyst Type Effects on Structure/Property Relations of Polypropylene Random Copolymers. *Macromol. Chem. Phys.* **2021**, 222 (23), 2100302.
(60) Hagen, H.; Boersma, J.; van Koten, G. Homogeneous Vanadium-Based Catalysts for the Ziegler–Natta Polymerization of α-Olefins. *Chem. Soc. Rev*. **2002**, 31 (6), 357–364.
(61) Zeynali, M.; Ranjbarbaranlo, H.; Olad, A. Study of Titanium/Vanadium Ziegler–Natta Hybrid Catalysts Performance in Slurry-Phase Ethylene Polymerization for Producing Polyethylene with Broad/Bimodal Molecular Weight Distribution. *Journal of Polymer Research* **2023**, 30 (3), 100.
(62) Vittoria, A.; Meppelder, A.; Friederichs, N.; Busico, V.; Cipullo, R. Demystifying Ziegler–Natta Catalysts: The Origin of Stereoselectivity. *ACS Catal.* **2017**, 7 (7), 4509–4518.
(63) Yu, Y.; Fu, Z.; Fan, Z. Chain Transfer Reactions of Propylene Polymerization Catalyzed by AlEt3 Activated TiCl4/MgCl2 Catalyst under Very Low Monomer Addition Rate. *J. Mol. Catal. A Chem.* **2012**, 363–364, 134–139.
(64) Amor Nait Ajjou, J.; Scott, S. L. A Kinetic Study of Ethylene and 1-Hexene Homo- and Copolymerization Catalyzed by a Silica-Supported Cr(IV) Complex: Evidence for Propagation by a Migratory Insertion Mechanism. *J. Am. Chem. Soc.* **2000**, 122 (37), 8968–8976.
(65) Wang, Y.; Wang, Q.; Tan, C.; Chen, C. Synthesis of Polar-Functionalized Isotactic Polypropylenes Using Commercial Heterogeneous Ziegler–Natta Catalyst. *J. Am. Chem. Soc.* **2024**, 146 (10), 6837–6845.
(66) Zaera, F. Designing Sites in Heterogeneous Catalysis: Are We Reaching Selectivities Competitive With Those of Homogeneous Catalysts? *Chem. Rev.* **2022**, 122 (9), 8594–8757.
(67) Kaminsky, W. The discovery and evolution of metallocene-based olefin polymerization catalysts. *Rend. Lincei* **2017**, 28 (1), 87−95.
(68) Ostoja Starzewski, A.; Steinhauser, N.; Xin, B. S. Decisive Progress in Metallocene-Catalyzed Elastomer Synthesis. *Macromolecules* **2008**, 41 (12), 4095–4101.
(69) Arriola, D. J.; Carnahan, E. M.; Hustad, P. D.; Kuhlman, R. L.; Wenzel, T. T. Catalytic Production of Olefin Block Copolymers via Chain Shuttling Polymerization. *Science* **2006**, 312 (5774), 714–719.
(70) Mundil, R.; Bravo, C.; Merle, N.; Zinck, P. Coordinative Chain Transfer and Chain Shuttling Polymerization. *Chem. Rev.* **2024**, 124 (1), 210–244.
(71) Gao, H.; Lu, X.; Chen, S.; Du, B.; Yin, X.; Kang, Y.; Zhang, K.; Liu, C.; Pan, L.; Wang, B.; Ma, Z.; Li, Y. Preparation of Well-Controlled Isotactic Polypropylene-Based Block Copolymers with

Superior Physical Performance via Efficient Coordinative Chain Transfer Polymerization. *Macromolecules* **2022**, 55 (12), 5038–5048.

(72) Qiu, N.; Sun, Z.; Yu, F.; Wang, K.; Long, C.; Dong, Z.; Li, Y.; Cao, K.; Chen, Z.-R. Chain Shuttling Polymerization for Cycloolefin Block Copolymers: From Engineering Plastics to Thermoplastic Elastomers. *Macromolecules* **2024**, 57 (12), 5729–5738.

(73) Sabic polypropylene: https://www.sabic.com, July **2025**

(74) Lyondell-Basell polyolefins: https://www.lyondellbasell.com/, July **2025**

(75) S&P; IHS Markit. Polypropylene Resins; **2024**.

(76) Utracki, L.A., Polypropylene blends with coomodity resins, in Polypropylene, an A-Z Reference, J. Karger-Kocsis, Editor. *Kluwer Publishers: Dordrecht*. **1999** p. 615-620.

(77) Chirayil, C. J.; Joy, J.; Maria, H. J.; Krupa, I.; Thomas, S. *Polyolefins in Automotive Industry. In Polyolefin Compounds and Materials: Fundamentals and Industrial Applications*; Al-Ali AlMa'adeed, M., Krupa, I., Eds.; Springer International Publishing: Cham, **2016**; pp 265−283.

(78) Patel, V.; Mahajan, Y. Polymer Nanocomposites: Emerging Growth Driver for the Global Automotive Industry. In Handbook of Polymernanocomposites. *Processing, Performance and Application*; Pandey, J. K., Reddy, K. R., Mohanty, A. K., Misra, M., Eds.; Springer: Berlin, **2014**; Vol. A, pp 511−538.

(79) Di Girolamo, R.; De Rosa, C.; Cioce, C.; Scoti, M. Random and Block Copolymers of Isotactic Polypropylene with Higher α-Olefins: The Role of the Chain Topology on the Side-Chains Confined Crystallization. *Macromolecules* **2024**, 57 (18), 8837–8850.

(80) Antinucci, G.; Pucciarelli, A.; Vittoria, A.; Zaccaria, F.; Urciuoli, G.; Ehm, C.; Cannavacciuolo, F. D.; Cipullo, R.; Busico, V. Fast Analytics of High-Impact Polypropylene (HIPP). *ACS Appl. Polym. Mater*. **2023**, 5 (6), 3894–3897.

(81) Gahleitner, M.; Tranninger, C.; Doshev, P. Heterophasic Copolymers of Polypropylene: Development, Design Principles, and Future Challenges. *J. Appl. Polym. Sci.* **2013**, 130 (5), 3028–3037.

(82) Liang, J. Z.; Li, R. K. Y. Rubber Toughening in Polypropylene: A Review. *J. Appl. Polym. Sci.* **2000**, 77 (2), 409–417.

(83) Mirabella, F. M. Impact Polypropylene Copolymers: Fractionation and Structural Characterization. *Polymer (Guildf)* **1993**, 34 (8), 1729–1735.

(84) Cancelas, A. J.; Yang, L.; Girod, R.; de Heer, J.; Kleppinger, R.; Delsman, E.; Wang, J.; Gahleitner, M.; Monteil, V.; McKenna, T. F. L. The Effect of Reactor Conditions on High-Impact Polypropylene Properties and Gas Phase Polymerization Kinetics. *Macromol. React. Eng.* **2018**, 12 (4), 1700063.

(85) Zhang, Z.-C.; Deng, L.; Lei, J.; Li, Z.-M. Isotactic Polypropylene Reinforced Atactic Polypropylene by Formation of Shish-Kebab Superstructure. *Polymer (Guildf)* **2015**, 78, 120–133.

(86) Blaakmeer, E. S. M.; Antinucci, G.; Correa, A.; Busico, V.; van Eck, E. R. H.; Kentgens, A. P. M. Structural Characterization of Electron Donors in Ziegler–Natta Catalysts. *The Journal of Physical Chemistry C* **2018**, 122 (10), 5525–5536.

(87) Zaccaria, F.; Vittoria, A.; Correa, A.; Ehm, C.; Budzelaar, P. H. M.; Busico, V.; Cipullo, R. Internal Donors in Ziegler–Natta Systems: Is Reduction by AlR3 a Requirement for Donor Clean-Up? *Chem. Cat. Chem.* **2018**, 10 (5), 984–988.

(88) Weng, Y.; Jiang, B.; Fu, Z.; Fan, Z. Mechanism of Internal and External Electron Donor Effects on Propylene Polymerization with $MgCl_2$-Supported Ziegler–Natta Catalyst: New Evidences Based on Active Center Counting. *J. Appl. Polym. Sci.* **2018**, 135 (32), 46605.

(89) Thayer, A. M. Metallocene Catalysts Initiate New Era in Polymer Synthesis. *Chemical & Engineering News* **1995**, 73 (37), 15–20.

(90) Zhang, Z.; Zhang, R.; Huang, Y.; Lei, J.; Chen, Y.-H.; Tang, J.; Li, Z.-M. Efficient Utilization of Atactic Polypropylene in Its Isotactic Polypropylene Blends via “Structuring” Processing. *Ind. Eng. Chem. Res.* **2014**, 53 (24), 10144–10154.

(91) Maier, R. D.; Bidell, W.; Shamiri, A. Polypropylene: Gas-Phase Polymerization and Reactor Blends. *In Reference Module in Materials Science and Materials Engineering*. Elsevier. **2016**.

(92) Townsend Solutions. Polypropylene: Technology Review; www.townsendsolutions.com

(93) Lummus Technology; www.NovolenTechnology.com.

(94) Albunia, A. R.; Prades, F.; Jeremic, D. Multimodal Polymers with Supported Catalysts. *Springer* **2019**, 9, 852–864.

(95) Yuan, H. G.; Taylor, T. W.; Choi, K. Y.; Ray, W. H. Polymerization of Olefins through Heterogeneous Catalysis, I. Low Pressure Propylene Polymerization in Slurry with Ziegler–Natta Catalyst. *J. Appl. Polym. Sci.* **1982**, 27 (5), 1691–1706.

(96) Konze, W. V.; Vanderlende, D. D. High Temperature Solution Polymerization Process. WO2007136497A2, **2007**.

(97) Kruszynski, J.; Nowicka, W.; Bouyahyi, M.; Liu, Y.; Yang, L.; Rozanski, A.; Anbuchezhian, N.; Jasinska-Walc, L.; Duchateau, R. Unprecedented Adhesive Performance of Propylene-Based Hydroxyl-Functionalized Terpolymers. *ACS Appl. Polym. Mater*. **2023**, 5 (5), 3875–3882.

(98) Kruszynski, J.; Nowicka, W.; Pasha, F. A.; Yang, L.; Rozanski, A.; Bouyahyi, M.; Kleppinger, R.; Jasinska-Walc, L.; Duchateau, R. Tuning the Adhesive Strength of Functionalized Polyolefin-Based Hot Melt Adhesives: Unexpected Results Leading to New Opportunities. *Macromolecules* **2025**, 58 (6), 2894–2904.

CHAPTER II

The research explores the potential of groundbreaking In-Reactor-Functionalized Polyolefins (IRF-PO) and their application as Hot Melt Adhesives component. Understanding the relationship between the structure and properties of hydroxyl functionalized polypropylene lead to discovery of unique adhesives. Importantly, IRF-PO blends with non-functionalized counterparts proved to be an efficient route towards products revealing tunable performance. The adhesive strength of IRF-PO and their blends to polar substrates matches that of thermoset structural adhesives, while their thermoplastic nature enables effortless debonding and rebonding, promoting reuse and recycling, vital for a circular economy.

Publications included in this chapter*:

1. Kruszynski J., Nowicka W., Bouyahyi M., Liu Y., Yang L., Rozanski A., Anbuchezhian N., Jasinska-Walc L., Duchateau R.; Unprecedented Adhesive Performance of Propylene-Based Hydroxyl-Functionalized Terpolymers; *ACS Applied Polymer Materials* **2023** *5* (5), 3875-3882.

2. Kruszynski J., Nowicka W., Pasha F.A, Yang L., Rozanski A., Bouyahyi M., Kleppinger R., Jasinska-Walc L., Duchateau R.; Tuning the Adhesive Strength of Functionalized Polyolefin-Based Hot Melt Adhesives: Unexpected Results Leading to New Opportunities; *Macromolecules* **2025** *58* (6), 2894-2904.

* The co-authors' approval to use this paper in the thesis was included with the documentation.

2.1 General introduction

2.1.1 Adhesion phenomena

Adhesion requires strong interfacial interactions between bonding components. Adhesives can be applied in a variety of forms for example as a liquid, a viscoelastic component, as a fluid that undergoes in-situ polymerization during the bonding process or non-Newtonian fluid that solidifies upon cooling.[1,2] The key benefit of adhesive-based polymers lies in the ability to precisely tailor the properties according to the specific requirements of the desired application. Among the available development strategies, the incorporation of hydroxyl- and carboxylic functional groups into the polymer backbone remains the most effective approach to enhance bonding strength.[3] To provide a comprehensive understanding of adhesive performance, it is necessary to consider several mechanisms underlying adhesion.

One of the most significant among adhesion mechanisms is chemical adhesion, wherein functional groups of adhesives interact with functional groups present on the bonding surface. This mechanism, predominantly driven by intermolecular forces is a fundamental tool in explaining adhesion phenomena.[4–7] The incorporation of functional groups such as catechol derivatives, ureidopyrimidinone (UPy), maleic anhydride, or randomly distributed hydroxyl and carboxylic moieties within the nonpolar alkyl chain significantly enhances adhesion, as these polar groups can form complexes with functional groups present on the substrate surface.[6,8–11] Despite chemical bonds being considered the strongest mechanism of adhesion, they alone are not sufficient to provide adequate strength in the adhesive applications.[12]

The subsequent mechanism involves the diffusion of adhesive into the bonding surface.[13] In this process, an interface is composed through the entanglement of the adhesive with the bonded polymer surface. Sufficient interfacial adhesion between polymers is not only crucial for effective bonding solutions but also serves as a fundamental requirement for the successful compatibilization in terms of mechanical recycling of mixed plastic waste streams.[14,15]

Mechanical interlocking, occurs when adhesives are applied as a liquid or viscoelastic fluid, which is able to penetrate the pores on the bonding surface. Interlocking is recognized as another major adhesion mechanism. On one hand,

interlocking provides physical strength of bonding system but also amplifies intermolecular interactions by enhancing the total contact surface area. This results in a higher overall strength from van der Waals forces and hydrogen bonds. Furthermore, mechanical interlocking acts as a robust physical barrier, decreasing the probability of interphase cracking. For instance, the electrochemical etching of steel leads to enhanced roughness of the system what translates to better adhesion on the metal surface.[16,17]

An additional adhesion mechanism that plays an important role in overall adhesive strength involves electrostatic interactions. This phenomenon is observed in various organisms, such as snails, slugs, and mussels, which release specific types of proteins containing dihydroxyphenylalanine (DOPA) and positively charged amino acids. These electrostatic, physical interactions—based on electron transfer between oppositely charged components—contribute significantly to the overall adhesion performance. These electrostatic interactions inspired researchers to develop bio-based wet and dry adhesives e.g Pressure Sensitive Adhesives (PSAs).[18–27]

2.1.2 Classification of adhesives

Adhesives can be classified in a number of ways (Figure 1) including chemical composition, physical form, source, function, application type, mode of specific application or application environment.[28–30]

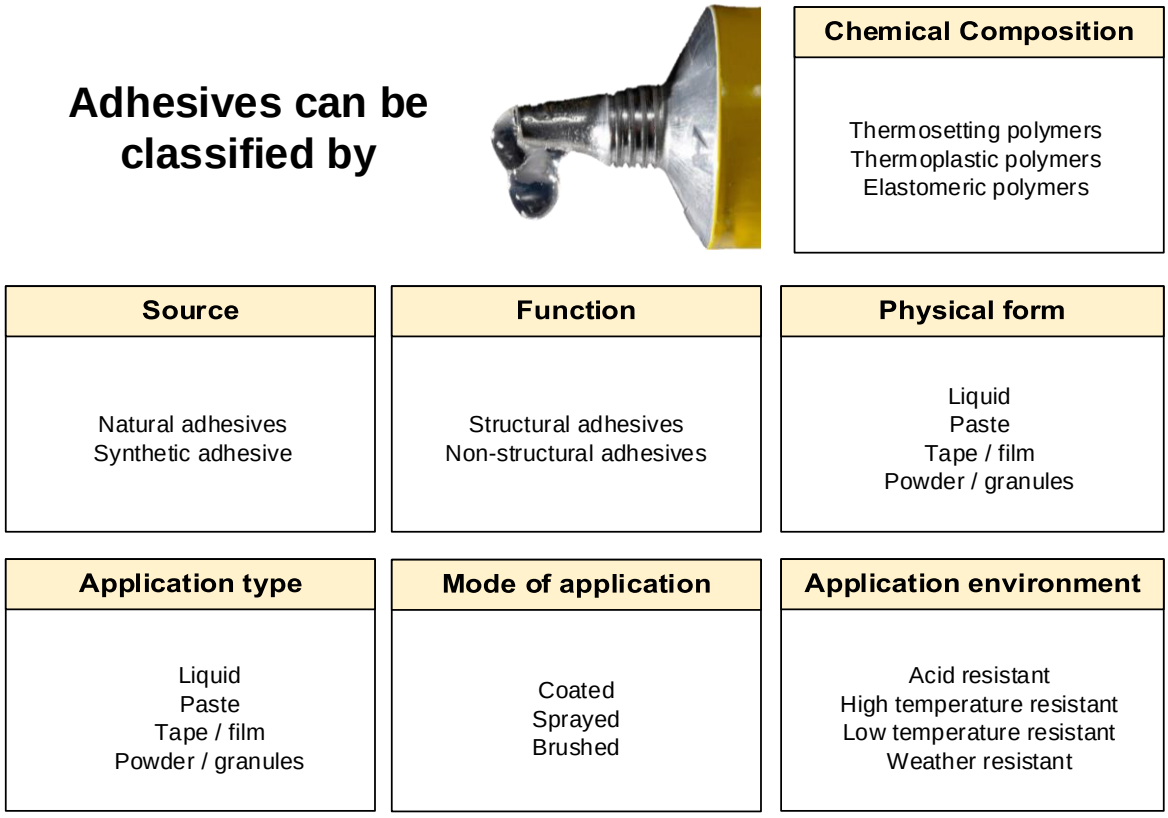

Figure 1. Classification of adhesives based on their source, chemical composition, and physical and application properties.[28–30]

Natural adhesives are composed of materials derived from animals or plants, while synthetic adhesives are typically polymer-based.[29,31] Chemical composition of adhesives categorize them into three types: thermoplastic polymers, thermosetting resins or elastomeric materials. Thermoplastic polymers soften when heated and solidify upon cooling, as seen in poly(ethylene-vinyl acetate) (EVA) or polyolefins (POs).[32] Thermosetting polymers undergo a chemical reaction during the bonding process, which cross-links the material, as exemplified by epoxy and phenolic polymer resins.[33] Elastomer-based adhesives are used when bonding properties need to be combined with elasticity and resilience under high deformation, as exemplified by butyl rubber adhesives commonly used in automotive and construction applications.[34] Moreover, as presented in Figure 1, adhesives can also be classified based on the physical form of the applied product (e.g., liquid, paste,

granules, or film) and the mode of application, such as coating, brushing, or spraying. Additionally, some manufacturers offer adhesives categorized according to their resistance to specific environmental conditions, including high or low temperatures, acidic environments, or varying weather conditions.

Structural adhesives are typically used to join components that must withstand significant external loads, whereas non-structural adhesives are primarily employed in low-strength applications, such as office or packaging use. Structural adhesives require a polymer that can adhere to the substrate while simultaneously providing sufficiently high internal strength between the joints. These properties are mostly provided by a thermosetting polymers, highly crosslinked two-component systems based on a unsaturated or functionalized polymer crosslinked by curing agent. The standard formulation of a first component includes derivatives of acrylic and methacylic acid, toughеners, adhesion promoters, crosslinkers, pigments, rheology modifiers, stabilizers, and fillers. The curing component mostly consists of an initiator with some additives.[35] Early, first-generation structural adhesives fully commercialized in the 1970s were based on poly(methyl methacrylate), toughened by fillers like powdered rubbers and acrylonitrile-butadiene-styrene terpolymers (ABS). Nevertheless, automotive industry was seeking products with reduced flammability, lower glass temperature (T_g), low odor, and low vapor pressure. In 1994, LORD Corporation successfully introduced into the market the structural adhesive based on poly(tetrahydrofurfuryl methacrylate), which was immediately adopted in the industry.[36]

Besides acrylic and epoxy structural adhesives, polyurethanes (PURs) can also be used as the primary polymer in adhesive formulations. PUR-based structural adhesives exhibit a favorable balance of mechanical strength and elasticity. They are commonly employed in applications such as layer bonding, gap filling, and the joining of dissimilar materials.[37,38]

A unique category of structural adhesives, described in the book of Professor Dillard, includes cyanoacrylates—commonly known as "superglues"—and anaerobic structural adhesives, often referred to as "threadlockers".[39–42] In 1953, researchers at Trinity College in Hartford made a groundbreaking discovery by identifying the first anaerobic adhesives, primarily composed of methacrylate esters such as 3,3,5-trimethylcyclohexyl methacrylate, 2-hydroxyethyl 2-methylprop-2-enoate, 2-hydroxypropyl methacrylate, and mixtures of maleic and acrylic acid.

These adhesives demonstrated a novel polymerization mechanism that occurs under low–oxygen conditions and is initiated by redox–active metal ions present on the bonding surface. Anaerobic adhesives, similar to cyanoacrylate adhesives, rapidly cure at room temperature following surface activation.[42,43] However, they should be considered as distinct systems, as the polymerization of cyanoacrylate adhesives is initiated by moisture and occurs in the presence of oxygen, whereas anaerobic adhesives—typically based on methacrylate functionalities—require an oxygen-free environment and are activated by metal ions. Due to their ease of use, rapid curing, and compatibility with a wide range of materials, cyanoacrylates have found extensive application in the cosmetics/beauty industry and individual households. In contrast, anaerobic adhesives are primarily used in threadlocking, flange sealing, and impregnation sealing. A well-known example of a widely applied cyanoacrylate and anaerobic adhesive is Loctite, a worldwide brand offered by Henkel.

Silicon-based adhesives represent group of elastic structural adhesives based on polysiloxanes. These versatile polymers, composed of a silicon–oxygen backbone with grafted aliphatic or aromatic side groups, are typically formed in situ during the bonding process. High molecular weight silicones exhibit a lower crosslink density compared to other structural adhesives, which translates into excellent elasticity but reduced cohesive strength, lower modulus, and slower cure rates than epoxy or polyurethane-based systems.[44] Silicone structural adhesives are characterized by their chemical and physical inertness, along with outstanding thermal and oxidative stability. The primary consumption of silicone-based adhesive is driven by their widespread use in construction and automotive applications.[45]

Nowadays the market of structural adhesives are mostly dominated by key global players such as Henkel AG & Co.KGaA (Germany), 3M (US), Sika AG (Switzerland), DuPont (US) and Huntsman Corporation (US). The value of global structural adhesive market reached 13.5 billion USD in 2024. It is estimated that the increasing trend will be maintained and reached 17.7 billion USD in 2029 with Compound Annual Growth Rate (CAGR) at 5.9 % from 2023 to 2030.[46]

2.1.3 Hot Melt Adhesives (HMAs)

The main feature of HMAs is that the adhesive is applied in a molten state and solidifies upon cooling to achieve the strength required to determined application. Typically, melting point of resin used as main component in HMA formulation occurs within a range of 65 to 180 °C. According with abovementioned classification (Figure 1), Hot Melt Adhesives can be categorized as thermoplastic or thermosetting polymers with function assigned to structural adhesives.[47,48] Classification, proposed by the Society of Manufacturing Engineers (SME),[49] display HMAs as a distinct type of adhesives where formulation include polymers based on polyurethanes, polyamides, and thermoplastic polymers, such as poly(ethylene–vinyl acetate), polyethylene, amorphous poly(α-olefin) and functionalized polyolefins. Beside the main polymer component, standard HMA composition includes also additives such as aging stabilizers, tackifiers and waxes to adjust viscosity and modify surface properties, fillers to influence thermal properties and reduce production costs. [49,50]

The most popular HMA formulation is a combination of copolymers of poly(ethylene-vinyl acetate) (EVA). This material exhibits excellent adhesion to a wide range of substrates, along with flexibility and high mechanical properties. It is widely used in packaging, woodworking, and bookbinding applications. However, EVA-based HMAs have several disadvantages. The main drawbacks include limited resistance to high and low temperatures, reduced durability, odor emissions during application, and, most notably, their non-eco-friendly and non-recyclable nature.[51,52]

Polyurethane-based HMAs are classified by their chemical compositions: thermoplastic and reactive.[53] Thermoplastic polyurethanes (TPU-HMAs) are crosslinked by non-covalent interactions, such as hydrogen bonding, which translates to better recyclability but weaker adhesion strength. In contrast, reactive polyurethanes (PUR-HMAs) exhibit outstanding adhesion, chemical resistance, and heat tolerance. Their reactive nature allows moisture from the atmosphere to react with isocyanate groups, leading to a highly crosslinked polymer network. Unfortunately, this permanent structure makes them non-recyclable, which has hindered their application in terms of sustainable industrial production.

Consequently, significant efforts have been made in recent years to develop high performance HMA in agreement with circular economy. So far, commercially available products have been dominated by solutions based on EVA and PUR. The

majority of functionalized polyolefins are being produced via a post-polymerization radical grafting process.[54–57] Nevertheless, dynamic development of cutting-edge technologies based on metallocene catalysts has led to the introduction of well-defined, functionalized polyolefin elastomers (POEs).[58,59] These new class of POs based polymers exhibit exceptional adhesion to a wide range of polar and nonpolar surfaces including metals, glass, stone, wood, and polyolefins.[60–69]

Observing current significant growing demand on adhesive products it is expected that EVA adhesives will reach 15.43 billion USD by 2028, with a compound annual growth rate (CAGR) of 6.39 % during the 2024 – 2028 period. Meanwhile, polyolefin elastomers (POEs) are gradually gaining popularity. The size of market of the functional polyolefins is projected to reach 10.8 billion USD by 2032, with an even higher CAGR of 7.1% during the forecast period of 2024 – 2032.[69] Economic factors, outstanding mechanical and recyclability properties of polyolefins clearly demonstrate that the growing popularity of POs in academia and industry is reasonable and has strong business fundamentals.

2.2 Scope of the chapter

The research presented in the first included paper explores the adhesive performance of the hydroxyl functionalized propylene-based terpolymers synthesized by catalytic solution olefin copolymerization technology patented by SABIC.[59,70] The incorporation of polar functionalities overcomes the inherent low affinity of polyolefins towards polar materials by enabling strong adhesive interactions with the surface of the polar materials. With even low functionality levels achieving remarkable adhesion, In-Reactor-Functionalized Polyolefins (IRF-PO) products behave like standard polyolefins also exhibiting excellent affinity towards polyolefins. Beyond its exceptional binding capabilities to polar substrates, the functional groups within IRF-PO serve an additional purpose. These polar functionalities integrate within a highly apolar polyolefinic matrix, creating hydrogen bonding polar nests. These clusters generate thermoreversible crosslinking, ensuring mechanical integrity and enhancing adhesive strength at service temperatures, while maintaining excellent processability during application. The low viscosity of IRF-PO at elevated temperatures enables the application of thin layers, optimizing material usage and resulting in clean, aesthetically joints without compromising adhesive strength. The thermoplastic nature of IRF-PO products enable effortless debonding and rebonding of substrates, which paves the way for enhanced reuse and recycling opportunities, promoting a sustainable and circular economy. Offering flexibility, this innovative technological approach allows easy customization of polymer properties, including the choice of polyolefin type, viscosity, crystallinity, and adhesive strength.

While the potential for producing a diverse range of functionalized polyolefins is vast, the presented study focuses on propylene-based functionalized terpolymers. The production of IRF-POs requires additional functional monomers and a high-temperature solution process, which may result in a higher cost compared to traditional polyolefin elastomers. Therefore, there is a need for a cheaper Hot Melt Adhesive composition usable for a large variety of material and having a tunable adhesion property allowing the HMA to fail before the surface on which it is applied. Second included paper explores a novel patented approach to enhance adhesive strength in functionalized polyolefins by blending them with nonfunctionalized counterparts. Through extensive characterization, the study reveals how crystallinity

and miscibility of the polymers significantly influence adhesive performance. Surprisingly, some blends maintain IRF-PO adhesive strength even after substantial dilution. Additionally, molecular dynamics simulations indicate a natural tendency of hydroxyl-functionalized polyolefins to interact effectively with surfaces, enhancing adhesion.[71,72]

2.3 References

(1) Onozuka, N.; Nakajima, K. Atomic Force Microscopy Analysis of Velocity Dependent Adhesive Viscoelastic Contact. *Langmuir* **2024**, 40 (46), 24565–24575.

(2) Mandriota, C.; Menga, N.; Carbone, G. Adhesive Contact Mechanics of Viscoelastic Materials. *Int. J. Solids Struct.* **2024**, 290, 112685.

(3) Lin, T.; Wu, Y.; Santos, E.; Chen, X.; Kelleher-Ferguson, J.; Tucker, C.; Ahn, D.; Mohler, C.; Chen, Z. Probing Covalent Interactions at a Silicone Adhesive/Nylon Interface. *Langmuir* **2022**, 38 (8), 2590–2600.

(4) Raos, G.; Zappone, B. Polymer Adhesion: Seeking New Solutions for an Old Problem. *Macromolecules* **2021**, 54 (23), 10617–10644.

(5) Matsumoto, T.; Shimizu, Y.; Nishino, T. Analyses of the Adhesion Interphase of Isotactic Polypropylene Using Hot-Melt Polyolefin Adhesives. *Macromolecules* **2021**, 54 (15), 7226–7233.

(6) Liu, Y.; Shigemoto, Y.; Hanada, T.; Miyamae, T.; Kawasaki, K.; Horiuchi, S. Role of Chemical Functionality in the Adhesion of Aluminum and Isotactic Polypropylene. *ACS Appl. Mater. Interfaces* **2021**, 13 (9), 11497–11506.

(7) Na, Y.; Chen, C. Catechol-Functionalized Polyolefins. *Angewandte Chemie International Edition* **2020**, 59 (20), 7953–7959.

(8) Sun, P.; Li, Y.; Qin, B.; Xu, J. F.; Zhang, X. Super Strong and Multi-Reusable Supramolecular Epoxy Hot Melt Adhesives. *ACS Mater. Lett.* **2021**, 3 (7), 1003–1009.

(9) García, B.; Saiz-Poseu, J.; Gras-Charles, R.; Hernando, J.; Alibés, R.; Novio, F.; Sedó, J.; Busqué, F.; Ruiz-Molina, D. Mussel-Inspired Hydrophobic Coatings for Water-Repellent Textiles and Oil Removal. *ACS Appl. Mater. Interfaces* **2014**, 6 (20), 17616–17625.

(10) Akram Bhuiyan, Md. S.; Roland, J. D.; Liu, B.; Reaume, M.; Zhang, Z.; Kelley, J. D.; Lee, B. P. In Situ Deactivation of Catechol-Containing Adhesive Using Electrochemistry. *J. Am. Chem. Soc.* **2020**, 142 (10), 4631–4638.

(11) Zhao, Y.; Song, S.; Ren, X.; Zhang, J.; Lin, Q.; Zhao, Y. Supramolecular Adhesive Hydrogels for Tissue Engineering Applications. *Chem. Rev.* **2022**, 122 (6), 5604–5640.

(12) Zhang, Y.; Hasegawa, K.; Kamo, S.; Takagi, K.; Ma, W.; Takahara, A. Enhanced Adhesion Effect of Epoxy Resin on Metal Surfaces Using Polymer with Catechol and Epoxy Groups. *ACS Appl. Polym. Mater.* **2020**, 2 (4), 1500–1507.

(13) Han, J.-W.; Sekiguchi, Y.; Shimamoto, K.; Akiyama, H.; Sato, C. Direct Measurement of the Diffusion Coefficient of Adhesives from Moisture Distribution in Adhesive Layers Using Near-Infrared Spectroscopy. *ACS Appl. Mater. Interfaces* **2024**, 16 (40), 54610–54626.

(14) Eagan, J. M.; Xu, J.; Di Girolamo, R.; Thurber, C. M.; Macosko, C. W.; LaPointe, A. M.; Bates, F. S.; Coates, G. W. Combining Polyethylene and Polypropylene: Enhanced Performance with PE/i PP Multiblock Polymers. *Science* **2017**, 355 (6327), 814–816.

(15) Kruszynski, J.; Nowicka, W.; Rozanski, A.; Liu, Y.; Parisi, D.; Yang, L.; Pasha, F. A.; Bouyahyi, M.; Jasinska-Walc, L.; Duchateau, R. IPP/HDPE Blends Compatibilized by a Polyester: An Unconventional Concept to Valuable Products. *Sci. Adv.* **2025**, 10 (21), eado1944.

(16) Kim, S.; Kim, A.; Yoo, D.; Yoo, H.-J.; Lee, S.-K.; Kim, J. Enhancement of Steel Sandwich Sheet Adhesion Using Mechanical Interlocking Structures Formed by Electrochemical Etching. *Langmuir* **2021**, 37 (22), 6702–6710.

(17) Yang, J.; Bai, R. Mechanics of Wet Adhesion. *In Mechanics of Flexible and Stretchable Electronics*; **2024**; pp 345–372.

(18) Izadi, H.; Zandieh, A.; Penlidis, A. Bio-Inspired Dry Adhesives: Contact Electrification and Electrostatic Interactions. *In Kirk-Othmer Encyclopedia of Chemical Technology*; **2017**; pp 1–35.

(19) Zhang, J.; Wang, W.; Zhang, Y.; Wei, Q.; Han, F.; Dong, S.; Liu, D.; Zhang, S. Small-Molecule Ionic Liquid-Based Adhesive with Strong Room-Temperature Adhesion Promoted by Electrostatic Interaction. *Nat. Commun*. **2022**, 13 (1), 5214.

(20) Chen, J.; Zeng, H. Designing Bio-Inspired Wet Adhesives through Tunable Molecular Interactions. *J. Colloid. Interface Sci.* **2023**, 645, 591–606.

(21) Sierra-Romero, A.; Novakovic, K.; Geoghegan, M. Adhesive Interfaces toward a Zero-Waste Industry. *Langmuir* **2022**, 38 (50), 15476–15493.

(22) Liu, Y.; Zhao, R.; Li, S.; Xue, X.; Zhang, Q.; Shi, F.; Cheng, M. Robust Electrostatically Interactive Hydrogel Coatings for Macroscopic Supramolecular Assembly via Rapid Wet Adhesion. *ACS Appl. Mater. Interfaces* **2023**, 15 (17), 21640–21650.

(23) Yuk, H.; Varela, C. E.; Nabzdyk, C. S.; Mao, X.; Padera, R. F.; Roche, E. T.; Zhao, X. Dry Double-Sided Tape for Adhesion of Wet Tissues and Devices. *Nature* **2019**, 575 (7781), 169–174.

(24) Burkstrand, J. M. Metal-polymer Interfaces: Adhesion and X-ray Photoemission Studies. *J. Appl. Phys.* **1981**, 52 (7), 4795–4800.

(25) Chang, Q.; Jiang, J. Nanoscale Hierarchical Structures Formed by Sequence-Defined Polycations and Homopolyanions for High Salt-Tolerance Adhesives. *Macromolecules* **2024**, 57 (4), 1859–1867.

(26) Jeong, Y. K.; Park, S. H.; Choi, J. W. Mussel-Inspired Coating and Adhesion for Rechargeable Batteries: A Review. *ACS Appl. Mater. Interfaces* **2018**, 10 (9), 7562–7573.

(27) Matos-Pérez, C. R.; White, J. D.; Wilker, J. J. Polymer Composition and Substrate Influences on the Adhesive Bonding of a Biomimetic, Cross-Linking Polymer. *J. Am. Chem. Soc*. **2012**, 134 (22), 9498–9505.

(28) Skeist, I. Handbook of Adhesives; Springer Science & Business Media, **2012**.

(29) Ebnesajjad, S.; Landrock, A. H. Adhesives Technology Handbook; William Andrew, **2014**.

(30) Petrie, E. M. *Handbook of Adhesives and Sealants*; McGraw-Hill Education, 2007.

(31) Messler, R. W. Joining of Materials and Structures: From Pragmatic Process to Enabling Technology; Butterworth-Heinemann, 2004.

(32) Pocius, A. V. *Adhesion and Adhesives Technology: An Introduction*; Carl Hanser Verlag GmbH Co KG, **2021**.

(33) Zalucha, D. J.; Abbey, K. J. The Chemistry of Structural Adhesives: Epoxy, Urethane, and Acrylic Adhesives. *In Kent and Riegel's Handbook of Industrial Chemistry and Biotechnology*; Kent, J. A., Ed.; Springer US: Boston, MA, **2007**; pp 591–622.

(34) Dayan, C. B.; Chun, S.; Krishna-Subbaiah, N.; Drotlef, D.-M.; Akolpoglu, M. B.; Sitti, M. 3D Printing of Elastomeric Bioinspired Complex Adhesive Microstructures. *Advanced Materials* **2021**, 33 (40), 2103826.

(35) Sapkal, S.; Maske, P.; Panigrahi, S. K.; Panda, H. S. Characterization of Various Structural Adhesive Materials. *In Structural Adhesives*; **2023**; pp 135–191.

(36) Abbey, K. J. 2 - Advances in Epoxy Adhesives. In Advances in Structural Adhesive Bonding; Dillard, D. A., Ed.; Woodhead Publishing, **2010**; pp 20–34.

(37) Kamo, Y.; Matsumoto, A. Stress Relaxation and Improved Fracture Toughness of Metal Bonding Using Flexible Monolith Sheets and an Epoxy Adhesive. *Polym. J.* **2025**, 57 (2), 203–214.

(38) Choffat, F.; Corsaro, A.; Di Fratta, C.; Kelch, S. 3 - Advances in Polyurethane Structural Adhesives. In Advances in Structural Adhesive Bonding (Second Edition); Dillard, D. A., Ed.; Woodhead Publishing, **2023**; pp 103–136.

(39) Masood, M. T.; Zahid, M.; Goldoni, L.; Ceseracciu, L.; Athanassiou, A.; Bayer, I. S. Highly Transparent Polyethylcyanoacrylates from Approved Eco-Friendly Fragrance Materials Demonstrating Excellent Fog-Harvesting and Anti-Wear Properties. *ACS Appl. Mater. Interfaces* **2018**, 10 (40), 34573–34584.

(40) Faggi, E.; Aguilera, J.; Sáez, R.; Pujol, F.; Marquet, J.; Hernando, J.; Sebastián, R. M. Wavelength-Tunable Light-Induced Polymerization of Cyanoacrylates Using Photogenerated Amines. *Macromolecules* **2019**, 52 (6), 2329–2339.

(41) Burns, B. 4 - Advances in Cyanoacrylate Structural Adhesives. In Advances in Structural Adhesive Bonding (Second Edition); Dillard, D. A., Ed.; Woodhead Publishing, 2023; pp 137–157.

(42) Condron, D. 5 - Advances in Anaerobic Adhesives. In Advances in Structural Adhesive Bonding (Second Edition); Dillard, D. A., Ed.; Woodhead Publishing, **2023**; pp 159–177.

(43) LOCTITE® Threadlockers, https://www.henkel-adhesives.com/us/en/products/industrial-adhesives/threadlockers.html/1000.html

(44) de Buyl, F.; Hayez, V.; Harkness, B.; Kimberlain, J.; Shephard, N. 6 - Advances in Structural Silicone Adhesives. In Advances in Structural Adhesive Bonding (Second Edition); Dillard, D. A., Ed.; Woodhead Publishing, **2023**; pp 179–219.

(45) Lin, T.; Wu, Y.; Santos, E.; Chen, X.; Ahn, D.; Mohler, C.; Chen, Z. Molecular Insights into Adhesion at a Buried Silica-Filled Silicone/Polyethylene Terephthalate Interface. *Langmuir* **2020**, 36 (49), 15128–15140.

(46) Structural Adhesive Market Size, Share & Trends Analysis Report By Product (Urethane, Epoxy, Acrylic), By Technology (Water-based, Solvent-based), By Application (Transportation, Construction), By Region, And Segment Forecasts, 2023 – 2030; https://www.grandviewresearch.com/industry-analysis/structural-adhesives-market

(47) Maw, M. R.; Tanas, A. K.; Dashtimoghadam, E.; Nikitina, E. A.; Ivanov, D. A.; Dobrynin, A. V; Vatankhah-Varnosfaderani, M.; Sheiko, S. S. Bottlebrush Thermoplastic Elastomers as Hot-Melt Pressure-Sensitive Adhesives. *ACS Appl. Mater. Interfaces* **2023**, 15 (35), 41870–41879.
(48) Hartshorn, S. R. Structural Adhesives: Chemistry and Technology; *Springer Science & Business Media*, **2012**.
(49) Gharde, S.; Sharma, G.; Kandasubramanian, B. Hot-Melt Adhesives: Fundamentals, Formulations, and Applications: A Critical Review. *In Progress in Adhesion and Adhesives*; 2021; pp 1–28.
(50) Lee, L.-H. Adhesive and sealant chemistry. Applied Polymer Science: 21st Century **2000**, 273.
(51) Li, S.; Zhang, H.; Liu, Z.; Cheng, J.; Li, H.; Yan, C. A Novel Hydroxyl-Rich Polyvinyl Alcohol Hot-Melt Adhesive with Excellent Ultra-Low Temperature Adhesion and Reusability. *J. Appl. Polym Sci*. **2024**, 141 (27), e55613.
(52) Hinsken, H. Influence of Tackifier Resins Storage Stability on EVA Based Hot Melt Adhesives. *Die Angewandte Makromolekulare Chemie* **1985**, 137 (1), 135–147.
(53) Wu, H.; Chen, Y.; Zhu, W.; Shangguan, Y.; Zheng, Q. Highly Adhesive and Tough Thermoplastic Polyurethanes Using a Furandicarboxamide Rigid Chain Extender with Noncovalent Interactions. *ACS Appl. Polym. Mater.* **2023**, 5 (5), 3515–3523.
(54) Walsh, D. J.; Hyatt, M. G.; Miller, S. A.; Guironnet, D. Recent Trends in Catalytic Polymerizations. *ACS Catal*. **2019**, 9 (12), 11153–11188.
(55) Tan, C.; Chen, C. Emerging Palladium and Nickel Catalysts for Copolymerization of Olefins with Polar Monomers. *Angewandte Chemie International Edition* **2019**, 58 (22), 7192–7200.
(56) Keyes, A.; Basbug Alhan, H. E.; Ordonez, E.; Ha, U.; Beezer, D. B.; Dau, H.; Liu, Y.-S.; Tsogtgerel, E.; Jones, G. R.; Harth, E. Olefins and Vinyl Polar Monomers: Bridging the Gap for Next Generation Materials. *Angewandte Chemie International Edition* **2019**, 58 (36), 12370–12391.
(57) Nakamura, A.; Anselment, T. M. J.; Claverie, J.; Goodall, B.; Jordan, R. F.; Mecking, S.; Rieger, B.; Sen, A.; van Leeuwen, P. W. N. M.; Nozaki, K. Ortho-Phosphinobenzenesulfonate: A Superb Ligand for Palladium-Catalyzed Coordination–Insertion Copolymerization of Polar Vinyl Monomers. *Acc. Chem. Res*. **2013**, 46 (7), 1438–1449.
(58) Jasinska-Walc, L.; Bouyahyi, M.; Duchateau, R. Potential of Functionalized Polyolefins in a Sustainable Polymer Economy: Synthetic Strategies and Applications. *Acc. Chem. Res*. **2022**, 55 (15), 1985–1996.
(59) Jasinska-Walc, L.; Duchateau, R.; Bouyahyi, M.; Badillo, N.; Kruszynski, J.; Hrachova, J.; Liu, Y.; Yang, L. Hot Melt Adhesive Comprising Functionalized Polyolefins. WO2022238352A1, **2022**.
(60) Tian, Z.; Cui, L.; Du, P. Synthesis of Polyurethane Hot Melt Adhesive without Solvent via Diels-Alder Reaction. *Int. J. Adhes.* **2024**, 129, 103567.
(61) Heucher, R.; Ford, I.; Joseph, J.; Crawford, A.; Debondable reactive hot melt adhesives. US 10,800,956 B2, 2017.
(62) Li, Y.; Heucher, R.; Cain, J. T. Moisture Curable Hot-Melt Adhesive and Method for Bonding Substrates Using Same. US 6,221,978 B1, **1999**.

(63) Wang, Q.; Feng, Z.; He, C.; Liu, T.; Lu, H.; Sun, R. Preparation and Performance Study of a Reactive Polyurethane Hot-Melt Adhesive/CS–Fe3O4 Magnetic Nanocomposite Film/Fabric. *RSC Adv*. **2022**, 12 (42), 27463–27472.
(64) Coates, G. W. Precise Control of Polyolefin Stereochemistry Using Single-Site Metal Catalysts. *Chem. Rev.* **2000**, 100 (4), 1223–1252.
(65) Khongtong, S.; Ferguson, G. S. A Smart Adhesive Joint: Entropic Control of Adhesion at a Polymer/Metal Interface. *J. Am. Chem. Soc*. **2002**, 124 (25), 7254–7255.
(66) Qian, Y.; Ikura, R.; Kawai, Y.; Park, J.; Yamaoka, K.; Takashima, Y. Improvement in Cohesive Properties of Adhesion Systems Using Movable Cross-Linked Materials with Stress Relaxation Properties. *ACS Appl. Mater. Interfaces* **2024**, 16 (3), 3935–3943.
(67) Hanifpour, A.; Bahri-Laleh, N.; Nekoomanesh-Haghighi, M. Preparation of Novel, Liquid, Solvent-Free, Polyolefin-Based Adhesives. *Polym. Adv. Technol*. **2020**, 31 (5), 922–931.
(68) Sunny, M. C.; Ramesh, P.; Mohanan, P. V; George, K. E. Metallocene Based Polyolefin: A Potential Candidate for the Replacement of Flexible Poly (Vinyl Chloride) in the Medical Field. *Polym. Adv. Technol.* **2010**, 21 (9), 621–631.
(69) Data Intelo; Polyolefin Elastomers (POE) Market; Global Industry Analysis, Growth, Share, Size, Trends, and Forecast 2025-203;
(70) Kruszynski, J.; Nowicka, W.; Bouyahyi, M.; Liu, Y.; Yang, L.; Rozanski, A.; Anbuchezhian, N.; Jasinska-Walc, L.; Duchateau, R. Unprecedented Adhesive Performance of Propylene-Based Hydroxyl-Functionalized Terpolymers. *ACS Appl. Polym. Mater.* **2023**, 5 (5), 3875–3882.
(71) Duchateau, R.; Jasinska-Walc, L.; Bouyahyi, M.; Kruszynski, J.; Nowicka, W.; Szot, W.; Gautam, P. S. Hot Melt Adhesives Based on Blends Comprising Non-Functionalized Polyolefins and Functionalized Polyolefins. EP4484457 A1, **2023**.
(72) Kruszynski, J.; Nowicka, W.; Pasha, F. A.; Yang, L.; Rozanski, A.; Bouyahyi, M.; Kleppinger, R.; Jasinska-Walc, L.; Duchateau, R. Tuning the Adhesive Strength of Functionalized Polyolefin-Based Hot Melt Adhesives: Unexpected Results Leading to New Opportunities. *Macromolecules* **2025**, 58 (6), 2894–2904.

2.4 Hot Melt Adhesives based on poly(propylene–co–hex-1-ene–co–hex-5-en-1-ol)

This subchapter has been published as:

Unprecedented Adhesive Performance of Propylene-Based Hydroxyl-Functionalized Terpolymers

Jakub Kruszynski, Weronika Nowicka, Miloud Bouyahyi, Yingxin Liu, Lanti Yang, Artur Rozanski, Nithish Anbuchezhian, Lidia Jasinska-Walc, and Rob Duchateau

ACS Applied Polymer Materials **2023** *5* (5), 3875-3882
DOI: 10.1021/acsapm.3c00566

ACS APPLIED POLYMER MATERIALS

pubs.acs.org/acsapm Article

Unprecedented Adhesive Performance of Propylene-Based Hydroxyl-Functionalized Terpolymers

Jakub Kruszynski, Weronika Nowicka, Miloud Bouyahyi, Yingxin Liu, Lanti Yang, Artur Rozanski, Nithish Anbuchezhian, Lidia Jasinska-Walc,* and Rob Duchateau*

Cite This: *ACS Appl. Polym. Mater.* 2023, 5, 3875−3882 Read Online

ACCESS | Metrics & More | Article Recommendations | Supporting Information

ABSTRACT: The synthesis of hydroxyl-functionalized propylene-based terpolymers and their performance as hot melt adhesives were investigated. The products comprise uniformly distributed butyl and 4-hydroxyl-butyl branches along the polypropylene backbone. Despite the low hydroxyl-functionality level of ≤ 0.5 mol %, hydroxyl-functionalized terpolymers show formidable adhesion to aluminum and steel, providing an adhesive strength exceeding 16 MPa, whereas the nonfunctionalized congeners hardly adhere to these metals. As evidenced by rheological measurements, the functional groups form dynamic crosslinks based on hydrogen bonding and electrostatic interactions with aluminum oxide hydroxide residues, remaining in the product after polymerization. At the industrial application temperature of 180 °C, nondeashed and deashed samples of polymers having 0.1 or 0.5 mol % incorporated 5-hexen-1-ol gave, upon cooling to room temperature, comparable adhesive strengths. Deashing and increasing the functionality level lead to a significant improvement of the adhesion strength at a lower application temperature (130 °C), allowing application of the hydroxyl-functionalized propylene-based terpolymers as high-strength hot melt adhesives for combinations of polypropylene and metals.

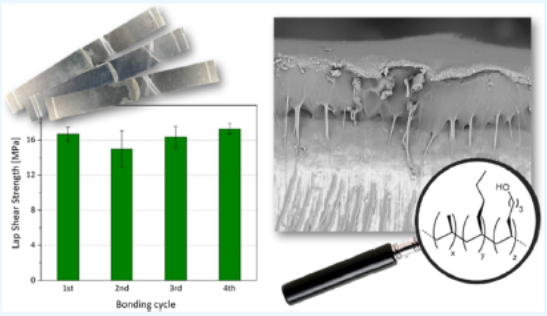

KEYWORDS: *functionalized polyolefin, hot melt adhesive, reversible bonding, polypropylene, steel, aluminum*

INTRODUCTION

Adhesives play an important role in our everyday life and find use in a wide variety of application areas such as building and construction, packaging, automotive, personal hygiene, consumer goods, furniture, and the electronic industry. Currently, more than 6 billion pounds of adhesives are used per annum.[1−5] The increasing demand for sustainability has also affected the adhesive industry, which as a consequence increasingly focuses on environmentally friendly, solvent-free, and volatile organic compound (VOC)-free adhesives.[6−10] In addition, there is an ever-growing demand for high-performance adhesives.[11] Hence, modern adhesive design should combine an ecological approach using a cost-effective technology with high product performance. For this reason, hot melt adhesives (HMAs) increasingly attract attention as they could be an answer for the demanding requirements of the market.[12−17] Typical adhesive strengths of commercially available ethylene−vinyl acetate (EVA) or polyurethane-based HMA are limited to 6−7 MPa.[18,19] Rapid development of high-performance lightweight products requires excellent adhesion to a vast range of individual materials. Hybrid systems, employing for example metal and polymer surfaces, are increasingly used in a wide range of applications.[20,21]

Although there are various adhesive solutions available for polar polymers, polyolefins, which account for over 65 % of all polymeric materials, are extremely difficult to bond to polar substrates due to their low surface free energy, chemical inertness, and absence of functional groups.[22−24] Chemical and physical methods of polyolefins' surface pretreatment result in increased polarity and improved wettability, which enhance adhesion to polymer substrates. However, such preparation of substrates requires advanced equipment and an extended production time, leading to serious safety hazards, potential damages to the surfaces, and higher costs.[25−28] Recent research is directed toward developing new generations of functional polymers with enhanced adhesion to both polar and apolar substrates, including functionalized polyolefins.[12,13] Various methods exist to introduce functional groups into polyolefins, ranging from in-reactor functionalization to postpolymerization functionalization.[29−32] For example, the high-pressure radical copolymerization process of ethylene and polar vinylic comonomers enables the synthesis of products such as ethylene−vinyl acetate and ethylene−acrylate

copolymers with a wide range of functionality levels. However, this technology requires harsh conditions and is restricted to low density polyethylene (LDPE)-like products.[33] Another proven route toward functionalized polyolefins is the peroxide-initiated functionalization of substrates such as maleic anhydride and acrylates via reactive extrusion. Yet, competitive side reactions such as crosslinking or β-scission complicate the process, typically resulting in rather ill-defined products.[34] Whereas randomly functionalized polyethylenes can be produced by the abovementioned high-pressure radical process, functionalized propylene-based copolymers, with a well-defined polymer microstructure, high-enough molecular weight, and sufficient incorporation of functionality, can only be prepared by copolymerization of propylene and functionalized comonomers. Although several reports describe the use of heterogeneous Ziegler−Natta catalysts,[35] most studies on the copolymerization of olefins with functionalized olefin comonomers use single-site catalysts.[32,36−38]

Herein, we present the synthesis and performance evaluation of propylene-based OH-functionalized copolymers and terpolymers as HMAs, with the main emphasis on adhering glass-filled isotactic polypropylene (*i*PP) to aluminum or steel, particularly relevant to the automotive industry.[39−41]

RESULTS AND DISCUSSION

The direct copolymerization of propylene with 1-hexene and triethyl aluminum (TEA)-passivated 5-hexene-1-ol, in the presence of a single-site hafnium catalyst, proved to be a facile route toward hydroxyl-functionalized *i*PP-based terpolymers (Figure 1 and Table 1).[42] The polymerization product needs to be treated with, preferably acidified, alcohol or water in order to remove the aluminum alkyl residue and to free the hydroxyl functionalities. Simple precipitation of the polymer in acidified methanol leads to a product that retains part of the aluminum remaining as aluminum oxide hydroxide (3, 4; Table 1). To fully remove the aluminum traces, the polymer has to be dissolved in hot toluene and treated with acidified alcohol (3D, 4D; Table 1). One of the thus-deashed samples 4D was used to produce the deprotonated, silyl ether product 4Si (Table 1, Figures 1, and S2). This sample, together with samples 1 and 2 of Table 1, were used as nonprotic and nonfunctionalized benchmarks in the study.

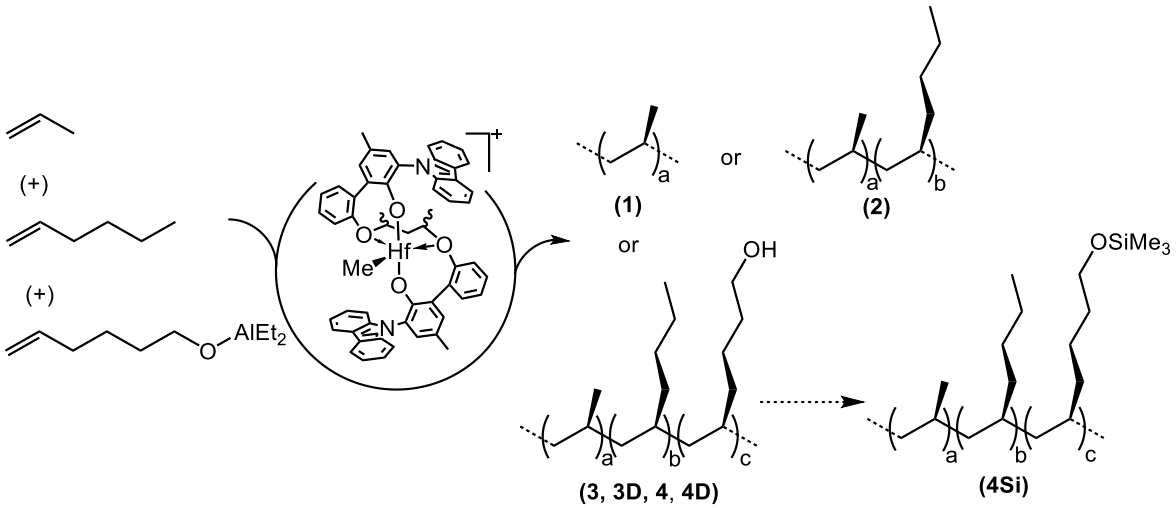

Figure 1. Synthetic path of the propylene-based copolymer and functionalized terpolymers: *i*PP (1), poly(C_3-*co*-C_6) (2), poly(C_3-*co*-C_6-*co*-C_6OH) (3, 3D, 4, 4D), and poly(C_3-*co*-C_6-*co*-C_6OSiMe$_3$) (4Si).

Table 1. Molecular Characterization and Thermal Properties of the Synthesized *i*PP and Propylene-Based Copolymers and Terpolymers.

Sample	Polymer	M_n [a]	M_w [a]	$Đ$ [a]	SCB [a]	OH [b]	C_6 [c]	Al [d]	T_m [e]	T_c [e]	T_g [f]
		kg/mol	kg/mol		$\bar{x}/1000C$	mol %	mol %	wt %	°C	°C	°C
1	polypropylene	25.1	101.4	4.0	335.5	0	0	0.78	148.0	115.4	2.1
2	poly(C_3–*co*–C_6)	25.7	78.5	3.1	319.6	0	8.1	0.42	85.9	25.5	1.7
3	poly(C_3–*co*–C_6–*co*–C_6OH)	37.6	128.6	3.4	313.8	0.1	9.0	2.19	78.8	22.5	-5.4
3D	poly(C_3–*co*–C_6–*co*–C_6OH)	37.8	140.7	3.7	315.5	0.1	9.0	0.05	80.8	22.6	-0.4
4	poly(C_3–*co*–C_6–*co*–C_6OH)	28.0	115.0	4.0	314.7	0.5	9.1	2.60	80.0	25.0	-3.3
4D	poly(C_3–*co*–C_6–*co*–C_6OH)	32.0	150.0	4.7	315.2	0.5	9.1	0.26	83.1	33.3	-0.1
4Si	poly(C_3–*co*–C_6–*co*–C_6OSiMe$_3$)	36.1	157.3	4.4	315.1	0.5	9.1	0.06	82.1	34.3	-0.3

[a] Determined by HT-SEC in 1,2-dichlorobenzene at 150°C; [b] Determined by 1H NMR; [c] Determined by ^{13}C NMR; [d] Determined by ICP-MS; [e] Determined by DSC; [f] Determined by DMA.

The relatively low molecular weights (M_n = 25−38 kg/mol) obtained under the applied polymerization conditions afforded good processability of the polymers as HMA.[43] The OH content was maintained low to preserve polyolefin properties and ranged from 0.1 to 0.5 mol %. Despite being low, this OH content proved sufficient

in providing significant improvement of the polymers' adhesion to polar substrates like aluminum or steel (*vide infra*). 1-Hexene was introduced to reduce the polymers' crystallinity, which is crucial for good adhesive strength of the material.[22,44] The 1-hexene content in the copolymers and terpolymers of approx. 9 mol % was estimated by NMR analysis. This is in agreement with the decreasing number of branches per 1000 carbons with increasing 1-hexene incorporation as determined by HT-SEC using an infrared (IR) detector (Figure S3). The HT-SEC also demonstrates that the branches are uniformly distributed over the polymer backbone with respect to molecular weight. The presence of butyl branches clearly suppresses the crystallinity of the corresponding polymers, which is reflected in the lower melting temperatures in comparison to the polypropylene (1, Tables 1 and 2) prepared with the same catalyst at 130 °C displaying a T_m at 148 °C and a crystallinity degree of 44 %.

Table 2. Thickness of lamellar crystals of *i*PP and propylene-based copolymers and terpolymers.

Sample	Long Period[a] (nm)	X_c[b] (%)	X_v[c] (vol%)	Thickness of crystals[d] (nm)	Thickness of crystals[e] (nm)
1	12.0	44.0	41.5	5.0	5.1
2	9.3	12.3	11.2	1.0	2.4
3	13.5	5.4	4.7	0.6	2.3
3D	9.8	10.6	9.2	0.9	2.4
4	9.8	9.0	8.2	0.8	2.3
4D	9.9	10.2	9.6	1.0	2.4

[a)] Determined by X-ray; [b)] Determined by DSC; [c)] Determined by transforming the crystalline mass fraction with the use of densities of crystalline and amorphous component: for polypropylene ρ_c = 0.946g/cm^3, ρ_a = 0.855g/cm^3; [d)] Estimated from long period and crystalline volume fraction; [e)] Determined by Thomson-Gibbs equation.

For the poly(C_3–*co*–C_6) (2) prepared under the same conditions, the melting point and crystallinity degree were reduced to 85.9 °C and 12.3 %, respectively (Tables 1, 2, S1, and Figure S4). Although only limited amounts of the functional comonomer (0.1−0.5 mol %) were introduced into the macromolecules, further reduction of their melting temperature and crystallinity degree was clearly evident. For the terpolymers, the average melting point and crystallinity were around 80 °C and 10 %, respectively (Tables 1 and 2).[45] Interestingly, there is a clear difference in the melting point for the same functionalized polyolefin before and after deashing (3

and 3D; 4 and 4D). Removal of aluminum oxide hydroxide residues, deriving from the methylaluminoxane (MAO) cocatalyst and TEA used as the scavenger and the passivating agent during the polymerization, gives rise to a somewhat higher T_m. Most likely, the aluminum oxide hydroxide residues induce some kind of network formation with the hydroxyl groups of the functionalized polyolefins, which hampers self-organization of the polymer chains, leading to a drop in crystallinity. In addition, the same physical crosslinking seems to extend the rubbery phase as the T_g of the functionalized polymers is significantly lower as compared to that of the poly(C_3–*co*–C_6) reference sample.[46,47] In agreement with DSC analyses, the presence of butyl branches significantly affects the thickness of the lamellar crystals as also determined by X-ray (SAXS) and atomic force microscopy (AFM) techniques (entry 4D, Table 2 and Figures S4−S6). On the other hand, the introduction of hydroxyl functionalities has a very limited influence on the crystal dimensions as the crystal sizes in all copolymers and terpolymers were practically identical. Hence, the influence of the microstructure of lamellar crystals during the analysis of the adhesive properties of copolymers and terpolymers (*vide infra*) can be neglected.

The flow behavior of an HMA and its open time, which means the time available for processing before the HMA solidifies, are crucial for the product's applicability. To study this behavior, rheology and DMA measurements were performed (Figures 2 and S7−S13) to determine the viscosity and modulus profiles as a function of temperature. The melt viscoelastic behavior of polypropylene is known to show a strong temperature dependency,[48] whereas (physical) crosslinks can lead to the thermoplastic−elastomeric transition.[49] As shown in Figure 2 (see also Tables S2 and S3), the presence of residual aluminum oxide hydroxide in the polymer has a profound effect on the viscosity, storage modulus (G′), and loss modulus (G″), which decrease with diminishing amounts of residual aluminum oxide hydroxide. DMA and rheological measurements, employing temperature ramp and frequency sweep modes, indicated that the nondeashed samples (3, 4) show a more pronounced shear thinning under low shear rates in comparison to 3D and 4D.

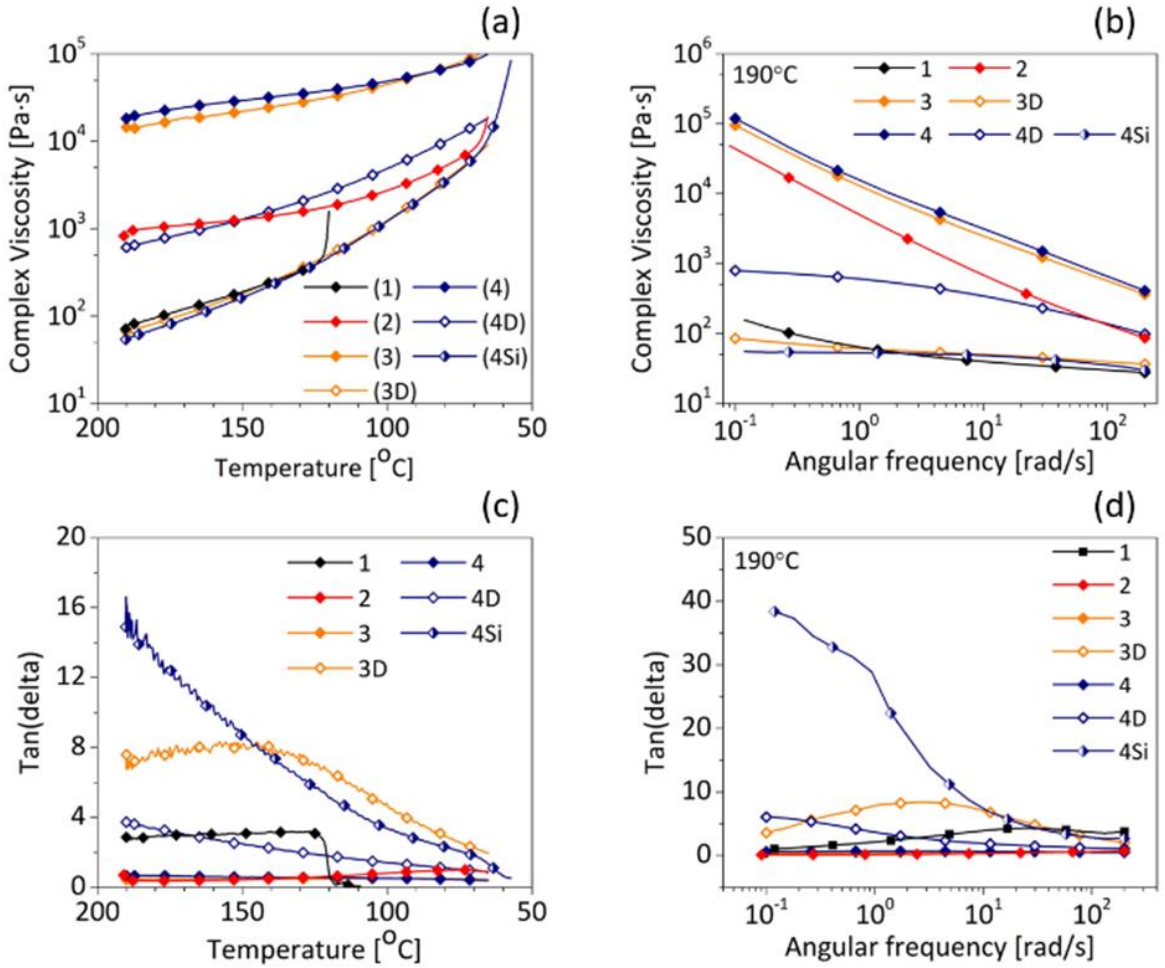

Figure 2. Temperature (a, c) and frequency (b, d) dependency of complex viscosity and loss factor of *i*PP and propylene-based copolymers and terpolymers.

These observations are characteristics of crosslinked systems, where the storage modulus is larger than the loss modulus (Figures S7 and S9). The dynamic crosslinks in the nondeashed samples 3 and 4 are assumed to originate from hydrogen bonding and electrostatic interactions between the polymers' hydroxyl functionality and the aluminum oxide hydroxide residues.[50] Removal of the aluminum oxide hydroxide residues (3D, 4D) changes the tan(δ) (loss factor) by means of decreasing the discrepancy or even inverting the ratio between G′ and G″. This transition from an elastic to a viscous nature, which takes place upon deashing and silylation, is displayed in Figure 2c. The increased "liquid-like" behavior leads to improved flowability and processability of the material, which is expected to be beneficial for the processing performance of the material as HMA.

Static mechanical properties are in good agreement with rheology outcomes. With a significant decrease in Young's modulus (Table S4, Figures S14, and S15),

removal of the aluminum oxide hydroxide traces also had a pronounced effect on the mechanical properties of the materials.

Before assessing the functionalized polyolefin's performance as HMA for glass-filled *i*PP, steel, and aluminum substrates, contact angle and surface wettability measurements and surface structure analysis of these materials were performed (Table S5). Regarding the nanoscale surface structure, quantitative roughness analysis by atomic force microscopy (AFM) exhibited that steel is less porous than aluminum, as the latter possesses well-defined and visible pores (Table S6 and Figure S16). Worth mentioning, the surface of the injection-molded glass-filled *i*PP plaques consists exclusively of *i*PP and not of glass. The surface wettability was evaluated by static contact angle measurements for water and diiodomethane. The relatively low static water contact angle and higher surface tension of aluminum (74.3°, 34.6 mN/m) as compared to those of steel (99.7°, 28.6 mN/m) and glass-filled *i*PP (101.0°, 29.0 mN/m) indicate a significantly more polar nature of the former.

The bonding strength of adhesives can be measured using various techniques such as peel tests, lap shear strength (LSS) tests, or double cantilever beam (DCB) tests.[51−55] Peel tests can only be performed on flexible substrates, whereas the LSS and DCB tests are suitable for rigid substrate materials. Although the DCB test method has been developed to obtain a deeper insight into the fundamental adhesion mechanism,[55] the LSS test is a more common and standardized technique, which made it our method of choice.

In an effort to assess the adhesive potential of the synthesized polymers, a series of LSS tests were performed using the hydroxyl- and siloxy-functionalized terpolymer (4Si), as well as the nonfunctionalized *i*PP (1) and poly(C_3–*co*–C_6) (2) reference samples as HMAs to bond glass-filled *i*PP, steel, and aluminum and combinations of glass-filled *i*PP with steel and aluminum, respectively (Table 3 and Figure 3). Keeping the melting temperature of *i*PP in mind, an application temperature of 130 °C was selected for all material combinations, but for the adhesion tests for aluminum and steel alone, additionally, an application temperature of 180 °C was evaluated to study the effect of temperature on the flow behavior of the polymer, the wettability, and the adhesion to the substrate.[13] Initial adhesion tests were performed using glass-filled *i*PP substrates.

Table 3. Lap shear test results of the *i*PP and propylene-based copolymers and terpolymers

Sample	Bonding T °C	glass filled iPP glass filled iPP, MPa	Aluminum aluminum, MPa	Steel steel, MPa	Aluminum glass-filled iPP, MPa	Steel glass-filled iPP, MPa
1	130	-[a]	-[a]	-[a]	-[a]	-[a]
	180	-[b]	0.6 ± 0.1	-[c]	-[b]	-[b]
2	130	5.1 ± 0.3	0.8 ± 0.3	2.7 ± 0.5	0.4 ± 0.2	0.5 ± 0.3
	180	-[b]	1.1 ± 0.3	2.0 ± 0.2	-[b]	-[b]
3	130	5.9 ± 0.5	2.3 ± 0.7	5.4 ± 0.9	2.5 ± 0.6	3.4 ± 0.9
	180	-[b]	4.7 ± 0.6	6.5 ± 0.3	-[b]	-[b]
3D	130	5.8 ± 0.3	7.5 ± 0.5[d]	8.3 ± 1.0	3.7 ± 0.4	4.7 ± 0.3
	180	-[b]	6.5 ± 1.0	9.7 ± 0.5	-[b]	-[b]
4	130	5.2 ± 0.6	2.4 ± 0.4	4.1 ± 0.7	2.7 ± 0.3	3.9 ± 0.6
	180	-[b]	7.6 ± 0.7[d]	16.7 ± 0.8	-[b]	-[b]
4D	130	5.8 ± 0.2	8.0 ± 0.3[d]	12.6 ± 2.3	5.2 ± 0.7	8.0 ± 0.3
	180	-[b]	7.7 ± 0.1[d]	14.5 ± 1.1	-[b]	-[b]
4Si	130	-[c]	7.2 ± 0.3	6.8 ± 0.2	1.1 ± 0.2	2.7 ± 0.9
	180	-[b]	7.6 ± 0.4[d]	8.2 ± 1.4	-[b]	-[b]

[a)]The high melting temperature of the examined iPP excludes it to be applied as HMA at 130 °C; [b)] Melting point of glass filled iPP plaques excludes it from bonding at 180 °C; [c)] Measurement not possible due to lack of adhesion; [d)] Cohesive failure of aluminum for some of the strips.

As no functionality is required for the propylene-based HMA to adhere to *i*PP, it is not surprising that comparable adhesive strengths are obtained for the nonfunctionalized sample 2 and the functionalized samples 3, 3D, 4, and 4D. Deashing of the functionalized samples does not seem to make any difference to the bonding to *i*PP substrates. The adhesion strength is exclusively governed by the mutual diffusion of the polymer chains at the interphase and their cocrystallization upon cooling, resulting in an average adhesive strength of 5−6 MPa. The relatively low adhesive strength, for example, as compared to welded *i*PP samples,[56] can be assigned to the low molecular-weight, low-isotactic material that typically migrates to the surface of injection-molded *i*PP samples, which hampers cocrystallization and/or effective entanglement formation between the *i*PP and HMA.[57] Unexpectedly, the siloxy-functionalized product 4Si showed a very low adhesive strength, which prevented a reliable LSS measurement. This was rather surprising as 4Si is derived from 4D, which showed reasonably good adhesion to the glass-filled *i*PP substrates.

The reason for this low adhesion is not yet understood. The *i*PP sample 1 could not be used as HMA as its melting temperature was too close to that of the glass-filled *i*PP substrates.

The unfunctionalized 1 and 2 (Table 3) show significantly lower adhesive strengths (<1 MPa) to aluminum compared to the functionalized materials (Figure 3). This result clearly demonstrates the importance of the polar functionality incorporated into the terpolymer backbone for their adhesion performance. For the application temperature of 130 °C, deashing of the hydroxyl-functionalized samples (3, 4 versus 3D, 4D) has a significant positive effect on the adhesive strength, leading to an increase in the LSS values from an average of 2.5 to 8 MPa. Deashing frees up the hydroxyl group from binding with the aluminum oxide hydroxyl residues retained in the polymer, allowing them to bind to the aluminum oxide surface of the aluminum substrates (Figure S17). Increasing the application temperature leads to a clear increase in adhesive strength for the nondeashed samples up to the level of the deashed samples (4, 4D Table 3 and Figure 4). This strongly suggests that the mobility of the hydroxyl groups in the nondeashed samples is restricted at 130 °C due to the polar interactions with the aluminum oxide hydroxide residues present in these samples and a higher temperature is required to achieve optimal interaction with the aluminum surface.[58]

Interestingly, when processed both at 130 °C and at 180 °C, the amount of hydroxyl functionalities of 0.1 versus 0.5 mol % has no significant difference in adhesion performance for deashed samples 3D and 4D (Table 3). For the unpurified samples 3 and 4, the higher functionality level for 4 positively affects the adhesive strength when processed at 180 °C, but no difference is seen when processed at 130 °C. It is worth mentioning that the actual adhesive strength of 3D (at 130 °C), 4 (at 180 °C), 4D, and 4Si (at 180 °C) was too high to measure as around 7.6 MPa cohesive failure of the aluminum plaques occurred (Figure S18).[59] To our surprise, the silyl-functionalized terpolymer 4Si performs equally well as the hydroxyl-functionalized ones. It was expected that passivation of the hydroxyl functionality with a silyl group would prevent the oxygen functionality from reacting/interacting with the polar surface. A possible explanation could be that during the adhesion process, the siloxy group reacts with a metal hydroxyl or strained metal oxide bond, creating a covalent bond between the polymer oxygen and the surface, similar to the hydroxyl-functionalized analogues 3(D) and 4(D).[60]

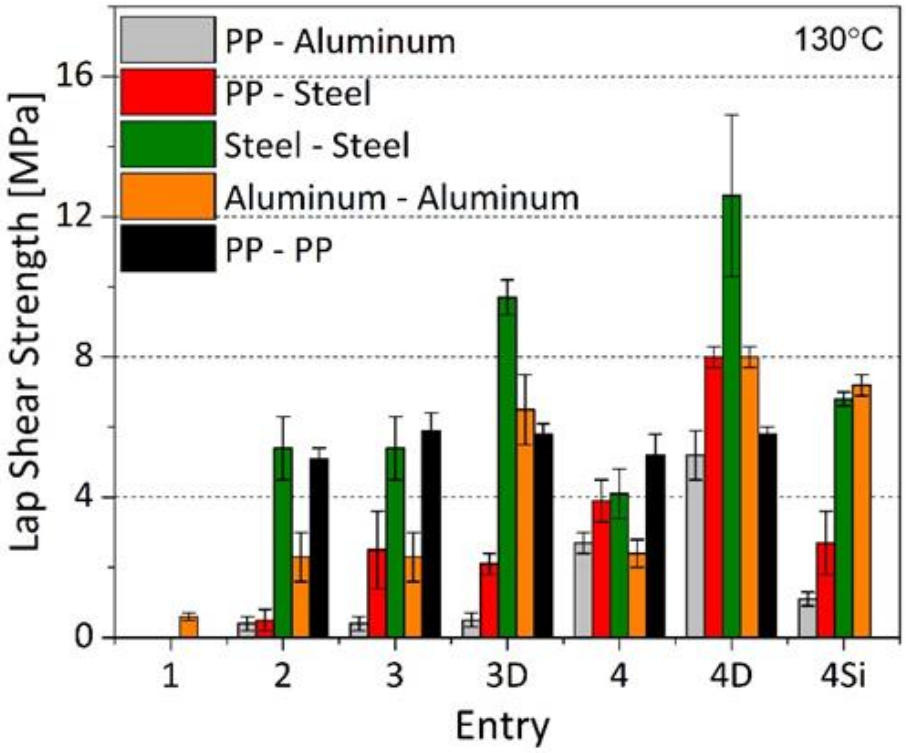

Figure 3. Adhesive strength for bonding different substrate combinations using non-functionalized and functionalized polypropylenes at 130 °C.

A similar situation was observed when testing the nonfunctionalized and functionalized polymers as HMA for the lamination of steel substrates. Whereas the nonfunctionalized samples 1 and 2 show poor adhesion to steel regardless of the application temperature, the hydroxyl- and siloxy-functionalized samples adhere strongly to the steel substrates. In this case, a higher functionality level clearly results in a higher adhesive strength (3, 3D versus 4, 4D). Deashing and increasing the application temperature lead to a further increase in the LSS values (Figures 4, S17, and Table S7). The largest increase is observed when increasing the application temperature for the nondeashed sample 4. The impressive adhesive strength of 16.7 MPa observed for 4 is in the range of the adhesive strengths typical for two component epoxy glues. For 4 processed at 180 °C, deashing does not lead to a further increase in adhesive strength. The observation that for 4D and 4 processed at 180 °C cohesive failure of the HMA occurs suggests that the maximum internal strength of the polymer has been reached. Albeit lower than found for its hydroxyl-functionalized analogue, the adhesive strength of 8.2 MPa of the siloxy-functionalized 4Si to steel is still excellent.

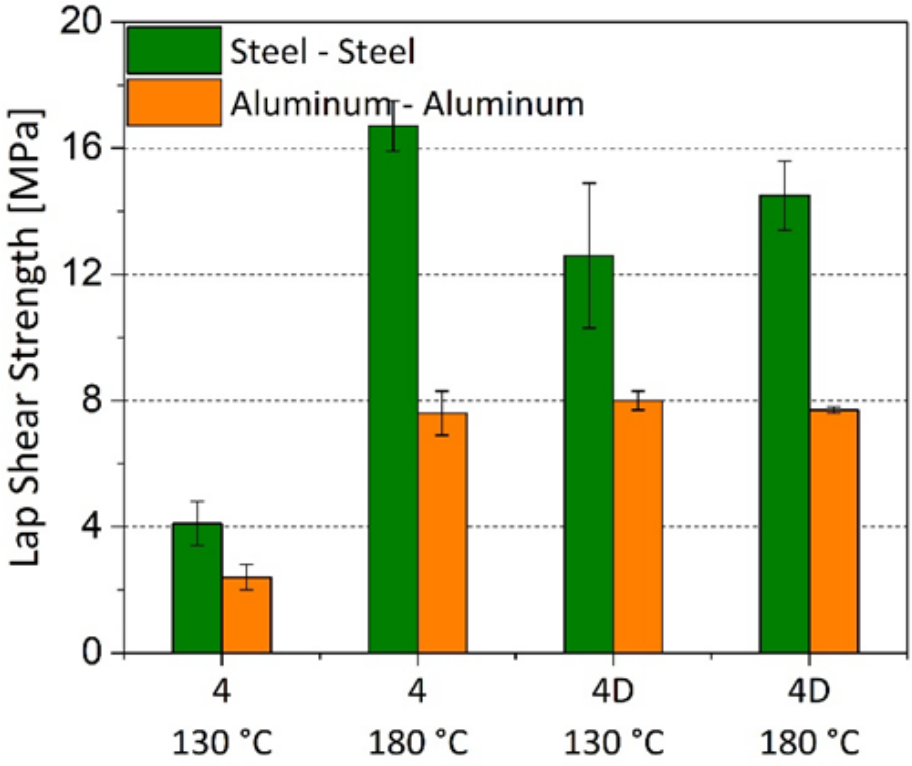

Figure 4. Effect of application temperature and deashing on the adhesive strength for bonding of aluminum and steel.

The difference in adhesive strength between aluminum and steel is interesting. Although in several cases the aluminum specimen broke during the LSS test, overall, the used functionalized propylene terpolymers show a lower adhesive strength to aluminum than to steel. Most likely, differences in morphology and polarity might play an important role.[61,62] Initial surface analyses show that the polarity of the aluminum surface is higher than of the steel surface (Table S5, Table S6). More detailed studies need to be performed to elucidate the cause of this difference.

To explore the reusability of the functionalized polypropylene-based HMA, multicycle lap shear tests of 4 for bonding steel substrates were performed. After every bonding procedure, the lap shear strength was measured, after which the detached steel strips were simply pressed together again at 180 °C without adding. The bonding/rebonding cycles were consecutively repeated 4 times without adding additional HMA. Figure S19 and Table S8 show remarkably consistent adhesion strengths of the laminated steel of 16.7, 15.0, 16.4, and 17.3 MPa, respectively. Surprisingly, even after the 4th bonding cycle, the adhesion strength was within the

error identical to the initial value of the tested materials. The data are in line with the rheology analysis, showing no changes of the polymers' performance while exposed to various temperatures during the multicycle rheology tests (Figure S19).

Next, the adhesion of the nonfunctionalized (1, 2) and functionalized (3−4Si) polymers to combinations of glass-filled *i*PP and aluminum or steel plaques was studied. Due to the melting point of *i*PP, the application temperature was limited to 130 °C, which resulted in limited adhesion of the nondeashed samples (3, 4) to the metals, especially aluminum. As expected, the deashed samples give the best results and a higher functionality level (4D versus 3D) further improves the adhesive strength. The LSS values of 4D for glass-filled *i*PP/aluminum and glass-filled *i*PP/steel of 5.2 and 8.0 MPa, respectively, are unprecedentedly high and clearly show the potential of these functionalized polyolefins as HMA for bonding polyolefin/metal combinations.

Finally, we studied two other important parameters: the crystallinity and the molecular weight of the polymers used as HMAs. Entanglements of the polymer chains are crucial for the adhesive strength of an HMA, as each entanglement functions as a spring, dissipating the energy enforced onto the HMA upon applying stress. It was reasoned that with a too high crystallinity, the fraction of the amorphous phase where entanglements are formed becomes too small to dissipate the energy.[43,63,64] Table S9 shows the characteristics and adhesive strength to aluminum and steel of hydroxyl-functionalized terpolymers with similar molecular weight (M_n) values (28−38 kg/mol), polydispersity (3.4−4.4), and functionality level (FOH = 0.1 mol %) but with different crystallinities. As expected, a higher crystallinity has a negative effect on the adhesive strength of the material to both aluminum and steel. It was furthermore reasoned that low-molecular-weight polymers would entangle less efficiently as compared to high molecular-weight polymers. Hence, for hydroxyl-functionalized polymers only differing in molecular weight, low-molecular weight samples are expected to show lower adhesive strength as compared to the high-molecular-weight ones. Table S10 shows samples of hydroxyl-functionalized terpolymers having comparably low crystallinity values (5.4−12 %) and functionality level (FOH = 0.1 mol %) but different molecular weights (M_n = 8.6 kg/mol versus M_n = 37.6 kg/mol). In general, the functionalized propylene terpolymer samples revealing higher molecular weights provided better LSS results, which result from

polymer chain entanglements, while the macromolecules still have sufficient mobility at the laminating temperature.

CONCLUSIONS

We report the synthesis of hydroxyl- and siloxy-functionalized propylene-based terpolymers and their adhesion to aluminum, steel, and glass-filled *i*PP and combinations of glass-filled *i*PP with aluminum or steel. Using a catalytic approach, materials with tailored molecular weight, crystallinity, and functionality level can be produced. The adhesive strength for bonding to glass-filled *i*PP is moderate. Most likely, this is due to the presence of a waxy and low-isotactic material at the surface of the injection-molded Ziegler−Natta-grade *i*PP plaques, which hampers the entanglement and cocrystallization of the HMA and the *i*PP. Nevertheless, the observed adhesive strength of 5−6 MPa is sufficient for most applications. Despite the low hydroxyl-functionality level of 0.1 or 0.5 mol %, samples 3 and 4 show formidable adhesion to aluminum and steel, whereas the nonfunctionalized congeners 1 and 2 hardly adhere to these metals. Especially when the application temperature is increased from 130 to 180 °C or when the hydroxyl functionalized terpolymers are deashed (3D, 4D) to free up the hydroxyl functionalities to interact with the metals' surface naturally covered by layers of metal oxides and hydroxides,[15] adhesive strengths of over 16 MPa comparable to those of two component epoxy glues are obtained. The good adhesion of the siloxy-functionalized 4Si to aluminum and steel of around 8 MPa is puzzling as it was thought that the silyl group would block the interaction of the polar group with the polar metal surfaces. Possibly, during the adhesion process, the siloxy group reacts with a metal hydroxyl or strained metal oxide bond, creating a covalent bond between the polymer oxygen and the surface. However, further research will be needed to verify this. Polyolefins containing polar hydroxyl functionalities can be an answer to the thus-far unmet market needs in terms of strong yet adaptable adhesives. For instance, their affinity toward polypropylene can be a highly anticipated solution to the industrial use of *i*PP in hot bonded joints, especially in combinations with other materials such as metals.[51] Industrially relevant hot bonding procedures require application at elevated temperatures, usually around 170−180 °C. Our results demonstrate excellent bonding properties at the standard application

temperature of 180 °C and also show that efficient bonding at a lower temperature of 130 °C can be achieved when the products are properly deashed.

REFERENCES

(1) Wang, S.; Liu, Z.; Zhang, L.; Guo, Y.; Song, J.; Lou, J.; Guan, Q.; He, C.; You, Z. Strong, Detachable, and Self-Healing Dynamic Crosslinked Hot Melt Polyurethane Adhesive. *Mater. Chem. Front.* **2019**, 3, 1833−1839.

(2) Yang, H.; Du, G.; Li, Z.; Ran, X.; Zhou, X.; Li, T.; Gao, W.; Li, J.; Lei, H.; Yang, L. Superstrong Adhesive of Isocyanate-Free Polyurea with a Branched Structure. *ACS Appl. Polym. Mater.* **2021**, 3, 1638−1651.

(3) Wei, Y.; Yao, J.; Shao, Z.; Chen, X. Water-Resistant Zein-Based Adhesives. *ACS Sustainable Chem. Eng.* **2020**, 8, 7668−7679.

(4) Heinzmann, C.; Weder, C.; de Espinosa, L. M. Supramolecular Polymer Adhesives: Advanced Materials Inspired by Nature. *Chem. Soc. Rev.* **2016**, 45, 342−358.

(5) Koricho, E. G.; Verna, E.; Belingardi, G.; Martorana, B.; Brunella, V. Parametric Study of Hot-Melt Adhesive under Accelerated Ageing for Automotive Applications. *Int. J. Adhes. Adhes.* **2016**, 68, 169−181.

(6) Zhu, Y.; Romain, C.; Williams, C. K. Sustainable Polymers from Renewable Resources. *Nature* **2016**, 540, 354−362.

(7) Engels, H. W.; Pirkl, H. G.; Albers, R.; Albach, R. W.; Krause, J.; Hoffmann, A.; Casselmann, H.; Dormish, J. Polyurethanes: Versatile Materials and Sustainable Problem Solvers for Today's Challenges. *Angew. Chem., Int. Ed.* **2013**, 52, 9422−9441.

(8) Laurichesse, S.; Avérous, L. Chemical Modification of Lignins: Towards Biobased Polymers. *Prog. Polym. Sci.* **2014**, 39, 1266−1290.

(9) Li, Y.; Krahn, J.; Menon, C. Bioinspired Dry Adhesive Materials and Their Application in Robotics: *A Review. J. Bionic Eng.* **2016**, 13, 181−199.

(10) Díaz López, F. J.; Montalvo, C. A Comprehensive Review of the Evolving and Cumulative Nature of Eco-Innovation in the Chemical Industry. *J. Cleaner Prod.* **2015**, 102, 30−43.

(11) Frost & Sullivan. North American and European Construction Adhesives and Sealants, Emphasis on Light Weighting in Building Components to Drive Revenue Growth Market, Forecast to 2022; Frost & Sullivan, **2016**.

(12) Zhong, K.; Guan, Q.; Sun, W.; Qin, M.; Liu, Z.; Zhang, L.; Xu, J.; Zhang, F.; You, Z. Hot-Melt Adhesive Based on Dynamic Oxime-Carbamate Bonds. Ind. Eng. Chem. Res. **2021**, 60, 6925−6931.

(13) Sun, P.; Li, Y.; Qin, B.; Xu, J. F.; Zhang, X. Super Strong and Multi-Reusable Supramolecular Epoxy Hot Melt Adhesives. *ACS Mater. Lett.* **2021**, 3, 1003−1009.

(14) Kucherov, F. A.; Gordeev, E. G.; Kashin, A. S.; Ananikov, V. P. Controlled Natural Biomass Deoxygenation Allows the Design of Reusable Hot-Melt Adhesives Acting in a Multiple Oxygen Binding Mode. *ACS Appl. Mater. Interfaces* **2020**, 12, 45394−45403.

(15) Hanifpour, A.; Bahri-Laleh, N.; Nekoomanesh-Haghighi, M. Preparation of Novel, Liquid, Solvent-Free, Polyolefin-Based Adhesives. *Polym. Adv. Technol.* **2020**, 31, 922−931.
(16) Liu, B.; Xu, Z.; Fan, C.; Cui, C.; Yao, Y.; Xiao, M.; Liu, W. A Solvent-Free and Water-Resistant Dipole−Dipole Interaction-Based Super Adhesive. *Macromol. Rapid Commun.* **2021**, 42, No. 2100010.
(17) Raos, G.; Zappone, B. Polymer Adhesion: Seeking New Solutions for an Old Problem. *Macromolecules* **2021**, 54, 10617−10644.
(18) 3M Industrial Adhesives and Tapes Division. 3M Hot Melt Adhesive Systems; Industrial Adhesives and Tapes Division, **2016**.
(19) Henkel Adhesives. LOCTITE HHD 3542TM, 2015. www.henkel.com/industrial (accessed Nov 28, 2022).
(20) Awaja, F.; Gilbert, M.; Kelly, G.; Fox, B.; Pigram, P. J. Adhesion of Polymers. *Prog. Polym. Sci.* **2009**, 34, 948−968.
(21) Teng, H. Overview of the Development of the Fluoropolymer Industry. Appl. Sci. **2012**, 2, 496−512.
(22) Liu, Y.; Shigemoto, Y.; Hanada, T.; Miyamae, T.; Kawasaki, K.; Horiuchi, S. Role of Chemical Functionality in the Adhesion of Aluminum and Isotactic Polypropylene. *ACS Appl. Mater. Interfaces* **2021**, 13, 11497−11506.
(23) Huang, S.; Wan, Y.; Ming, X.; Zhou, J.; Zhou, M.; Chen, H.; Zhang, Q.; Zhu, S. Adhering Low Surface Energy Materials without Surface Pretreatment via Ion-Dipole Interactions. *ACS Appl. Mater. Interfaces* **2021**, 13, 41112−41119.
(24) Viswanathan, K.; Ozhalici, H.; Elkins, C. L.; Heisey, C.; Ward, T. C.; Long, T. E. Multiple Hydrogen Bonding for Reversible Polymer Surface Adhesion. Langmuir **2006**, 22, 1099−1105.
(25) Sato, T.; Ise, S.; Horiuchi, S.; Akiyama, H.; Miyamae, T. Influences of Low-Temperature Ambient Pressure N2 Plasma and Flame Treatments on Polypropylene Surfaces. Int. J. Adhes. **2019**, 93, No. 102322.
(26) Kim, S. R. Surface Modification of Poly(Tetrafluoroethylene) Film by Chemical Etching, Plasma, and Ion Beam Treatments. *J. Appl. Polym. Sci.* **2000**, 77, 1913−1920.
(27) Kim, H. J.; Lee, K. J.; Seo, Y. Enhancement of Interfacial Adhesion between Polypropylene and Nylon 6: Effect of Surface Functionalization by Low-Energy Ion-Beam Irradiation. *Macromolecules* **2002**, 35, 1267−1275.
(28) Jia, Y.; Chen, J.; Asahara, H.; Asoh, T. A.; Uyama, H. Polymer Surface Oxidation by Light-Activated Chlorine Dioxide Radical for Metal-Plastics Adhesion. *ACS Appl. Polym. Mater.* **2019**, 1, 3452− 3458.
(29) Boaen, N. K.; Hillmyer, M. A. Post-Polymerization Functionalization of Polyolefins. *Chem. Soc. Rev.* **2005**, 34, 267−275.
(30) Zhou, H.; Wang, S.; Huang, H.; Li, Z.; Plummer, C. M.; Wang, S.; Sun, W. H.; Chen, Y. Direct Amination of Polyethylene by Metal- Free Reaction. *Macromolecules* **2017**, 50, 3510−3515.

(31) Williamson, J. B.; Czaplyski, W. L.; Alexanian, E. J.; Leibfarth, F. A. Regioselective C−H Xanthylation as a Platform for Polyolefin Functionalization. *Angew. Chem., Int. Ed.* **2018**, 130, 6369−6373.

(32) Hagihara, H.; Tsuchihara, K.; Takeuchi, K.; Murata, M.; Ozaki, H.; Shiono, T. Copolymerization of Ethylene or Propylene With- Olefins Containing Hydroxyl Groups with Zirconocene/Methylaluminoxane Catalyst. *J. Polym. Sci., Part A: Polym. Chem.* **2004**, 42, 52− 58.

(33) Franssen, N. M. G.; Reek, J. N. H.; de Bruin, B. Synthesis of Functional 'Polyolefins': State of the Art and Remaining Challenges. *Chem. Soc. Rev.* **2013**, 42, 5809−5832.

(34) Williamson, J. B.; Lewis, S. E.; Johnson, R. R.; Manning, I. M.; Leibfarth, F. A. C−H Functionalization of Commodity Polymers. *Angew. Chem., Int. Ed*. **2019**, 58, 8654−8668.

(35) Pillai, S. K. T.; Kretschmer, W. P.; Trebbin, M.; Förster, S.; Kempe, R. Tailored Nanostructuring of End-Group-Functionalized High-Density Polyethylene Synthesized by an Efficient Catalytic Version of Ziegler's "Aufbaureaktion.". *Chem. Eur. J.* **2012**, 18, 13974−13978.

(36) Song, X.; Cao, L.; Tanaka, R.; Shiono, T.; Cai, Z. Optically Transparent Functional Polyolefin Elastomer with Excellent Mechanical and Thermal Properties. ACS Macro Lett. **2019**, 8, 299−303.

(37) Klimovica, K.; Pan, S.; Lin, T. W.; Peng, X.; Ellison, C. J.; Lapointe, A. M.; Bates, F. S.; Coates, G. W. Compatibilization of IPP/ HDPE Blends with PE-g-IPP Graft Copolymers. *ACS Macro Lett.* **2020**, 9, 1161−1166.

(38) Jasinska-Walc, L.; Bouyahyi, M.; Kruszynski, J.; Tercjak, A.; Rozanski, A.; Troisi, E. M.; Liu, Y.; Yang, L.; Ivashkiv, O.; Sienkiewicz, M.; Duchateau, R. Preparation of Well-Compatibilized PP/PC Blends and Foams Thereof. *ACS Appl. Polym. Mater.* **2021**, 3, 5509−5516.

(39) Banea, M. D.; da Silva, L. F. M.; Carbas, R. J. C. Debonding on Command of Adhesive Joints for the Automotive Industry. *Int. J. Adhes. Adhes.* **2015**, 59, 14−20.

(40) Hutchinson, A. R.; Winfield, P. H.; McCurdy, R. H. Automotive Material Sustainability through Reversible Adhesives. *Adv. Eng. Mater.* **2010**, 12, 646−652.

(41) Machado, J. J. M.; Nunes, P. D. P.; Marques, E. A. S.; da Silva, L. F. M. Adhesive Joints Using Aluminium and CFRP Substrates Tested at Low and High Temperatures under Quasi-Static and Impact Conditions for the Automotive Industry. *Composites, Part B* **2019**, 158, 102−116.

(42) Duchateau, R.; Bouyahyi, M.; Jasinska-Walc, L.; Goswami, P. P. et al. Process for the Preparation of a Graft Copolymer Comprising a Polyolefin Main Chain and One or a Multiple Polymer Side Chains and the Products Obtained Therefrom. U.S. Patent US10,519,267B22019.

(43) Pawlak, A. The Entanglements of Macromolecules and Their Influence on the Properties of Polymers. Macromol. Chem. Phys. **2019**, 220, No. 1900043.

(44) Hagihara, H.; Ito, K.; Kimata, S. Comprehensive Study of Altered Amorphous Structure in Functionalized Polypropylenes Exhibiting High Tensile Strength. *Macromolecules* **2013**, 46, 4432−4437.

(45) Lee, H. J.; Baek, J. W.; Kim, T. J.; Park, H. S.; Moon, S. H.; Park, K. L.; Bae, S. M.; Park, J.; Lee, B. Y. Synthesis of Long-Chain Branched Polyolefins by Coordinative Chain Transfer Polymerization. *Macromolecules* **2019**, 52, 9311−9320.

(46) Khonakdar, H. A.; Morshedian, J.; Wagenknecht, U.; Jafari, S. H. An Investigation of Chemical Crosslinking Effect on Properties of High-Density Polyethylene. *Polymer* **2003**, 44, 4301−4309.
(47) Scott, P. J.; Meenakshisundaram, V.; Chartrain, N. A.; Sirrine, J. M.; Williams, C. B.; Long, T. E. Additive Manufacturing of Hydrocarbon Elastomers via Simultaneous Chain Extension and Cross-Linking of Hydrogenated Polybutadiene. *ACS Appl. Polym. Mater.* **2019**, 1, 684−690.
(48) Kurzbeck, S.; Oster, F.; Münstedt, H.; Nguyen, T. Q.; Gensler, R. Rheological Properties of Two Polypropylenes with Different Molecular Structure. *J. Rheol.* **1999**, 43, 359−374.
(49) Saed, M. O.; Lin, X.; Terentjev, E. M. Dynamic Semicrystalline Networks of Polypropylene with Thiol-Anhydride Exchangeable Crosslinks. *ACS Appl. Mater. Interfaces* **2021**, 13, 42044−42051.
(50) Jasinska-Walc, L.; Duchateau, R.; Bouyahyi, M.; Ginzburg, A.; Zhu, J.; Kruszynski, J.; Aikaterini, T.; Nogales, M. T. Process for Preparation of Amorphous Polyolefinic Ionomers. U.S. Patent US20210087310A12021.
(51) Matsumoto, T.; Shimizu, Y.; Nishino, T. Analyses of the Adhesion Interphase of Isotactic Polypropylene Using Hot-Melt Polyolefin Adhesives. *Macromolecules* **2021**, 54, 7226−7233.
(52) Boutar, Y.; Naïmi, S.; Mezlini, S.; Da Silva, L. F. M.; Hamdaoui, M.; Ben Sik Ali, M. Effect of Adhesive Thickness and Surface Roughness on the Shear Strength of Aluminium One-Component Polyurethane Adhesive Single-Lap Joints for Automotive Applications. *J. Adhes. Sci. Technol.* **2016**, 30, 1913−1929.
(53) Washiyama, J.; Kramer, E. J.; Hui, C. Y. Fracture mechanisms of polymer interfaces reinforced with block copolymers: transition from chain pullout to crazing. *Macromolecules* **1993**, 26, 2928−2934.
(54) Creton, C.; Brown, H. R.; Deline, V. R. Influence of Chain Entanglement on the Failure Modes in Block Copolymer Toughened Interfaces. *Macromolecules* **1994**, 27, 1774−1780.
(55) Lyu, L.; Ohnuma, Y.; Shigemoto, Y.; Hanada, T.; Fukada, T.; Akiyama, H.; Terasaki, N.; Horiuchi, S. Toughness and Durability of Interfaces in Dissimilar Adhesive Joints of Aluminum and Carbon-Fiber-Reinforced Thermoplastics. *Langmuir* **2020**, 36, 14046−14057.
(56) Liu, S. J.; Chang, I. T.; Hung, S. W. Factors Affecting the Joint Strength of Ultrasonically Welded Polypropylene Composites. *Polym. Compos.* **2001**, 22, 132−141.
(57) Chaffin, K. A.; Knutsen, J. S.; Brant, P.; Bates, F. S. Highstrength welds in metallocene Polypropylene/Polyethylene laminates. *Science* **2000**, 288, 2187−2189.
(58) Li, J.; Niu, H.; Yu, Y.; Gao, Y.; Wu, Q.; Wang, F.; Sun, P. Supramolecular Polydimethylsiloxane Elastomer with Enhanced Mechanical Properties and Self-Healing Ability Engineered by Synergetic Dynamic Bonds. *ACS Appl. Polym. Mater.* **2021**, 3, 3373−3382.
(59) Nomura, Y.; Sato, A.; Sato, S.; Mori, H.; Endo, T. Synthesis of Novel Moisture-Curable Polyurethanes End-Capped with Trialkoxysilane and Their Application to One-Component Adhesives. *J. Polym. Sci., Part A: Polym. Chem.* **2007**, 45, 2689−2704.
(60) Yoshida, W.; Castro, R. P.; Jou, J. D.; Cohen, Y. Multilayer Alkoxysilane Silylation of Oxide Surfaces. *Langmuir* **2001**, 17, 5882−5888.

(61) Haubrich, J.; Löbbecke, M.; Watermeyer, P.; Wilde, F.; Requena, G.; da Silva, J. Buried Interfaces A Systematic Study to Characterize an Adhesive Interface at Multiple Scales. *Appl. Surf. Sci.* **2018**, 433, 546−555.
(62) Horiuchi, S.; Liu, Y.; Hanada, T.; Akiyama, H. Enhancement in Adhesive Bonding of Aluminum Alloy by Steam Treatment Studied by Energy Loss near Edge Fine Structures in Electron Energy Loss Spectroscopy. *Appl. Surf. Sci.* **2022**, 599, No. 153964.
(63) Horiuchi, S.; Nakagawa, A.; Liao, Y.; Ougizawa, T. Interfacial Entanglements between Glassy Polymers Investigated by Nanofractography with High-Resolution Scanning Electron Microscopy. *Macromolecules* **2008**, 41, 8063−8071.
(64) Horiuchi, S.; Hakukawa, H.; Jong Kim, Y.; Nagata, H.; Sugimura, H. Study of the Adhesion and Interface of the Low- Temperature Bonding of Vacuum Ultraviolet-Irradiated Cyclo-Olefin Polymer Using Electron Microscopy. *Polym. J.* **2016**, 48, 473−479.

Supporting Information for

Unprecedented Adhesive Performance of Propylene-Based Hydroxyl-Functionalized Terpolymers

Jakub Kruszynski, Weronika Nowicka, Miloud Bouyahyi, Yingxin Liu, Lanti Yang, Artur Rozanski, Nithish Anbuchezhian, Lidia Jasinska-Walc, and Rob Duchateau

ACS Applied Polymer Materials **2023** *5* (5), 3875-3882
DOI: 10.1021/acsapm.3c00566

This subchapter contains complete experimental part, description of materials and methods, supplementary text, and supporting figures.

General considerations

Commercially available ethylene-vinyl acetate (EVA)-based hot melt adhesives invincibly constitute approximately 60 % of global hot melt adhesives market. One of the most widely-used commercial EVA-based adhesive represents strength values for bonding steel and aluminum in the range of 6 MPa (see Figure S1). Another major part of HMA market share, reaching almost 16 % in 2018, belongs to thermoplastic polyurethane-based materials. Typical performance of reactive PU hot melts in aluminum bonding is 7.2 MPa. Different polyurethane HMA guarantees adhesion strength at the level of 4.1 MPa for stainless steel substrates. Interestingly, in case of stainless steel and aluminum connections, Zhang and co-workers report lap shear strength values reaching maximum 2 MPa for this particular adhesive. Our hydroxyl functionalized terpolymers give an opportunity to obtain an adhesion strength exceeding commercially available products, regardless of its structural simplicity.

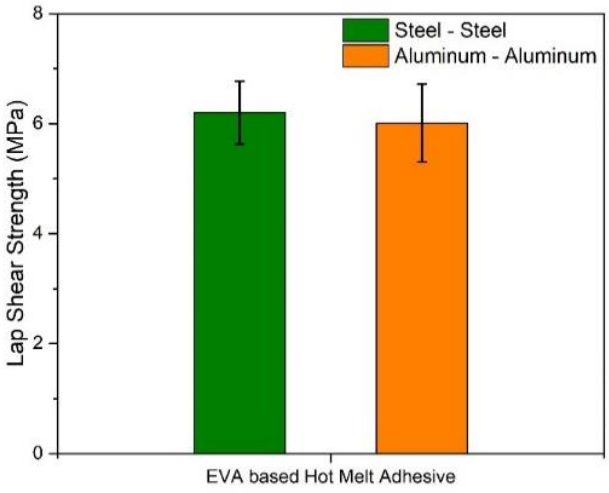

Figure S1. Lap Shear Strength of EVA-based HMA.

Additional experimental details, materials and methods

Materials.

All experiments were performed under an inert dry nitrogen atmosphere using either standard Schlenk or glove box techniques. 1-Hexene, 5-hexene-1-ol and triethylaluminum (TEA, 1.0 M solution in toluene) were purchased from Sigma-Aldrich, distilled and dried with 3 Å molecular sieves under an inert atmosphere. Methylaluminoxane (MAO, 30 wt % solution in toluene) was purchased from Lanxess. The catalyst precursor bis((2-oxoyl-3-(dibenzo-1H-pyrrole-1-yl)-5-(methyl)phenyl)-2-phenoxy)-2,4-pentanediylhafnium (IV) dimethyl, {CH_2[CH(Me)O-C_6H_4-2-(2-$NC_{12}H_8$)-4-Me-C_6H_2O]$_2$}$HfCl_2$, (HfO_4) [CAS: 958665-18-4] was purchased from Lomonosov Moscow State University (A. Z. Voskoboynikov). Dry, oxygen-free pentamethylheptane (PMH) was employed as solvent for the polymerization experiments. Hydrochloric acid (37.0 %, VWR), dry toluene (99.9 %, CHROMASOLV, Honeywell) and methanol (98.5 %, VWR) were employed as chemicals for deashing experiments. Trimethylsilyl chloride (TMCS, for synthesis, Sigma-Aldrich), triethylamine (99 %, Acros Organics), 4-(dimethylamino)pyridine (DMAP for synthesis, Merck) were used without further purification. Polypropylene (PP filled by 40 % glass fiber, Stamax 40Y240, SABIC), aluminum (A35, mill finish, Q-Panel) and steel (QD35, smooth finish, Q-Panel) were employed as surfaces for adhesive experiments.

Synthesis of isotactic polypropylene. The propylene polymerization experiments were carried out using a stainless steel BÜCHI reactor (2 L) filled with

pentamethylheptane (PMH) solvent (1 L) using a stirring speed of 600 rpm. The reactor was first heated to 40 °C followed by the addition of TiBA (1.0 M solution in toluene, 2 mL). The reactor was loaded at 40 °C with gaseous propylene (100 g) and was heated to the desired polymerization temperature of 130 °C, resulting in a partial propylene pressure of about 15 bar. Once the set temperature was reached, the polymerization reaction was initiated by the injection of the pre-activated catalyst precursor HfO_4/MAO (0.25 mg, 0.25 *μ*mol of HfO_4 in MAO 30 wt % solution in toluene, 11.3 mmol) in toluene (5 mL). The reaction was stopped by pouring the polymer solution into an Erlenmeyer flask containing acidified isopropanol (2.5 % v/v HCl (37 %), 500 mL) and Irganox 1010 (1.0 M, 0.5 mmol). The resulting suspension was stirred for 4 h, filtered, washed with demineralized water/*i*PrOH (50 wt %, 2 × 500 mL) and dried at 80 °C in a vacuum oven, prior to the addition of Irganox 1010 as antioxidant (1.0 M, 0.5 mmol, 5 mL).

Synthesis of poly(propylene–*co*–1-hexene) copolymer: poly(C_3–*co*–C_6). Experiments were carried out using a stainless steel BÜCHI reactor (2 L) filled with pentamethylheptane (PMH) solvent (1 L) using a stirring speed of 600 rpm. The reactor was first heated to 40 °C, followed by the addition of TiBA (1.0 M solution in toluene, 2 mL). The reactor was loaded at 40 °C with gaseous propylene (100 g) and 1-hexene (30 ml, 242 mmol) and was heated up to the desired polymerization temperature of 130 °C resulting in a partial propylene pressure of about 15 bar. Once the set temperature was reached, the polymerization reaction was initiated by the injection of the pre-activated catalyst precursor HfO_4/MAO (0.25 mg, 0.25 *μ*mol) in MAO (30 wt % solution in toluene, 11.3 mmol) in toluene (5 mL). The reaction was stopped by pouring the polymer solution into an Erlenmeyer flask containing acidified isopropanol (2.5 % v/v HCl (37 %), 500 mL) and Irganox 1010 (1.0 M, 0.5 mmol). The resulting suspension was stirred for 4 h, filtered, washed with demineralized water/*i*PrOH (50 wt %, 2 × 500 mL) and dried at 80 °C in a vacuum oven, prior the addition of Irganox 1010 as antioxidant (1.0 M, 0.5 mmol, 5 mL).

Synthesis of Randomly Hydroxyl-Functionalized Polypropylene, poly(C_3–*co*–C_6–*co*–C_6OH). The polymerization experiment was carried out using a stainless steel BÜCHI reactor (2 L) filled with pentamethylheptane (PMH) solvent (1L) using a stirring speed of 600 rpm. The reactor was first heated to 40 °C followed by the addition of TEA (1.0 M solution in toluene, 2 mL), 1-hexene (neat 30 mL, 242 mmol), and triethylaluminum (TEA)-passivated 5-hexen-1-ol (1.0 M solution in toluene,

TEA:5-hexen-1-ol mol ratio = 1; 10 mL). The reactor was charged at 40 °C with gaseous propylene (100 g) and heated to the desired polymerization temperature of 130 °C resulting in a partial propylene pressure of about 15 bar. Once the set temperature was reached, the polymerization reaction was initiated by the injection of the pre-activated catalyst HfO_4 (2.0 mg, 2.0 μmol) in MAO (30 wt % solution in toluene, 11.2 mmol) in toluene (5 mL). The reaction was stopped by pouring the polymer solution into an Erlenmeyer flask containing acidified isopropanol (2.5 % v/v HCl (37 %), 500 mL) and Irganox 1010 (1.0 M, 0.5 mmol). The resulting suspension was stirred for 4 h, filtered, washed with demineralized water/iPrOH (50 wt %, 2 × 500 mL) and dried at 80 °C in a vacuum oven, prior the addition of Irganox 1010 as antioxidant (1.0 M, 0.5 mmol, 5 mL).

Procedure of the deashing of Hydroxyl-Functionalized Polypropylene. The polymer obtained from the solution process may be deashed in order to remove traces of protective species. To do so, the copolymer or terpolymer (10 g) was dispersed in mixture of dry toluene (400 mL) and concentrated (37 %) HCl (10 mL, 0.13 mol, 4.74 g) and heated under reflux until the polymer dissolved. Once the polymer was properly dissolved, methanol (250 mL) was added to the hot mixture and the mixture was heated under stirring at 70 – 80 °C for 1 additional hour. Then the polymer was precipitated in cold methanol, filtered and washed 2 times with methanol. The resulting polymer was dried at 80 °C in a vacuum oven for 24 hours.

Silylation of Hydroxyl-Functionalized Polypropylene. The reaction was carried out under a nitrogen atmosphere using standard Schlenk techniques. Poly(C_3–*co*–C_6–*co*–C_6OH) based terpolymer (Table 1, Sample 4D, 10.2 g, 0.32 mmol) was dissolved in 300 mL of toluene at 60 °C. The mixture was stirred until solution became transparent. Solutions of trimethylsilyl chloride (274 mg, 2.50 mmol) and NEt3 (511 mg, 5.00 mmol) were prepared in air- and moisture-free environment and transferred to the polymer solution via sealed rubber septum at 40 °C. The reaction mixture was allowed to stir for approximately 10 minutes and then DMAP (8.2 mg, 0.07 mmol) was added. After this step, the solution became opaque and was left stirring at 40 °C overnight. Then the solution was poured into cold methanol and precipitated. Filtration led to poly(C_3–*co*–C_6–*co*–C_6OSiMe$_3$) as a white solid product, which was quenched with methanol and eventually dried (yield: 9.7 g).

Measurements

^{1}H NMR analysis was carried out at 130 °C using deuterated tetrachloroethane (TCE-D2) as solvent and recorded in 5 mm tubes on a Varian Mercury spectrometer operating at a frequency of 400 MHz. Chemical shifts are reported in ppm versus tetramethylsilane and were determined by reference to the residual solvent protons.

Size Exclusion Chromatography (SEC). The measurements were performed at 150 °C using a Polymer Char GPC-IR® built around an Agilent GC oven model 7890, equipped with an autosampler and the viscometer and refractive index detector. 1,2-Dichlorobenzene (o-DCB) was used as an eluent at a flow rate of 1 mL/min. A PP molar mass calibration was obtained after conversion from PE to PP using the Mark-Houwink constants of PE and PP. The data were processed using Calculations Software GPC One®. Information about the short-chain branching can also be obtained with the GPC/SEC technique using an on-line infrared (IR) detector with at least two interference filters; one filter for measuring the overall absorption of the C–H region, and another filter for measuring the absorption of the C–H from the methyl groups. These IR detectors inform about the comonomer incorporation (short-chain branches) in polyolefin copolymers by measuring the number of methyl groups per 1000 carbon atoms (CH_3/1000C).[3]

Differential Scanning Calorimetry (DSC). Melting (T_m) and crystallization (T_c) temperatures as well as the enthalpies of melting (ΔH_m) were measured using an indium calibrated Differential Scanning Calorimeter (Q100, TA Instruments). The measurements were carried out at a heating and cooling rate of 10 °C/min from −50 °C to 230 °C under nitrogen flow. The transitions were deducted from the second heating and cooling curves. The degree of crystallinity (crystalline mass fraction) of the studied samples was determined according to a formula:

$$X_c = \frac{\Delta H_m}{\Delta H_m^0} \times 100\%$$

where: ΔH_m is the measured specific heat of melting, ΔH_m^0 is the heat of fusion of the crystal. The following values of ΔH_m^0 have been assumed: 209 J/g. The thickness of lamellar crystals was determined according to a Thomson-Gibbs equation:

$$l_c = \frac{2\gamma_e}{\Delta H_m^0} \frac{T_m^0}{T_m^0 - T_m}$$

where l_c is the thickness of lamellar crystals, Tm is the melting temperature of a lamellar crystals, T_m^0 is the equilibrium melting temperature of an infinite crystal, γ_e is the surface energy of the basal surface of a lamellar crystal and ΔH_m^0 is the enthalpy of fusion for the lamellar crystal. To estimate the thickness of crystals the following values of constants characteristic for polypropylene were applied: γ_e = $62.3 \cdot 10^{-7}$ J/cm^2, ΔH_m^0 = 209 J/g, T_m = 208 °C.[4,5]

Inductively Coupled Plasma Mass Spectrometry (ICP-MS). Residual aluminum was established by ICP-MS. Approximately 150 mg of each sample was digested in 6 mL concentrated nitric acid (trace metal grade) by microwave assisted acid digestion using an Anton Paar Multiwave PRO equipped with closed high pressure Quartz digestion vessels. After the microwave digestion run, the acid was analytically transferred into a pre-cleaned plastic centrifuge tube containing 1 mL of internal standard solution and is diluted with MilliQ water up to the 50 mL mark. The elements in the sample are quantified using a multi-element calibration set from Inorganic Ventures using an Agilent 8900 ICP-MS system.

Scanning Electron Microscopy (SEM) images were recorded using a Phenom Pro (Phenom-World) apparatus operating at an accelerating voltage of 5 kV. The samples were sputter-coated using Q150R Rotary-Pumped Sputter Coater (Quorum Technologies) with Au.

Atomic Force Microscopy (AFM). Sample preparation: PP and FPO film samples were prepared by adding around 100 mg PP or FPO pellet between two aluminum foil discs with reflective side inwards and then compress molded at 190 °C. During compression molding, the pellets were first molten for 60 seconds and then for another 60 seconds with two tons pressure. Then the pressure was released and the film was cooled to room temperature. For AFM analysis, a piece of compression molded film was cut and put onto a glass slide. Then a heating cycle was applied to the film sample using a hot stage setup from Linkam. In order to mimic the hot melting processing, the film was first heated up to 130 °C and kept at

130 °C for 5 min. with a heating rate of 20 °C/min. Then the film cooled down to room temperature with a cooling rate of 10 °C/min.

AFM characterization. AFM experiments were performed using a Dimension FastScan AFM system (Dimension FastScan, Bruker, Santa Barbara, USA). Software Nanoscope Analysis 9.4 was used as computer interface for operation and Nanoscope Analysis 2.0 from Bruker for the analysis of AFM measurements. All AFM measurements were performed at ambient conditions. For the PP and FPO film lamellar structure characterization AFM peakforce tapping mode was used with a frequency of 4 Hz utilizing a fast scan type AFM tips (Fastscan-C, k = 0.8 N/m, f = 300 kHz). After imaging, section analysis in the Nanoscope Analysis 2.0 from Bruker was used to measure the lamellar thickness.

Small-Angle X-ray Scattering (SAXS). The lamellar structure of the samples was probed with 2-dimensional small angle X-ray scattering. The Kiessig-type camera with sample detector distance of 1.2 m was coupled to an X-ray CuK a low divergence microsource, operating at 50 kV and 1 mA (GeniX Cu-LD by Xenocs, France). The scattering produced by the sample was recorded with the Pilatus 100 K solid-state area detector of the resolution of 172 × 172 μm^2 (Dectris, Switzerland). Long period was determined from one dimensional sections of 2-D pattern. Background and Lorentz corrections were applied to the curves. Long period was then calculated from position of the maximum of corrected curves using the Braggs law. The thickness of lamellar crystals was determined from long period and crystalline volume fraction according to a formula:

$$l_c = LP \times X_v$$

Where: l_c is the thickness of lamellar crystals, LP is the long period, X_v is the degree of crystallinity (crystalline volume fraction).
Crystalline volume fraction was determined by transforming the crystalline mass fraction with the use of densities of crystalline and amorphous component of polypropylene according to a formula:

$$X_v = \frac{X_c \times d_a}{d_c - \frac{X_c}{100}(d_c - d_a)}$$

Where d_a is the density of amorphous component, 0.855 g/cm^3 for polypropylene, dc is the density of crystalline component, 0.946 g/cm^3 for polypropylene.[6]

Dynamic mechanical analysis (DMA) was performed using a TA Instruments Q800 DMA. Samples were tested by strain-controlled temperature ramp with the frequency of 1 Hz. The measurements were performed using film-tension mode. The temperature profile was from −60 °C to the melting point of the sample with the ramp 2 °C/min. The glass transition temperature was calculated as the maximum of the tangent delta signal.

Melt rheology measurements were performed using a plate-plate (gap distance 1 mm) MCR 720 rheometer (Anton Paar, Graz, Austria). Disc samples (Ø25 mm, 1 mm thickness) were obtained by compression molding. The temperature dependent analysis was conducted from 190 °C to 55 °C (a ramp step of 5 °C/min), with constant angular frequency 1 rad/s and amplitude strain of 1 %, as well as a nitrogen atmosphere.

Surface analysis. The static contact angle was determined by fitting the baseline and contour of the liquid droplets using ellipsoidal method. For each liquid, 10 droplets of 2.0 *μ*L in volume were deposited on the surface and imaged using a camera. The surface free energy was calculated using the Owens-Wendt-Rabel-Kaelble (OWRK) theory in which surface energy is separated into a polar and disperse component and based on the measurements with water and diiodomethane.

Procedure of adhesive laminates preparation. The laminate samples, used for the lap shear test, were prepared via compression-molding using PP ISO settings on LabEcon 600 high-temperature press (Fontijne Presses, the Netherlands). Namely, the films (25 mm × 12.5 mm × 0.5 mm) of iPP and propylene-based copolymers and terpolymers were loaded between the substrates: STAMAX

40Y240, Steel QD35, Aluminum A35 or their combination with overlap of 12.5 mm (312.5 mm^2 bonding area). Then, the compression-molding cycle was applied: (i) heating to 130 °C or 180 °C, (ii) stabilizing for 5 min with no force applied, (iii) applying for 5 min with 100 kN (2 MPa) normal force and cooling down to 40 °C with the cooling speed of 10 °C/min under 100 kN (0.6 MPa) normal force.

Lap Shear Strength analysis. The measurements were performed using Zwick type Z020 tensile tester equipped with a 10 kN load cell. Before measurements, samples were conditioned for 7 days at room temperature. The tests were performed on specimens (10 cm × 2.5 cm) with surface overlapping 12.5 mm under room temperature. A grip-to-grip separation of 140 mm was used. The samples were pre-stressed to 3 N, then loaded with a constant cross-head speed 100 mm/min. To calculate the lap shear strength the reported force value divided by the bonding surface (312.5 mm2) of the specimens. The reported values are an average of at least 5 measurements of each composition.

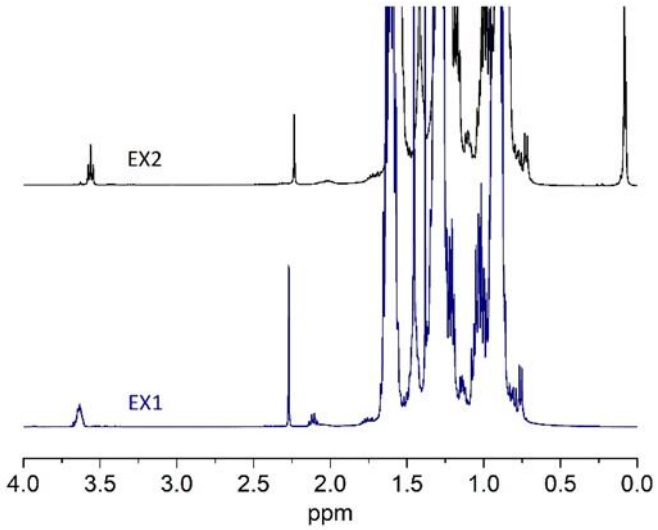

Figure S2. ^{1}H NMR analysis of poly(C_3–*co*–C_6–*co*–C_6OH) (4, bottom) poly(C_3–*co*–C_6–*co*–C_6OSiMe_3) (4Si, top).

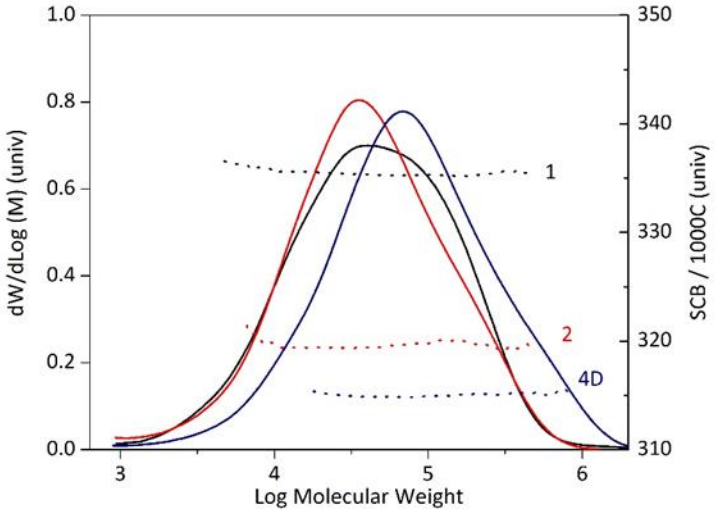

Figure S3. Molecular weight and short chain branches distribution analysis of *i*PP (1), poly(C_3–*co*–C_6) (2) and poly(C_3–*co*–C_6–*co*–C_6OH) (4D).

Table S1. Thermal properties of the synthesized *i*PP and propylene-based copolymers and terpolymers analyzed by DSC.

Sample	T_m [°C]	T_c [°C]	ΔH_c [J/g]	ΔH_m [J/g]	X_c [%]
1	148.0	115.4	88.7	91.0	44.0
2	85.9	25.5	29.4	25.5	12.3
3	78.8	22.5	16.6	11.2	5.4
3D	80.8	22.6	27.4	21.9	10.6
4	80.0	27.0	20.9	14.8	7.2
4D	83.1	43.3	30.8	21.0	10.2
4Si	82.1	34.4	33.3	21.4	10.3

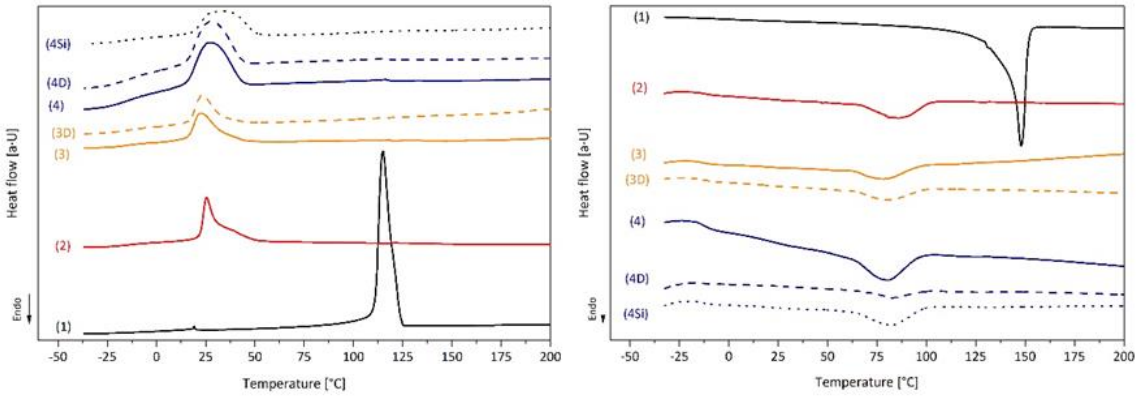

Figure S4. Crystallization and melting profiles of the synthesized *i*PP and propylene-based copolymers and terpolymers determined by DSC.

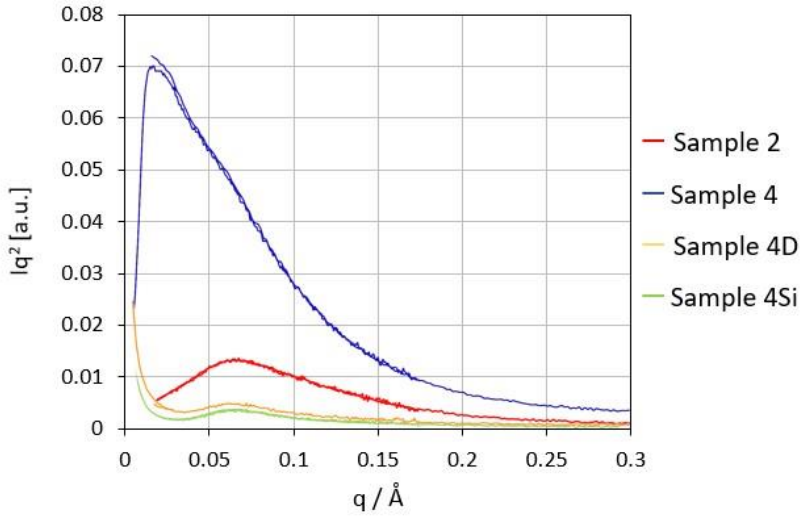

Figure S5. SAXS profiles of the selected samples.

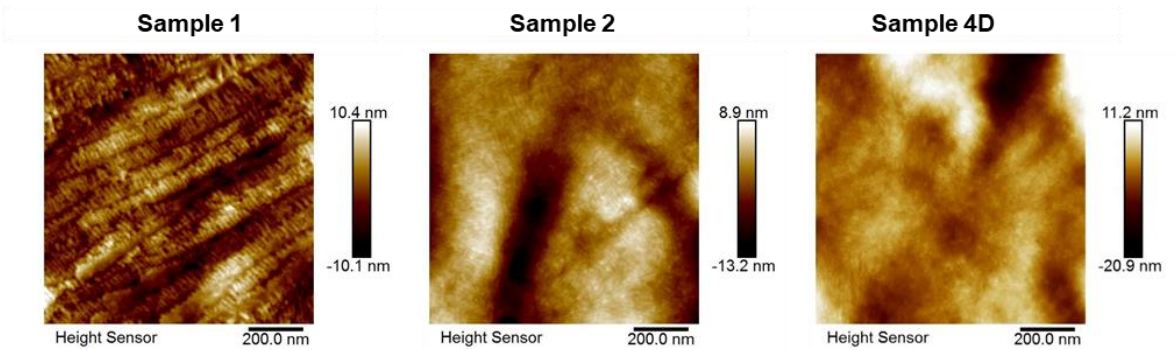

Figure S6. Morphology analysis of the *i*PP and propylene-based copolymer and terpolymer by AFM.

Table S2. DMA analysis of the *i*PP and propylene-based copolymers and terpolymers.

	Modulus [MPa]				
Sample	Storage (E')		Loss (E'')		T_g [°C]
	–40 °C	25 °C	–40 °C	25 °C	
1	5560	1780.8	115	98.3	2.1
2	2496	137.5	46	15.6	1.7
3	3510	95.8	72	8.3	–5.4
3D	3319	102.4	61	11.0	–0.4
4	3775	154.7	92	13.2	–3.3
4D	3461	125.0	64	12.7	–0.1
4Si	2246	109.9	39	11.9	–0.3

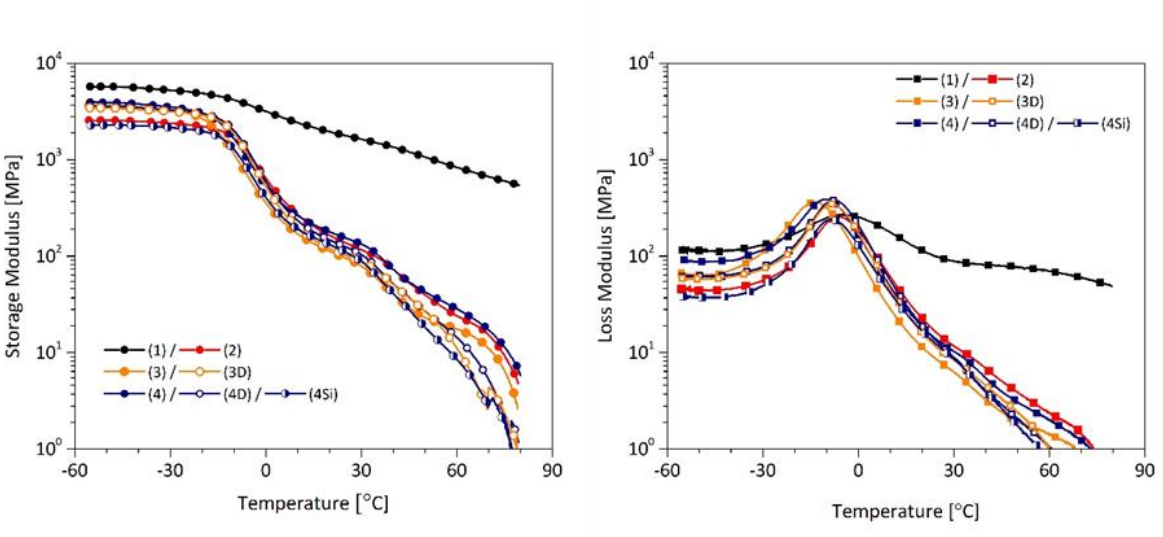

Figure S7. Temperature dependency of the storage and loss modulus of *i*PP and propylene-based copolymers and terpolymers.

Table S3. Rheology analysis of the synthesized *i*PP and propylene-based copolymers and terpolymers.

Sample	Modulus at 180°C		Complex viscosity at 180 °C Pa·s	Max loss factor
	Storage (G') Pa	Loss (G") Pa		
1	31	91	96	3.5
2	362	1028	1027	1.0
3	14186	6904	15777	0.5
3D	11	81	82	8.3
4	17827	12079	21534	0.7
4D	208	704	734	3.8
4Si	6	71	71	18.6

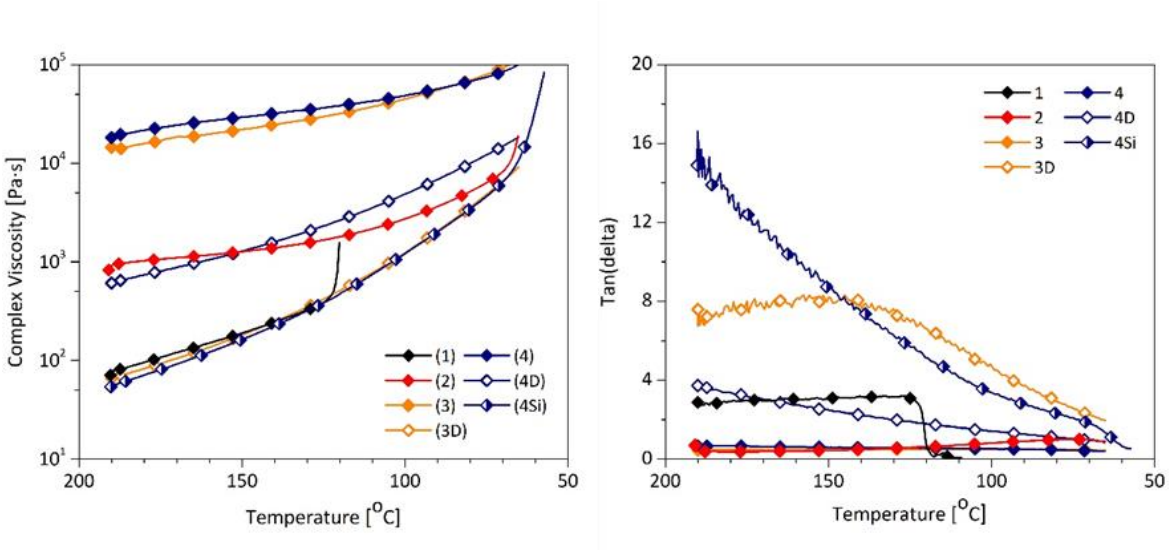

Figure S8. Temperature dependency of the complex viscosity (left) and loss factor (right) of *i*PP and propylene-based copolymers and terpolymers.

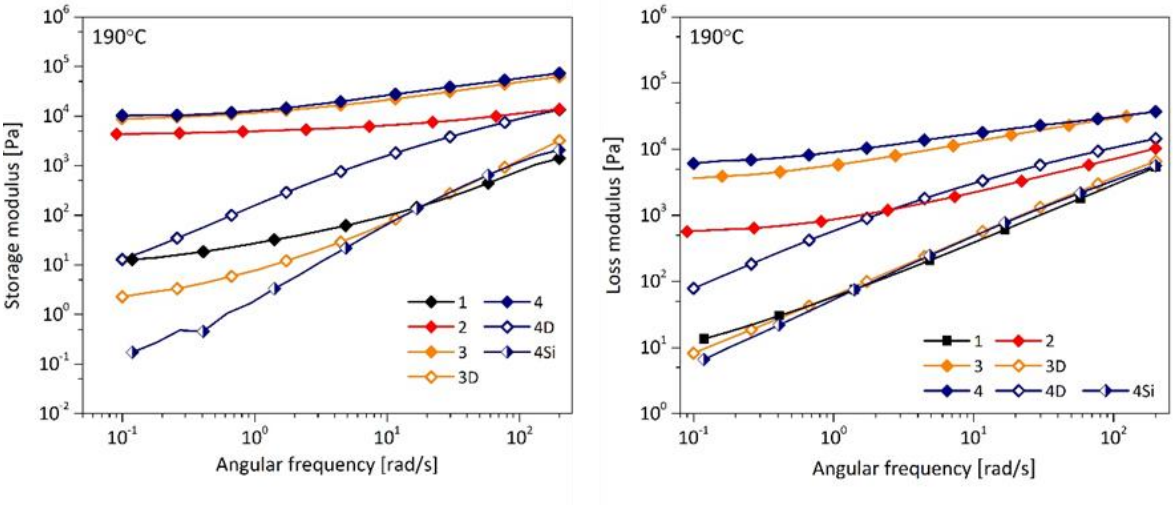

Figure S9. Frequency dependency of the storage (left) and loss modulus (right) of *i*PP and propylene-based copolymers and terpolymers.

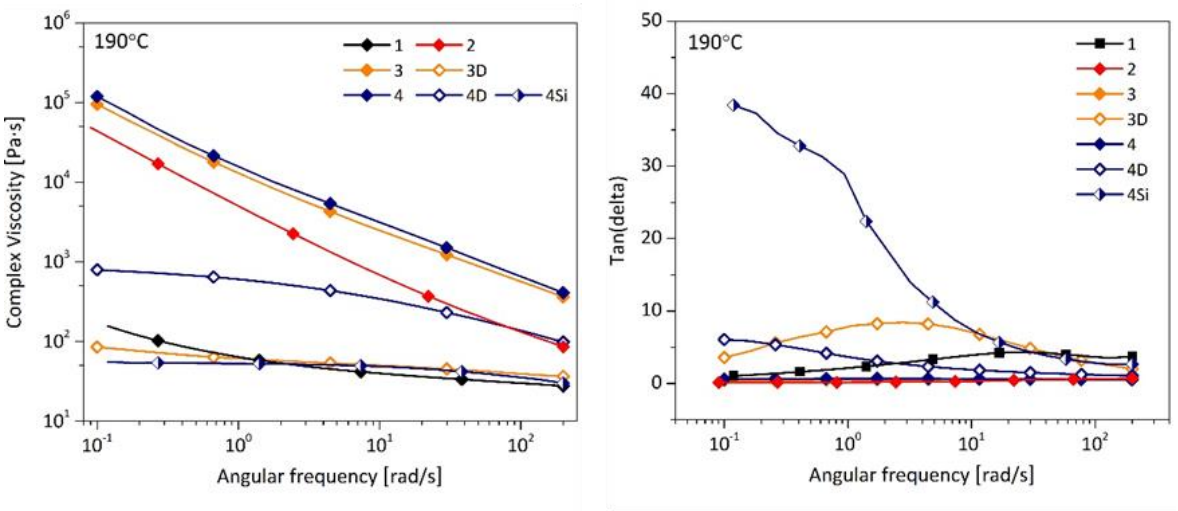

Figure S10. Frequency dependency of the complex viscosity (left) and loss factor (right) of *i*PP and propylene-based terpolymers.

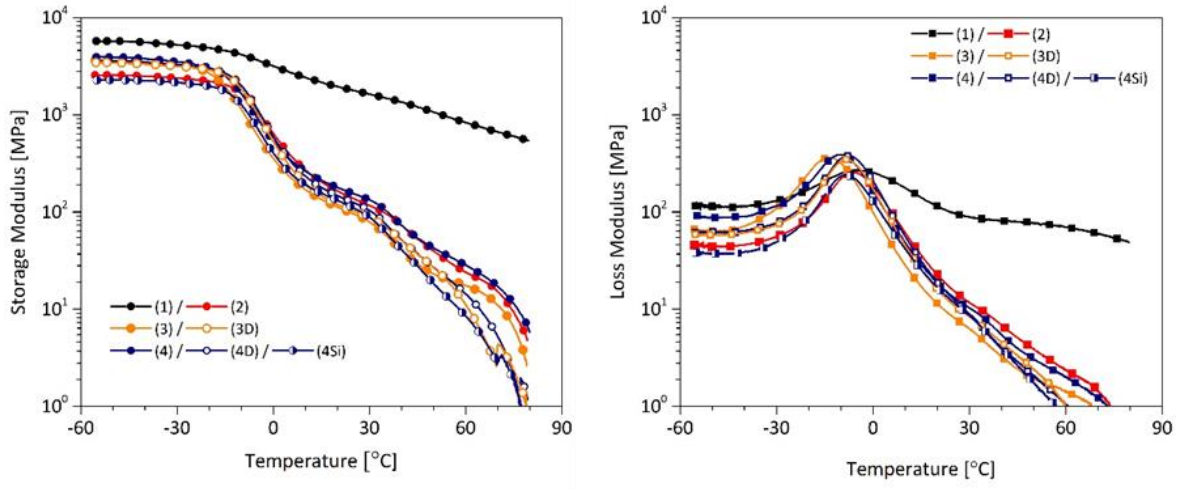

Figure S11. Storage (left) and loss (right) modulus of the synthesized *i*PP and propylene-based copolymers and terpolymers determined by DMTA.

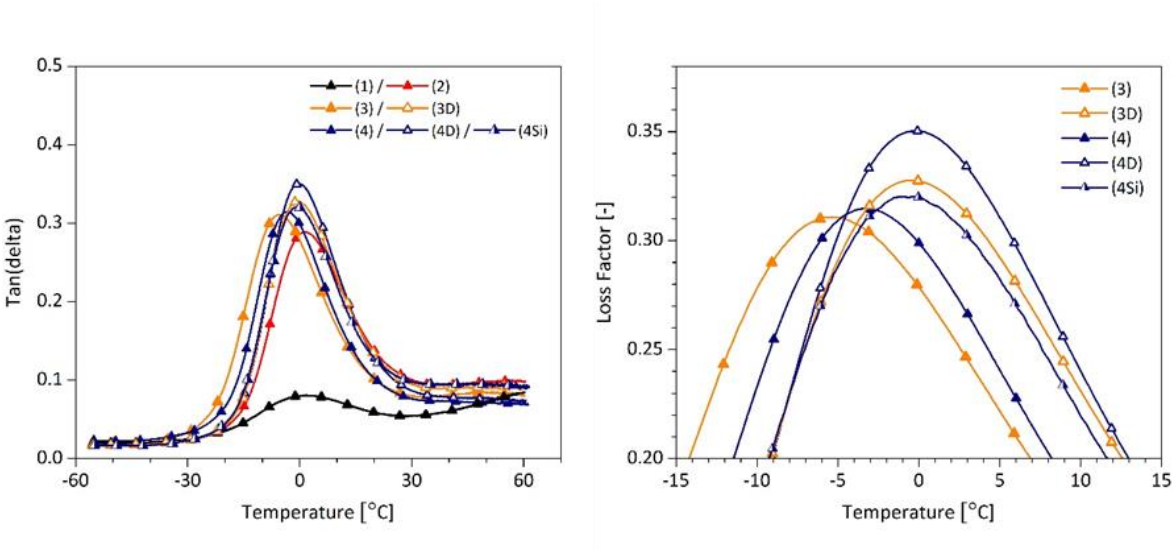

Figure S12. Left: Loss factor of the synthesized *i*PP and propylene-based copolymers and terpolymers determined by DMTA. Right: Detailed changes of the curve maxima of 3, 3D, 4, 4D, 4Si.

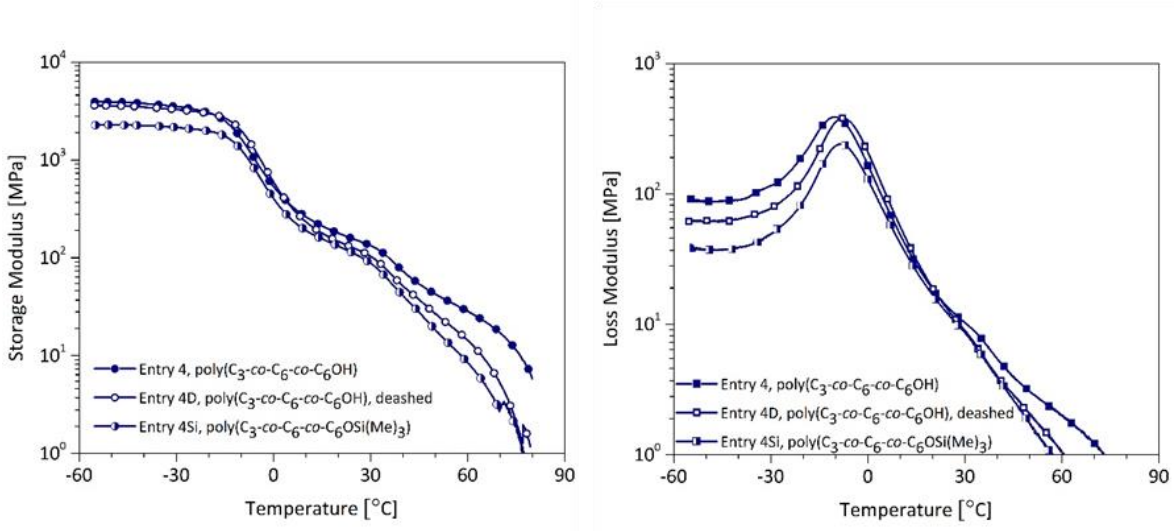

Figure S13. Temperature dependency of the storage modulus (left) and loss modulus (right) of poly(C_3–*co*–C_6–*co*–C_6OH) before/after deashing (4, 4D) and after silylation (4Si).

Table S4. Static mechanical properties of selected samples

Sample	Young modulus [MPa]	Yield strength [MPa]	Tensile strength at break [MPa]	Elongation at break [%]
1	302.1 ± 34.5	31.3 ± 1.6	17.5 ± 1.9	210 ± 80
2	79.0 ± 9.6	10.8 ± 0.3	15.6 ± 2.2	749 ± 92
3	151.8 ± 23.2	9.6 ± 0.9	28.6 ± 2.2	1027 ± 66
3D	158.1 ± 19.1	9.7 ± 1.1	28.5 ± 2.9	1040 ± 40
4	134 ± 13	9.1 ± 0.3	24.5 ± 2.2	701 ±38
4D	62 ± 23	10.4 ± 0.5	26.1 ± 1.8	758 ± 27
4Si	48 ± 36	8.1 ± 0.3	21.9 ± 2.0	680 ± 52

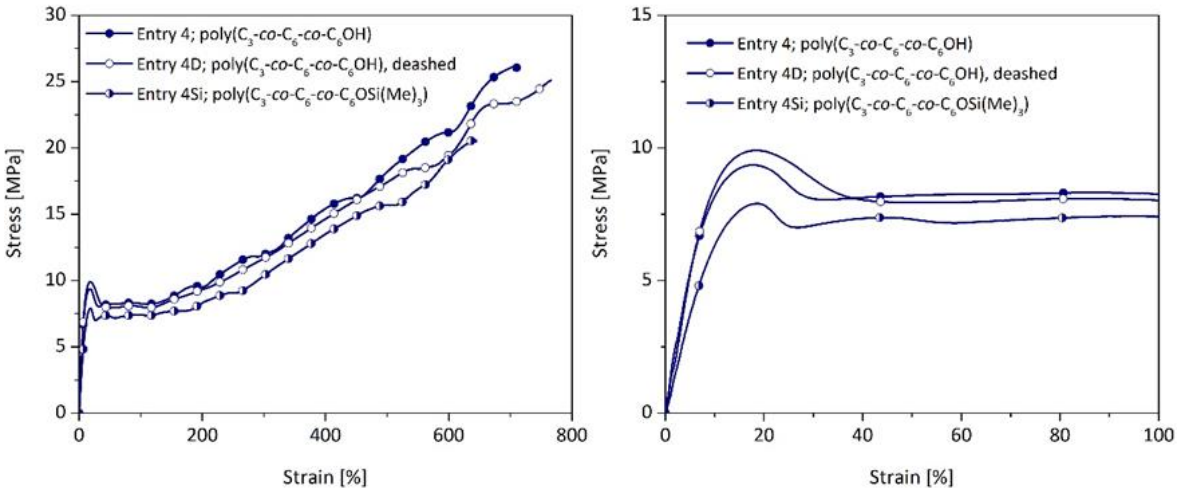

Figure S14. Left: Stress-strain curve of sample 4, 4D and 4Si. Right: Stress changes of 4, 4D and 4Si in narrow strain region.

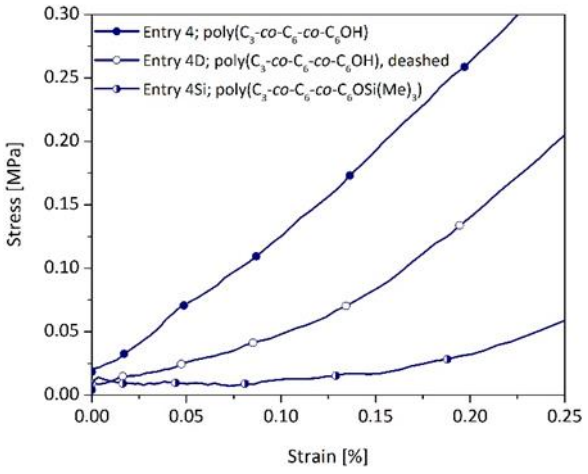

Figure S15. Stress-strain curve of 4, 4D and 4Si at 0.05 – 0.25 % strain.

Table S5. Surface characterization of aluminum, steel, Stamax substrates used for the adhesion tests.

Parameter	BONDED SURFACES		
	aluminum AT35	steel QD35	Stamax 40Y240
CA Water [°] [a]	74.3 ± 4.6	99.7 ± 1.6	101.0 ± 3.5
CA Di-IM [°] [a]	49.4 ± 2.5	61.1 ± 4.5	59.9 ± 2.0
Total surface energy [mN/m] [b]	41.6 ± 3.5	28.6 ± 3.0	29.0 ± 1.5
Surface energy of disperse component [mN/m] [b]	34.6 ± 1.4	28.0 ± 2.6	28.6 ± 1.2
Surface energy of polar component [mN/m] [b]	6.9 ± 2.1	0.6 ± 0.3	0.4 ± 0.4

[a] Static water and diiodomethane contact angle was determined using ellipsoidal method
[b] Free surface energy was calculated using Owens-Wendt-Rabel-Kaelble (OWRK) theory and separated into a polar and dispersed components.

Table S6. Roughness of aluminum, steel and Stamax surfaces determined by Atomic Force Microscopy (AFM).

	aluminum AT35	steel QD35	Stamax 40Y240
Area 1	44.2	49.1	14.0
Area 2	64.9	62.8	20.4
Area 3	84.8	53.2	-
Average	64.6±20.3 nm	55±7.1 nm	17.2±4.6 nm

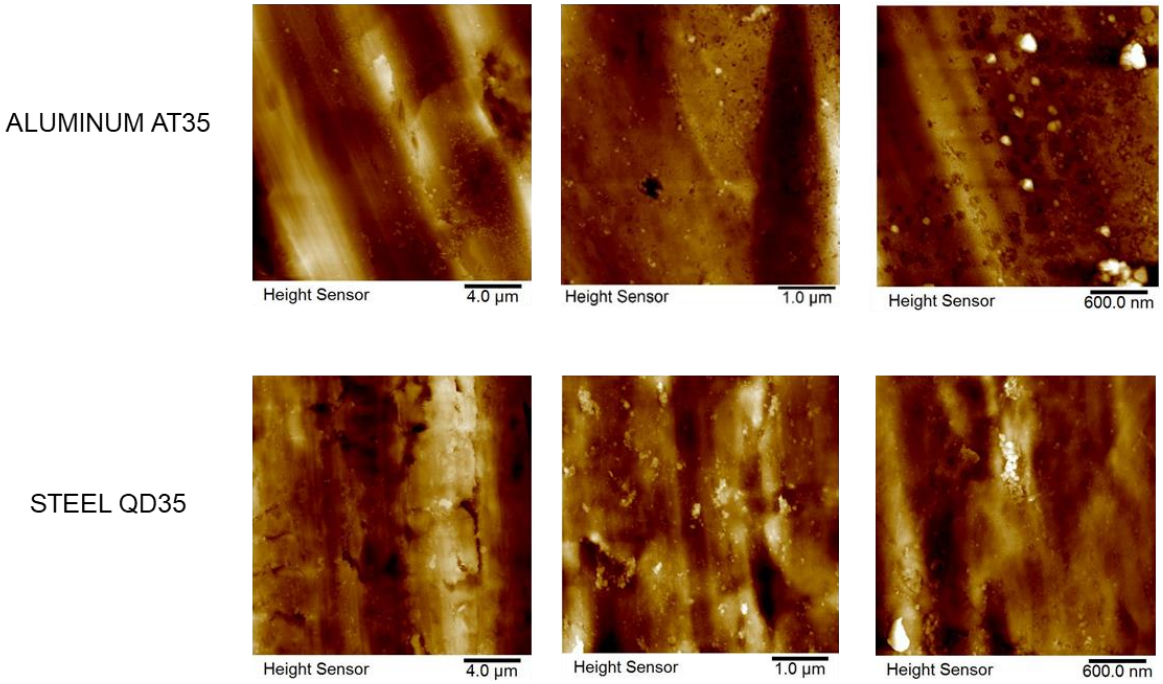

Figure S16. AFM analysis of metal surfaces.

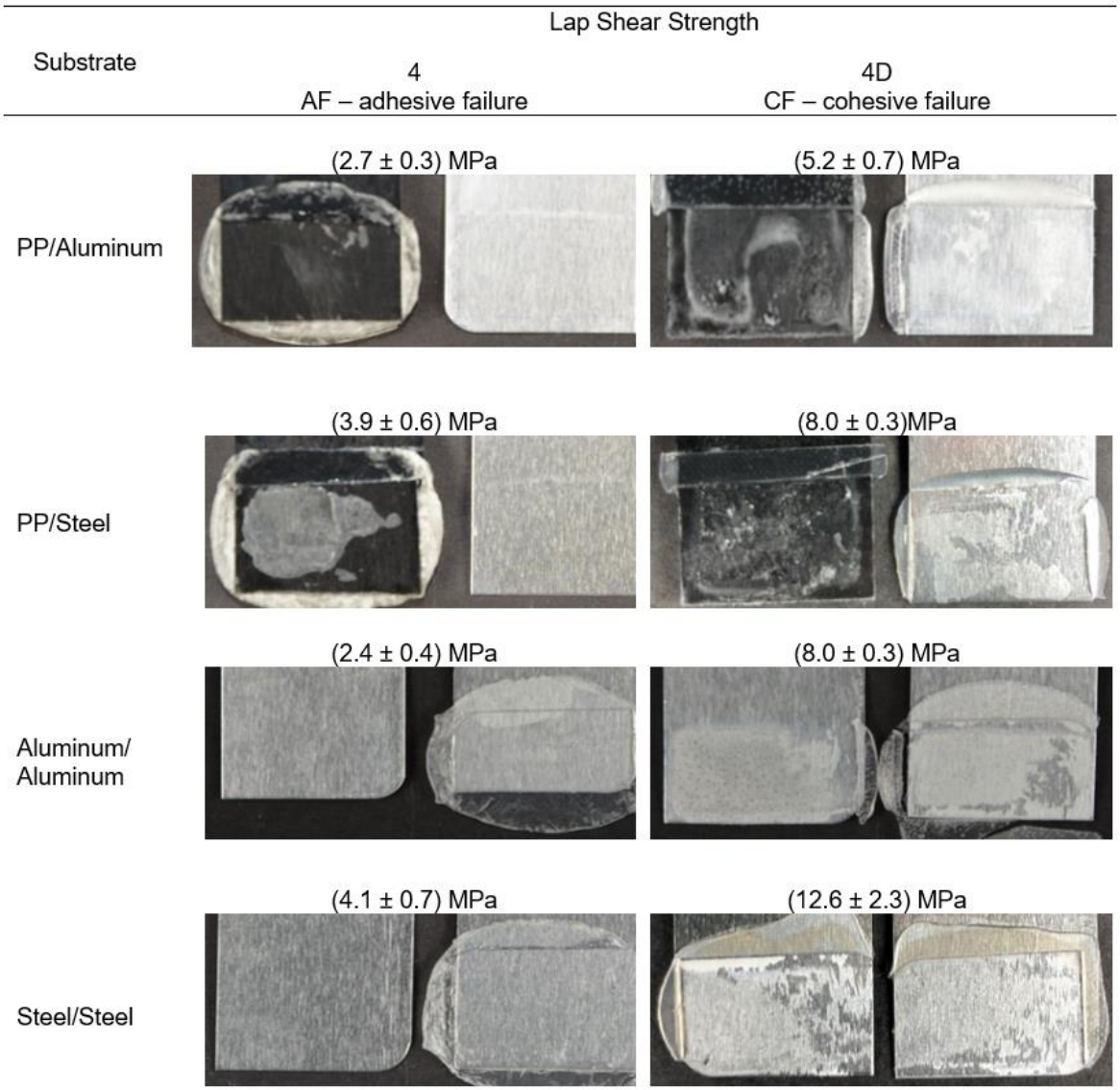

Figure S17. Failure analysis of 4 and 4D used as the adhesive for iPP/aluminum, *i*PP/steel, aluminum/aluminum, steel/steel bonding. The images are recorded after the lap shear test of the samples.

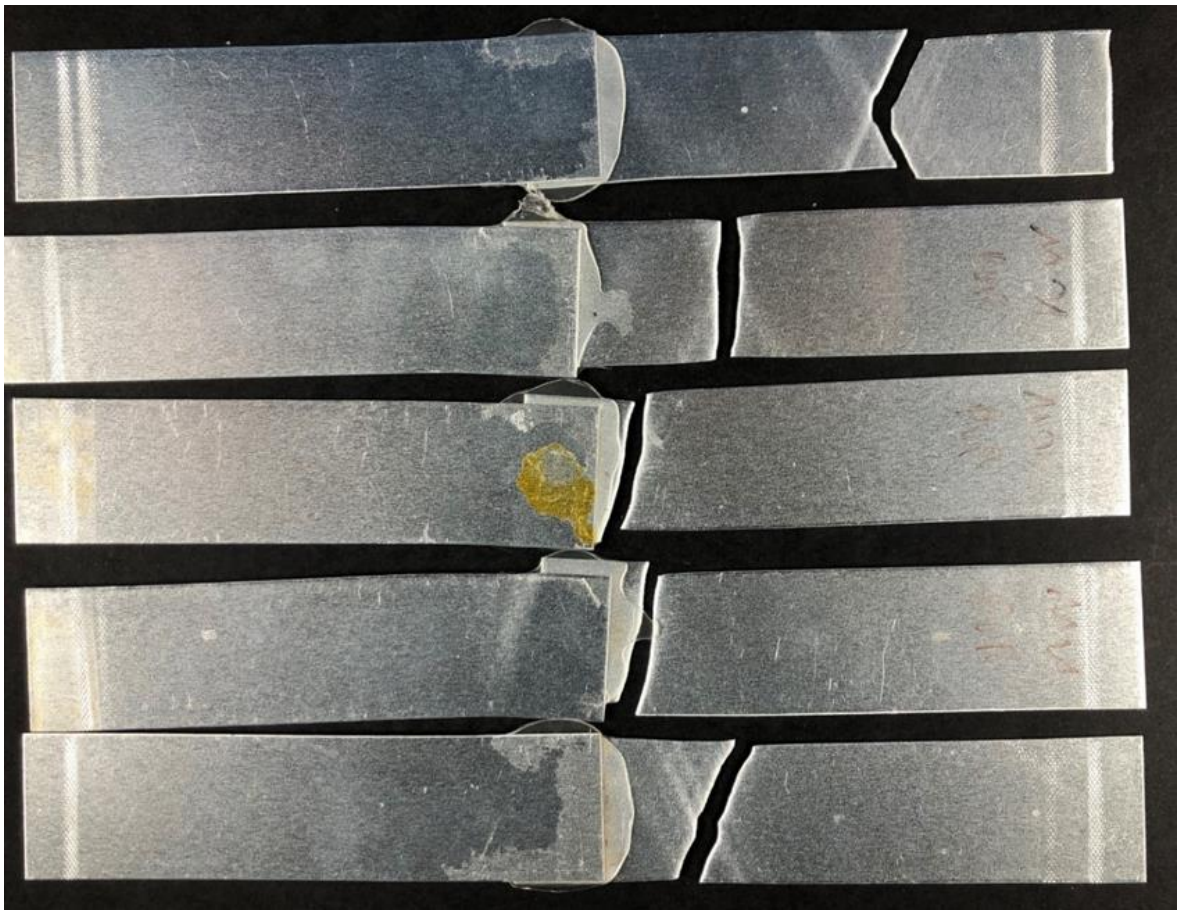

Figure S18. Aluminum plates after lap shear test of 4D.

Table S7. Lap shear test results of 4 and 4D laminated at 130 °C and 180 °C.

Sample	Lap Shear Strength [MPa]			
	Aluminum - Aluminum		Steel - Steel	
	130 °C	180 °C	130 °C	180 °C
4	2.4 ± 0.4	7.6 ± 0.7	4.1 ± 0.7	16.7 ± 0.8
4D	8.0 [a] ± 0.3	7.7 [a] ± 0.1	12.6 ± 2.3	14.5 ± 1.1

[a] Cohesive failure of aluminum laminated at 130 °C under 20 bar pressure.

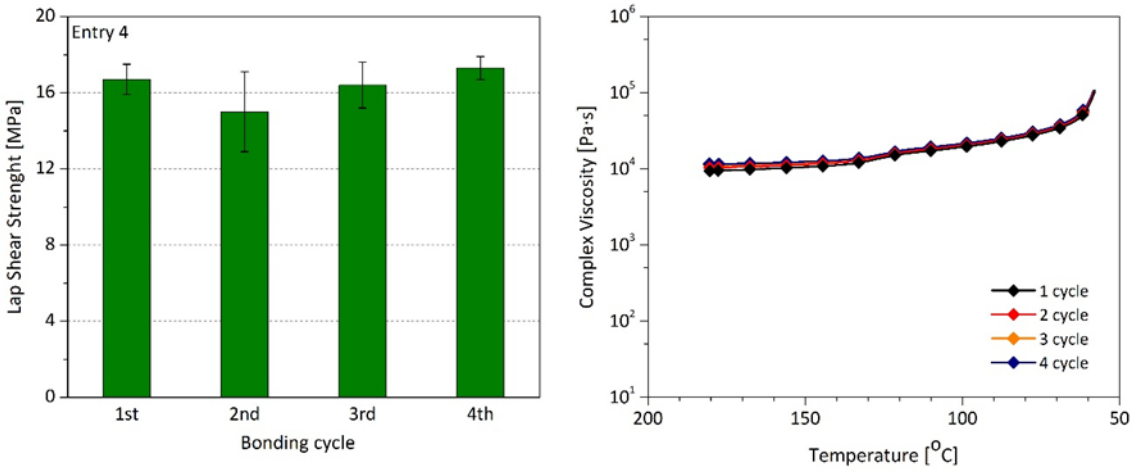

Figure S19. Adhesive properties of Sample 4 (Table S1) during multicycle Lap Shear Test of steel-steel laminates (left). The samples were prepared at 180 °C under 20 Ba pressure. Multicycle rheology test of the investigated laminates (right).

Table S8. Adhesive properties of 4 during multicycle lap shear tests of steel-steel laminates prepared at 180 °C.

Sample	Sample	Lap Shear Strength [MPa]			
		1st bonding	2nd bonding	3rd bonding	4th bonding
4	poly (C_3–*co*–C_6–*co*–C_6OH)	16.7 ± 0.8	15.0 ± 2.1	16.4 ± 1.2	17.3 ± 0.6

Table S9. Lap shear test results of 3 and 3D, 3C, 3CD of the samples prepared at 180 °C : effect of crystallinity

Sample	M_n kg/mol	M_w kg/mol	$Đ$	T_m °C	T_c °C	X_c %	LSS [MPa] Aluminum Aluminum	Steel Steel
3	37.6	128.6	3.4	78.8	22.5	5.4	6.5 ± 0.3	4.7 ± 0.6
3D	37.8	140.7	3.7	80.8	22.6	10.6	9.7 ± 0.5	6.5 ± 1.0
3C[a]	28.8	126.1	4.4	112.1	77.3	29.8	0.8 ± 0.5	2.5 ± 0.8
3CD[a]	19.5	86.6	4.4	115.4	84.7	20.5	3.9 ± 1.2	5.2 ± 2.5

[a] 3C is a more crystalline sample with a similar molecular weight as 3. 3CD is the deashed 3C sample on the adhesive strength.

Table S10. Lap shear strength results of propylene-based terpolymers 3 and 3L.

Sample	M_n kg/mol	X_c %	Lap Shear Strength [MPa] Glass filled iPP Glass filled iPP	Aluminum Aluminum	Steel Steel	Aluminum Glass filled iPP	Steel Glass filled iPP
3	37.6	5.4	5.9 ± 0.5	6.5 ± 0.3	4.7 ± 0.6	2.5 ± 0.6	3.4 ± 0.9
3L	8.6	12.0	3.9 ± 0.4	4.3 ± 0.8	8.8 ± 0.4	1.5 ± 0.4	0.4 ± 0.3

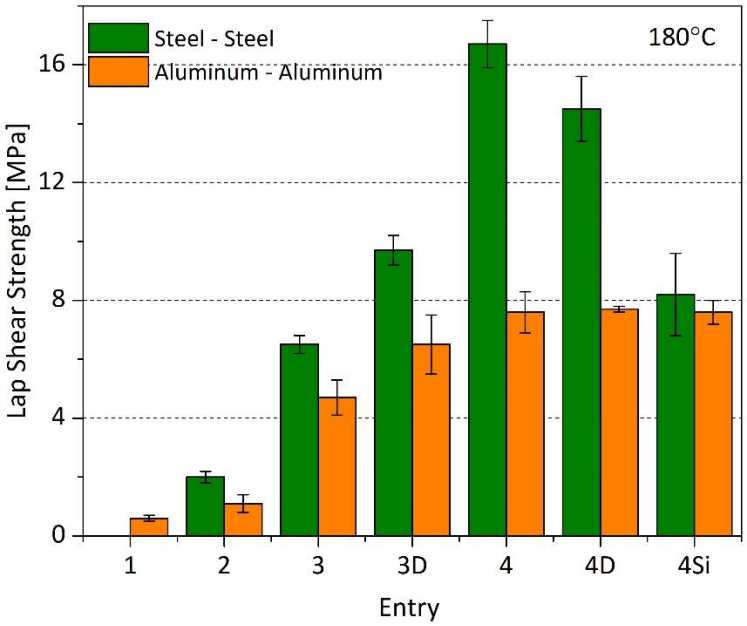

Figure S20. Adhesive strength for bonding metal substrate combinations using non-functionalized and functionalized polypropylene at 180ºC.

References:

(1) Global Adhesives And Sealants Market, 52252, Domain: Chemicals and Materials Sub-domain: Adhesives and Sealants Base, **2018**, Forecast Period for 2019-2024.

(2) Sun, P.; Li, Y.; Qin, B.; Xu, J. F.; Zhang, X. Super Strong and Multi-Reusable Supramolecular Epoxy Hot Melt Adhesives. *ACS Mater. Lett.* **2021**, 3 (7), 1003–1009. DOI: 10.1021/acsmaterialslett.1c00277

(3) GPC-IR ® , the HT-SEC system for Polyolefin Analysis; www.polymerchar.com.

(4) Monasse, B., Haudin, J.M. Growth transition and morphology change in polypropylene. *Colloid Polym. Sci.* 1985, 263, 822–831. DOI: 10.1007/BF01412960

(5) Brandrup, J.; Immergut, E.H.; Grulke, E. A. Polymer Handbook. **1999**, New York: John Wiley&Sons.

(6) Awaya, H. Morphology of Different Types of Isotactic Polypropylene Spherulites Crystallized from Melt. *Polymer* **1988**, 29, 591 – 596. DOI: 10.1016/0032-3861(88)90071-7

2.5 Hot melt adhesives based on blends consisting of poly(propylene–co–hex-1-ene–co–hex-5-en-1-ol) with non functionalized polyolefin-based copolymers

This subchapter has been published as:

Tuning the adhesive strength of functionalized polyolefin-based hot melt adhesives: unexpected results leading to new opportunities

Jakub Kruszynski, Weronika Nowicka, Farhan Ahmad Pasha, Lanti Yang, Artur Rozanski, Miloud Bouyahyi, Ralf Kleppinger, Lidia Jasinska-Walc, Rob Duchateau

Macromolecules **2025** *58* (6), 2894-2904

DOI: 10.1021/acs.macromol.4c02945

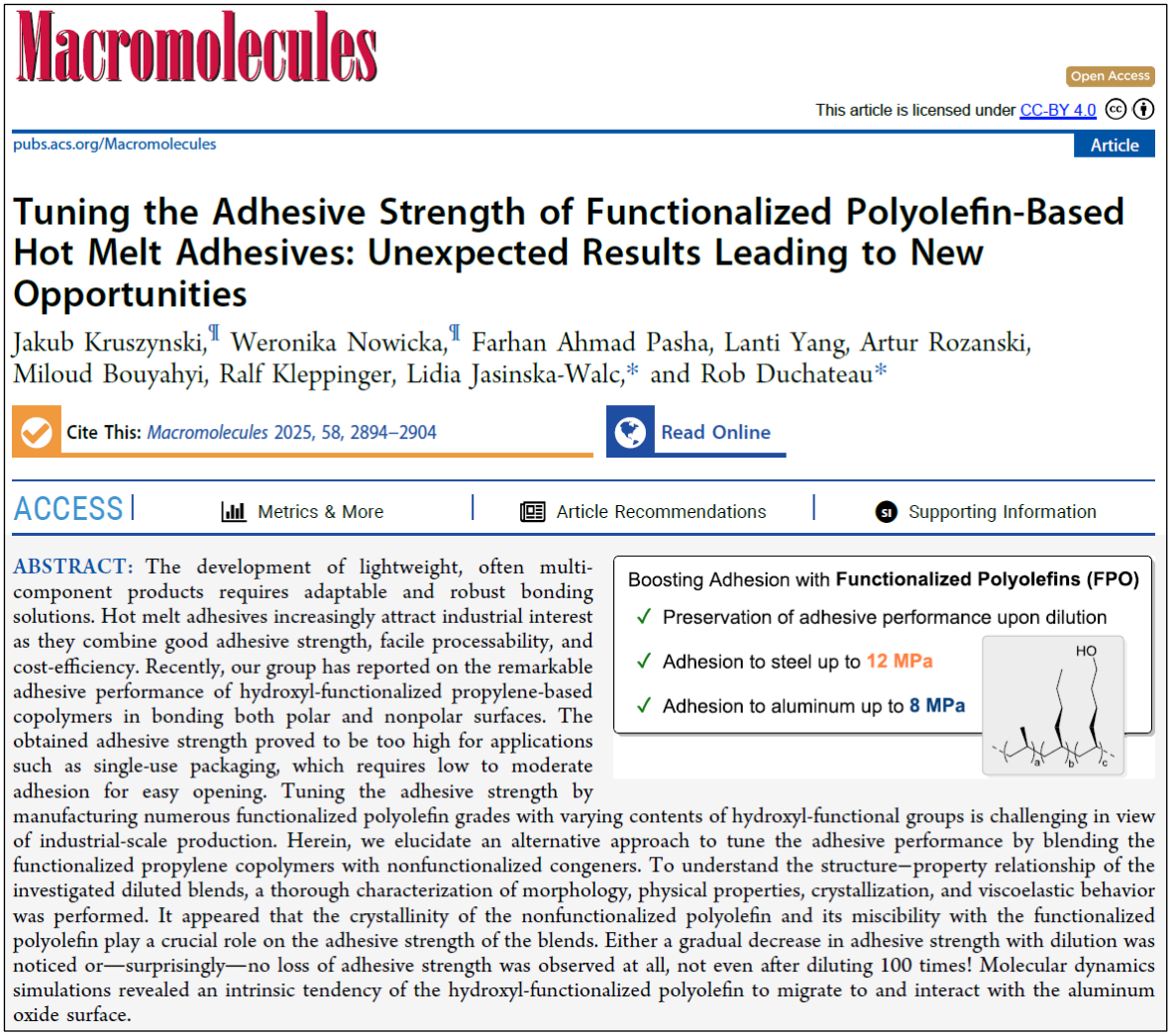

Macromolecules

pubs.acs.org/Macromolecules

Article

Tuning the Adhesive Strength of Functionalized Polyolefin-Based Hot Melt Adhesives: Unexpected Results Leading to New Opportunities

Jakub Kruszynski,[¶] Weronika Nowicka,[¶] Farhan Ahmad Pasha, Lanti Yang, Artur Rozanski, Miloud Bouyahyi, Ralf Kleppinger, Lidia Jasinska-Walc,* and Rob Duchateau*

Cite This: *Macromolecules* 2025, 58, 2894–2904

Read Online

ACCESS | Metrics & More | Article Recommendations | Supporting Information

ABSTRACT: The development of lightweight, often multi-component products requires adaptable and robust bonding solutions. Hot melt adhesives increasingly attract industrial interest as they combine good adhesive strength, facile processability, and cost-efficiency. Recently, our group has reported on the remarkable adhesive performance of hydroxyl-functionalized propylene-based copolymers in bonding both polar and nonpolar surfaces. The obtained adhesive strength proved to be too high for applications such as single-use packaging, which requires low to moderate adhesion for easy opening. Tuning the adhesive strength by manufacturing numerous functionalized polyolefin grades with varying contents of hydroxyl-functional groups is challenging in view of industrial-scale production. Herein, we elucidate an alternative approach to tune the adhesive performance by blending the functionalized propylene copolymers with nonfunctionalized congeners. To understand the structure–property relationship of the investigated diluted blends, a thorough characterization of morphology, physical properties, crystallization, and viscoelastic behavior was performed. It appeared that the crystallinity of the nonfunctionalized polyolefin and its miscibility with the functionalized polyolefin play a crucial role on the adhesive strength of the blends. Either a gradual decrease in adhesive strength with dilution was noticed or—surprisingly—no loss of adhesive strength was observed at all, not even after diluting 100 times! Molecular dynamics simulations revealed an intrinsic tendency of the hydroxyl-functionalized polyolefin to migrate to and interact with the aluminum oxide surface.

INTRODUCTION

Adhesives have been vital since the dawn of civilization and remain essential across many fields in our daily life. Their importance continues to grow as technology advances, making them fundamental to the development of new hybrid materials and products. Many applications demand specialized bonding technologies and precise formulations, resulting in a wide range of adhesive types.[1−4] These include solvent-based systems, adhesive melts, reactive adhesives like UV- or water curable systems, and nonreactive thermoplastics.[5,6] Hot melt adhesives (HMAs) become increasingly important due to their environmentally friendly profile compliant with low VOC emission regulations, excellent properties, simple application, and low costs.[3] So far, commercially available HMAs have been dominated by EVA-based solutions and polyurethanes, while polyolefin elastomers (POEs) gradually gain market share in certain applications like building and construction, packaging, and the automotive industry.[7,8] For high-performance applications, typically reactive HMAs are applied as chemical cross-linking is required to ensure sufficient adhesive strength.[5]

Driven by the desire to debond substrates after use for improved recyclability, nonreactive high strength HMAs are being searched for. For example, Sun et al.[9] developed a bisphenol A-based polyether-amine with dynamic noncovalent bonds (DCBs), while Saito and co-workers[10] reported on borate ester-based adhesives having DCBs that showed excellent adhesion to steel.

Recently, our group has reported on the unprecedented high adhesive strength of randomly functionalized propylene-based copolymers, namely, poly(propylene−*co*−hex-1-ene−*co*−hex-5-en-1-ol) (poly(C_3−C_6−C_6OH)), to both polar and nonpolar substrates, viz., aluminum, steel, glass, wood, and *i*PP.[2,11] We argued that by tuning the adhesive strength of these functionalized polyolefins, we could obtain a simple sustainable HMA solution for a wide range of market segments ranging from durable building and construction and automotive and transportation industries–requiring high adhesive strength–to single-use end-of-line packaging and personal hygiene for which a significantly lower adhesive strength is essential. Here, we describe the results of our study on tuning the adhesive strength of functionalized polyolefin-based HMA systems by either varying the functionality

level of the functionalized polymers or by diluting functionalized polyolefins with nonfunctionalized congeners.[12]

RESULTS AND DISCUSSION

Adhesion of polymers is a complex matter and numerous mechanisms portray the complexity of the bonding process, including diffusion of the adhesive into polymer substrates, interlocking on rough surfaces and chemical interactions of functional groups with polar surfaces.[13] Although the strength of the chemical bonds typically contributes to only a small fraction of the final adhesive strength, it is believed that increasing the functionality level of the functionalized polyolefin enhances the adhesive strength. To confirm this, we have prepared functionalized propylene-based copolymers with varying levels of randomly distributed short chain branches (SCBs) and hydroxyl functionalities, and we have applied these polymers as single-component HMAs for gluing aluminum and steel. Well-defined hydroxyl-functionalized propylene-based elastomers, poly(C_3−C_6−C_6OH) with hex-1-ene and hex-5-en-1-ol levels ranging from 9 to 10 mol % and 0.1 to 0.5 mol %, respectively, and weight-average molecular weights in the range of 140 to 200 kg·mol^{-1} were synthesized by copolymerization of propylene, hex-1-ene, and triethylaluminum-passivated hex-5-en-1-ol (Figure 1, Table 1 A−C). Corresponding nonfunctionalized poly(propylene−*co*−hex-1-ene) (poly(C_3−C_6); Table 1, D, E) elastomers containing 7 to 9 mol % of hex-1-ene were synthesized as well and were used as a benchmark together with commercially available poly(propylene−*co*−but-1-ene) (poly(C_3−C_4)) and poly-(propylene−*co*−ethylene) (poly(C_3−C_2)) elastomers (Table 1, F, G), with 17 mol % and 19 mol % of the comonomer, respectively.

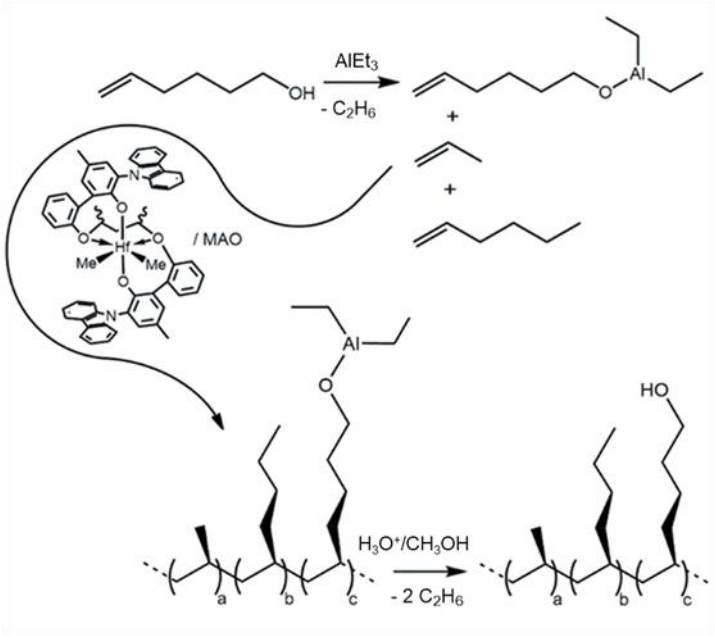

Figure 1. Synthetic path towards poly(propylene–*co*–hex-1-ene–*co*–hex-5-en-1-ol) (poly(C_3–C_6–C_6OH)).

The incorporation level of hex-5-en-1-ol into the polymer backbone was determined by ^{1}H NMR spectroscopy using the −CH_2−OH resonance signals at around 3.5 ppm (Table S1, Figures S1 and S2). The introduction of randomly distributed butyl branches provided materials with suppressed crystallinities and melting transitions when compared with isotactic polypropylene (Figure 2). The targeted melting temperature (T_m) of the copolymers determined by Differential Scanning Microscopy (DSC) was around 80 ºC (Tables S1 and S2, Figure S3). Glass transition temperatures (T_g) of the materials, determined by Dynamic Mechanical Thermal Analysis (DMTA), are typical for propylene-rich copolymers and were recorded in the range from −3 to 0 ºC, except for the poly(C_3−C_2) benchmark material, revealing a T_g of −19 ºC (Table 1).

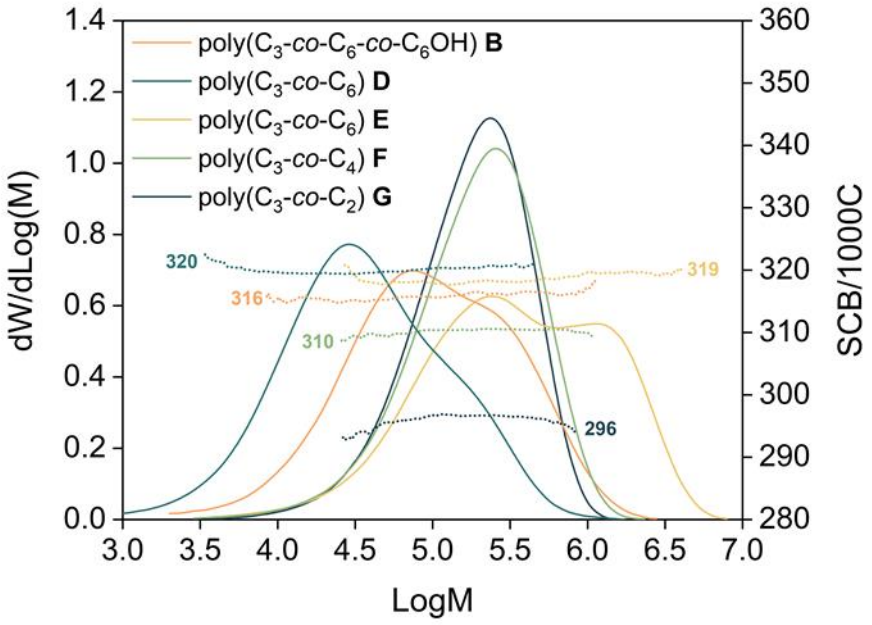

Figure 2. High Temperature-Size Exclusion Chromatography (HT-SEC) and short chain branch (SCB) analysis of poly(C_3–C_6–C_6OH) sample B, non-functionalized poly(C_3–C_6) sample D, E, poly(C_3–C_4) sample F and poly(C_3–C_2) sample G.

Table 1. Molecular weight, thermal properties, and adhesive strengths of poly(C_3–C_6–C_6OH), poly(C_3–C_6), poly(C_3–C_4) and poly(C_3–C_2) samples.

Entry	Composition	$\bar{M}_n$[a] kg·mol^{-1}	$\bar{M}_w$[a] kg·mol^{-1}	$Đ$[a]	C_6OH[b] mol %	T_m[c] °C	T_g[d] °C	Al LSS[e] MPa	Steel LSS[f] MPa
A	poly(C_3–C_6–C_6OH)	57.6	208.7	3.6	0.5	81.2	0	n.a.[g]	14.5 ± 1.1
B	poly(C_3–C_6–C_6OH)	51.2	204.8	4.0	0.4	77.7	−1	7.7 ± 0.7	11.2 ± 1.0
C	poly(C_3–C_6–C_6OH)	37.8	140.7	3.7	0.1	76.6	0	2.7 ±0.6	5.8 ± 0.8
D	poly(C_3–C_6)	25.7	78.5	3.1	–	85.9	0	1.1 ± 0.3	2.0 ± 0.2
E	poly(C_3–C_6)	203.4	752.6	3.7	–	80.5	−1	1.7 ± 0.5	0.8 ± 0.8
F	poly(C_3–C_4)	119.8	270.1	2.3	–	78.2	−3	1.6 ± 0.3	1.6 ± 0.4
G	poly(C_3–C_2)	117.4	258.2	2.2	–	106.0	−19	1.3 ± 0.2	0.9 ± 0.3

a) Determined by HT-SEC in 1,2-dichlorobenzene at 150 °C; b) Hex-5-en-1-ol content, determined by ^{1}H NMR; c) Determined by DSC; d) Determined by DMTA; e) Aluminum/aluminum lap shear strength; f) Steel/steel lap shear strength; g) Aluminum substrate failure.

Adhesion Performance of Functionalized Polyolefins.

The adhesion performance of poly(C_3−C_6−C_6OH) samples A−C containing 0.5 mol %, 0.4 mol %, and 0.1 mol % of hex-5-en-1-ol, respectively, was compared with nonfunctionalized poly(C_3−C_x) (x = 2, 4, 6) copolymers D−G. The adhesive strength was measured by performing Lap Shear Strength (LSS) tests, a facile and standardized technique especially for performance screening purposes.[14−18]

Functionalized polyolefins A−C demonstrated seriously stronger adhesion to aluminum and steel when compared to the nonfunctionalized reference samples D−G (Table 1, Figure 3). As anticipated, the sample having the highest hydroxyl functionality per chain provided the highest adhesive strength. Increasing the polyolefin functionality level from 0.1 to 0.5 mol % resulted in a nearly three times higher adhesion to aluminum up to 7.7 MPa. A similar trend was observed for the steel lamination where the adhesion strength exceeded 14 MPa for sample A. As already indicated, these adhesive strengths are orders of magnitude higher than the maximum bond strength of the chemical interactions. Assuming a coverage of 5 oxide/hydroxide groups per nm^2 on the aluminum oxide surface that could react with the functionalized polyolefin's hydroxyl functionality,[19] the maximum strength of the sum of the chemical interactions is approximately 30 kPa, which is 3 orders of magnitude lower than the observed adhesive strength.[13] Keeping in mind that adhesion is a complex property governed by numerous factors, such as wettability, viscosity, and entanglements, the adhesive contribution (component) of functional groups is minute yet requisite for efficient bonding.

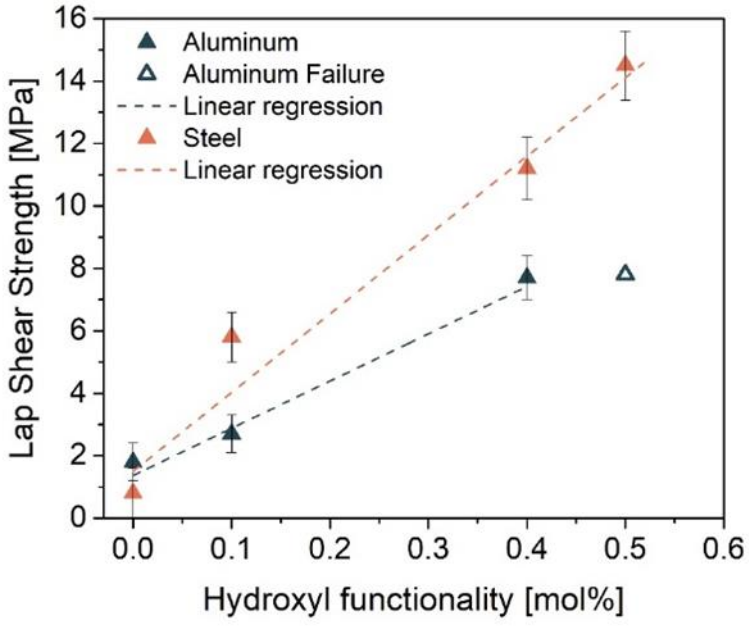

Figure 3. Lap shear test results of the poly(C_3–C_6–C_6OH) samples: A (C_6OH mol % = 0.5), B (C_6OH mol % = 0.4), C (C_6OH mol % = 0.5) compared with non-functionalized poly(C_3–C_6) sample D.

One of the clear advantages of producing functionalized polyolefins by catalysis is the flexibility of the process allowing tailoring of various polymer properties including the hydroxyl functionality level and thereby their adhesion strength. Although easily applicable on a lab scale, for the commercial manufacturing of such products, changing the functionality level by tuning the functionalized comonomer feed conditions will result in significant amounts of off-spec material during grade transitions in the reactor. We envisioned that diluting functionalized polyolefins with a nonfunctionalized polyolefin might be an easier and economically more viable approach to tune the adhesive strength of the functionalized polyolefin.

To investigate this hypothesis, sample B was selected to prepare blends with several nonfunctionalized propylene-based POEs: low- and a high-molecular-weight unfunctionalized congeners of B (poly(C_3−C_6) (D, E)) and two commercially available propylene copolymers, poly(C_3−C_4) (F; TAFMER, Mitsui Chemicals) and poly(C_3−C_2) (G; Vistamaxx, ExxonMobil). Sample B was chosen for this study as the adhesive strength of sample A was too high to be determined for aluminum specimen as aluminum substrate failure occurred. By blending B, revealing a moderate functionality level, with varying amounts of a nonfunctionalized propylene-based POE, a product with a tunable average hex-5-en-1-ol content between 0 and 0.4 mol % was obtained (Figure S2). For each product combination (B/D, B/E, B/F, and B/G), blend compositions containing either 70, 50, 30, 10, 5, or 1 wt % of the functionalized polyolefin B (Tables S1 and S2) were studied. The blends were characterized and subsequently subjected to LSS tests.

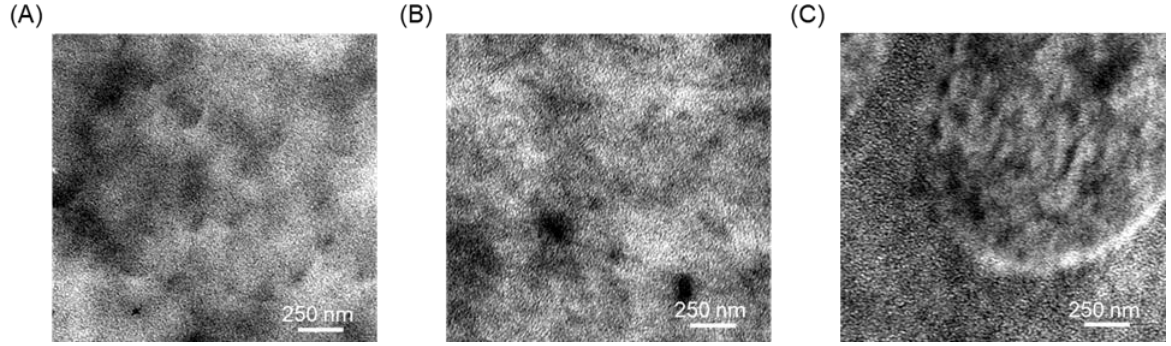

Figure 4. TEM analysis of the 30/70 w/w blend comprising (A) poly(C_3–C_6–C_6OH)/poly(C_3–C_6) (30B/70D), (B) poly(C_3–C_6–C_6OH)/poly(C_3–C_4) (30B/70F), (C) poly(C_3–C_6–C_6OH)/poly(C_3–C_2) (30B/70G).

Blend Characterization.

First, the morphology and physical properties of the blends were thoroughly examined. Transmission Electron Microscopy (TEM) micrographs (Figure 4) of the blends (30:70 w/w) consisting of poly(C_3−C_6−C_6OH) and either poly(C_3−C_6) or poly(C_3−C_4) reveal excellent miscibility of the blend components, whereas comparable 30:70 w/w compositions comprising poly(C_3−C_6−C_6OH) and poly(C_3−C_2) clearly exhibit a two phase system. Though, the presence of a rough interphase suggests partial inter-diffusion of the amorphous phases of each of the latter blend components in the B/G blend, evincing some degree of miscibility. The investigated compositions reveal a fine-crystalline structure with crystal thickness oscillating around 2−3 nm. These results were also confirmed by Atomic Force Microscopy (AFM) analysis (Figure S4).

As anticipated, the physical properties of the thus prepared blends (B/D, B/E, B/F, and B/G) are dependent on their composition. While T_m and X_c of the investigated alloys fall within the values set by the pristine components, the T_c of the blends depends on their composition (Table S1 and Figures 5, S5, and S6). The well-miscible blends B/D and B/E comprising poly(C_3−C_6−C_6OH) and poly(C_3−C_6) reveal higher T_c (even above 20 °C) when compared to the reference copolymer (Figure 5A, B). This phenomenon can be explained by the similarities of the polymers' crystal structure and epitaxial crystal growth.[20] Clearly, the interactions between the individual blend components and their similarity stabilize the crystalline structure and improve molecular alignment and packing, raising the crystallization temperature of the blend above that of individual polymers. Conversely, the differences of the chemical structure and thus topology between poly(C_3−C_6−C_6OH) and poly(C_3−C_4) (blends B/F) resulted in a significant decrease of the T_c of up to 40 °C for the corresponding blend (Figure 5C). Although TEM and AFM micrographs of this blend composition do not reveal significant phase separation, the differences of the interplanar distances between polymer chains within poly(C_3−C_4) and the functionalized copolymer (*vide infra*) clearly decrease their crystallization temperature. The thermal properties and crystallinity level of the B/G blends (Figure 5D) are governed by the semicrystalline poly(C_3−C_6−C_6OH) component as G is essentially amorphous (Tables S1 and S2).

A DMTA studies of the polymer blends B/D, B/E, and B/F show single glass transition temperatures in the range of −3 to 4 °C (Table S1, Figure S7). In the B/G

blends, revealing more distinct morphologies and containing up to 10 wt % of functionalized polyolefin B, a single T_{g1} deriving from component G is visible at −19 °C. Upon reaching 30 wt % of component B, the second tan δ peak T_{g2} appears around 0 °C. Interestingly, with an increasing concentration of B, the distance between the two distinct glass transitions increases. As presented in Table 1, the T_{g1} decreases from −19 to −22 °C, while T_{g2} increases from 0 to 3 °C in 30B/70G and 70B/30G, respectively. Lehman and co-workers have reported a comparable trend, where the T_g of polypropylene was decreasing with an increasing amount of the amorphous component. Evidently, that deflection of the T_g derives from the amplification of the negative pressure related to the differential thermal coefficients of the blend components.[21] Furthermore, selected elastomers E and F exhibit stable moduli above the melting point, which clearly differentiates their behavior from that of the functionalized polyolefin B and low molecular-weight nonfunctionalized copolymer D. As presented in Figure S7, blending B with relatively high-molecular weight E and F translates to improved deformation resistance above the melting point, which is the result of increased entanglement next to the network formed by agglomerated hydroxyl functionalities.[22] Such viscoelastic behavior holds significant importance in polymers with vitrimeric and shape memory phenomena as the presence of entangled networks can be sustained even in a molten state.[23−27]

Before studying the crystallization behavior of the blends, the pristine blend components, B, D, E, and F, were subjected to thermal fractionation through Successive Self-nucleation and Annealing (SSA) measurements (Figure S8). Numerous reports describe SSA as a useful tool to determine the lamellar thickness and qualitative characterization of comonomer distribution within copolymers that crystallize over a broad temperature range.[28,29] The SSA of B, D, and E revealed a broad distribution of 8 distinct thermal fractions, which in each case initiates around 110 °C and terminates close to 35 °C. This great similarity derives from nearly the same sample topologies and type of branching of B, D, and E and is the result of using a mixture of stereoisomeric single-site catalysts, which result in a broadening of the polydispersity. Conversely, F displayed 6 distinct thermal fractions between 94 and 45 °C, which might be ascribed to a narrower polydispersity characteristic for a product produced by a single-site catalyst. Additionally, F has a well-defined peak in the high-temperature range that translates to thick and well-defined crystals, in agreement with Wide Angle X-ray Scattering (WAXS) results (Figure 5).[30] The

main advantage of B−E over F is the capability of crystallizing over a broad temperature range, which provides better surface wetting, resulting in an improved anchoring during the bonding process.

To gain further insight into the crystal structure of B and its blends with the nonfunctionalized copolymers D−G, WAXS analyses were performed. All investigated copolymers displayed X-ray profiles typical for the monoclinic unit cell being characteristic for polypropylene and for this reason, the 30/70 w/w compositions 30B/70D and 30B/70E provided profiles resembling the corresponding pristine components (Figure 5).[31,32] The decrease of the 2θ angle values of the blends is indicative of a higher interplanar distance between polymer chains in these blends. Although TEM did not show phase separation between B and F, the poly(C_3−C_4) copolymer F reveals distinct crystalline morphology in comparison with B, D, and E. 2θ angle signals of F are shifted toward lower values, which is indicative for higher interplanar distances within the unit cell of the crystal in comparison with B and incorporation of but-1-ene chain fragments into the crystal unit cell of the polymers. In agreement with DSC analyses, we assume that the pronounced differences in unit cell dimensions between B and F impede the crystallization process within the composition (Figure 5). It is known that the existence of various types of lamella populations introduces crystalline moieties of different thermodynamic stabilities.[33] The WAXS profile of the blend 30B/70F supports this idea since interplanar distances of unit cells are nearly identical as that of a neat F, while the crystallinity level is significantly diminished (13 % for 30B/70F vs 20 % for F). Furthermore, WAXS analysis revealed the presence of the residual crystalline phase of component G agreeing with DSC results (Table 1, Figure S5). 2θ angle signals at 13 and 17° for G overlay the WAXS profile of B illustrating certain resemblance of lamella populations, as is supported by TEM analysis.

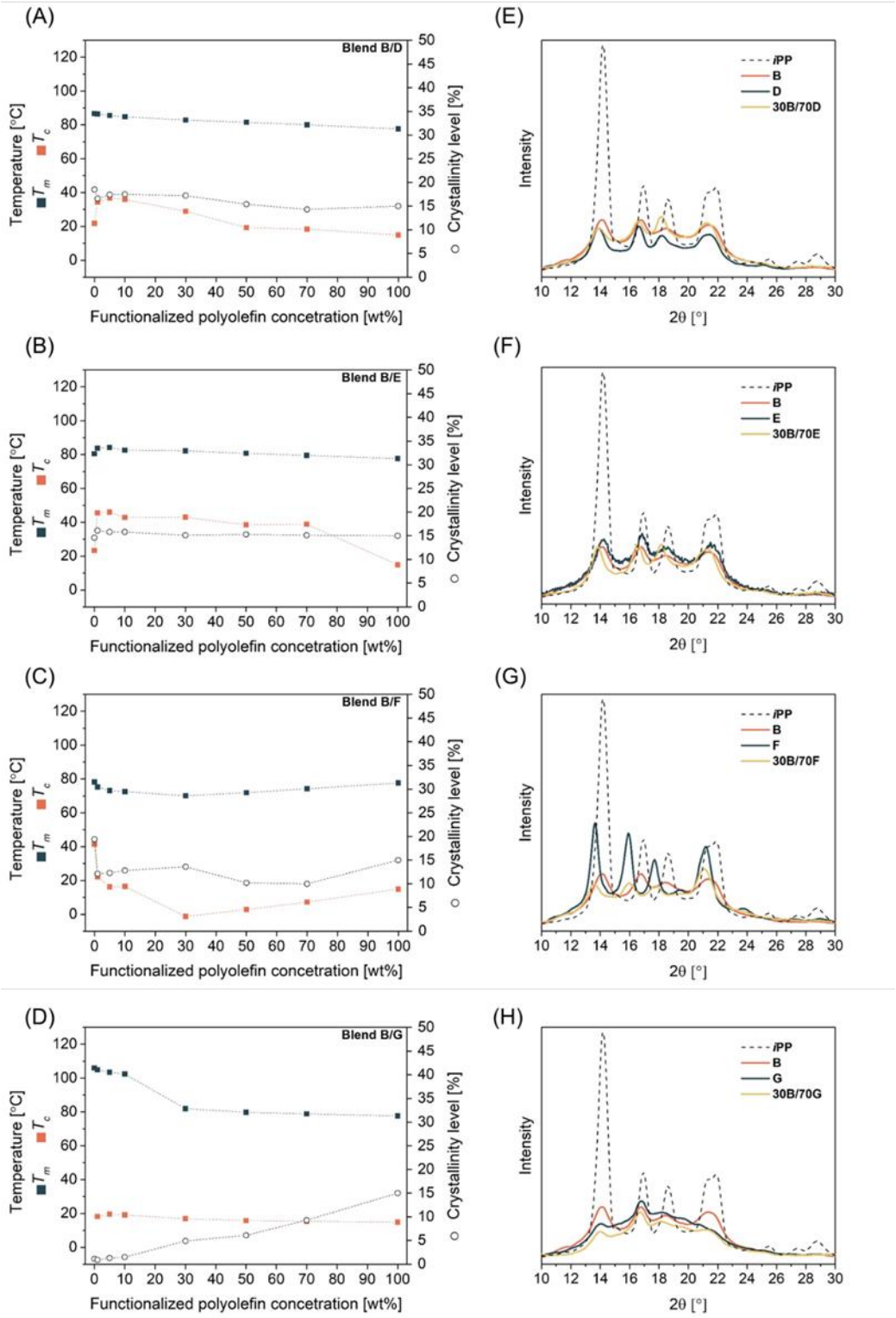

Figure 5. Melting and crystallization temperatures, crystallinity level (A-D) as well as WAXS profiles (E-H) of B, D – G and blends of B with D – G.

The effect of blending functionalized polyolefin B with nonfunctionalized copolymers D−G was also assessed by means of shear rheology in the linear viscoelastic regime (Figure 6). The rheological properties of sample B indicate that functionalization and molecular interactions significantly influence the flow behavior of these polyolefins. The presence of OH functionalities and their intermolecular interactions via hydrogen bonds provide materials displaying a low-frequency viscosity upturn as a result of the formation of “polar nests”.[22,34] Diluting B with lower-molecular-weight D decreases the overall viscosity of the product, which is relevant for the processability of the HMAs. Conversely, when required, the blend’s viscosity can easily be increased by mixing B with higher molecular weight E. Partial miscibility of B with commercially available copolymers F and G, albeit synthesized using different comonomer combination, was additionally proven by intact shear thinning regions for a broad range of sample compositions. Sufficient affinity between blend components is crucial for the formation of uniform phases, ensuring efficient stress transfer leading to consistent mechanical performance and optimal adhesive strength. Importantly, the presence of hydroxyl functional groups in component B of the investigated blends is essential for strong adhesive bond formation to aluminum or steel substrates (*vide infra*).

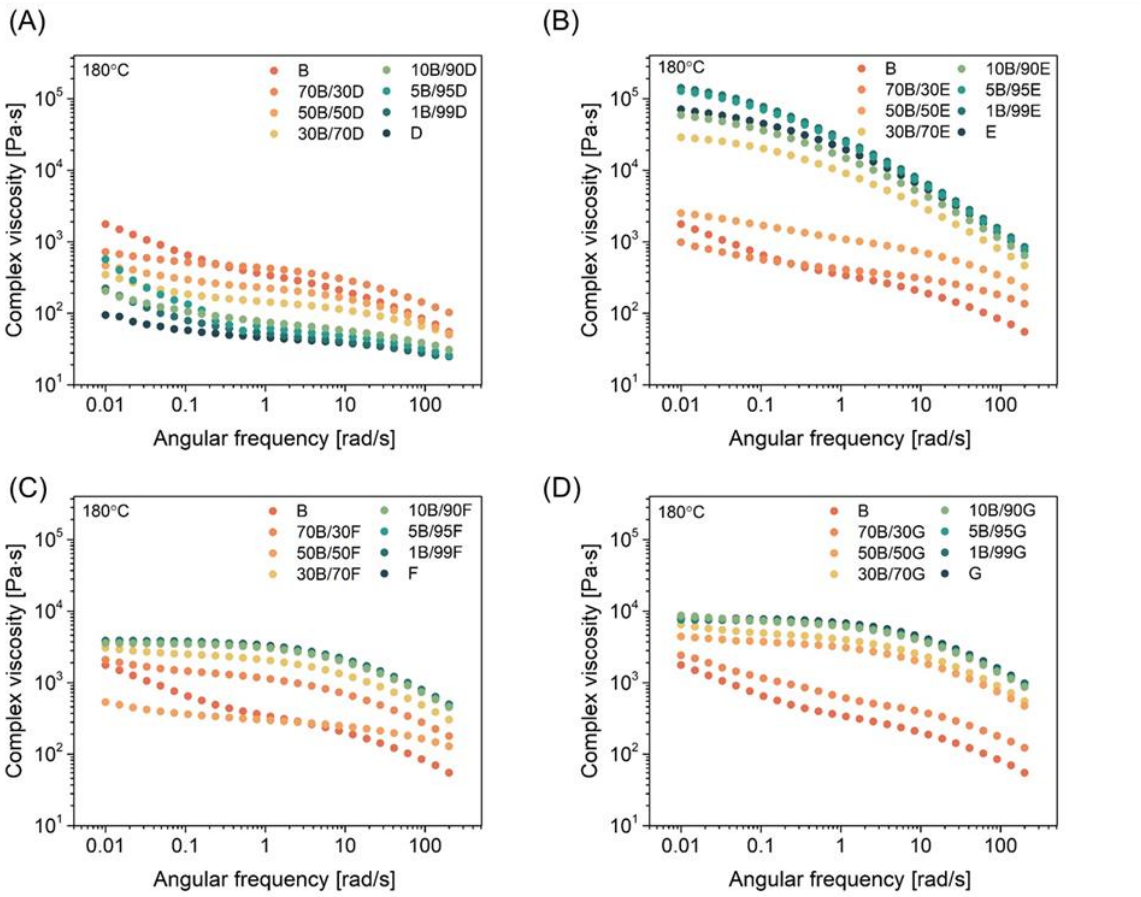

Figure 6. Complex viscosity (η*) of polymer reference materials and blends consisting of poly(C_3–C_6–C_6OH) B and poly(C_3–C_6) D, E (A, B); poly(C_3–C_4) F (C); poly(C_3–C_2) G (D). Samples were tested under oscillation frequency (ω) in a constant temperature 180 °C.

Adhesion Performance of Blends.

Before assessing the performance of functionalized polyolefins and blends thereof as HMAs, the surface energies of the substrate materials steel and aluminum were compared with the polymers used as adhesives. The surface energies of steel (29 mN/m) and aluminum (42 mN/m) are significantly higher than surface energies of the investigated polyolefins B (13 $mN \cdot m^{-1}$), D (16 $mN \cdot m^{-1}$), E (18 $mN \cdot m^{-1}$), F (13 $mN \cdot m^{-1}$), and G (17 $mN \cdot m^{-1}$) (Table S3, Figure S9). The compression-molded functionalized sample B, prepared in a PTFE mold, revealed unexpectedly low surface energies, which can be explained by the formation of a OH polar nest in the apolar polyolefin matrix and lack of migration of the polar units to the highly apolar surface of PTFE.

Initially, lap-shear tests were performed to quantitatively asses the adhesion strength of the samples. As described above, increasing the functionality level of poly(C_3−C_6−C_6OH) from 0.1 to 0.5 mol % (A − C) resulted in a 3-fold improvement of the adhesion strength of the functionalized polyolefin to aluminum and steel (Figure 7, Table S4). Comparison of the adhesive strength and failure modes in bonding aluminum revealed two distinct regions. Where up to 3 MPa adhesive failure is dominant, above 4.5 MPa cohesive between adhesive and bonded surfaces prevails. Steel connections display mainly cohesive failures above 6 MPa. Interfacial failure, being mixed mode between adhesive and cohesive failure, is observed throughout the whole range for both aluminum and steel, respectively (Figure S10). As a comparison, the nonfunctionalized copolymers D−F revealed a negligible adhesion strength at the level of 1−2 MPa. Next, we attempted to tune the adhesion strength by diluting functionalized polyolefins with less expensive nonfunctionalized counterparts. Surprisingly, blending B with the nonfunctionalized congeners D, E, and F provided materials showing adhesive strengths that are essentially independent of the blend compositions (Figure 7, Table S4). Most striking are the results for the blends of B and the high-molecular-weight poly(C_3−C_6) E as there is – within the error of the measurement– preservation of adhesive strength despite diluting B 100 times! Blends of B with the low-molecular-weight D also show a constant adhesive strength independent of the blend composition but the value is somewhat lower than for neat B. The difference in adhesive strength between B/D and B/E blends is likely caused by the difference in the molecular weight of D and E. Low viscous, low-molecular-weight polymers tend to migrate to the surface under pressure or shear.[35] Hence, the migration of the functionalized polyolefin B to the surface of B/E blends is likely to be faster and more efficient than that in B/D blends. Additionally, the entanglement strength in B/E will be higher than in B/D due to the higher molecular weight of E as compared to that in D. Both effects contribute to a higher adhesive strength for the B/E system. Blends of B and F give similar results as observed for the B/D and B/E blends. Although the adhesive strength is slightly lower than that of pure B, the adhesive strength is independent of the blend composition ranging from 70B/30F to 1B/99F. Interestingly, blending of functionalized polyolefin B with the nonfunctionalized G reveals a near linear decrease in adhesion strength to both aluminum and steel with decreasing concentration of B (Figure 7D). For this blend, varying the blend composition can

effectively be used to tune the adhesive strength of the material. The major difference between B, D−F and G is that the latter has a much lower crystallinity. Consequently, there is a proportional relationship between the B/G blend composition and the overall crystallinity and adhesion performance of the blend. A higher overall crystallinity provides a robust crystalline network which efficiently prevents deformation of the adhesives during the performance testing.[36,37] Furthermore, TEM and AFM analyses have demonstrated that blends of B and D−F are fully miscible, whereas B and G are at best only partly miscible. This lower miscibility and inability to cocrystallize, as is possible for B/D and B/E, most likely also contributes to the different behavior of B/G blends compared to all other blends.

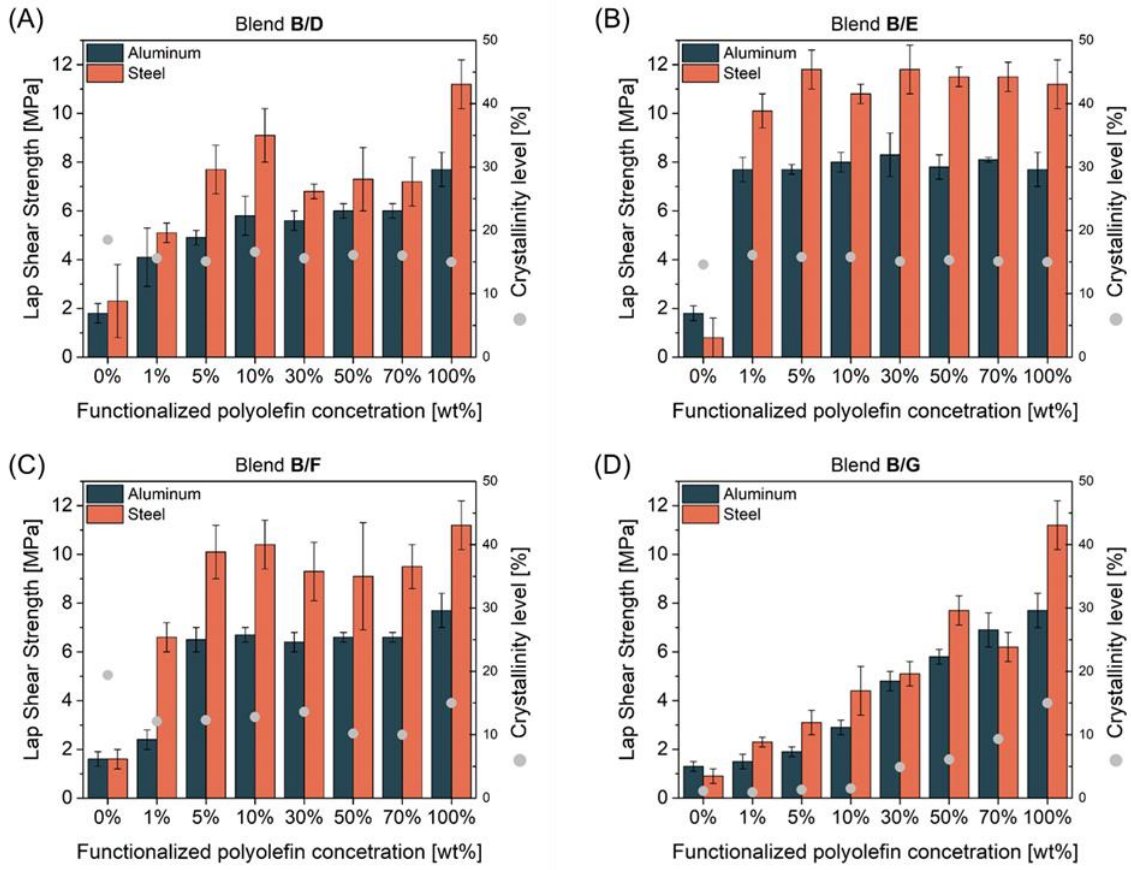

Figure 7. Lap shear test results for bonding steel and aluminum by poly(C_3–C_6–C_6OH) (B), poly(C_3–C_6) (D, E), poly(C_3–C_4) (F), poly(C_3–C_2) (G) and blends thereof.

AFM was employed to further investigate the affinity toward polar surfaces of functionalized polyolefin within the blend (Figures 8 and S11). The 30B/70G blend was chosen for the difference in the modulus of the essentially amorphous matrix G and semicrystalline B (Figure S7), which provides sufficient contrast while mapping the nanoscale morphology. In agreement with TEM analysis, also the AFM images

of 30B/70G reveal that B partly penetrates the nonfunctionalized matrix G (Figure 8). Notably, a clear distinction in the shape of the dispersed phase domains is observed when comparing the core of the sample with the area near the aluminum layer (Figure 8A−C). The functionalized polyolefin's domains adjacent to the aluminum layer are more elongated and densely packed compared to those in the core of the adhesive layer. Bearing analysis confirmed that near the aluminum surface, the blend is enriched with B (39.1 vol %), whereas the bulk of the polymer blend consists of 30.8 vol % of B. As mentioned earlier, this surface enrichment of B can be ascribed to the lower viscosity of B compared to G, but it could also be the result of an intrinsic tendency of functionalized polyolefins to migrate toward the surface of polar substrates.

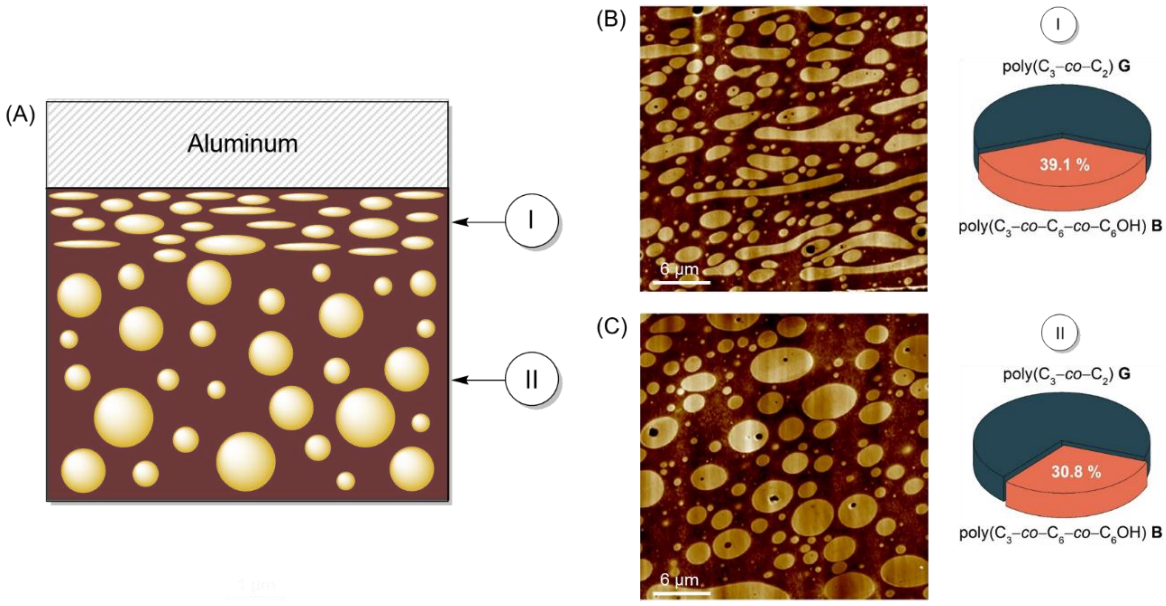

Figure 8. Graphical representation of 30B/70G blend morphology at the interface with aluminum and core of the blend (A); AFM analysis of the 30B/70G blend morphology at the interface with aluminum (B) and core of the blend (C).

Molecular dynamics simulations were used to study if the hydroxyl-functionalized polyolefins, as part of a blend with a nonfunctionalized congener, indeed tend to migrate to the interface with a polar substrate like aluminum. First, a miscibility analysis was performed to determine the affinity of B with the nonfunctionalized samples E−G. The miscibility of polymer blends is usually described by parameters like the Mixing Energy (ΔE_{mix})[38] and the Flory−Huggins interaction parameter (χ),[39−41] which depend on the Hildebrand solubility parameter

(δ) and cohesive energy densities.[42−44] The latter can be obtained from molecular dynamics simulations.[45−48] The molecular compositions of the functionalized (B) and nonfunctionalized (E−G) polyolefins are given in Table S5. For each combination of B and E−G, we used five blend compositions (80/20, 70/30, 50/50, 20/80, and 10/90, Table S6) to comprehensively assess the impact of the composition and the compatibility (Figure 9).

Of the five B/E models, the one with a B/E ratio of 71/29 exhibits the most negative ΔE_{mix} and χ values, indicating the highest miscibility between the components. Increasing the content of E in the blend leads to a decrease of the ΔE_{mix} and χ values and hence the miscibility gradually decreases with increasing E content in the B/E blend. Similarly, also for the B/F and B/G blends, the models with a 70/30 ratio (B/F = 69.9:30.1) and B/G (70.3:29.7) demonstrate the most negative ΔE_{mix} and χ values and the miscibility gradually decreases with increasing content of F and G. Decreasing the amount of nonfunctionalized polyolefin E−G to 20 wt % resulted in a surprisingly steep increase in the ΔE_{mix} and χ values, indicating a significant decrease in miscibility with just a slight change in composition from 70:30 to 80:20 wt/wt. Taking a holistic view of ΔE_{mix} and χ data related to the best miscible models (70/30) of three different blend types (B + E−G) reveals an interesting trend: B/E (ΔE_{mix} = −14.74 J·m−3, χ = −803.19) < B/F (ΔE_{mix} = −12.44 J·m−3, χ = −677.62) < B/G (ΔE_{mix} = −9.72 J·m−3, χ = −529.48). This suggests that E shows the highest miscibility with B, followed by F, while G stands at the lowest corner among the three and is in line with the expectation based on the copolymers' structures.

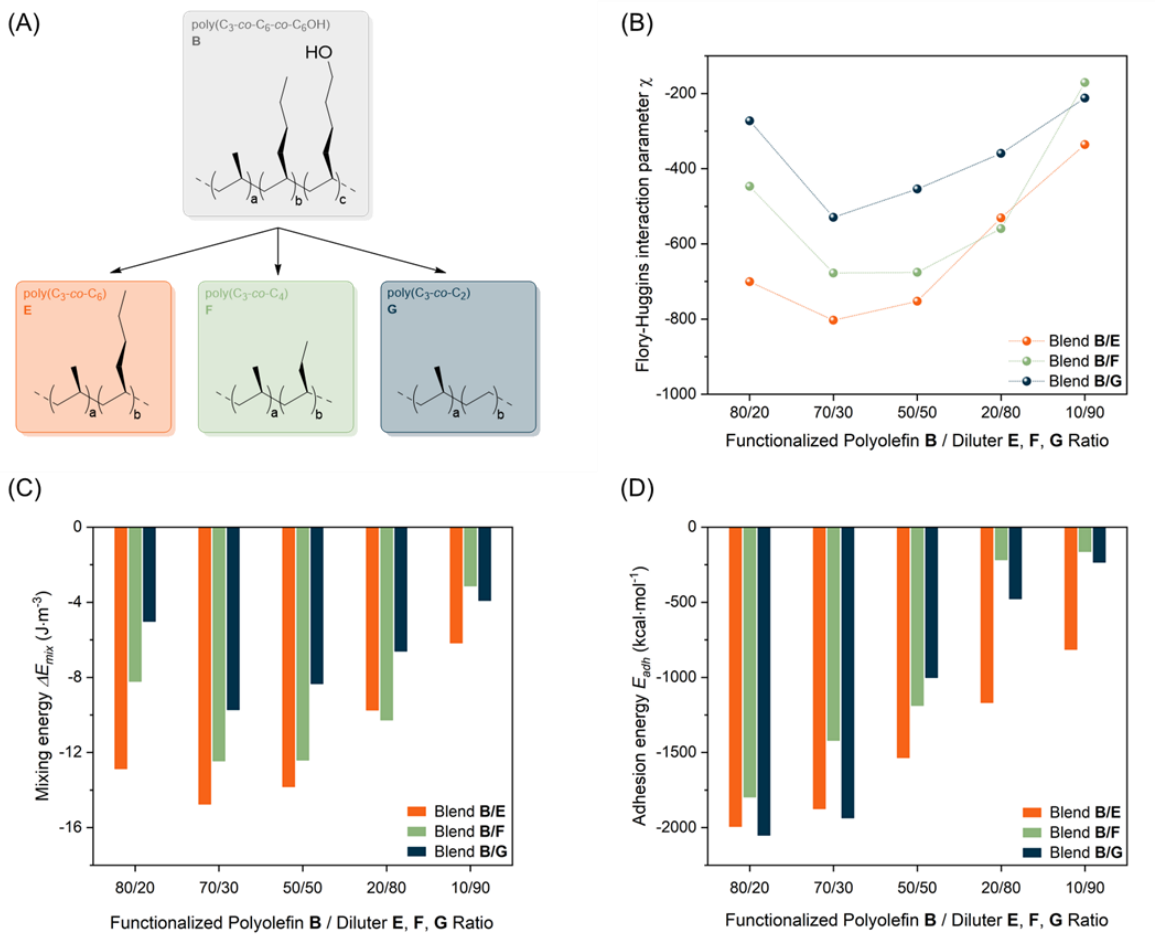

Figure 9. Structures of B, E, F and G used in the molecular dynamics simulations (A), Flory-Huggins interaction parameter (B), Mixing Energy (C) and Adhesion Energy (D) of the five blend combinations (80:20 – 10:90 ratio) of each of the blends types (B + E – G).

All five blend combinations (80:20−10:90 ratio) of each of the blend types (B + E−G) have been examined for their adhesion to aluminum oxide, the surface layer of an aluminum specimen (Figure 9D). In all studied blends, the functionalized polyolefin B is clearly located at the interface (Figure S12), indicating an intrinsic tendency of the hydroxyl-functionalized polyolefin to interact with the aluminum oxide surface, thereby improving the adhesion. For blends containing high content of B, the adhesion to the aluminum oxide is good for all blends regardless the type of nonfunctionalized polyolefin used. However, for blends containing lower B contents, the B/E blends clearly outperform the B/F and B/G blends. Since the miscibility of each of the blend types (B/E, B/F, and B/G) follows the same decreasing trend with a decreasing content of B, most likely the difference is caused

by the higher molecular weight of E as compared to F and G, which might result in a preferred migration of the lower molecular weight B to the surface.

CONCLUSIONS

The adhesive strength of randomly hydroxyl-functionalized propylene copolymers of the type poly(propylene−*co*−hex-1-ene−*co*−hex-5-en-1-ol) to metals like aluminum or steel is impressive for an HMA. It was demonstrated that the adhesive strength of these copolymers shows a linear correlation with the hydroxyl functionality level of the copolymers, which allows the materials' adhesive strength to be tuned. However, producing many different grades with varying content of hex-5-en-1-ol is impractical for commercial-scale production of such materials. Dilution of the functionalized propylene copolymers with nonfunctionalized congeners seemed to be a simple approach to lower the average hydroxyl content in the thus obtained blend and thereby the adhesive strength. Unexpectedly, however, for blends of the functionalized poly(propylene−*co*−hex-1-ene−*co*−hex-5-en-1-ol) and the closely related nonfunctionalized poly(propylene−*co*−hex-1-ene) or poly-(propylene−*co*−but-1-ene), the adhesive strength remained maintained regardless of the content of the nonfunctionalized copolymers, even for blends containing just 1 wt % of the functionalized polyolefin. Obviously, this can result in significant cost-savings for HMA production. Yet, when blends based on the low-crystalline poly(propylene−*co*−ethylene) and functionalized poly(propylene−*co*−hex-1-ene−*co*−hex-5-en-1-ol) that phase separate were tested as HMAs, a near linear drop in adhesive strength with decreasing amount of the functionalized copolymer in the blend was observed. This opens a much wider range of applications for the functionalized polyolefin as an HMA component. It is clear that the crystallinity level of the nonfunctionalized polyolefin and its miscibility with the functionalized polyolefin play a crucial role in potential to tune the adhesive strength by varying the blend composition.

REFERENCES

(1) Heucher, R.; Ford, I.; Joseph, J.; Crawford, A. Debondable reactive hot melt adhesives U.S. Patent 10,800,956 B2, **2020**.

(2) Kruszynski, J.; Nowicka, W.; Bouyahyi, M.; Liu, Y.; Yang, L.; Rozanski, A.; Anbuchezhian, N.; Jasinska-Walc, L.; Duchateau, R. Unprecedented Adhesive Performance of Propylene-Based Hydroxyl-Functionalized Terpolymers. *ACS Appl. Polym. Mater.* **2023**, 5 (5), 3875−3882.

(3) Li, W.; Bouzidi, L.; Narine, S. S. Current Research and Development Status and Prospect of Hot-Melt Adhesives: A Review. *Ind. Eng. Chem. Res.* **2008**, 47 (20), 7524−7532.

(4) Herbert, K. M.; Dolinski, N. D.; Boynton, N. R.; Murphy, J. G.; Lindberg, C. A.; Sibener, S. J.; Rowan, S. J. Controlling the Morphology of Dynamic Thia-Michael Networks to Target Pressure-Sensitive and Hot Melt Adhesives. *ACS Appl. Mater. Interfaces* **2021**, 13 (23), 27471−27480.

(5) Awaja, F.; Gilbert, M.; Kelly, G.; Fox, B.; Pigram, P. J. Adhesion of polymers. *Prog. Polym. Sci.* **2009**, 34 (9), 948−968.

(6) Raos, G.; Zappone, B. Polymer Adhesion: Seeking New Solutions for an Old Problem. *Macromolecules* **2021**, 54 (23), 10617−10644.

(7) Khairullin, I. K. Adhesive-melts-the most dynamically developing area in world production and consumption of adhesives. *Polym. Sci., Ser. D* **2013**, 6 (1), 77−81.

(8) Jozef, R.; Lyda, R.; Igor, N.; Vladimír, V.; Jozef, P.; Ivica, J.; Ivan, C. Thermooxidative stability of hot melt adhesives based on metallocene polyolefins grafted with polar acrylic acid moieties. *Polym. Test*. **2020**, 85, 106422.

(9) Sun, P.; Li, Y.; Qin, B.; Xu, J.-F.; Zhang, X. Super Strong and Multi-Reusable Supramolecular Epoxy Hot Melt Adhesives. *ACS Mater. Lett*. **2021**, 3 (7), 1003−1009.

(10) Rahman, M. A.; Bowland, C.; Ge, S.; Acharya, S. R.; Kim, S.; Cooper, V. R.; Chen, X. C.; Irle, S.; Sokolov, A. P.; Savara, A.; et al. Design of tough adhesive from commodity thermoplastics through dynamic crosslinking. *Sci. Adv.* **2021**, 7 (42), No. eabk2451.

(11) Jasinska-Walc, L.; Duchateau, R.; Bouyahyi, M.; Badillo Sampedro, N.; Kruszynski, J.; Hrachova, J.; Liu, Y.; Yang, L. Hot melt adhesive comprising functionalized polyolefins. U.S. Patent 20,240,263,052 A1, **2022**.

(12) Jasinska-Walc, L.; Duchateau, R.; Bouyahyi, M.; Kruszynski, J.; Gautam, P. S.; Nowicka, W.; Szot, W. Hot Melt Adhesives Based on Blends Comprising Non-Functionalized and Functionalized Polyolefins. WO 2025002627 A1, **2025**.

(13) Ahagon, A.; Gent, A. N. Effect of interfacial bonding on the strength of adhesion. *J. Polym. Sci., Polym. Phys. Ed.* **1975**, 13 (7), 1285−1300.

(14) Matsumoto, T.; Shimizu, Y.; Nishino, T. Analyses of the Adhesion Interphase of Isotactic Polypropylene Using Hot-Melt Polyolefin Adhesives. *Macromolecules* **2021**, 54 (15), 7226−7233.

(15) Boutar, Y.; Naïmi, S.; Mezlini, S.; da Silva, L. F. M.; Hamdaoui, M.; Ben Sik Ali, M. Effect of adhesive thickness and surface roughness on the shear strength of aluminium one-component polyurethane adhesive single-lap joints for automotive applications. *J. Adhes. Sci. Technol.* **2016**, 30 (17), 1913−1929.

(16) Washiyama, J.; Kramer, E. J.; Hui, C. Y. Fracture mechanisms of polymer interfaces reinforced with block copolymers: transition from chain pullout to crazing. *Macromolecules* **1993**, 26 (11), 2928−2934.
(17) Creton, C.; Brown, H. R.; Deline, V. R. Influence of Chain Entanglement on the Failure Modes in Block Copolymer Toughened Interfaces. *Macromolecules* **1994**, 27 (7), 1774−1780.
(18) Lyu, L.; Ohnuma, Y.; Shigemoto, Y.; Hanada, T.; Fukada, T.; Akiyama, H.; Terasaki, N.; Horiuchi, S. Toughness and Durability of Interfaces in Dissimilar Adhesive Joints of Aluminum and Carbon-Fiber-Reinforced Thermoplastics. *Langmuir* **2020**, 36 (46), 14046−14057.
(19) Merkx, M. J. M.; Angelidis, A.; Mameli, A.; Li, J.; Lemaire, P. C.; Sharma, K.; Hausmann, D. M.; Kessels, W. M. M.; Sandoval, T. E.; Mackus, A. J. M. Relation between Reactive Surface Sites and Precursor Choice for Area-Selective Atomic Layer Deposition Using Small Molecule Inhibitors. *J. Phys. Chem. C* **2022**, 126 (10), 4845−4853.
(20) Pepels, M. P. F.; Kleijnen, R. G.; Goossens, J. G. P.; Spoelstra, A. B.; Tandler, R.; Martens, H.; Soliman, M.; Duchateau, R. Compatibility and epitaxial crystallization between Poly(ethylene) and Poly(ethylene)-like polyesters. *Polymer* **2016**, 88, 63−70.
(21) Thirtha, V.; Lehman, R.; Nosker, T. Morphological effects on glass transition behavior in selected immiscible blends of amorphous and semicrystalline polymers. *Polymer* **2006**, 47 (15), 5392−5401.
(22) Wouters, M. E. L.; Goossens, J. G. P.; Binsbergen, F. L. Morphology of Neutralized Low Molecular Weight Maleated Ethylene−Propylene Copolymers (MAn-g-EPM) As Investigated by Small-Angle X-ray Scattering. *Macromolecules* **2002**, 35 (1), 208−216.
(23) Maaz, M.; Riba-Bremerch, A.; Guibert, C.; Van Zee, N. J.; Nicolaÿ, R. Synthesis of Polyethylene Vitrimers in a Single Step: Consequences of Graft Structure, Reactive Extrusion Conditions, and Processing Aids. *Macromolecules* **2021**, 54 (5), 2213−2225.
(24) Xi Wang, T.; Mei Chen, H.; Li, T.; Siang Lucas Ng, B.; Xie, H.; Xiao, R.; Min Huang, W. Tan-delta plateau in vitrimer-like polyurethanes. *Mater. Lett.* **2022**, 325, 132884.
(25) Balzade, Z.; Sharif, F.; Ghaffarian Anbaran, S. R. Tailor-Made Functional Polyolefins of Complex Architectures: Recent Advances, Applications, and Prospects. *Macromolecules* **2022**, 55 (16), 6938−6972.
(26) Odenwald, L.; Wimmer, F. P.; Mast, N. K.; Schußmann, M. G.; Wilhelm, M.; Mecking, S. Molecularly Defined Polyolefin Vitrimers from Catalytic Insertion Polymerization. *J. Am. Chem. Soc.* **2022**, 144 (29), 13226−13233.
(27) Ahmadi, M.; Hanifpour, A.; Ghiassinejad, S.; van Ruymbeke, E. Polyolefins Vitrimers: Design Principles and Applications. *Chem. Mater.* **2022**, 34 (23), 10249−10271.
(28) Müller, A. J.; Arnal, M. L. Thermal fractionation of polymers. *Prog. Polym. Sci.* **2005**, 30 (5), 559−603.
(29) Müller, A. J.; Michell, R. M.; Pérez, R. A.; Lorenzo, A. T. Successive Self-nucleation and Annealing (SSA): Correct design of thermal protocol and applications. *Eur. Polym. J.* **2015**, 65, 132−154.

(30) Urciuoli, G.; Ruiz de Ballesteros, O.; Cipullo, R.; Trifuoggi, M.; Giarra, A.; Auriemma, F. Thermal Fractionation of Ethylene/1-Octene Multiblock Copolymers from Chain Shuttling Polymerization. *Macromolecules* **2022**, 55 (13), 5656−5668.
(31) Androsch, R.; Wunderlich, B. Reversible Crystallization and Melting at the Lateral Surface of Isotactic Polypropylene Crystals. *Macromolecules* **2001**, 34 (17), 5950−5960.
(32) De Rosa, C.; Dello Iacono, S.; Auriemma, F.; Ciaccia, E.; Resconi, L. Crystal Structure of Isotactic Propylene−Hexene Copolymers: The Trigonal Form of Isotactic Polypropylene. *Macromolecules* **2006**, 39 (18), 6098−6109.
(33) Duan, Y.; Zhang, J.; Shen, D.; Yan, S. In Situ FTIR Studies on the Cold-Crystallization Process and Multiple Melting Behavior of Isotactic Polystyrene. *Macromolecules* **2003**, 36 (13), 4874−4879.
(34) Ricarte, R. G.; Tournilhac, F.; Leibler, L. Phase Separation and Self-Assembly in Vitrimers: Hierarchical Morphology of Molten and Semicrystalline Polyethylene/Dioxaborolane Maleimide Systems. *Macromolecules* **2019**, 52 (2), 432−443.
(35) Lee, B. L.; White, J. L. An Experimental Study of Rheological Properties of Polymer Melts in Laminar Shear Flow and of Interface Deformation and Its Mechanisms in Two-Phase Stratified Flow. *Trans. Soc. Rheol.* **1974**, 18 (3), 467−492.
(36) Nakao, K. Relationship Between Bond Strength and Crystallinity of High Polymers-Polyethylene, Polyethyleneterephthalate, and Nylon. *J. Adhes.* **1972**, 4 (2), 95−108.
(37) Hoecker, F.; Karger-Kocsis, J. Effects of crystallinity and supermolecular formations on the interfacial shear strength and adhesion in GF/PP composites. Polym. Bull. **1993**, 31 (6), 707−714.
(38) Gomes, A. D. S. Polymerization; IntechOpen: Rijeka, **2012**.
(39) Abou-Rachid, H.; Lussier, L.-S.; Ringuette, S.; Lafleur-Lambert, X.; Jaidann, M.; Brisson, J. On the Correlation between Miscibility and Solubility Properties of Energetic Plasticizers/Polymer Blends: Modeling and Simulation Studies. *Propellants, Explos., Pyrotech.* **2008**, 33 (4), 301−310.
(40) Ahmadi, A.; Freire, J. J. Molecular dynamics simulation study of compatibility for the polyvinylmethylether/polystyrene mixture. *Mol. Simul.* **2008**, 34 (10−15), 1253−1258.
(41) Cui, X. W.; Zhang, L. Amorphous State and Solubility Simulation of Poly(N-arylenebenzimidazole ketone). *Appl. Mech. Mater.* **2014**, 513−517, 295−298.
(42) Gestoso, P.; Brisson, J. Orientation of uniaxially stretched poly(vinyl phenol)/poly(vinyl methyl ether) blends. *Polymer* **2001**, 42 (20), 8415−8424.
(43) Gestoso, P.; Brisson, J. Effect of hydrogen bonds on the amorphous phase of a polymer as determined by atomistic molecular modelling. *Comput. Theor. Polym. Sci.* **2001**, 11 (4), 263−271.
(44) Zhang, M.; Choi, P.; Sundararaj, U. Molecular dynamics and thermal analysis study of anomalous thermodynamic behavior of poly (ether imide)/polycarbonate blends. *Polymer* **2003**, 44 (6), 1979−1986.
(45) Tambasco, M.; Lipson, J. E. G.; Higgins, J. S. Blend Miscibility and the Flory−Huggins Interaction Parameter: A Critical Examination. *Macromolecules* **2006**, 39 (14), 4860−4868.
(46) Gupta, J.; Nunes, C.; Vyas, S.; Jonnalagadda, S. Prediction of Solubility Parameters and Miscibility of Pharmaceutical Compounds by Molecular Dynamics Simulations. *J. Phys. Chem. B* **2011**, 115 (9), 2014−2023.

(47) Guo, Y.; Liu, J.; Lu, Y.; Dong, D.; Wang, W.; Zhang, L. A combined molecular dynamics simulation and experimental method to study the compatibility between elastomers and resins. *RSC Adv.* **2018**, 8 (26), 14401−14413.
(48) Lebga-Nebane, J. L.; Sankarasubramanian, M.; Chojecki, G.; Ning, B.; Yuya, P. A.; Moosbrugger, J. C.; Rasmussen, D. H.; Krishnan, S. Polyetheretherketone hexagonal boron nitride, and tungsten carbide cobalt chromium composite coatings: Mechanical and tribological properties. *J. Appl. Polym. Sci.* **2021**, 138 (21), 50504.

Supporting Information for

Tuning the adhesive strength of functionalized polyolefin-based hot melt adhesives: unexpected results leading to new opportunities

Jakub Kruszynski, Weronika Nowicka, Farhan Ahmad Pasha, Lanti Yang, Artur Rozanski, Miloud Bouyahyi, Ralf Kleppinger, Lidia Jasinska-Walc, Rob Duchateau

Macromolecules **2025** *58* (6), 2894-2904
DOI: 10.1021/acs.macromol.4c02945

This subchapter contains additional experimental details, molecular dynamics modelling details, materials, methods, surface characterization and ^{1}H NMR, SEC, DSC, WAXS, AFM, DMA, rheology, and lap shear tests.

Additional experimental details, materials and methods

Materials. All experiments were performed under an inert dry nitrogen atmosphere using either standard Schlenk or glove box techniques. Hex-1-ene, hex-5-ene-1-ol and triethylaluminum (TEA, 1.0 M solution in toluene) were purchased from Sigma-Aldrich, distilled and dried with 3 Å molecular sieves under an inert atmosphere. Methylaluminoxane (MAO, 30 wt % solution in toluene) was purchased from Lanxess. The catalyst precursor bis((2-oxoyl-3-(dibenzo-1H-pyrrole-1-yl)-5-(methyl)phenyl)-2-phenoxy)-2,4-pentanediyl hafnium (IV) dimethyl, {CH_2[CH(Me)O-C_6H_4-2-(2-$NC_{12}H_8$)-4-Me-C_6H_2O]2}$HfCl_2$, (HfO_4) [CAS: 958665-18-4] was purchased from Lomonosov Moscow State University (A. Z. Voskoboynikov). Dry, oxygen-free heptane was employed as solvent for the polymerization experiments. Phosphoric acid (85 %, Sigma Aldrich), dry toluene (99.9 %, CHROMASOLV, Honeywell) and methanol (98.5 %, VWR) were employed as chemicals for deashing experiments. Aluminum (AQ36, mill finish, Q-Panel) and steel (QD35, smooth finish, Q-Panel) were employed as surfaces for adhesive experiments.

Synthesis of poly(propylene–co–hex-1-ene) copolymer:

Poly(C_3–C_6). Copolymerization experiments were carried out using a stainless steel BÜCHI reactor (2 L) filled with heptane (PMH) as solvent (1 L). The solution was stirred using a stirring speed of 600 rpm. The reactor was first heated to 40 °C, charged with triethylaluminum (TEA; 1.0 M solution in toluene, 2 mL), hex-1-ene (30 ml, 242 mmol) and gaseous propylene (100 g) after which the mixture was heated to the desired polymerization temperature of 130 °C resulting in a pressure of about 15 bar. Once the set temperature was reached, the copolymerization reaction was initiated by the injection of the catalyst precursor HfO_4 (0.25 mg, 0.25 µmol) pre-activated with MAO (30 wt % solution in toluene, 11.3 mmol, 5 mL). The copolymerization was followed by monitoring the pressure drop. The copolymerization reaction was stopped by pouring the polymer solution into an Erlenmeyer flask containing acidified isopropanol (2.5 % v/v HCl (37 %), 500 mL) and Irganox 1010 (1.0 M in acetone, 0.5 mmol). The resulting suspension was stirred for 4 h, filtered, washed with demineralized water *i*PrOH (50 wt %, 2 × 500 mL) and dried at 80 °C in a vacuum oven prior to the addition of Irganox 1010 as antioxidant (1.0 M in acetone, 0.5 mmol, 5 mL).

Synthesis of Randomly Hydroxyl-Functionalized Polypropylene, poly(C_3–C_6–C_6OH). The copolymerization experiment was carried out using a stainless steel BÜCHI reactor (2 L) filled with heptane as solvent (1L). The solution was stirred using a stirring speed of 600 rpm. The reactor was first heated to 40 °C, charged with triethylaluminum (TEA; 1.0 M solution in toluene, 2 mL), hex-1-ene (30 mL, 242 mmol) and triethylaluminum-passivated hex-5-en-1-ol (1.0 M solution in toluene, TEA:hex-5-en-1-ol mol ratio = 1.0; 10 mL). Then the reactor was charged with gaseous propylene (100 g) and heated to the desired polymerization temperature of 130 °C resulting in a pressure of about 15 bar. Once the set temperature was reached, the copolymerization reaction was initiated by the injection of the catalyst precursor HfO_4 (2.0 mg, 2.0 *µ*mol) pre-activated with MAO (30 wt % solution in toluene, 11.2 mmol, 5 mL). The copolymerization was followed by monitoring the pressure drop. The copolymerization reaction was stopped by pouring the polymer solution into an Erlenmeyer flask containing acidified isopropanol (2.5 % v/v HCl (37 %), 500 mL) and Irganox 1010 (1.0 M in acetone, 0.5 mmol). The resulting suspension was stirred for 4 h, filtered, washed with demineralized water/iPrOH (50

wt %, 2 × 500 mL) and dried at 80 °C in a vacuum oven prior to the addition of Irganox 1010 as antioxidant (1.0 M, 0.5 mmol, 5 mL).

Procedure of the deashing of Hydroxyl-Functionalized Polypropylene. The polymer obtained from the solution process may be deashed to remove traces of protective species. To do so, the copolymer or terpolymer (10 g) was dispersed in mixture of dry toluene (400 mL) and concentrated (85 %) H_3PO_4 (10 mL, 0.17 mol, 16.9 g) and heated under reflux until the polymer dissolved. Once the polymer was properly dissolved, methanol (250 mL) was added to the hot mixture and the mixture was heated under stirring at 65 °C for 1 additional hour. Then the polymer was precipitated in cold methanol, filtered, and washed 2 times with methanol. The resulting polymer was sprinkled with IRGANOX 1010 solution (6 g Irganox in 1 L acetone) and dried at 65 °C in a vacuum oven for 24 hours.

Procedure of the preparation of blend comprising functionalized and non-functionalized polyolefin. Solid poly(C_3–C_6–C_6OH) (B), poly(C_3–C_x) (x = 2, 4, 6; D – G) and Irganox 1010 (1000 ppm) were dissolved in toluene and the mixture was heated under nitrogen at 100 °C at 300 rpm until the polymers dissolved. The solution of polymer was dried at 70 °C in a vacuum oven for 48 hours.

Measurements

^{1}H NMR analysis was carried out at 130 °C using deuterated tetrachloroethane (TCE-d2) as solvent and recorded in 5 mm tubes on a Varian Mercury spectrometer operating at a frequency of 400 MHz. Chemical shifts are reported in ppm versus tetramethylsilane and were determined by reference to the residual solvent protons.

Size Exclusion Chromatography (SEC). The measurements were performed at 150 °C using a Polymer Char GPC-IR® built around an Agilent GC oven model 7890, equipped with an autosampler and the viscometer and refractive index detector. 1,2-Dichlorobenzene (o-DCB) was used as an eluent at a flow rate of 1 $mL \cdot min^{-1}$. A PP molar mass calibration was obtained after conversion from PE to PP using the Mark-Houwink constants of PE and PP. The data were processed using Calculations Software GPC One®. Information about the short-chain branching can also be obtained with the GPC/SEC technique using an on-line

infrared (IR) detector with at least two interference filters; one filter for measuring the overall absorption of the C–H region, and another filter for measuring the absorption of the C–H from the methyl groups. These IR detectors inform about the comonomer incorporation (short-chain branches) in polyolefin copolymers by measuring the number of methyl groups per 1000 carbon atoms (CH_3/1000C).[3]

Differential Scanning Calorimetry (DSC). Melting (T_m) and crystallization (T_c) temperatures as well as enthalpies of the transitions were measured by DSC using a DSC 250 from TA Instruments. The measurements were carried out at a heating and cooling rate of 10 °C·min^{-1} from −40 °C to 230 °C under nitrogen flow (15 ml·min^{-1}). The transitions were deduced from the second heating and cooling curves. The degree of crystallinity (crystalline mass fraction) of the studied samples was determined according to a formula:

$$\mathrm{X_c} = \frac{\Delta H_m}{\Delta H_\mathrm{m}^0} \times 100\%$$

where: ΔH_m is the measured specific heat of melting, ΔH_m^0 is the heat of fusion of the crystal. The following values of ΔH_m^0 have been assumed: 207 J·g^{-1}. The thickness of lamellar crystals was determined according to a Thomson-Gibbs equation:

$$l_c = \frac{2\gamma_e}{\Delta H_\mathrm{m}^0} \frac{T_\mathrm{m}^0}{T_\mathrm{m}^0 - T_\mathrm{m}}$$

where l_c is the thickness of lamellar crystals, T_m is the melting temperature of a lamellar crystals, T_m^0 is the equilibrium melting temperature of an infinite crystal, γe is the surface energy of the basal surface of a lamellar crystal and ΔH_m^0 is the enthalpy of fusion for the lamellar crystal. To estimate the thickness of crystals the following values of constants characteristic for polypropylene were applied: γ_e = 62.3·10^{-7} J·cm^{-2}, ΔH_m^0 = 209 J·g^{-1}, T_m = 208 °C.[4,5]

Successive Self-Nucleation and Annealing (SSA) Fractionation. The crystallization behavior of the samples was studies using SSA protocol. SSA thermal protocol comprised the following steps: (1) Erasing the thermal history of polymer by heating the sample to 230 °C and annealing it isothermally for 3 minutes; (2) Cooling the sample at 10 °C·min^{-1} to 0 °C and annealing for 3 minutes; (3) Heating

the sample at 10 °C·min^{-1} from 0 °C to 120 °C and annealing the sample isothermally for 30 minutes; (4) Cooling the sample at 10 °C·min^{-1} rate from 120 °C to 0 °C to reflect the influence of thermal protocol on the crystallization of the sample. (5) From this point sample was consecutively cooled down with 5 °C intervals for each fractionation step and annealed isothermally for 30 minutes. Fractionation was performed at the temperature range from 120 °C to 35 °C. Each fractionation step was followed by cooling to 0 °C to reflect the influence of thermal protocol on the crystallization; (6) Eventually, the sample was heated at 10 °C·min^{-1} rate to 230 °C to give multiple melting endotherm.

Atomic Force Microscopy (AFM). Sample preparation. The adhesives obtained from the blends 30B/70G were prepared by adding around 2 g of blend pellet between two aluminum foils with reflective side inwards and then, the compression-molding cycle was applied: (i) 180 °C, (ii) stabilizing for 5 min with no force applied, (iii) applying for 5 min with 100 kN normal force and cooling down to 40 °C with the cooling speed of 10 °C·min^{-1} under 100 kN (0.6 MPa) normal force. For AFM measurements, the compression molded films were cut to size and the cross-section of the samples in the flow direction of molding was cryo-microtomed at −120 °C using microtoming equipment (LEICA EM UC7) to obtain a flat cross-sectional surface. To understand the film morphology in the bulk of the cross-section and close to the adhered Aluminum foil, the sample was microtomed throughout the whole cross-section thickness. A diamond knife (Diatome) mounted in a stainless-steel holder was used for microtoming the samples. After cryo-microtoming, the microtomed blocks were used for AFM measurements directly without further treatment.

AFM characterization. AFM experiments were performed using a Dimension FastScan AFM system (Dimension FastScan, Bruker, Santa Barbara, USA). Software Nanoscope Analysis 9.4 was used as computer interface for operation and Nanoscope Analysis 2.0 from Bruker for the analysis of AFM measurements. All AFM measurements were performed at ambient conditions. For the Vistamaxx and poly(C_3–C_6–C_6OH) film morphology characterization, AFM peak force tapping mode was used with a frequency of 4 Hz utilizing a fast scan type AFM tip (Fastscan-C, k = 0.8 N·m^{-1}, f = 300 kHz). After imaging, bearing analysis in the Nanoscope Analysis

2.0 from Bruker was used to understand the percentage of different phases based on the AFM image. Bearing analysis reveals how much of the scanned surface lies above or below a given z-scale value. By using bearing analysis, it is possible to determine what percentage of the image lies above or below any chosen z-scale, which can provide the percentage of different phases in the image with very clear z-scale difference.

Wide-Angle X-ray Scattering (WAXS). Wide-angle X-ray scattering (WAXS) measurements were performed on a computer-controlled goniometer coupled with a CuKα radiation source (λ = 0.154 nm) at 30 kV and 50 mA (Panalytical B.V., Almelo, The Netherlands). The analyzed samples were prepared using compression molding procedure.

Dynamic mechanical analysis (DMA) was performed using a TA Instruments DMA850. Samples were tested by strain-controlled temperature ramp with the frequency of 1 Hz under 0.016 % strain. The measurements were performed using film-tension mode. The temperature profile was from −50 °C to the melting point of the sample with the ramp 2 °C·min^{-1}. The glass transition temperature (T_g) was calculated as the maximum of the tangent delta signal.

Melt rheology measurements were performed using a plate-plate (gap distance 1 mm) MCR 720 rheometer (Anton Paar, Graz, Austria). Disc samples (Ø 25 mm, 1 mm thickness) were obtained by compression molding. The shear dependent analysis was conducted from 0.01 rad·s^{-1} to 200 rad·s^{-1}, under constant temperature 180 °C and amplitude strain of 1 %, as well as a nitrogen atmosphere.

Surface analysis. The static contact angle was determined by fitting the baseline and contour of the liquid droplets using ellipsoidal method. For each liquid, 10 droplets of 2.0 μL in volume were deposited on the surface and imaged using a camera. The surface free energy was calculated using the Owens-Wendt-Rabel-Kaelble (OWRK) theory in which surface energy is separated into a polar and disperse component and based on the measurements with water and diiodomethane.

Procedure of adhesive laminates preparation. The laminate samples, used for the lap shear test, were prepared via compression-molding using PP ISO settings on LabEcon 600 high-temperature press (Fontijne Presses, the Netherlands). Namely, the films (25 mm × 12.5 mm × 0.5 mm) of iPP and propylene-based copolymers and terpolymers were loaded between the substrates Steel QD35, Aluminum A35 with overlap of 12.5 mm (312.5 mm^2 bonding area). Then, the compression-molding cycle was applied: (i) 180 °C, (ii) stabilizing for 5 min with no force applied, (iii) applying for 5 min with 100 kN (0.63 MPa) normal force and cooling down to 40 °C with the cooling speed of 10 $°C \cdot min^{-1}$ under 100 kN (0.63 MPa) normal force.

Lap Shear Strength analysis. The measurements were performed using Zwick type Z020 tensile tester equipped with a 10 kN load cell according to ISO 4587. Before measurements, samples were conditioned for 7 days at room temperature. The tests were performed on specimens (10 cm × 2.5 cm) with surface overlapping 12.5 mm under room temperature. A grip-to-grip separation of 140 mm was used. The samples were pre-stressed to 3 N, then loaded with a constant crosshead speed 100 $mm \cdot min^{-1}$. To calculate the lap shear strength the reported force value divided by the real bonding surface of the specimens measured with caliper (since pressing step might lead to misalignment of the bars). The reported values are an average of at least 5 measurements of each composition.

Table S1. Molecular characterization and thermal properties of poly(propylene-co-hex-1-ene-*co*-hex-5-en-1-ol (A – C), poly(propylene–*co*–hex-1-ene) (D – E), poly(propylene–*co*–but-1-ene) (F), poly(propylene–*co*–ethylene) (G) samples and blends thereof.

Sample	Composition	$\bar{M}_n$[a]	$\bar{M}_w$[a]	$Đ$[a]	C_6OH[l]	X_c[c]	T_m[c]	T_c[c]	T_g[d]
		kg·mol^{-}	kg·mol^{-1}	-	mol %	%	°C	°C	°C
A	poly(C_3–C_6–C_6OH)	57.6	208.7	3.6	0.52	19.0	81.2	31.6	0
B	poly(C_3–C_6–C_6OH)	51.2	204.8	4.0	0.40	15.0	77.7	14.9	−1
C	poly(C_3–C_6–C_6OH)	37.8	140.7	3.7	0.13	14.1	76.6	12.8	0
D	poly(C_3–C_6)	20.8	71.4	3.4	0.00	18.5	86.7	21.8	0
E	poly(C_3–C_6)	203.4	752.6	3.7	0.00	14.6	80.5	23.3	−1
F	poly(C_3–C_4)	119.8	270.1	2.3	0.00	19.4	78.2	41.4	−3
G	poly(C_3–C_2)	117.4	258.2	2.2	0.00	1.1	106.0	n/a	−19
1B/99D	1% sample B; 99% sample D	19.3	71.8	3.7	0.00	16.6	86.5	34.4	2
5B/95D	5% sample B; 95% sample D	20.6	77.7	3.8	0.01	17.4	85.6	36.7	−1
10B/90D	10% sample B; 90% sample D	23.1	83.8	3.6	0.03	17.5	84.8	35.9	0
30B/70D	30% sample B; 70% sample D	21.8	108.8	5.0	0.11	17.2	82.9	28.9	4
50B/50D	50% sample B; 50% sample D	27.1	133.0	4.9	0.20	15.4	81.6	19.3	0
70B/30D	70% sample B; 30% sample D	32.2	148.0	4.6	0.28	14.3	80.1	18.4	0
1B/99E	1% sample B; 99% sample E	154.6	742.1	4.8	0.00	16.1	83.8	45.5	3
5B/95E	5% sample B; 95% sample E	157.3	723.6	4.6	0.01	15.8	84.2	46.0	4
10B/90E	10% sample B; 90% sample E	161.6	692.7	4.3	0.03	15.8	82.6	42.8	2
30B/70E	30% sample B; 70% sample E	128.8	579.6	4.5	0.11	15.1	82.2	43.0	2
50B/50E	50% sample B; 50% sample E	85.3	435.0	5.1	0.20	15.3	80.8	38.5	3
70B/30E	70% sample B; 30% sample E	83.3	316.6	3.8	0.28	15.1	79.5	38.8	2
1B/99F	1% sample B; 99% sample F	103.4	259.9	2.5	0.00	12.1	75.3	22.1	−3
5B/95F	5% sample B; 95% sample F	81.3	242.4	3.0	0.01	12.3	73.1	16.2	0
10B/90F	10% sample B; 90% sample F	98.9	267.9	2.7	0.03	12.8	72.5	16.4	−3
30B/70F	30% sample B; 70% sample F	63.1	233.8	3.7	0.11	13.1	70.1	−1.3	1
50B/50F	50% sample B; 50% sample F	73.7	236.9	3.2	0.20	10.2	71.9	2.8	3
70B/30F	70% sample B; 30% sample F	56.2	208.2	3.7	0.28	10.0	74.2	7.2	−2
1B/99G	1% sample B; 99% sample G	95.1	229.3	2.4	0	0.9	104.9	18.2	−19
5B/95G	5% sample B; 95% sample G	105.5	250.6	2.4	0.01	1.3	103.5	19.6	−19

10B/90G	10% sample B; 90% sample G	105.6	251.5	2.4	0.03	1.5	102.4	19.1	−19
30B/70G	30% sample B; 70% sample G	72.2	229.3	3.2	0.11	4.9	82.0	16.9	−19/0
50B/50G	50% sample B; 50% sample G	70.1	239.8	3.4	0.20	6.1	79.8	15.8	−22/1
70B/30G	70% sample B; 30% sample G	62.4	201.2	3.2	0.28	9.3	78.9	15.3	−22/3

a) Determined by HT-SEC in 1,2-dichlorobenzene at 150 °C; b) Average hex-5-en-1-ol content, determined by ^{1}H NMR; c) Determined by DSC; d) Determined by DMA.

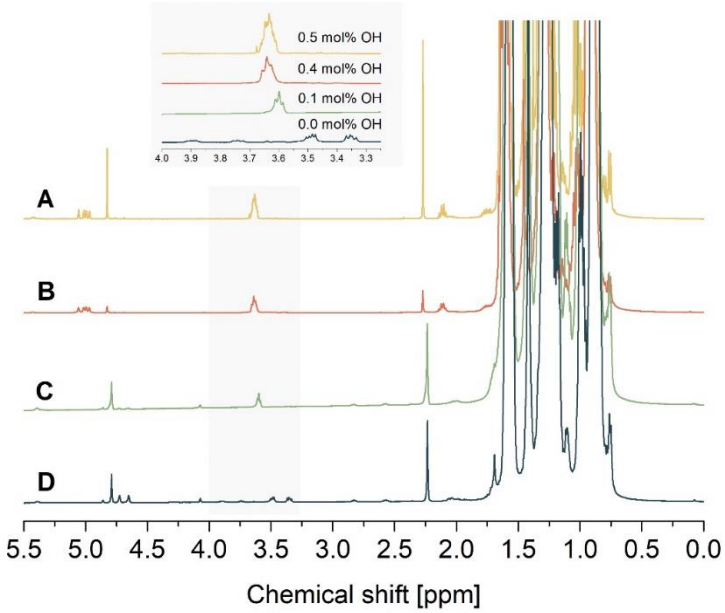

Figure S1. ^{1}H NMR analysis of poly(propylene-*co*-hex-1-ene-*co*-hex-5-en-1-ol) (A, B, C) and poly(propylene-*co*-hex-1-ene) (D).

Table S2. Branches content and crystallinity level analysis of B – G.

Sample	Composition	Branches content	X_c[a]	X_c[b]
		mol %	%	vol%
B	poly(C_3–C_6–C_6OH)	10.5	15	39
D	poly(C_3–C_6)	6.8	18	-
E	poly(C_3–C_6)	8.4	15	35
F	poly(C_3–C_4)	17.3	19	46
G	poly(C_3–C_2)	18.8	1	-

a) Calculated from DSC; [b] calculated from WAXS.

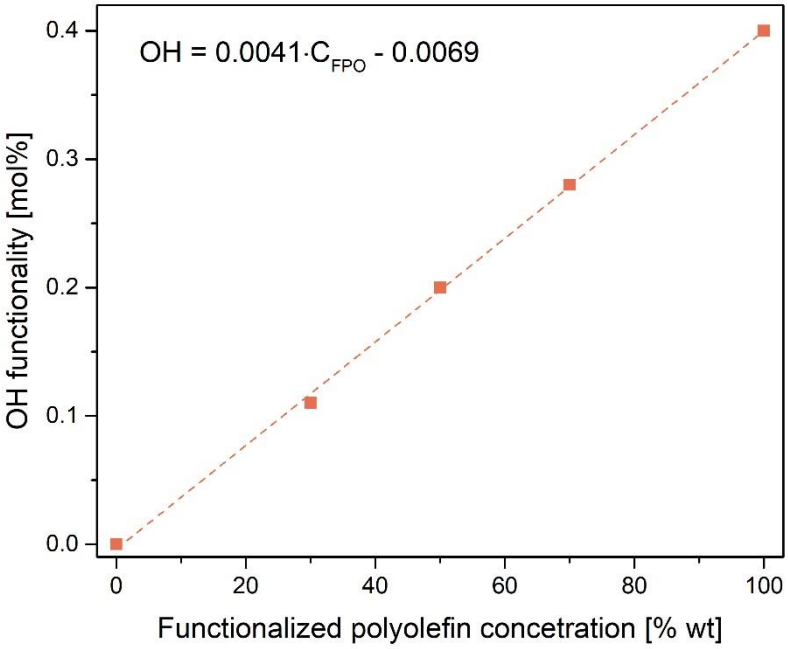

Figure S2. Functionality level of the reference polymers B and D as well as 30B/70D, 50B/50D, 70B/30D w/w blends thereof.

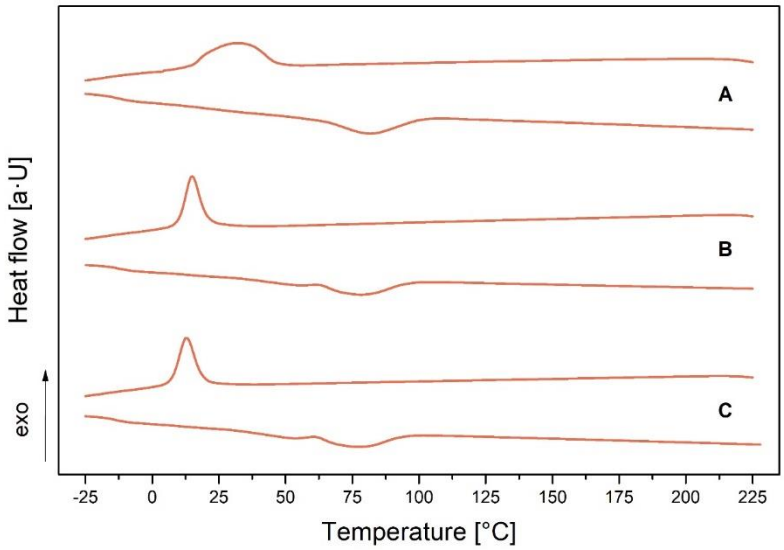

Figure S3. DSC profiles of samples A, B, C.

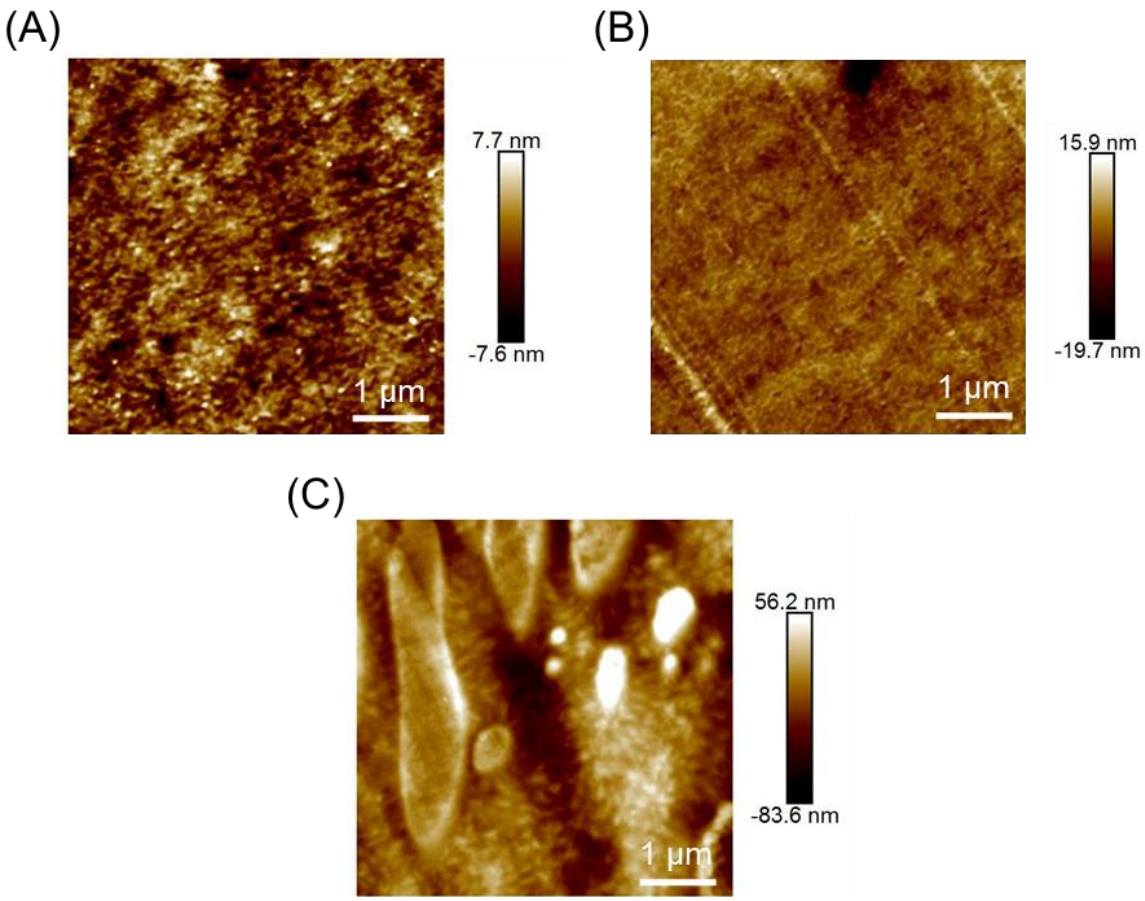

Figure S4. Morphology analysis of the polymer blends: 30B/70D (A), 30B/70F (B) and 30B/70G (C) by AFM.

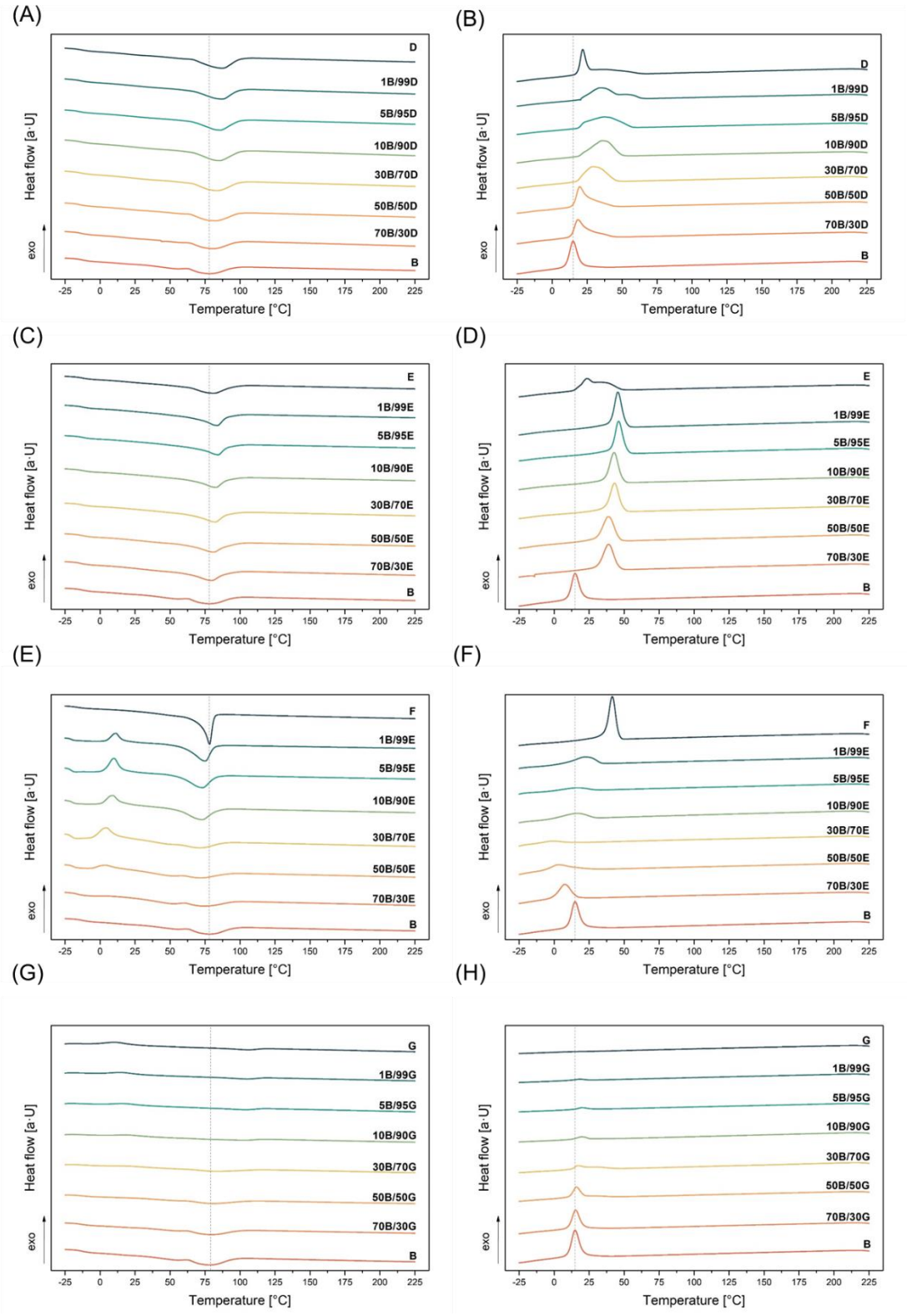

Figure S5. Melting and crystallization profiles of the pristine components and blends thereof: B/D (A, B); B/E (C, D); B/F (E, F); B/G (G, H).

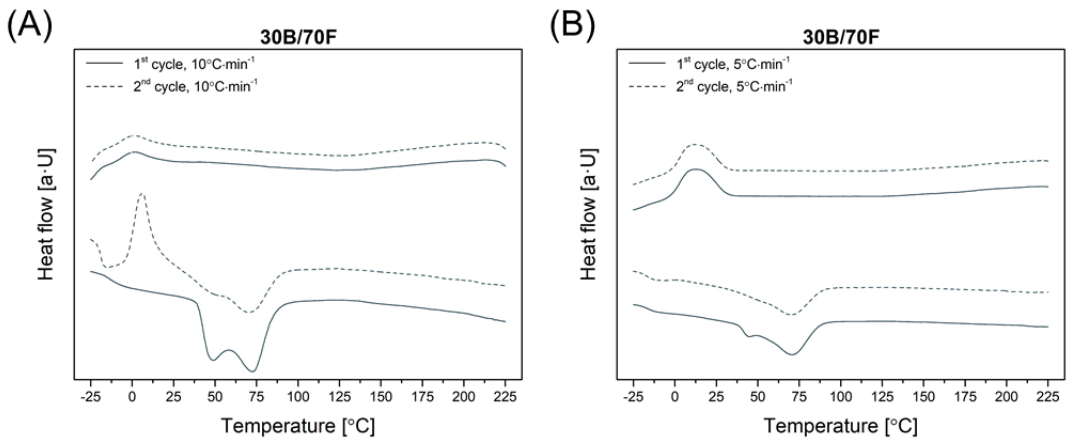

Figure S6. Melting and crystallization profiles of 30B/70F blends determined by DSC under temperature ramp 10 °C·min^{-1} (A) and 5 °C·min^{-1} (B).

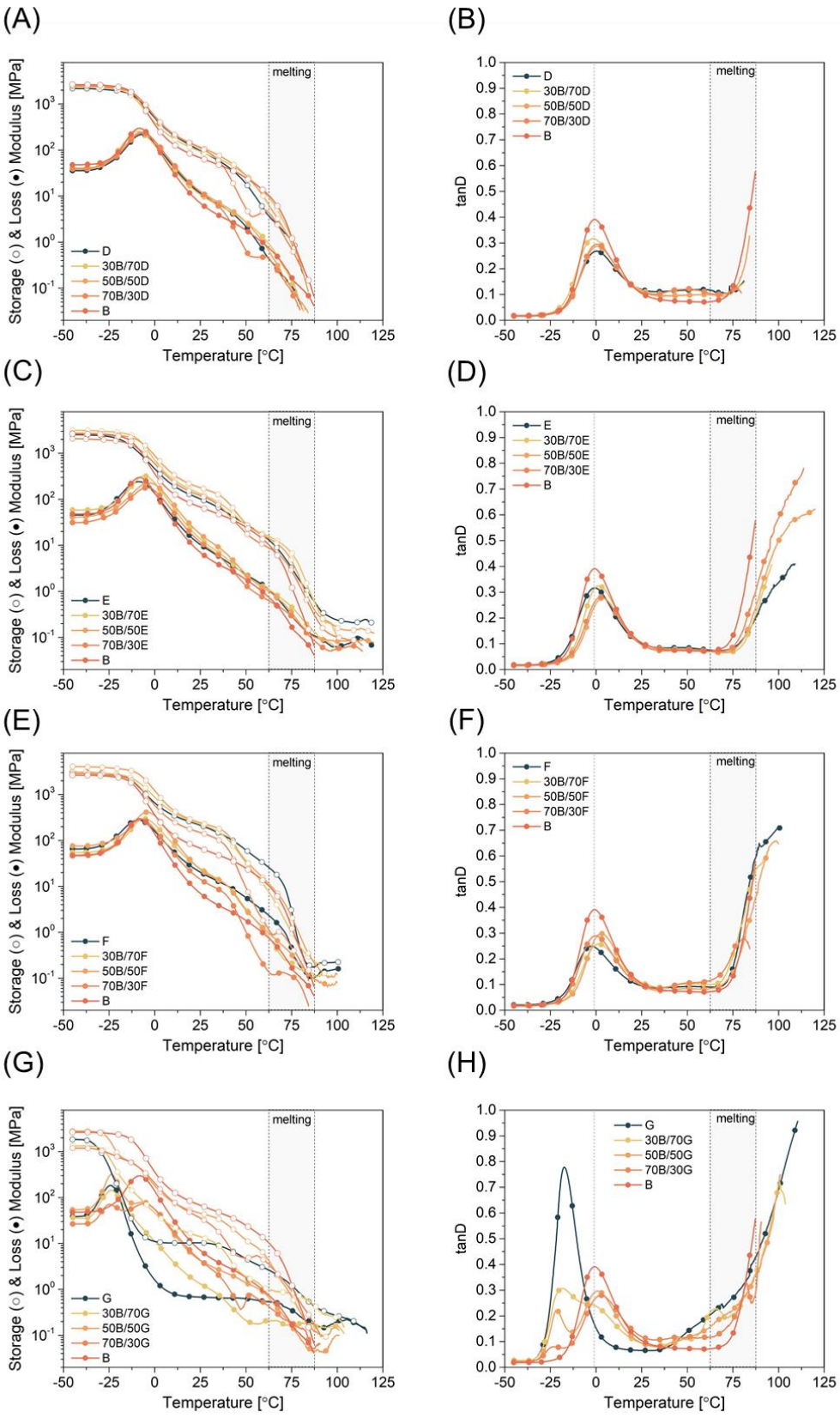

Figure S7. Storage and loss modulus as well as tanδ of B (A, B); D, E (C, D); F (E, F); G (G, H).

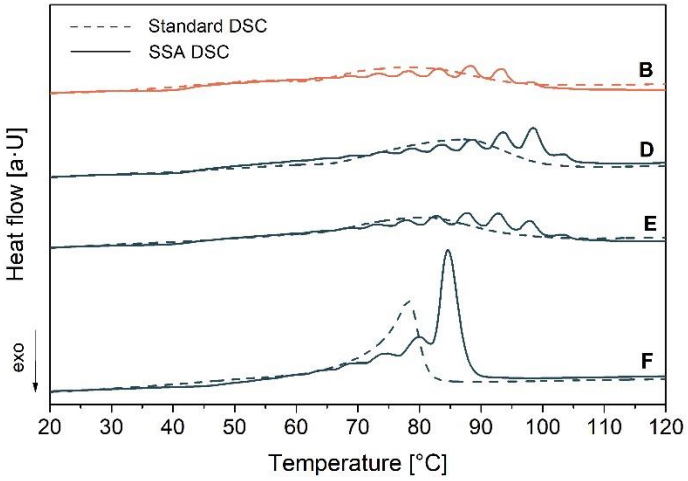

Figure S8. Melting temperatures of B, D, E, F determined by successive self-nucleation (SSA) and annealing (DSC).

Table S3. Surface characterization of samples B, D – G with aluminum and steel substrates used for the adhesion tests.

Entry	Composition	Surface Energy [mN·m^{-1}]
B	poly(C_3–C_6–C_6OH)	13
D	poly(C_3–C_6)	16
E	poly(C_3–C_6)	18
F	poly(C_3–C_4)	13
G	poly(C_3–C_2)	17
Aluminum	-	42
Steel	-	29

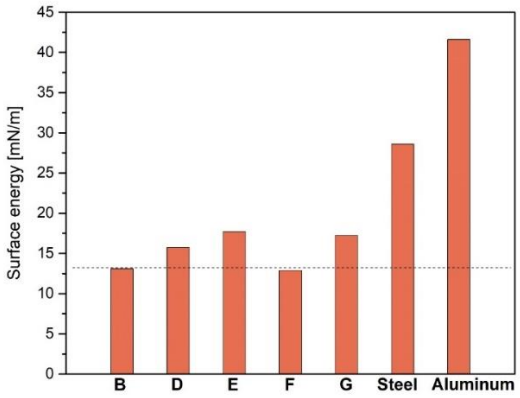

Figure S9: Surface characterization of samples **B**, **D** – **G** with aluminum and steel substrates used for the adhesion tests. The bar diagram represents data given in Table S3.

Table S4. Lap shear test results of A – G and blends thereof.

Name	Composition	C_6OH[a] mol %	LSS [MPa] Aluminum (Failure mode) *	LSS [MPa] Steel (Failure mode) *
A	poly(C_3–C_6–C_6OH)	0.52	AlF[b]	14.5 ± 1.1 (CF)
B	poly(C_3–C_6–C_6OH)	0.40	7.7 ± 0.7 (CF)	11.2 ± 1.0 (CF)
C	poly(C_3–C_6–C_6OH)	0.13	2.7 ± 0.6 (CF)	5.8 ± 0.8 (CF)
D	poly(C_3–C_6)	0.00	1.8 ± 0.4 (IF)	2.3 ± 1.5 (IF)
E	poly(C_3–C_6)	0.00	1.7 ± 0.5 (IF)	0.8 ± 0.8 (IF)
F	poly(C_3–C_4)	0.00	1.6 ± 0.3 (AF)	1.6 ± 0.4 (IF)
G	poly(C_3–C_2)	0.00	1.3 ± 0.2 (AF)	0.9 ± 0.3 (IF)
1B/99D	1% sample B; 99% sample D	0.00	4.1 ± 1.2 (IF)	5.1 ± 0.4 (CF)
5B/95D	5% sample B; 95% sample D	0.01	4.9 ± 0.3 (CF)	7.7 ± 1.0 (CF)
10B/90D	10% sample B; 90% sample D	0.03	5.8 ± 0.8 (CF)	9.1 ± 1.1 (CF)
30B/70D	30% sample B; 70% sample D	0.11	5.6 ± 0.4 (CF)	6.8 ± 0.3 (CF)
50B/50D	50% sample B; 50% sample D	0.20	6.0 ± 0.3 (CF)	7.3 ± 1.3 (CF)
70B/30D	70% sample B; 30% sample D	0.28	6.0 ± 0.4 (CF)	7.2 ± 1.0 (CF)
1B/99E	1% sample B; 99% sample E	0.00	7.7 ± 0.5 (IF)	10.1 ± 0.7 (IF)
5B/95E	5% sample B; 95% sample E	0.01	7.7 ± 0.2 (IF)	11.8 ± 0.8 (IF)
10B/90E	10% sample B; 90% sample E	0.03	8.0 ± 0.4 (IF)	10.8 ± 0.4 (IF)
30B/70E	30% sample B; 70% sample E	0.11	8.3 ± 0.9 (CF)	11.8 ± 1.0 (IF)
50B/50E	50% sample B; 50% sample E	0.20	7.8 ± 0.5 (CF)	11.5 ± 0.4 (CF)
70B/30E	70% sample B; 30% sample E	0.28	8.1 ± 0.1 (CF)	11.5 ± 0.6 (CF)
1B/99F	1% sample B; 99% sample F	0.00	2.4 ± 0.4 (AF)	6.6 ± 0.6 (IF)
5B/95F	5% sample B; 95% sample F	0.01	6.5 ± 0.5 (IF)	10.1 ± 1.1 (IF)
10B/90F	10% sample B; 90% sample F	0.03	6.7 ± 0.3 (CF)	10.4 ± 1.0 (IF)
30B/70F	30% sample B; 70% sample F	0.11	6.4 ± 0.4 (CF)	9.3 ± 1.2 (IF)
50B/50F	50% sample B; 50% sample F	0.20	6.6 ± 0.2 (CF)	9.1 ± 2.2 (IF)
70B/30F	70% sample B; 30% sample F	0.28	6.6 ± 0.2 (CF)	9.5 ± 0.9 (IF)
1B/99G	1% sample B; 99% sample G	0	1.5 ± 0.3 (AF)	2.3 ± 0.2 (IF)
5B/95G	5% sample B; 95% sample G	0.01	1.9 ± 0.2 (AF)	3.1 ± 0.5 (IF)
10B/90G	10% sample B; 90% sample G	0.03	2.9 ± 0.3 (AF)	4.4 ± 1.0 (IF)
30B/70G	30% sample B; 70% sample G	0.11	4.8 ± 0.4 (IF)	5.1 ± 0.5 (IF)
50B/50G	50% sample B; 50% sample G	0.20	5.8 ± 0.3 (CF)	7.7 ± 0.6 (CF)
70B/30G	70% sample B; 30% sample G	0.28	6.9 ± 0.7 (CF)	6.2 ± 0.6 (CF)

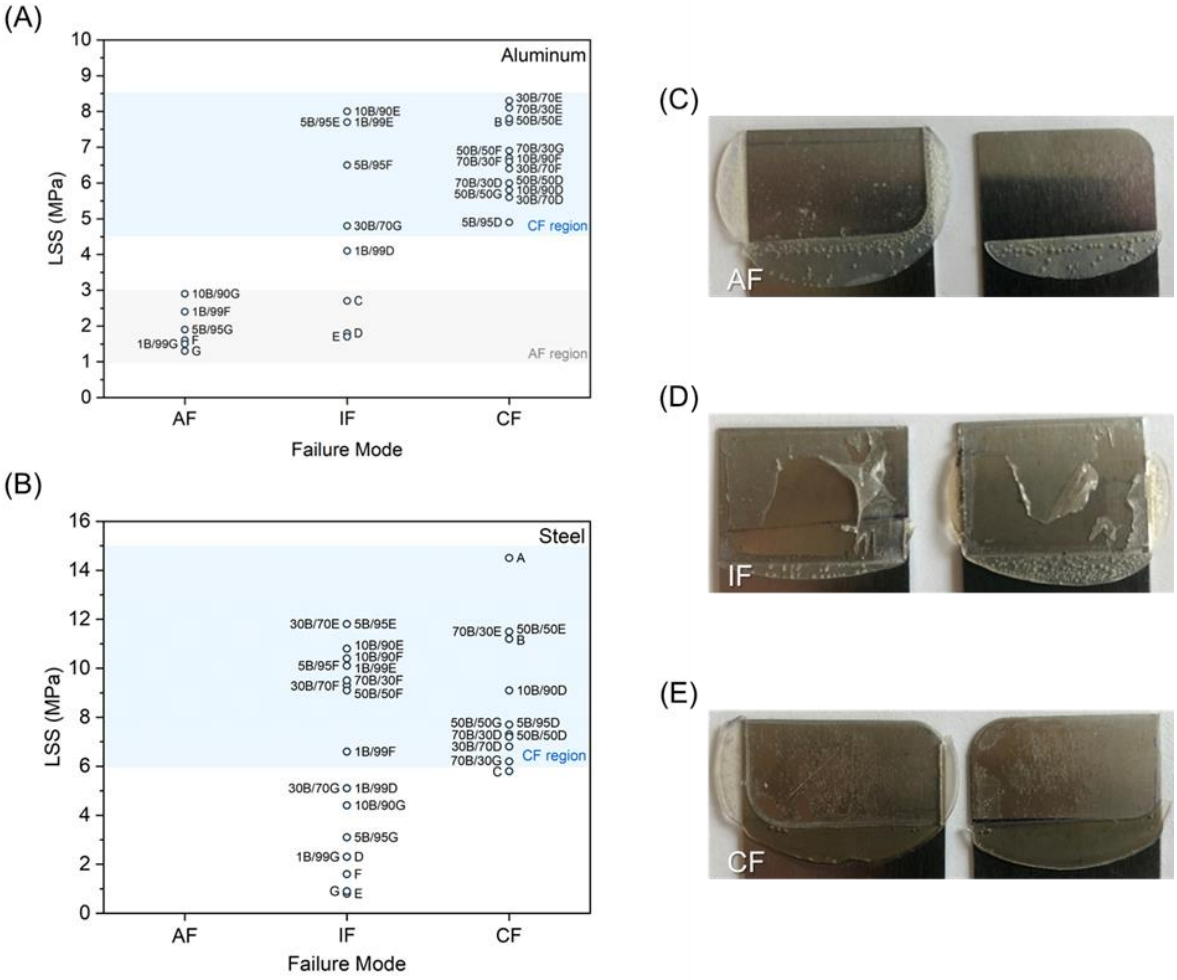

Figure S10. Adhesive failure mode analysis for A – G and blends thereof for aluminum (A) and steel (B) connections. The photos (right) represent examples of the adhesive failure (C), interfacial (mixed) failure (D) and cohesive failure (E) after lap shear strength test.

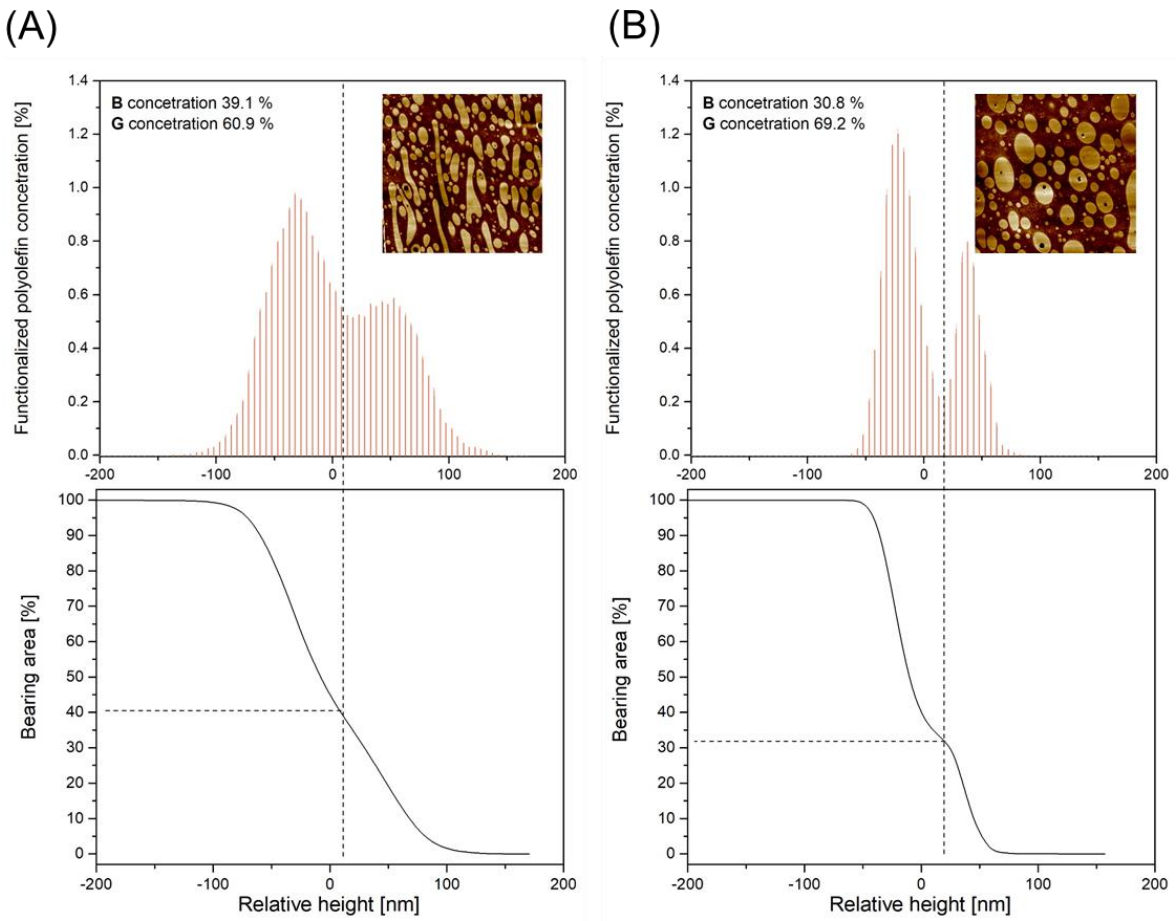

Figure S11. AFM analysis and bearing analysis based on AFM mapping of the blend comprising 30B/70G at the interface location with aluminum (A), and in the core of the laminate (B).

Molecular dynamics model preparation: To create a realistic model, the molecular chain of B, E – G were modelled in the appropriate ration of C_3/C_x as reported in Table S5. The molecular weights needed to be normalized by a factor of 10 resulting in polymeric chains consisting of B (108 of C_3, 6 of C_6 and 3 of C_6OH monomeric units), E (439 of C_3, 23 of C_6 monomeric units), F (196 of C3, 67 of C_4 monomeric units) and G (235 of C_3, 67 of C_2 monomeric units), respectively (Table S5). All Molecular Dynamics Simulations performed at the process temperature at which the polymers were blended experimentally (190 °C). This temperature was also chosen to avoid complexity due to the semi-crystalline nature of the polymers. Based on calculations and experimental data, at 190 °C the initial density of 0.76 $g \cdot cm^{-3}$ was selected for the polymer mixtures. The simulations were performed

using BIOVIA Materials Studio 2022.7 The Amorphous Cell module was used to construct representative models of the different polymer mixtures.[8] The Forcite module was used for periodic boundary condition-based molecular dynamics calculations to predict key properties. The most advanced Condensed-phase Optimized Molecular Potentials for Atomistic Simulations Studies (COMPASSIII) was selected for the molecular dynamic simulations.[9-12] In COMPASSIII, the total energy (E_{total}) of the simulation system is represented by the summation and non-bonding interactions (eq. 1, 2).

$$E_{\mathrm{Total}} = E_{\mathrm{b}} + E_{\mathrm{q}} + E_{\emptyset} + E_{\chi} + E_{\mathrm{cross}} + E_{\mathrm{vdw}} + E_{\mathrm{ele}} \quad (1)$$

$$E_{\mathrm{Total}} = E_{\mathrm{valence}} + E_{\mathrm{cross}} + E_{\mathrm{nonbond}} \quad (2)$$

For each blend B + E – G, five different models with different ratios of functionalized and non-functionalized polyolefins were used. Detailed description of these models is covered in Table S6. Each model was constructed in a 3D cubic cell, which was subjected to a series of geometry optimizations and molecular dynamics simulations using a Forcite module as implemented in Materials Studio 2022. Firstly, the cell was annealed with a periodic boundary condition to 190 °C for 0.5 ps with a pressure of 10−3 GPa to eliminate internal stress. Subsequently, the cells were subjected to equilibration: First, the geometry was optimized using the smart method (including steepest descent, conjugate gradient, and the Newton method) for more than 105 steps until a convergent value was reached. Then the cubic cells were refined by ultra-short molecular dynamics NVT (constant number of particles, N, volume, V, and temperature, T) simulation equilibrated at 190 °C with a time step of 0.5 fs for 5000 steps followed by an NPT ensemble run at 190 °C with a time step of 0.5 fs for 30000 steps. Minimum fluctuations in density and energy were two cut off criteria to determine the equilibrium of the system. Finally, the equilibrated cells were subjected to a production run of NPT (constant number of particles, pressure, and temperature) ensembled at 190 °C for 1000 ps. The miscibility parameters such as Mixing energy ΔEmix, and Flory-Huggins interaction parameter (χ) were calculated for all fifteen models and respected values are reported in Table S6. The conceptual basis of the calculated properties is reported elsewhere.[13]

Adhesion modelling: The Al_2O_3 crystal structure was taken from the BIOVIA library, and a surface (1 1 1) was created using 5 × thickness. The resulting surface was transformed into an 8 × 5 supercell consisting of 6000 atoms with lattice parameters (65.942638 × 69.176254 Å) having sufficient surface area to interact with polymers of the constituting the blends. Because there is no covalent bond in the metal oxide layer between the aluminum and oxide atoms, the aluminum and oxygen atoms in Al_2O_3 were set to constraints to avoid any disruption during minimization and simulation. The surface geometry was minimized using the COMPASSIII force field method. Furthermore, each polymeric blend obtained at the end of molecular dynamics simulation for miscibility was used to place over the Al_2O_3 surface. The final simulation box was built using the layer module along with 30 Å vacuum to break the periodic boundary conditions. The geometry optimization of the layer was carried out using the COMPASSIII force field method. Then annealing was carried out for 2 cycles with NVT Ensemble, and a short-term molecular dynamic 50 ps was performed using NVT Ensemble. Furthermore, three energy calculations were performed: surface-polymer system, surface alone, and polymer alone using the same box size, and the adhesion energy was calculated using equation 3.

$$\Delta E_{Ad} = E_{Surface-polymer} - \left(E_{Surface} + E_{Polymer}\right) \quad (3)$$

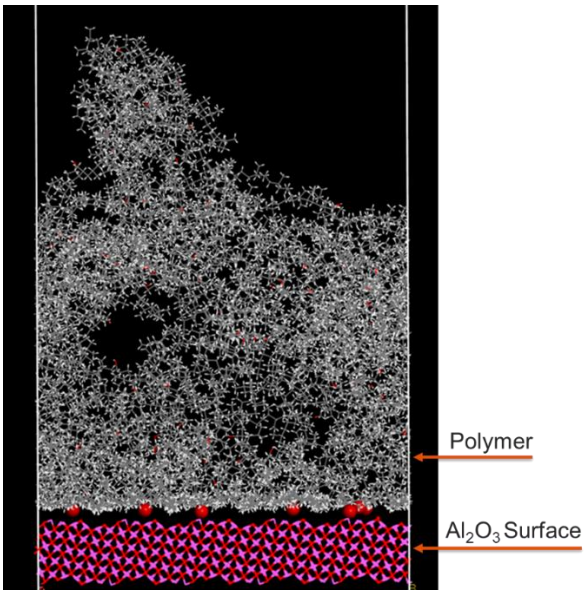

Figure S12. The polymer adhesion molecular dynamics simulation over an aluminum oxide (Al_2O_3) surface.

Table S5. Number average molecular weight and composition of the functionalized (B) and non-functionalized (E – G) polyolefins used for the molecular dynamics simulations.

Sample	$\bar{M}_n$	C_3	C_2	C_4	C_6	C_6OH	$nC_3/nC_x(/nC_6OH)$
	$kg \cdot mol^{-1}$	mol %	mol %	mol %	mol %	mol %	
B	51.2	89.5			10.1	0.4	108/6/3
E	203.4	90.5			9.5	–	439/23
F	119.8	68.7		31.3		–	196/67
G	117.4	84.0	16.0			–	235/67

n is number of monomers

Table S6. Actual blend compositions of different blends of B and E – G used for the molecular dynamics simulations.

B/E blends					
Composition	**80/20**	**70/30**	**50/50**	**20/80**	**10/90**
wt % of **B**	78.01	71	52.2	21.5	8.3
wt % of **E**	21.99	29	47.8	79.5	91.7
Number of chains **B**/**E**	13/1	9/1	4/1	1/1	1/3
Mixing Energy (E_{mix}, J·m^3)	−12.86	−14.74	−13.82	−9.74	−6.16
Chi parameter (χ)	−700.73	−803.19	−752.75	−530.94	−335.90
Adhesion Energy (E_{Adh}, kcal·mol^{-1})	−1991.84	−1873.87	−1533.38	−1167.63	−813.14
B/F blends					
Composition	**80/20**	**70/30**	**50/50**	**20/80**	**10/90**
wt % of **B**	80.67	69.89	48.14	17.09	10.39
wt % of **F**	19.33	30.11	51.86	82.93	89.61
Number of chains **B**/**F**	9/1	5/1	2/1	1/2	1/4
Mixing Energy (E_{mix}, J·m^3)	−8.21	−12.44	−12.40	−10.27	−3.13
Chi parameter (χ)	−447.12	−677.62	−675.72	−559.53	−170.78
Adhesion Energy (E_{Adh}, kcal·mol^{-1})	−1795.90	−1418.82	−1185.86	−216.25	−162.20
B/G blends					
Sample	**80/20**	**70/30**	**50/50**	**20/80**	**10/90**
wt % of **B**	79.1	70.28	48.61	19.12	10.57
wt % of **G**	20.9	29.72	51.39	80.88	89.43
Number of chains **B**/**G**	8/1	5/1	2/1	1/2	1/4
Mixing Energy (E_{mix}, J·m^3)	−5.01	−9.72	−8.33	−6.60	−3.90
Chi parameter (χ)	−272.79	−529.48	−453.96	−359.45	−212.39
Adhesion Energy (E_{Adh}, kcal·mol^{-1})	−2050.36	−1934.97	−1000.23	−475.84	−232.90

References

(1) Global Adhesives and Sealants Market, Domain: Chemicals and Materials Sub-domain: Adhesives and Sealants Base, **2018**, Forecast Period for 2019-2024.

(2) Sun, P.; Li, Y.; Qin, B.; Xu, J. F.; Zhang, X. Super Strong and Multi-Reusable Supramolecular Epoxy Hot Melt Adhesives. *ACS Mater. Lett.* **2021**, 3 (7), 1003–1009.

(3) GPC-IR®, the HT-SEC system for Polyolefin Analysis; www.polymerchar.com.

(4) Monasse, B.; Haudin, J.M. Growth transition and morphology change in polypropylene. *Colloid Polym. Sci.* **1985**, 263, 822–831.

(5)Brandrup, J.; Immergut, E.H.; Grulke, E. A. Polymer Handbook. **1999**, New York: John Wiley&Sons.

(6) Awaya, H. Morphology of Different Types of Isotactic Polypropylene Spherulites Crystallized from *Melt. Polymer* **1988**, 29, 591 – 596.

(7) Dassault Systemes. BIOVIA MATERIALS: Studio Overview, 2017.

(8) Theodorou, D. N.; Suter, U. W. Detailed molecular structure of a vinyl polymer glass. *Macromolecules* **1985**, 18, 1467–1478.

(9) Sun, H. Ab initio characterizations of molecular structures, conformation energies, and hydrogen-bonding properties for polyurethane hard segments. *Macromolecules* 1993, 26, 5924–5936.

(10) Sun, H. COMPASS: An ab Initio Force-Field Optimized for Condensed-Phase Applications. Overview with Details on Alkane and Benzene Compounds. *J. Phys. Chem. B* **1998**, 102, 7338–7364.

(11) McQuaid, M. J.; Sun, H.; Rigby, D. Development and validation of COMPASS force field parameters for molecules with aliphatic azide chains. *J. Comput. Chem.* **2004**, 25, 61–71.

(12) Akkermans, R. L. C.; Spenley, N. A.; Robertson, S. H. COMPASS III: Automated fitting workflows and extension to ionic liquids. *Mol. Simul.* **2021**, 47, 540–551.

(13) Kruszynski, J.; Nowicka, W.; Rozanski, A.; Liu, Y.; Parisi, D.; Yang, L.; Pasha, F. A.; Bouyahyi, M.; Jasinska-Walc, L.; Duchateau, R. iPP/HDPE blends compatibilized by a polyester: An unconventional concept to valuable products. *Sci. Adv.* **2024**, 10, eado1944.

CHAPTER III

This research focuses on developing innovative compatibilization strategies for polyolefin-based polymer blends using in-house synthesized amphiphilic graft and block copolymers, as well as aliphatic polyesters. The presented compatibilizers significantly improve blend morphology, enabling the scalable production of highly ductile polyolefin materials with enhanced mechanical properties. These solutions offer a promising pathway for upgrading and recycling PP, PE, and PC waste streams into high-value products, contributing to a more sustainable polymer economy.

Publications included in this chapter*:

1. Jasinska-Walc L., Bouyahyi M., Kruszynski J., Tercjak A., Rozanski A., Troisi E., Liu Y., Yang L., Ivashkiv O., Sienkiewicz M., Duchateau R., Preparation of Well-Compatibilized PP/PC Blends and Foams Thereof, *ACS Applied Polymer Materials* **2021** *3* (11), 5509-5516

2. Kruszyński J., Nowicka W., Rozanski A, Liu Y., Parisi D., Yang L, Pasha F.A., Bouyahyi M., Jasinska-Walc L., Duchateau R., iPP/HDPE blends compatibilized by a polyester: An unconventional concept to valuable products, *Science Advances* **2024**, eado1944

* The co-authors' approval to use this paper in the thesis was included with the documentation.

4.1 General introduction

It is remarkable that based on only a handful of monomeric building blocks such a wide range of polyolefins with different chemical composition topologies have been produced. Importantly polypropylene, the primary focus of this study, exhibits several limitations, including relatively low impact strength, poor adhesion and printability, toughness and performance at low temperature.[1–3] These drawbacks significantly restrict its application in advanced materials and its recycling. Blending of polypropylene with engineering plastics such as polycarbonate offers a practical and cost-effective strategy to overcome these shortcomings and achieve mechanical properties not feasible by individual components.[4]

Scale of plastic production and scant percentage of recycling represent the most crucial problem of the society. As depicted in Figure 1, since last 70 years, the production of plastic based on petroleum has risen exponential. Less than 2 million tons of polymers were produced in 1950 while 413 million tons were released in 2023. It means that at least 13 tons of plastic are produced every second! According to UNEP's 2021 report from 1950 to 2017, 9,200 million tonnes of plastic were produced, while only 7.6% was recycled, part of which was incinerated (10.9%), disposed of in landfills or oceans (57.6%) or still in use (31.5%).[5,6]

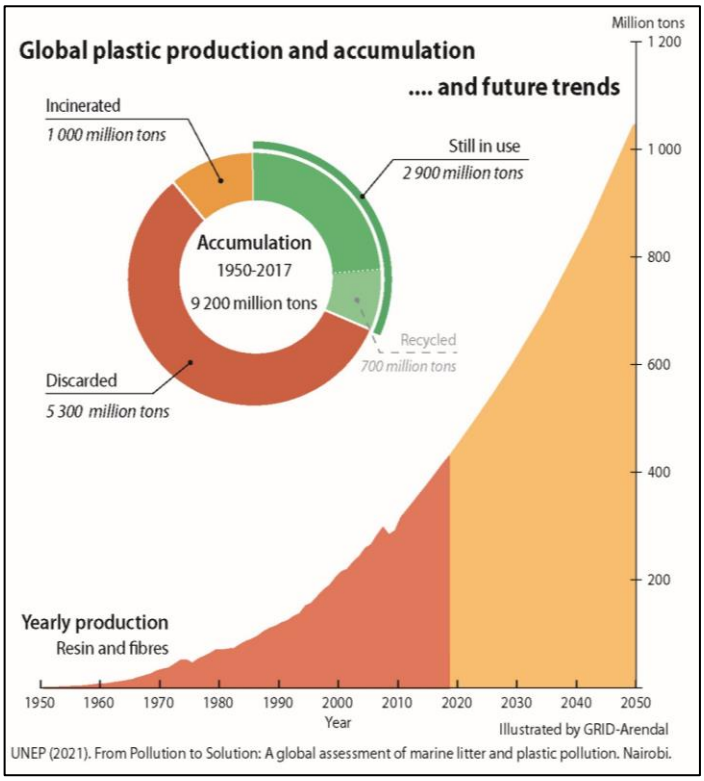

Figure 1. Global plastic production and accumulation and future trends.[5]

Polyolefin based products account for approximately 45 % of global plastic production. With applications in packaging, automotive, building, and construction, polyolefins are everywhere around us and progressively take over the position originally reserved for engineering plastics. However, especially as packaging material, the lifetime of polyolefins is unsettlingly short before it is being disposed. Among all range of plastic applications over 40% of polymer waste is produced for packaging applications, where most of plastics come from petroleum-based sources. There is an increasing awareness of the need to recycle plastics.[7] Year over year, the production of polymers from alternative, renewable feedstocks is increasing. Nevertheless, such materials—named as circular polymers—accounted for only 9.6 % of the 413.8 Mt of plastic produced in 2023 (Figure 2). The majority of circular polymers was derived from mechanical recycling (8.7%). The remaining 1.1 % refer to bio-based polymers (0.7 %), polymers from chemical recycling (0.2 %), and technologies based on CO_2 capture (0.1%).[8] Mechanical recycling of plastics seems to be a logical route to reuse discarded polymer products but there are several challenges to be overcome. One of them is sorting of the different polymers. Whereas sophisticated sorting technologies exist to separate mixed plastic waste, due to their similar structure and density, separating different types of polyolefins is complicated. Despite they are being structurally quite similar, different types of polyolefins are hardly miscible and blends of polyolefins typically suffer from poor optical and mechanical properties. Hence, it is crucial to find a solution to improve the mechanical properties of polyolefin blends in order to obtain highly performing material from recycled polymers.[9–13]

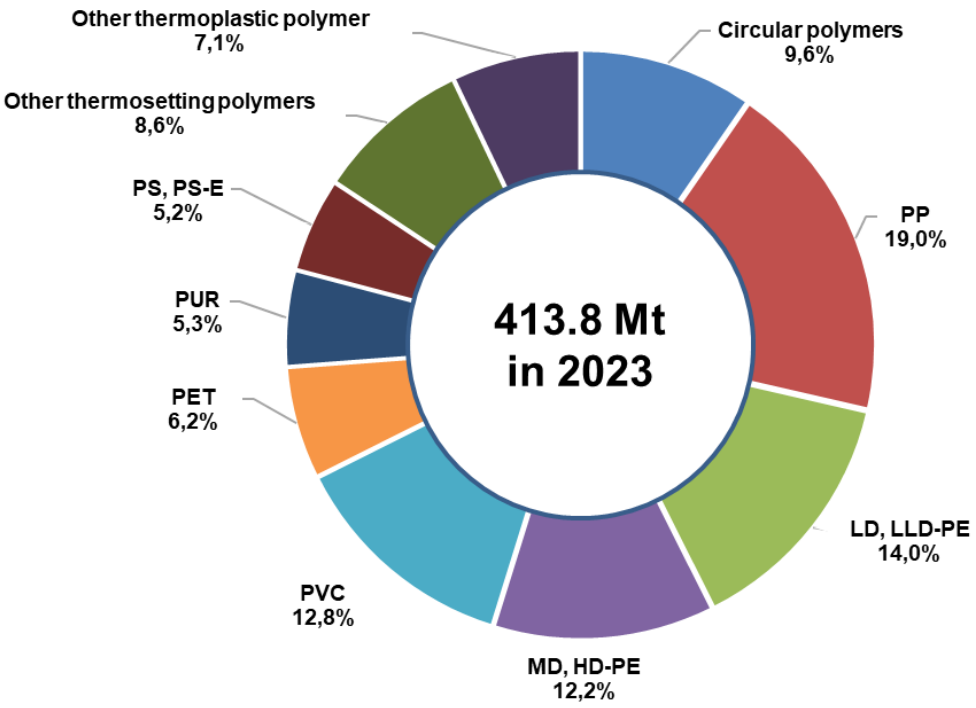

Figure 2. Global plastic production by polymer.[8]

4.2 Strategies of polyolefin-based blends compatibilization

The majority of polymers do not mix with each other due to differences in chemical structure, morphology and visco-elastic properties. Improving of the compatibility between polymers is essential for enhancing mechanical performance and enabling efficient processing and recycling. Compatibility can be achieved through either reactive or non-reactive approaches.[14–16]

Reactive compatibilization involves the addition of reactive coupling agents or the in-situ formation of copolymers within polymer blends. These coupling agents include silanes, carbodiimides, isocyanates, biscaprolactam, and additives containing anhydride groups, all of which can chemically react with functional groups present in the individual blend components. Reactive compatibilization can also occur during melt blending; for instance, ionic bonds or telechelic oligomers may form compatibilizing species in situ during processing.[17–19] At the industrial scale, maleic anhydride is the most widely used reactive coupling agent, commonly applied to improve adhesion in multilayer packaging and enhance compatibility in polyolefin blends.

Non-reactive methods include employing of additives - compatibilizers - or improvement of blends processing techniques. Compatibilization of polymer blends primarily relies on Janus architecture nanoparticles or functionalized block or graft

copolymers, which contain segments with selective affinity for each component.[20–22] The compatibilization mechanism is primarily based on the migration of amphiphilic compatibilizers to the interface between domains, where they reduce interfacial tension by physically anchoring their respective segments into each phase.[9,23–26] The incorporation of compatibilizing agents within the blend mitigates the coalescence of the dispersed phase, thereby reducing domain sizes. Sufficiently integrated compatibilizer molecules into both the matrix and the dispersed phase, allowing them to become entangled with the polymer chains, they significantly enhance interfacial adhesion between the two phases in the solid state. Effective interfacial adhesion promotes stress transfer between the phases and inhibits the propagation of cracks that may originate at the interface.[27,28] Among the non-reactive methods, solid-state shear pulverization (SSSP) can be also distinguished as strong tool to achieve compatibility between polyolefin-based blends. This improved processing technique induces compatibilization through intense shearing in a twin-screw extruder operated slightly below the melting point of the mixed polymers. Compared to the traditional melt processing, operating in the solid or semi-solid state avoids thermal degradation of the polymers. Processing polymers using the SSSP technique breaks down crystalline regions, generating high shear stress and promoting interfacial interactions. This technique is gaining increasing popularity, particularly for the recycling of polyolefin waste streams.[29]

Polyolefins namely polypropylene (PP) and polyethylene (PE) are immiscible not only with polar polymers but also with each other. Despite apparent similarities in polymer chain morphology, those polymers demonstrate incompatibility. In contrast to *i*PP, PE crystallizes rapidly, leading to the formation of large crystals. These differences in crystallization behavior result in weak intermolecular interactions between the formed *i*PP and PE crystalline phases, which tend to remain separated rather than mix.[30] Even minor amounts of PE domains dispersed in a *i*PP matrix result in increased brittleness and reduced strain at break, thereby deteriorating the mechanical performance of the blend and significantly hindering the recycling of polymer waste streams. Industrial polyolefin compatibilizers are gaining popularity year by year. In blends where PE is the major component, mechanical performance can be effectively tailored using polar-functionalized ethylene copolymers, which are commercially available under trade names such as Retain™, Fusabond™, Elvaloy™, Surlyn™, or Lotader™. [31,32]

Nevertheless, compatibilizing blends in which *i*PP is the majority component remains a significant challenge. The development of isotactic polypropylene (*i*PP) – based alpha–olefin copolymers and terpolymers still lags that of their PE–based analogues. In recent years, major chemical companies have intensified efforts to develop and commercialize *i*PP copolymers featuring highly structured and well-distributed alpha-olefin blocks and branches, such as Vistamaxx™, Tafmer™ and InTune™. [32–34]

4.3 Scope of the chapter

The scope of the presented PhD research includes the compatibilization of polymer blends containing polyolefins. This chapter explores the efficiency of in-house synthesized FPO-based amphiphilic copolymers or polyolefin-like polyesters as compatibilizers for polymer blends containing abundantly available polymers such as polypropylene (PP), polyethylene (PE), and engineering plastics like polycarbonate (PC). The selection of the above-mentioned polymers is based on the fact that polyolefins play by far the most prominent role in our daily lives, and there is a continuous need to improve their properties and recyclability. To overcome the drawbacks of polypropylene, bisphenol A-based polycarbonate was chosen for blending due to its exceptional impact resistance, lightweight nature, and polar character.

In the first attached scientific publication, the compatibilization performance of polypropylene–poly(ethylene brassylate) block and graft copolymers (PP-*graft/block*-PEB), as well as a polypropylene–polycaprolactone graft copolymer (PP–*graft*–PCL), was described. Microscopy methods, employed in this study (SEM, TEM, AFM), demonstrated that the addition of PP–*graft*–PEB and PP–*graft*–PCL copolymers lead to finer and more stable phase morphologies by reducing the domain size of the dispersed PC phase. Mechanical analysis showed that the compatibilizers help to foam the material and maintain closed-cell structures and inhibit cell coalescence due to improved interfacial adhesion and morphological stability during the foaming process. This study shows that a well-compatibilized PP/PC blend offers a promising, cost-effective, and scalable approach for the extrusion of low-density foams. This approach provides a viable method for repurposing PP and PC waste streams, thereby reducing carbon emissions and supporting environmental sustainability in the polymer industry.[35]

Research presented in the second attached publication reveals the performance of synthesized polypentadecalactone (PPDL) — a polyester produced from renewable pentadecalactone (PDL) — as a compatibilizer for blends consisting of polypropylene and polyethylene. A meticulous examination was carried out through the preparation of a series of two- and three-component blends to assess the inherent potential of PPDL as a compatibilizer for polyolefin blends. Based on advanced techniques, including DFT, AFM, TEM, GPC, WAXS, DSC, DMTA, and

rheology, the affinity of PPDL to both the *i*PP and HDPE phases was confirmed. Tensile testing revealed that the addition of 5 % PPDL has a profound effect on mechanical properties, transforming brittle *i*PP/HDPE blends into materials capable of withstanding unprecedented elongation. Demonstrated approach provide a simple and scalable solutions that can help to convert polyolefin waste stream into valuable high-volume products.

4.4 References

(1) Williamson, J. B.; Na, C. G.; Johnson, R. R. I. I. I.; Daniel, W. F. M.; Alexanian, E. J.; Leibfarth, F. A. Chemo- and Regioselective Functionalization of Isotactic Polypropylene: A Mechanistic and Structure–Property Study. *J. Am. Chem. Soc.* **2019**, 141 (32), 12815–12823.

(2) Utracki, L. A. Polypropylene Blends with Commodity Resins. In Polypropylene: An A-Z reference; Karger-Kocsis, J., Ed.; Springer Netherlands: Dordrecht, **1999**; pp 615–620.

(3) Li, G.; Li, J.; Wang, J.; Feng, J.; Guo, Q.; Zhou, J.; Mitrouchev, P. The Effect of Temperature on Mechanical Properties of Polypropylene. In Advanced Manufacturing and Automation VII; Wang, K., Wang, Y., Strandhagen, J. O., Yu, T., Eds.; Springer, Singapore, **2018**; pp 143–149.

(4) Kim, D.-K.; Lee, S. H.; Hong, S.-K.; Han, S. W.; Lee, D. H.; Yu, S. Low-Temperature-Toughened Polypropylene Blends with Highly Packed Elastomeric Domains. *ACS Appl. Polym. Mater.* **2022**, 4 (10), 7834–7840.

(5) United Nations Environment Programme (UNEP). From Pollution To Solution A Global Assessment Of Marine Litter And Plastic Pollution; **2021**.

(6) S&P, IHS Markit Plastic Recycling; **2022**.

(7) S&P, IHS Markit, Polypropylene Resins; **2024**.

(8) Plastics Europe AISBL. Circular Economy for Plastics – A European Overview; **2023**.

(9) Eagan, J. M.; Xu, J.; Di Girolamo, R.; Thurber, C. M.; Macosko, C. W.; LaPointe, A. M.; Bates, F. S.; Coates, G. W. Combining Polyethylene and Polypropylene: Enhanced Performance with PE/iPP Multiblock Polymers. *Science* **2017**, 355 (6327), 814–816.

(10) Xu, J.; Eagan, J. M.; Kim, S.-S.; Pan, S.; Lee, B.; Klimovica, K.; Jin, K.; Lin, T.-W.; Howard, M. J.; Ellison, C. J.; LaPointe, A. M.; Coates, G. W.; Bates, F. S. Compatibilization of Isotactic Polypropylene (IPP) and High-Density Polyethylene (HDPE) with IPP–PE Multiblock Copolymers. *Macromolecules* **2018**, 51 (21), 8585–8596.

(11) Wolff, P.; Dickert, A.; Kretschmer, W. P.; Kempe, R. IPP/PE Multiblock Copolymers for Plastic Blend Recycling Synthesized by Coordinative Chain Transfer Polymerization. *Macromolecules* **2022**, 55 (15), 6435–6442.

(12) López-Barrón, C. R.; Tsou, A. H. Strain Hardening of Polyethylene/Polypropylene Blends via Interfacial Reinforcement with Poly(Ethylene-*cb*-Propylene) Comb Block Copolymers. *Macromolecules* **2017**, 50 (7), 2986–2995.

(13) Yang, Y.; Xu, M.; Luo, Z.; He, R.; Xie, J.; Yang, S.; Chen, H.; Li, H. Long-Chain-Branched Polypropylene with an Ester Group as an Effective Compatibilizer To Improve the Performance of PP/PET Blends. *ACS Appl. Polym. Mater.* **2024**, 6 (23), 14580–14589.
(14) RUNT, J. P.; MARTYNOWICZ, L. M. Crystallization and Melting in Compatible Polymer Blends. In Multicomponent Polymer Materials; *Advances in Chemistry*; American Chemical Society, **1985**; Vol. 211, pp 111–123.
(15) Kumar, S. K. Pressure Effects on the Thermodynamics of Polymer Blends. *Macromolecules* **2000**, 33 (14), 5285–5291.
(16) Yang, Z.; Han, C. D. Rheology of Miscible Polymer Blends with Hydrogen Bonding. *Macromolecules* **2008**, 41 (6), 2104–2118.
(17) Xie, S.; Karnaukh, K. M.; Yang, K.-C.; Sun, D.; Delaney, K. T.; Read de Alaniz, J.; Fredrickson, G. H.; Segalman, R. A. Compatibilization of Polymer Blends by Ionic Bonding. *Macromolecules* **2023**, 56 (10), 3617–3630.
(18) Wang, H.; Dong, W.; Li, Y. Compatibilization of Immiscible Polymer Blends Using in Situ Formed Janus Nanomicelles by Reactive Blending. *ACS Macro Lett.* **2015**, 4 (12), 1398–1403.
(19) Ashcraft, E.; Ji, H.; Mays, J.; Dadmun, M. A Novel Reactive Processing Technique: Using Telechelic Polymers To Reactively Compatibilize Polymer Blends. *ACS Appl. Mater. Interfaces* **2009**, 1 (10), 2163–2173.
(20) Hu, J.; Hao, X.; Ning, N.; Yu, B.; Tian, M. Reactive Janus Particle Compatibilizer with Adjustable Structure and Optimal Interface Location for Compatibilization of Highly Immiscible Polymer Blends. *ACS Appl. Mater. Interfaces* **2023**, 15 (19), 23963–23970.
(21) Zhang, W.; Lin, M.; Winesett, A.; Dhez, O.; Kilcoyne, A. L. D.; Ade, H.; Rubinstein, M.; Shafi, K. V. P. M.; Ulman, A.; Gersappe, D.; Tenne, R.; Rafailovich, M.; Sokolov, J.; Frisch, H. L. The Use of Functionalized Nanoparticles as Non-Specific Compatibilizers for Polymer Blends. *Polym Adv. Technol.* **2011**, 22 (1), 65–71.
(22) Chen, Y.; Wu, J.; Qu, Y.; Ling, X.; Wang, H.; Li, Y. Immiscible Polymer Blends Compatibilized through Noncovalent Forces: Construction of a “Quasi-Block/Graft Copolymer” by Interfacial Stereocomplex Crystallites. ACS Appl Polym Mater **2022**, 4 (12), 9378–9387.
(23) Cigana, P.; Favis, B. D.; Albert, C.; Vu-Khanh, T. Morphology−Interface−Property Relationships in Polystyrene/Ethylene−Propylene Rubber Blends. 1. Influence of Triblock Copolymer Interfacial Modifiers. *Macromolecules* **1997**, 30 (14), 4163–4169.
(24) Malik, R.; Hall, C. K.; Genzer, J. Phase Separation Dynamics for a Polymer Blend Compatibilized by Protein-like Copolymers: A Monte Carlo Simulation. Macromolecules **2011**, 44 (20), 8284–8293.
(25) Ihm, D. J.; White, J. L. Interfacial Tension of Polyethylene/Polyethylene Terephthalate with Various Compatibilizing Agents. *J Appl. Polym. Sci*. **1996**, 60 (1), 1–7.
(26) Lyatskaya, Y.; Balazs, A. C. Using Copolymer Mixtures To Compatibilize Immiscible Homopolymer Blends. *Macromolecules* **1996**, 29 (23), 7581–7587.
(27) Ayan, U.; Nouranian, S.; Majdoub, M.; Al-Ostaz, A.; Ucak-Astarlioglu, M. G.; Villacorta, B. S. Supertoughened Polylactic Acid/Polybutylene Adipate Terephthalate Blends Compatibilized with

Ethylene-Methyl Acrylate-Glycidyl Methacrylate: Morphology and Mechanical Properties by the Response Surface Methodology. *ACS Appl. Mater. Interfaces* **2024**, 16 (20), 26833–26848.

(28) Yokoyama, K.; Guan, Z. A Vitrimer Acts as a Compatibilizer for Polyethylene and Polypropylene Blends. *Angewandte Chemie International Edition* **2024**, 63 (20), e202317264.

(29) Will, T. A.; Lu, Y.; Wakabayashi, K. Effects of Polymer Properties on Solid-State Shear Pulverization: Thermoplastic Processability and Nanofiller Dispersibility. *ACS Appl. Polym. Mater.* **2023**, 5 (3), 1848–1858.

(30) Cicolella, A.; Scoti, M.; Talarico, G.; Müller, A. J.; Di Girolamo, R.; De Rosa, C. Crystallization Kinetics of Crystalline–Crystalline and Crystalline–Amorphous Block Copolymers of Linear Polyethylene and Isotactic Polypropylene. *Macromolecules* **2024**, 57 (18), 8748–8762.

(31) SK Functional Polymers®, https://sk-fp.com/product-category/lotader/.

(32) DOW®, https://www.dow.com.

(33) ExxonMobil®, https://www.exxonmobilchemical.com/en.

(34) Mitsui Chemicals®, https://jp.mitsuichemicals.com/en/special/tafmer/.

(35) Embabi, M.; Kweon, M. S.; Anstey, A.; Tuccitto, A. V; Park, C. B.; Shivokhin, M. E.; Lee, P. C. Effect of Ethylene Comonomer Content on the Foam Processing Window of Long-Chain Branched Polypropylene. *ACS Appl. Polym. Mater.* **2023**, 5 (4), 2417–2429.

4.5 Compatibilization of polypropylene / polycarbonate blends

This subchapter has been published as:

Preparation of Well-Compatibilized PP/PC Blends and Foams Thereof

Lidia Jasinska-Walc, Miloud Bouyahyi, Jakub Kruszynski, Agnieszka Tercjak, Artur Rozanski, Enrico M. Troisi, Yingxin Liu, Lanti Yang, Ostap Ivashkiv, Maciej Sienkiewicz, and Robbert Duchateau

ACS Applied Polymer Materials **2021** *3* (11), 5509-5516

DOI: 10.1021/acsapm.1c00813

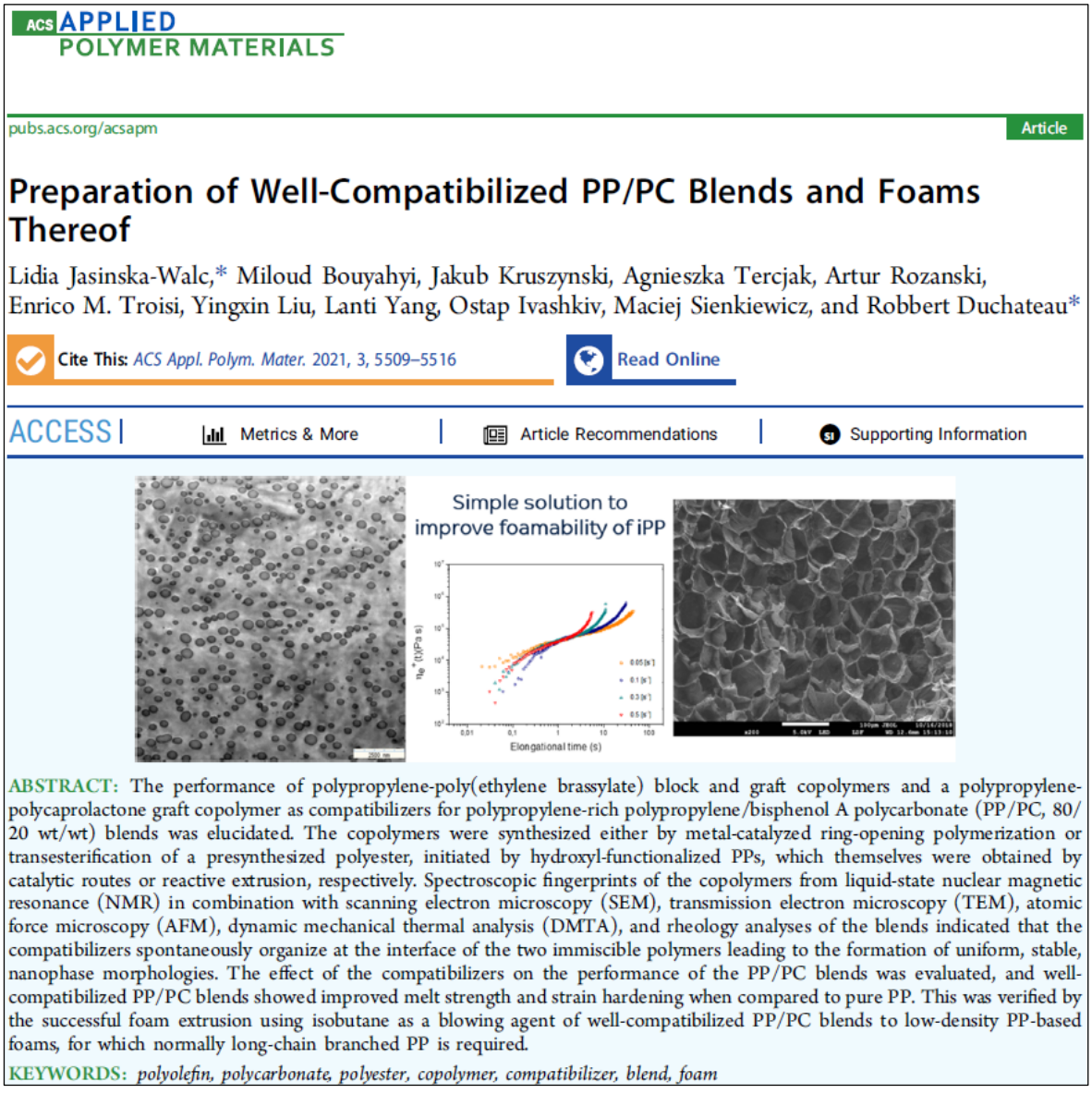

ACS APPLIED POLYMER MATERIALS

pubs.acs.org/acsapm Article

Preparation of Well-Compatibilized PP/PC Blends and Foams Thereof

Lidia Jasinska-Walc,* Miloud Bouyahyi, Jakub Kruszynski, Agnieszka Tercjak, Artur Rozanski, Enrico M. Troisi, Yingxin Liu, Lanti Yang, Ostap Ivashkiv, Maciej Sienkiewicz, and Robbert Duchateau*

Cite This: ACS Appl. Polym. Mater. 2021, 3, 5509−5516 Read Online

ACCESS | Metrics & More | Article Recommendations | Supporting Information

ABSTRACT: The performance of polypropylene-poly(ethylene brassylate) block and graft copolymers and a polypropylene-polycaprolactone graft copolymer as compatibilizers for polypropylene-rich polypropylene/bisphenol A polycarbonate (PP/PC, 80/20 wt/wt) blends was elucidated. The copolymers were synthesized either by metal-catalyzed ring-opening polymerization or transesterification of a presynthesized polyester, initiated by hydroxyl-functionalized PPs, which themselves were obtained by catalytic routes or reactive extrusion, respectively. Spectroscopic fingerprints of the copolymers from liquid-state nuclear magnetic resonance (NMR) in combination with scanning electron microscopy (SEM), transmission electron microscopy (TEM), atomic force microscopy (AFM), dynamic mechanical thermal analysis (DMTA), and rheology analyses of the blends indicated that the compatibilizers spontaneously organize at the interface of the two immiscible polymers leading to the formation of uniform, stable, nanophase morphologies. The effect of the compatibilizers on the performance of the PP/PC blends was evaluated, and well-compatibilized PP/PC blends showed improved melt strength and strain hardening when compared to pure PP. This was verified by the successful foam extrusion using isobutane as a blowing agent of well-compatibilized PP/PC blends to low-density PP-based foams, for which normally long-chain branched PP is required.

KEYWORDS: *polyolefin, polycarbonate, polyester, copolymer, compatibilizer, blend, foam*

INTRODUCTION

Blending of polymers provides the opportunity to combine advantageous properties of different polymers in a new material. Blends of different polyolefins (POEs) have been used to optimize, for example, the impact/stiffness/adhesion properties of the product.[1] Blends consisting of polyolefins and engineering plastics have attracted attention, e.g., for their potential to obtain polyolefin-based products with improved adhesion to other polar materials as well as engineering plastics with, for example, improved chemical resistance.[2−15] Polypropylene (PP)–based blends containing high-density polyethylene (HDPE), low-density polyethylene (LDPE), POE, or engineering plastics like polystyrene (PS) have also been used to improve the foamability of PP.[16−18] Foaming of conventional PP is challenging due to its relatively low crystallization rate and low melt strength.[19−23] The polymer blends used to improve the foamability typically contain a linear polymer as the main component (i.e., PP) and a long-chain branched polymer to improve the overall melt strength of the blend. Blends consisting of exclusively linear polymers have only been used in injection molding or pressure-quenching foaming processes, which is less demanding but yields significantly more dense foams in comparison to extrusion foaming. The comparison of ethylene-styrene diblock copolymer and comb-like copolymers as compatibilizers of linear low-density polyethylene (LLDPE)/PS blends and their application as foam precursors was thoroughly studied by Wang.[24] The used comb-like copolymers significantly improved the CO_2 foaming capacity of the investigated blends. Other studies related to PP–based blends describe, for example, microcellular polypropylene/thermoplastic polyurethane[25] and polypropylene/acrylonitrile butadiene styrene (ABS) compositions.[26] Interesting work was recently reported by Su et al.[27] who used PP/ polycarbonate (PC) blend, compatibilized by a commercially available PP–co–maleic anhydride, PP–co–glycidyl methacrylate, and ethylene–acrylic ester–glycidyl methacrylate, to produce foams via injection molding. The authors reported that the PC enhances the cell formation of neat PP. However, the density of the obtained foams was rather high as a result of the injection foaming process applied.

As part of our interest in obtaining stable blends of polyolefins with engineering plastics, in the current study, we investigated the efficiency of various compatibilizers for PP/PC blends. We argued that foaming of the compatibilized PP/PC blends could be a valuable way to evaluate the efficiency of the applied

compatibilizer, as proper interaction between the different phases should lead to an increase in melt strength. Additionally, PC reveals high sound transmission loss, making the investigated foamed blend relevant for automotive applications. As injection molding foaming only results in a density reduction of typically <20 %, the measurable effect is expected to be rather limited. Hence, as an ultimate check of the well-behaving of the compatibilized PP/PC blends, a PP/PC blend stabilized with the best-performing compatibilizer was subjected to extrusion foaming tests with the aim to produce PP/PC foams with densities <50 kg/m^3. The advantage of our proposed approach is that a high melt strength composition should be formed by simply compounding readily available components like PP and PC (in an 80/20 wt/wt ratio) plus a small amount of the compatibilizer (5 wt %). Normally, high melt strength PP materials require longchain branched PP, which is challenging and rather costly to produce.

RESULTS AND DISCUSSION

Preparation and characterization of compatibilizers and blends.

Here, we describe the comparison of the compatibilizing effect of polypropylene–*block*–poly(ethylene brassylate) (PP–*block*–PEB), PP–*graft*–PEB, and PP–*graft*–polycaprolactone (PCL) copolymers (Table 1) on PP/PC blends. The compatibilizers were either produced by catalytic ring-opening polymerization (cROP) or transesterification starting from OH–functionalized polypropylene macroinitiators (Tables S1 and S2 and Figures S1 – S6).[13]

Table 1. Molecular Characterization of PP–*block*–PEB, PP–*graft*–PEB, and PP–*graft*–PCL copolymers

Entry	Sample	M_n [kg/mol][a]	M_w [kg/mol][a]	$Đ$ [a]
1	PP(**1**)–*block*–PEB$_{TE}$	18.1	36.5	2.0
2	PP(**2**)–*graft*–PEB$_{TE}$	30.3	73.4	2.4
3	PP(**4**)–*graft*–PEB$_{TE}$	29.7	190.8	6.4
4	PP(**3**)–*graft*–PCL$_{ROP}$	13.4	43.6	3.3
5	PP(**4**)–*graft*–PCL$_{TE}$	37.4	179.5	4.8

[a] Molecular weight and polydispersity determined by high-temperature size-exclusion chromatography (HT-SEC) in 1,2-dichlorobenzene at 150 °C.

Transesterification of presynthesized PEB or PCL proved to be an effective, solvent-free and therefore environmentally friendly method to produce the corresponding block- and graft copolymers for all types of OH–functionalized PPs. As a benchmark,[14] PP–*graft*–PCL was also produced by cROP. Thus, the obtained PP–PEB and PP–PCL block/graft copolymers were tested as compatibilizers for PP/PC blends, and their performance was verified by scanning electron microscopy (SEM), transmission electron microscopy (TEM), and atomic force microscopy (AFM) techniques. Given the fact that PP–based block/graft copolymers reveal different topologies and different polydispersity indices, it was expected that the morphology of the PP/PC blends might be significantly affected by investigated compatibilizers. Subsequently, a selected sample of the thus prepared compatibilized PP/PC blend composition was submitted for foam preparation.

TEM and SEM images (Figures 1, S7, and S8) show that PP(4)–*graft*–PEB_{TE}, PP(4)–*graft*–PCL_{TE} (copolymers produced by transesterification), and PP(3)–*graft*–PCL_{ROP} (reference copolymer produced by cROP) provided more favorable blend morphologies than PP(1)–*block*–PEB_{TE} and PP(2)–*graft*–PEB_{TE} (see Table 1 for codes). The PC dispersed phase droplet size is clearly reduced to 352, 208, and 297 nm upon using PP(4)–*graft*–PEB_{TE} and PP(3)–*graft*–PCL_{ROP} and PP(4)–*graft*–PCL_{TE} as the compatibilizers, respectively (Figures 1 and S8). With a similar PC domain size of 500 nm as observed for the uncompatibilized blend, the PP/PC blend containing PP(1)–*block*–PEB_{TE} copolymer clearly does not show any compatibilizing effect. For PP(2)–*graft*–PEB_{TE}, the compatibilizing effect is not very convincing either. SEM micrographs of freeze fractured samples (Figure S7) exhibit that most of the compatibilizers improved the adhesion between isotactic polypropylene and polycarbonate, as the polycarbonate dispersed phase is broken rather than pulled out of the polypropylene matrix during the fracturing. The SEM results are in line with TEM analysis (Figure 1), revealing that the same trends in the dispersed phase size diameter decrease for the compatibilized blends.

The rather poor compatibilizing effect of PP(1)–*block*–PEB_{TE} and PP(2)–*graft*–PEB_{TE} might be attributed to the relatively low molecular weight of PP blocks in these copolymers. As presented in Table S1 (entries 1 and 2), M_n values of the functionalized PP used in the copolymerization with PEB are around 14 and 12 kg/mol for PP–OH (1) and PP–co–C_{11}OH (2), respectively. It is likely that the PP block lengths of these two particular copolymers are insufficient to effectively

interact with the PP matrix of the PP/PC blends. The graft copolymers PP(4)–*graft*–PEB_{TE} and PP(4)–*graft*–PCL_{TE} (Table 1, entries 3 and 5), also prepared by transesterification, show a remarkably good compatibilizing effect. Here, the number average molecular weight of PP blocks in copolymers exceeded 28 kg/mol. However, the most significant changes in the PP/PC blend morphology were observed upon adding PP(3)–*graft*–PCL_{ROP} (Table 1, entry 4) as the compatibilizer. This can be explained by the synergetic effect of the high molecular weight of the PP macroinitiator (PP–*co*–$C_{11}OH$ (3), M_n above 25 kg/mol) and a higher polyester graft density in the copolymer. Coates and co–workers1 reported that the interfacial activity of multiblock copolymers in polyolefin–based blends is higher than that of diblock copolymers. The better performance of grafted products having >1.5 polyester grafts per PP chain compared to the diblock copolymer agrees with that.

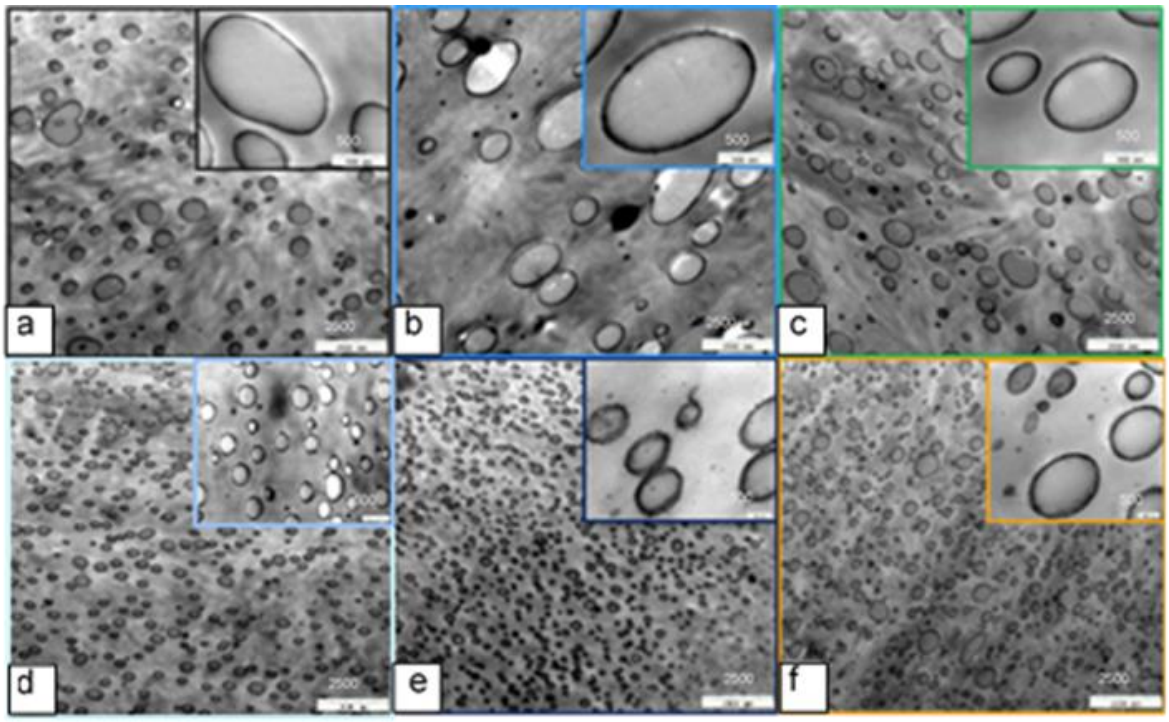

Figure 1. TEM micrographs of an uncompatibilized PP/PC blend (a) and a PP/PC blend compatibilized by PP(1)–*block*–PEB_{TE} (b), PP(2)–*graft*–PEB_{TE} (c), PP(4)–*graft*–PEB_{TE} (d), PP(3)–*graft*–PCL_{ROP} (e), and PP(4)–*graft*–PCL_{TE} (f). The scale bars on the images are 2500 and 500 nm.

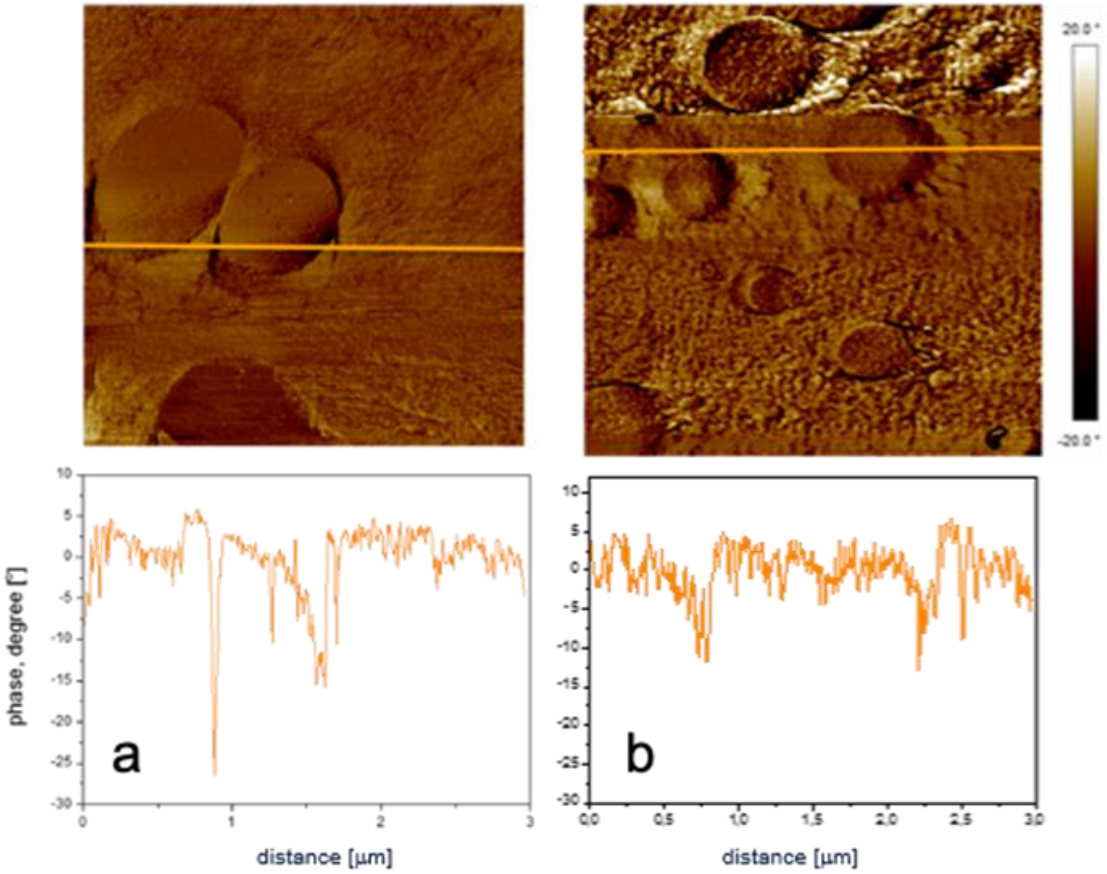

Figure 2. AFM phase images (3 *µ*m × 3 *µ*m) of the PP/PC blend (a) and PP/PC blend compatibilized by PP(3)–*graft*–PCL_{ROP} (b).

Unfortunately, a detailed evaluation of how the overall molecular weight of the corresponding PP–*block/graft*–PEB and PP–*graft*–PCL affects their performance as compatibilizers is challenged by the amphiphilic character of these block/graft copolymers, which dramatically complicates their analysis by SEC even when using multiple detection.[28] The solubility and radius of gyration in size–exclusion chromatography differs significantly from chain-end hydroxyl-functionalized (1) to randomly hydroxyl-functionalized (2−4) polypropylenes and the corresponding block and graft copolymers (Table 1). This effect is emphasized for an amphiphilic block or graft copolymers where the polar branches and their end groups can strongly interact with each other. To verify this discrepancy, the molecular weight of PP(3)–*graft*–PCL_{ROP} synthesized by ring-opening polymerization was calculated based on 1H nuclear magnetic resonance (NMR) spectra integrals (for the details, please see Figure S4). The calculated average M_n of the copolymer is 31.7 kg/mol based on NMR data and is significantly higher than the value obtained by SEC (13.4 kg/mol).

Unfortunately, the NMR spectra of the copolymers prepared by transesterification (Figure S4), the main synthetic approach used in this study, cannot be used for molecular weight estimations. The reason is that transesterification products consist not only of copolymers but also of polycaprolactone (PCL) being a side product of the transesterification process. Further proof that the molecular weights of the amphiphilic block and graft copolymers is incorrect is given by the fact that the molecular weight of PP–*graft*–PCLs (e.g., Table 1, entry 4) obtained by SEC is lower than that of the corresponding hydroxyl-functionalized polypropylene (3), which should not be possible. Hydrolysis of the graft copolymer yielded the hydroxyl-functionalized polypropylene (3), which showed the same molecular weight as before, indicating that no degradation had occurred. Not unexpectedly, attempts to determine the presence of long chain branches in the synthesized copolymers also failed. In contrast to a reference LCBPP sample, the Mark−Houwink plots (Figure S6) did not show any clear evidences of long chain branches in the synthesized copolymers, and the block/graft copolymers were behaving more like a linear PP reference sample. On the other hand, the Mark−Houwink plots of amphiphilic block/graft copolymers showed a deviation from the theoretical linear correlation in the low-molecular-weight region, whereas the hydroxyl-functionalized polypropylene precursors of the block/graft copolymers perfectly followed the linear correlation. Hence, SEC of amphiphilic block/graft copolymers provides at most qualitative information; quantitative conclusions cannot be drawn.

To verify the morphology and to study the interaction between the polypropylene and polycarbonate phases, AFM imaging in tapping mode was performed on both the uncompatibilized PP/PC reference blend and compatibilized PP/PC blends (Figures 2, S9, and S10). While AFM topography images allow investigation of the blends' morphological details, phase images give insight into the interactions of the component phases.[29] AFM images of the uncompatibilized blend show a strong agglomeration of the polycarbonate dispersed phase. These findings are in line with the TEM analysis (vide supra), showing both large average droplet size and a nonuniform size distribution of the polycarbonate phase. On the other hand, both phase images and phase graphs of compatibilized compositions demonstrate a reduced average domain size and an enhanced adhesion between polypropylene and polycarbonate in the presence of certain compatibilizers. This is visible by the absence of cracks between the polypropylene matrix and polycarbonate domains,

and the effect is the strongest for PP(4)–*graft*–PEB$_{TE}$, PP(4)–*graft*–PCL$_{TE}$ and PP(3)–*graft*–PCL$_{ROP}$. Here, the decrease of the polycarbonate domain size, their uniform distribution as well as the enhanced adhesion between the phases are in line with the TEM analysis of the compatibilized blends described above. The dark interphase layer between the polypropylene matrix and the polycarbonate dispersed phase might originate from softer PEB/PCL–based copolymers that are predominantly localized in these interface regions. Besides, the interphase, measured at the borders of the blend components, is significantly improved compared to that of the uncompatibilized reference sample (Figures 2 and S10). The effect of PEB and PCL segments influencing the polycarbonate dispersed phase in the blends is well demonstrated by the change in the roughness of the polycarbonate droplet surface. The presence of certain topographical patterns with the thickness of several nanometers might result from local fluctuations of the dispersed phase composition. This can be explained by a partial miscibility of PEB and PCL segments of the compatibilizers with PC.

The influence of the compatibilizers on the thermal properties of the corresponding PP/PC blends was measured by differential scanning calorimetry (DSC) analysis (Figure S11 and Table S3). The neat PC displays a T_g at 150 °C, while T_m and T_c for the neat PP were 165 and 108 °C, respectively. In the uncompatibilized blend, the melting point of polypropylene drops somewhat whereas the crystallization point increases. The nucleation rate of polymer crystals is strongly related to the number and nature of heterogeneities,[5,6] and the presence of polycarbonate droplets obviously has an effect. Clearly, adding compatibilizers not only increases the interaction between the polypropylene and polycarbonate phases but increases the interfacial surface area as well. Subsequently, the PP–*block/graft*–polyester copolymers themselves can also act as nucleating agents generating heterogeneous nucleation. Consequently, polypropylene melting points in the compatibilized PP/PC blends drops 5−7 °C, whereas the crystallization temperature increased by 4−10 °C. The nucleating effect of these components is especially visible for the PP/PC sample compatibilized by PP(3)–*graft*–PCL$_{ROP}$, where the T_c of PP was raised from 108 to 118.5 °C (Table S3, entry 6). The morphology of this particular blend is correspondingly improved in comparison to the uncompatibilized reference sample (see TEM and AFM imaging Figures 1 and S8−S10). The presence of semicrystalline compatibilizers in the samples

complicates the discussion of the ΔH_m and ΔH_c of the compositions. Nevertheless, ΔH values recorded for all compositions containing only 5 wt % of the compatibilizer and 80 wt % of PP are in line with the expectations as they are ca. 20% lower than the PP reference. The T_m decrease of PP can be explained by the lamella thickness and size decrease upon blends' formation with PC. Most likely, the presence of amorphous PC in the blends causes defective, lower crystallites.[30]

Glass transition temperatures of PP, PC and their blends were investigated by dynamic mechanical thermal analysis (DMTA) (Figure S12 and Table S4). Compared to the reference PP, the T_g's of the PP matrix of well-compatibilized blends are slightly higher, whereas the T_g of the PC was significantly lower. The increase of the T_g of PP is in line with the presence of nanometer-size hard PC domains that restrict motions of the amorphous fraction of the PP matrix, which can be attributed to the improved interaction of both phases. Conversely, the drop in PC T_g from 150 °C for pure PC to 142 °C for the PP(4)–*graft*–PEB_{TE} compatibilized blend can be ascribed to an enhanced interaction between the two phases as well as to a plasticizing effect of the PEB block present in the compatibilizers. The effect is the strongest for the blend compatibilized by the reference PP(3)–*graft*–PCL_{ROP}, as the T_g value of PC domains decreases to 104.8 °C.

Static mechanical properties of polypropylene, polycarbonate, and polymer blends were investigated by tensile tests carried out at room temperature. While polypropylene samples show plastic deformation typical for a ductile material, polycarbonate fractures already at lower elongation (Figure S13 and Table 2). The incorporation of 20 wt % of polycarbonate into the polypropylene matrix did not lead to a significant increase in the yield stress of the material regardless of the presence of a compatibilizer.

Table 4. Mechanical properties of PP, PC and PP/PC blends.

composition	compatibilizer	σ_{max} [MPa]	$\varepsilon_{at\ break}$ [%]
PP	-	39.1 ± 0.3	593.7 ± 26.6
PC	-	64.6 ± 0.4	211.2 ± 12.1
PP/PC	-	41.9 ± 0.5	204.5 ± 10.4
PP/PC	PP(1)–*block*–PEB_{TE}	42.2 ± 0.5	173.5 ± 12.3
PP/PC	PP(2)–*graft*–PEB_{TE}	40.7 ± 0.3	181.9 ± 16.2
PP/PC	PP(4)–*graft*–PEB_{TE}	38.9 ± 0.7	147.3 ± 11.6
PP/PC	PP(3)–*graft*–PCL_{ROP}	42.0 ± 0.8	328.9 ± 22.4
PP/PC	PP(4)–*graft*–PCL_{TE}	37.7 ± 0.7	159.2 ± 19.7

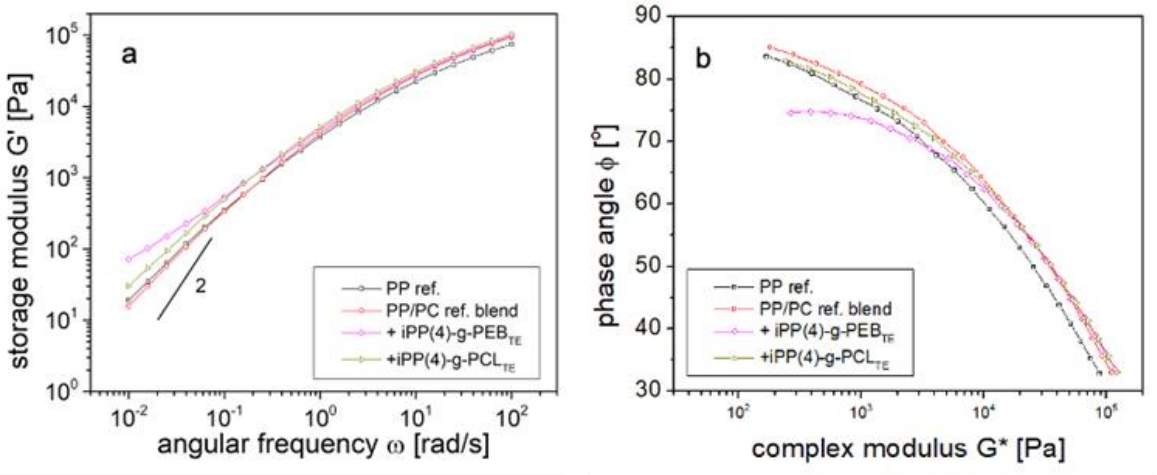

Figure 4. Storage modulus vs angular frequency (a) and van Gurp Palmen plots (b) measured at 190 °C for the PP reference, PP/PC uncompatibilized blend and blends compatibilized with *i*PP(4)–*graft*–PEB_{TE} and *i*PP(4)–*graft*–PCL_{TE}. The terminal relaxation slope for the storage modulus of 2 is indicated in the plot.

A plausible explanation of such mechanical behavior is that polypropylene-based blends upon deformation might change from shear yielding plastic deformation to cavitation followed even by crazing, reducing the ductility of polypropylene. Alternatively, the difference in crystallization degree as well as in chemical composition between the skin and core of the PP/PC injection molded samples might affect their mechanical performance.[31,32] To support these explanations, the measurements of the complex viscosity of PP and PC as a function of frequency were performed (Figure S14). Clearly, the complex viscosity (η*) of PC is higher than that of PP. The differences in η* are especially pronounced at higher

frequencies where a significant shear thinning behavior of PP is visible, which influences the blend's morphology of the skin and the core of the samples. On the other hand, these differences in η* will provide beneficial properties during the foam formation process. It is worth mentioning that the PP/PC blend compatibilized by PP(3)–*graft*–PCL_{ROP} showed an elongation at a break of above 300% and thus the highest ductility. These results are in line with DMTA analysis where the strongest plasticizing effect, affecting T_g of PC dispersed phase, was found for the same compatibilizer.

Melt rheology experiments were performed on the polypropylene reference sample, the uncompatibilized PP/PC blend, and all of the compatibilized PP/PC blends (Figures 3 and S15). The experiments were performed at 190, 210, and 230 °C. The time evolutions of the storage modulus normalized to the value of the storage modulus at the beginning of the measurements (G′/G′0) are reported in Figure S15 for the three different measuring temperatures used. As expected for thermally stable systems, the storage modulus of the polypropylene reference and of the uncompatibilized PP/PC blend stays constant for all of the monitored time interval (4500 s) at 190 °C. At higher temperatures (210 and 230 °C), a slight decrease of the storage modulus can be observed for both the polypropylene reference and the uncompatibilized PP/PC blend after around 3000 s. Since the magnitude of the decrease is fairly comparable for both the polypropylene and the uncompatibilized blend PP/PC, the decrease in modulus could be attributed to thermal degradation of the PP matrix, resulting in a decrease of molecular weight and a consequent lower elastic component at the relaxation time scale corresponding to the experimental frequency used (0.5 rad/s). Differently from the reference material and rather surprisingly, blends compatibilized by PP(1)–*block*–PEB_{TE}, PP(2)–*graft*–PEB_{TE}, and PP(4)–*graft*–PCL_{ROP} show a steady increase of the storage modulus at 190 °C during the entire investigated time interval. At the same temperature, blends compatibilized with PP(4)–*graft*–PEB_{TE} and PP(4)–*graft*–PCL_{TE} show a slight increase of the storage during the 20 min prior to frequency sweep measurements and seem to reach a plateau value within 1000 s. At 210 °C, the same increasing trend for the storage modulus is observed for blends compatibilized with PP(1)–*block*–PEB_{TE}, PP(2)–*graft*–PEB_{TE}, PP(4)–*graft*–PCL_{ROP}, and PP(4)–*graft*–PEB_{TE}, whereas the PP(4)–*graft*–PCL_{TE} compatibilized blend shows a slight decrease similarly to the reference blend. At 230 °C, all of the

compatibilized blends analyzed show a small increase in modulus followed by a decrease comparable to the one observed for the reference materials, with the exception of the blend compatibilized with PP(1)–*block*–PEB_{TE}, which still shows a steady increase. At the current stage, the observed increase in modulus cannot be unambiguously correlated with a single cause and several hypotheses can be formulated. We remind the reader that since time sweep experiments were performed at a constant frequency of 0.5 rad/s, the measured storage modulus is the only representative of a certain time scale.

Incompatible polymer blends are known to show pronounced elastic properties, very long relaxation times, and failure of the TTS.[33–35] A typical feature is the appearance of extra relaxation mechanisms in the low-frequency region, related to the relaxation of the interfaces and to the relaxation of the shape of the droplets. Typically, a plateau of the storage modulus is found between these two relaxation mechanisms and the level and the time scale (frequency range) of the plateau is dependent on interfacial energy, droplet size, and zero-shear viscosity of the dispersed phase. This rheological behavior can be described quantitatively by the emulsion model proposed by Palierne.[36]

An increase in the zero-shear viscosity of the polycarbonate dispersed phase would translate in a decrease in the plateau modulus and a shift to lower frequencies due to an increase in the droplet and interface relaxation time. Based on this, we can rule out that the observed increase in modulus is due to crosslinking or chain extension of the polycarbonate phase (which would cause an increase in zero-shear viscosity). According to Palierne's model, an increase of the storage modulus can be either related to an increase of the interfacial tension between the phases or to a decrease in droplet radius.

Based on the time evolutions of the storage modulus, we analyzed only the frequency sweeps performed at 190 °C for the polypropylene reference, uncompatibilized PP/PC blend, and blends compatibilized with PP(4)–*graft*–PEB_{TE} and PP(4)–*graft*–PCL_{TE} since those showed a constant value of the storage modulus before, during, and after the frequency sweeps were performed. The storage modulus dependency from the frequency and the van Gurp−Palmen plots (phase angle φ vs complex modulus G*) are shown in Figure 3b. It appears evident that the uncompatibilized blend does not show any clear interface/droplet relaxation mechanism in the investigated frequency range, probably due to the big dimension

of the droplets of the polycarbonate phase, whereas the compatibilized blends show an increased elasticity in the low-frequency range, which could be correlated with smaller droplet sizes observed in microscopy images.

Foaming Experiments.

We argued that strong interactions between the different phases of a polymer blend, induced by the presence of an effective compatibilizer, should lead to an increase in the melt strength of the material. As melt strength is crucial for a material to foam, foaming the compatibilized PP/PC blends could be a valuable way to evaluate the efficiency of the applied compatibilizer. To illustrate the melt strength of a PP/PC blend, the sample compatibilized by PP(4)–*graft*–PCL_{TE} (Table 1, entry 5) was submitted for foaming and the performance was compared with the uncompatibilized PP/PC blend as well as long-chain branched polypropylene (LCBPP). This particular compatibilizer was used based on its good performance and easily scalable synthesis via transesterification using the extrusion process, which is relevant from a commercial point of view. As the bubble growth during the foaming process is dominated by biaxial flow, a rapid screening of the ability of a material to foam can be performed by observing the rheological behavior in uniaxial elongational flow experiments, as reported by Naguib.[37] Experiments under various Hencky strain rates ranging from 0.05 till 0.5/s were performed and presented in Figure 4. Contrary to the uncompatibilized PP/PC blend, the compatibilized PP/PC composition revealed a sudden increase of elongational viscosity, confirming the strain-hardening property of the melt, as required for proper foaming. This observation is certainly attributed to the uniformly distributed polycarbonate phase, strongly interacting with the matrix via the compatibilizer and bearing a prominent hardening property to polypropylene. The increase of PP/PC blends' elongational viscosity depends on the Hencky strain rate where, with an increasing Hencky strain rate from 0.05 to 0.5 s^{-1}, the strain hardening of the sample becomes more prominent. The enhanced melt strength of compatibilized PP/PC blends clearly demonstrates that these materials are suitable candidates for foams preparation by extrusion.

As proven, foams with densities below 40 kg/m^3 could be obtained at a broad temperature range, namely, 140−170 °C, being nearly as broad as the range of LCBPP (Daploy) commercialized for foam preparation (Figure S16). Conversely,

neat PP could only be foamed to the desired low density within the narrow temperature range of 140−145 °C and at 30 MPa saturation pressure of the blowing agent, which is unpractical. It is worth underlining that the foamed compatibilized PP/PC blend afforded an expansion ratio of over 30, while polypropylene only at the lowest foaming temperature succeeded a 25-fold expansion ratio.

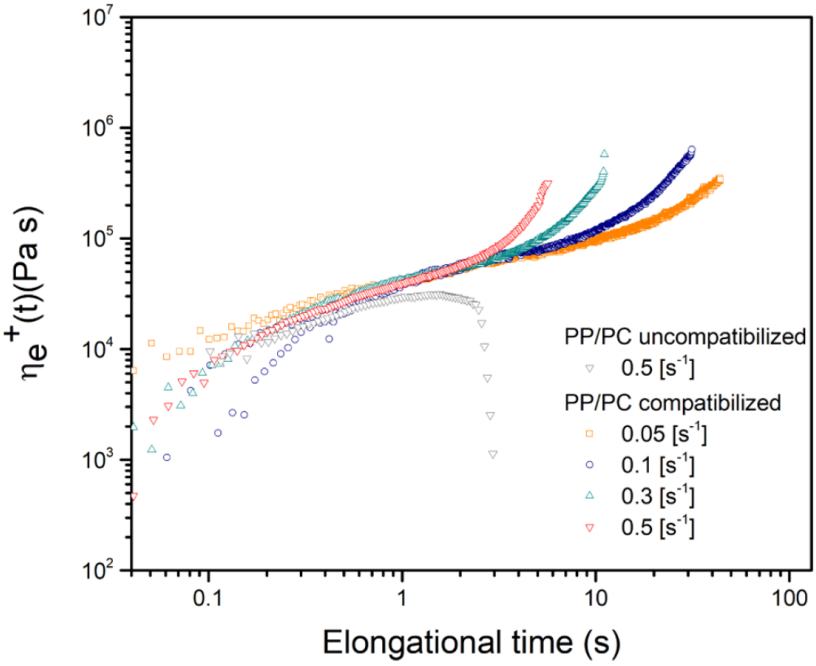

Figure 4. Elongational viscosity of PP/PC blends compatibilized by PP(4)–*graft*–PCL_{TE} (Table 1, entry 5) and an uncompatibilized PP/PC blend reference as a function of elongational time tested at 160 °C under various Hencky strain rates.

The obtained foams have a well-defined and uniform pore structure consisting of spherical close cells with an average diameter of around 100 μm, as was confirmed by SEM analysis (Figure 5). The foams retain as well-developed threedimensional (3D) cell structures with the walls of the close cells on the backside being clearly recognized (Figure 5b). Additionally, technical SEM images, recorded using tabletop SEM apparatus for the foams produced at various temperatures, are presented in Figure S17.

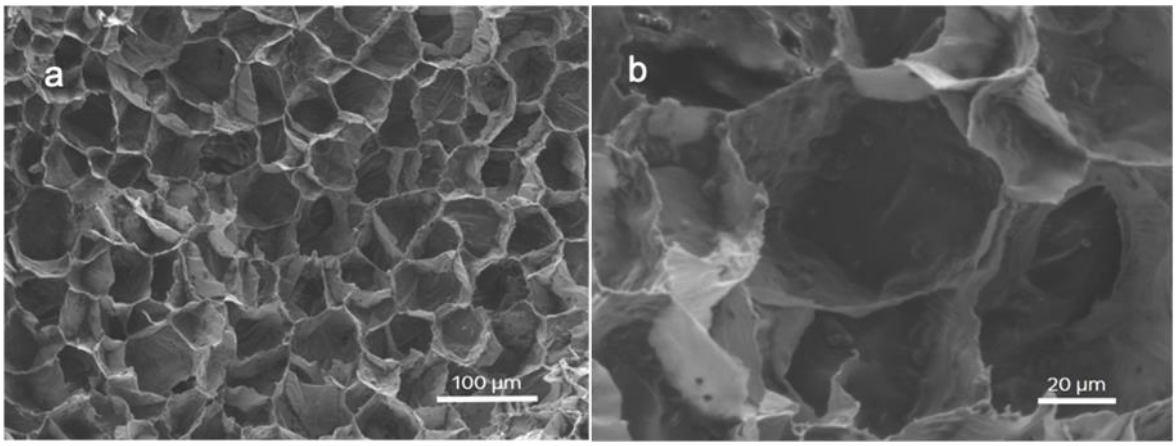

Figure 5. SEM micrographs of the foam prepared of the PP/PC blend compatibilized by PP(4)–*graft*–PCL_{TE} ((a) 200× and (b) 750×).

CONCLUSIONS

In summary, PP/PC blends compatibilized with several PP–*block/graft*–PEB and PP–*graft*–PCL copolymers were obtained and compared with the PP/PC uncompatibilized blends. The SEM, TEM, and AFM results demonstrated that among the investigated copolymers the application of PP–*graft*–PEB_{TE} and PP–*graft*–$PCL_{TE/ROP}$ with an average of >1.5 grafts per chain and a PP segment with an M_n of ≥25 kg/mol leads to a significantly enhanced adhesion between the polycarbonate and polypropylene phases and the polycarbonate domain size reduction from ≥500 to ≤200 nm, making the investigated blends suitable candidates for the preparation of lightweight materials. The easily scalable transesterification of presynthesized PEB or PCL, using randomly OH-functionalized polypropylene as macroinitiator, produces graft copolymers, which behave just as good as compatibilizers as the PP–*graft*–PCL_{ROP} produced by cROP. Hence, the grafting onto approach by transesterification forms a very attractive alternative to cROP to yield the desired block and graft copolymers, as this process can be performed in an extruder under solvent-free conditions and is therefore easily scalable.

The morphologies of the samples are in line with their thermomechanical properties: in well-compatibilized blends, the ΔT_g's of the blend components drop, while the stiffness at elevated temperature is considerably higher than for both neat polypropylene and uncompatibilized PP/PC blends. The melt rheology experiments revealed that the uncompatibilized blend does not show any clear interface/droplet relaxation mechanism in the investigated frequency range, probably due to the big

dimension of the droplets of the polycarbonate phase, whereas the compatibilized blends show a clear increased elasticity in the low-frequency range, related to the smaller droplet sizes of the polycarbonate. The PP/PC blends compatibilized with PP(4)–*graft*–PCL_{TE} displayed a clear increase in elongational viscosity as was proven by foaming experiments. Extrusion foaming experiments of a PP(4)–*graft*–PCL_{TE} compatibilized PP/PC blend revealed a density below 40 kg/m^3, closed cells structure with controlled cell dimensions and morphology. This work demonstrates that using a properly compatibilized PP/PC blend affords an interesting cost-efficient and easily scalable way to produce low-density foams via the extrusion process.

REFERENCES

(1) Eagan, J. M.; Xu, J.; Girolamo, R. D.; Thurber, C. M.; Macosko, C. W.; LaPointe, A. M.; Bates, F. S.; Coates, G. W. Combining polyethylene and polypropylene: Enhanced performance with PE/iPP multiblock polymers. *Science* **2017**, 355, 814−816.

(2) Lu, B.; Chung, T. C. New maleic anhydride modified PP copolymers with block structure: synthesis and application in PP/polyamide reactive blends. *Macromolecules* **1999**, 32, 2525−2533.

(3) Inoue, Y.; Matsugi, T.; Kashiwa, N.; Matyjaszewski, K. Graft copolymers from linear polyethylene via Atom Transfer Radical Polymerization. *Macromolecules* **2004**, 37, 3651−3658.

(4) Xu, Y.; Thurber, C. M.; Lodge, T. P.; Hillmyer, M. A. Synthesis and remarkable efficiency of model polyethylene-graft-poly(methyl methacrylate) copolymers as compatibilizers in polyethylene/poly-(methyl methacrylate) blends. *Macromolecules* **2012**, 45, 9604−9610.

(5) Schellekens, M. A. J.; Klumperman, B. Synthesis of polyolefin block and graft copolymers. *J. Macromol. Sci., Part C: Polym. Rev.* **2000**, 40, 167−192.

(6) Wang, Y. B.; Hillmyer, M. A. Polyethylene-poly(L-lactide) diblock copolymers: Synthesis and compatibilization of poly(Llactide)/ polyethylene blends. *J. Polym. Sci., Part A: Polym. Chem.* **2001**, 39, 2755−2766.

(7) Pepels, M. P. F.; Hofman, W. P.; Kleijnen, R.; Spoelstra, A. B.; Koning, C. E.; Goossens, H.; Duchateau, R. Block copolymers of PE-like poly(pentadecalactone) and poly(L-lactide): Synthesis, properties, and compatibilization of polyethylene/poly(L-lactide) blends. *Macromolecules* **2015**, 48, 6909−6921.

(8) Ring, J. O.; Thomann, R.; Mülhaupt, R.; Raquez, J.-M.; Degée, P.; Dubois, P. Controlled synthesis and characterization of poly-[ethylene-block-(L,L-lactide)]s by combining catalytic ethylene oligomerization with “coordination-insertion” ring-opening polymerization. *Macromol. Chem. Phys.* **2007**, 208, 896−902.

(9) Chung, T. C. Synthesis of functional polyolefin copolymers with graft and block structures. *Prog. Polym. Sci.* **2002**, 27, 39−85.

(10) Ho, C. H.; Wang, C. H.; Lin, C. I.; Lee, Y. D. Synthesis and characterization of TPO-PLA copolymer and its behavior as compatibiliser for PLA/TPO blends. *Polymer* **2008**, 49, 3902−3910.

(11) Kashiwa, N.; Matsugi, T.; Kojoh, S.; Kaneko, H.; Kawahara, N.; et al. Functionalization of polyethylene based on metallocene catalysis and its application to syntheses of new graft copolymers possessing polar polymer segments. *J. Polym. Sci., Part A: Polym. Chem.* **2003**, 41, 3657−3666.

(12) Han, C. J.; Lee, M. S.; Byun, D. J.; Kin, S. Y. Synthesis of hydroxyl-terminated polyethylene via controlled chain transfer reaction and poly(ethylene-b-caprolactone) block copolymer. *Macromolecules* **2002**, 35, 8923−8925.

(13) Rutkowski, S.; Zych, A.; Przybysz, M.; Bouyahyi, M.; Sowinski, P.; Koevoets, R.; Haponiuk, J.; Graf, R.; Hansen, M. R.; Jasinska-Walc, L.; Duchateau, R. Toward Polyethylene−Polyester Block and Graft Copolymers with Tunable Polarity. *Macromolecules* **2017**, 50, 107−122.

(14) Chung, T. C.; Rhubright, D. Polypropylene-graft-polycaprolactone: synthesis and application in polymer blends. *Macromolecules* **1994**, 27, 1313−1319.

(15) Zhihui, Y.; Yajie, Z.; Xiaomin, Z.; Jinghua, Y. Effect of the compatibilizer PP-g-GMA on morphology and mechanical properties of PP/PC blends. *Polymer* **1998**, 39, 547−551.

(16) Lee, P. C.; Wang, J.; Park, C. B. Extruded open-cell foams using two semicrystalline polymers with different crystallization temperatures. *Ind. Eng. Chem. Res.* **2006**, 45, 175−181.

(17) Gunkel, F.; Sporrer, G. T.; et al. Understanding melt rheology and foamability of polypropylene-based TPO blends. *J. Cell. Plast.* **2008**, 44, 307−325.

(18) Zhai, W.; Wang, H.; Yu, J.; Dong, J.; He, J. Foaming behavior of polypropylene/polystyrene blends enhanced by improved interfacial compatibility. *J. Polym. Sci., Part B: Polym. Phys.* **2008**, 46, 1641− 1651.

(19) Yu, C.; Wang, B.; Wu, Y.; Xie, C.; Yu, S.; Chen, S.; Li, W. Evaluating the foamability of polypropylene with nitrogen as the blowing agent. *Polym. Test.* **2011**, 30, 887−892.

(20) Zhai, W.; Kuboki, T.; Wang, L.; Park, C. B.; Lee, E. K.; Naguib, H. E. Cell Structure Evolution and the Crystallization Behavior of Polypropylene/Clay Nanocomposites Foams Blown in Continuous Extrusion. *Ind. Eng. Chem. Res.* **2010**, 49, 9834−9845.

(21) Zhai, W.; Wang, H.; Yu, J.; Dong, J.; He, J. Cell coalescence suppressed by crosslinking structure in polypropylene microcellular foaming. *Polym. Eng. Sci.* **2008**, 48, 1312−1321.

(22) Zheng, W.; Lee, Y.; Park, C. Use of Nanoparticles for Improving the Foaming Behaviors of Linear PP. *J. Appl. Polym. Sci.* **2010**, 117, 2972−2979.

(23) Weingart, N.; Raps, D.; Lu, M.; Ender, L.; Altstadt, V. Comparison of the foamability of linear and long-chain branched polypropylene-the legend of strain hardening as a requirement for good foamability. *Polymers* **2020**, 12, 725−746.

(24) Wang, Y.; Zhang, S.; Jiang, H.; Lin, Y.; Xing, H.; Tang, T. Insight on compatibilization of LLDPE/PS blends from morphology, interfacial state, mechanical properties and melt properties: Comb-like copolymer vs diblock copolymer. *Polymer* **2021**, 218, No. 123540.

(25) Wang, J.; Li, J.; Li, H.; Zhou, H. Thermoplastic polyurethane (TPU) modifier to develop bimodal cell structure in polypropylene/TPU microcellular foam in presence of supercritical CO_2. *J. Vinyl Addit. Technol.* **2021**, 27, 127−136.

(26) Tan, X.-T.; Zhou, Y.-G.; Zhou, J.-J.; Dong, B.-B.; Liu, C.-T.; Xu, B.-P. Effect of acrylonitrile−butadiene−styrene terpolymer on the foaming behavior of polypropylene. *Cell. Polym*. **2019**, 38, 47−67.

(27) Su, B.; Zhou, Y.-G.; Dong, B.-B.; Yan, C. Effect of compatibility on the foaming behavior of injection molded polypropylene and polycarbonate blend parts. Polymers **2019**, 11, No. 300.

(28) Gaborieau, M.; Castignolles, P. Size-exclusion chromatography (SEC) of branched polymers and polysaccharides. *Anal. Bioanal. Chem.* **2011**, 399, 1413−1423.

(29) Yablon, D. G.; Gannepalli, A.; Proksch, R.; Killgore, J.; Hurley, D. C.; Grabowski, J.; Tsou, A. H. Quantitative viscoelastic mapping of polyolefin blends with contact resonance atomic force microscopy. *Macromolecules* **2012**, 45, 4363−4370.

(30) Rim, P. B.; Runt, J. P. Melting point depression in crystalline/ compatible polymer blends. *Macromolecules* **1984**, 17, 1520−1526.

(31) Zhihui, Y.; Yajie, Z.; Xiaomin, Z.; Jinghua, Y. Effect of the compatibilizer PP-g-GMA on morphology and mechanical properties of PP/PC blends. *Polymer* **1998**, 39, 547−551.

(32) Ghijsels, A.; Groesbeek, N.; Yip, C. W. Multiple crystallization behaviour of polypropylene/thermoplastic rubber blends and its use in assessing blends morphology. *Polymer* **1982**, 23, 1913−1916.

(33) Han, C. D. Multiphase Flow in Polymer Processing; Elsevier, **1981**.

(34) Vinckier, I.; Moldenaers, P.; Mewis, J. Relationship between rheology and morphology of model blends in steady shear flow. *J. Rheol.* **1996**, 40, 613−631.

(35) Graebling, D.; Muller, R. Rheological behavior of polydimethylsiloxane/ polyoxyethylene blends in the melt. Emulsion model of two viscoelastic liquids. *J. Rheol.* **1990**, 34, 193−206.

(36) Graebling, D.; Muller, R.; Palierne, J. F. Linear viscoelastic behavior of some incompatible polymer blends in the melt. Interpretation of data with a model of emulsion of viscoelastic liquids. *Macromolecules* **1993**, 26, 320−329.

(37) Naguib, H. E.; Park, C. B.; Panzer, U.; Reichelt, N. Strategies for achieving ultra low-density polypropylene foams. *Polym. Eng. Sci.* **2002**, 42, 1481−1492.

Supporting Information for

Preparation of Well-Compatibilized PP/PC Blends and Foams Thereof

Lidia Jasinska-Walc, Miloud Bouyahyi, Jakub Kruszynski, Agnieszka Tercjak, Artur Rozanski, Enrico M. Troisi, Yingxin Liu, Lanti Yang, Ostap Ivashkiv, Maciej Sienkiewicz, and Robbert Duchateau

ACS Applied Polymer Materials **2021** *3* (11), 5509-5516
DOI: 10.1021/acsapm.1c00813

This subchapter contains complete experimental part, description of the characterization techniques: NMR, TEM, AFM, DSC, DMTA analysis, and rheology employed in the research about compatibilization of PP/PC blends.

Additional experimental details, materials and methods

Materials. Cyclic ethylene brassylate (CEB) (95 %, Sigma-Aldrich), ε-caprolactone (CL; 97 %,Sigma-Aldrich) and benzyl alcohol (BnOH; 99 %, Merck) were dried over CaH_2 (95 %, Sigma-Aldrich) and distilled under reduced pressure. Methanol was used as received. Toluene (anhydrous, Sigma-Aldrich) and tetrahydrofuran (THF; anhydrous, Sigma-Aldrich) were purified using an MBraun-SPS-800 purification column system and were kept in glass bottle with 4-Å molecular sieves under an inert atmosphere. 10-undecen-1-ol was purchased from Sigma Aldrich, distilled and dried with 4-Å molecular sieves under an inert atmosphere. Methylaluminoxane (MAO; 30 wt. % solution in toluene) was purchased from Chemtura. Diethyl zinc (DEZ; 1.0 M solution in hexanes), triisobutylaluminum (TiBA; 1.0 M solution in hexanes), di-n-butyl magnesium ($MgBu_2$; 1.0 M solution in heptane), sodium hydride (NaH; 95 % dry solid) and 2,6-di-tert-butyl-4-methylphenol (BHT; 99 %, purum) were purchased from Sigma-Aldrich. *rac*-Me_2Si(2-Me-4-Ph-Ind)$2ZrCl_2$ was purchased from MCAT GmbH, Konstanz, Germany. Isotactic polypropylene (SABIC - PP500P, MFR = 3 g/10 min (230 °C/2.16 kg), polycarbonate (PC LEXAN™ Resin 105 MFR

= 7 g/10 min (300 °C, 1.2 kg)), tin(II) 2-ethylhexanoate (Sn(Oct)2) (92 - 100 %, Sigma-Aldrich), Irganox 1010 (antioxidant, BASF) were used as received.

Synthesis of hydroxyl-functionalized PP's. The OH-functionalized polypropylene macroinitiators have been prepared via several approaches (Table 1, Figure S1, S2). The chainend functionalized polypropylene (PPOH (1)) has been obtained by propylene polymerization under coordinative chain transfer polymerization conditions, followed by selective oxidation with oxygen and workup using acidified alcohol. Typically, the functionalization efficiency of this process is around 80 %. Randomly functionalized polypropylenes (PP–*co*–C_{11}OH (2) – PP–*co*–C_{11}OH (3)) were obtained in good yields, with tunable molecular weights and various functionality levels by copolymerization of propylene and triisobutyl aluminum-pacified 10-undecen-1-ol (Table 1). Final products contained from 1.5 to 1.8 OH-functionalized branches per 1000 C. These randomly functionalized macroinitiators (1 – 3) were subsequently used for the preparation of (1) block or (2, 3) graft copolymers. As an alternative to the catalytic processes, a reactive extrusion (REX) approach towards hydroxyl-functionalized polypropylene—involving the modification of maleic anhydride-functionalized polypropylene with ethanolamine was also applied. The PP–OH_{REX} (4) product prepared by REX contains around 1-2 hydroxy functionality per chain.

Synthesis of PP–OH (1). The polymerization reaction was carried out in a stainless steel Büchi reactor (300 mL). Prior to the polymerization, the reactor was dried in vacuo and flushed with nitrogen. Toluene (100 mL) and MAO (30 wt. % solution in toluene, 2.0 mL) were introduced into the reactor and stirred at 100 rpm for 20−30 min. TiBA (1.0 M solution in hexanes, 2.0 mL) and DEZ (1.0 M solution in hexanes, 0.5 mL), were added under a nitrogen atmosphere. The mixture was stirred for 10 min and saturated with low flow of propylene (5 bar). In a glovebox, a stock solution of rac-Me_2Si(2-Me-4-Ph-Ind)2$ZrCl_2$ (5 mg, 8 µmol) in toluene (20 mL) was prepared and the catalyst solution (4 mL, 1.6 µmol) was transferred into the reactor using an overpressure of nitrogen. The propylene pressure was maintained constant during the polymerization time (30 min). At the end of the polymerization, the propylene feed was stopped and the residual propylene was vented off. The reactor was pressurized with synthetic air (3 bar) and the polymer suspension was rigorously

stirred (600 rpm) at 60 °C for 60 min before being quenched with acidified methanol (300 mL, 2.5 wt. % of concentrated hydrochloric acid 37 wt.%), filtered and washed with demineralized water. The resulting powder (1) was dried in a vacuum oven under reduced pressure at 60 °C overnight.

Synthesis of PP–*co*–$C_{11}OH$ (2, 3). The copolymerization reaction was carried out in a stainless steel Büchi reactor (300 mL). Prior to the polymerization, the reactor was dried in vacuo and flushed with nitrogen. Toluene (100 mL) was introduced into the reactor followed by TiBA (1.0 M solution in hexanes, 5 mL) and the functionalized comonomer (10-unedecen-1-ol; 1 mL, 2.5 mmol) under a nitrogen atmosphere. The resulting solution was stirred for 15 – 20 min. Subsequently MAO (30 wt. % solution in toluene, 2.0 mL) was introduced into the reactor under nitrogen atmosphere. The solution was saturated with propylene (5 bar). In a glovebox, a stock solution of rac-Me_2Si(2-Me-4-Ph-Ind)2$ZrCl_2$ (5 mg, 8 µmol) in toluene (10 mL) was prepared and the catalyst solution (5 mL) was transferred into the reactor under a nitrogen atmosphere. The propylene pressure was maintained constant for 30 min. At the end of the reaction, the propylene feed was stopped and the residual propylene was released from the reactor. The resulting mixture was quenched in acidified methanol (300 mL, 2.5 wt. % of concentrated hydrochloric acid, 37 wt.%), filtered and washed with demineralized water. The obtained powder (2 and 3) was dried in a vacuum oven under reduced pressure at 60 °C overnight.

Synthesis of hydroxyl-functionalized PP by reactive extrusion (PP–OH_{REX} 4). PP–*g*–MAH (Exxelor: 0.43 wt.% MAH, 10.0 g, M_n = 22 kg/mol, Đ = 4.4) with antioxidant (2500 ppm) was applied into a mini-extruder chamber under nitrogen atmosphere set with three different temperature zones 160 °C, 180 °C and 190 °C, respectively. Next, ethanolamine (0.08 g, 0.44 mmol) was added through a syringe. The amount was calculated to the content of anhydride groups (molar ratio of ethanolamine:MAH was equal to 1.1:1). The mixture was processed for 60 seconds and next the mini-extruder chamber was evacuated. The OH-functionalized polypropylene (4) was purified by dissolution in xylenes at 120 °C and precipitation in cold acetone. Afterwards the product was dried in a vacuum oven for 24 h at 40 °C.

Synthesis of $Mg(BHT)_2(THF)_2$ catalyst. In the glovebox, 2,6-di-tert-butyl-4-methylphenol (BHT, 4.40 g, 20 mmol) was introduced into a Schlenk flask and dissolved in dry tetrahydrofuran (30 mL). The mixture was cooled down to 0 °C in an ice bath. Subsequently $MgBu_2$ (3.89 ml of 1 M solution in hexane, 20 mmol of $MgBu_2$) was added to BHT solution in THF and stirred at room temperature for 24 h under nitrogen atmosphere. The solvent was removed under reduced pressure. The obtained white powder was rinsed with dry heptane (3 × 15 mL) and dried under reduced pressure. Yield: 4.41 g (73.3 %).

Synthesis of $Na_3(BHT)_3(THF)_3$ catalyst. In a glovebox, a mixture of 2,6-di-tert-butyl-4- methylphenol (8.8 g, 40 mmol) and NaH (1.00 g, 42 mmol) was stirred in tetrahydrofuran (30 mL) at room temperature for 24 h. After the reaction, a residual NaH was removed by filtration while the solvent was removed under reduced pressure. The thus obtained white powder was washed with heptane (3 × 15 mL) and dried in vacuo. Typical polymerization procedure of PCL via catalytic ring-opening polymerization. A roundbottom glass reactor equipped with a mechanical stirrer was charged with benzyl alcohol (118.4 mg, 1.1 mmol), $Mg(BHT)_2(THF)_2$ catalyst (1331.6 mg, 2.2 mmol) and CL (250 g, 2.2 mol) and the reactor was closed. All manipulations were carried out in a glovebox. The reactor was removed from the glovebox and placed in an oil bath. Subsequently, the reaction mixture was rigorously stirred (800 rpm) at 150 °C for 3 h. An aliquot of crude polymer was withdrawn at the end of the polymerization reaction in order to determine the conversion of the monomers by ^1H NMR spectroscopy. The reaction was then stopped by quenching the crude product with acidified methanol (0.1 M HCl solution in methanol). The polymer was isolated and dried at 40 °C for 24 h under reduced pressure.

Typical polymerization procedure of CEB via catalytic ring-opening polymerization. In a glovebox, benzyl alcohol (0.40 mg, 3.7 *μ*mol), $Na_3(BHT)_3(THF)_3$ catalyst (1.16 mg, 1.23 *μ*mol) and CEB (500 mg, 1.85 mmol) were introduced into a small glass crimp cap vial and the vial was capped. The reaction mixture was removed from the glovebox and stirred for 3 h in a carrousel reactor at 200 °C. An aliquot of crude polymer was withdrawn at the end of the polymerization reaction in order to determine the conversion of the monomers by ^1H NMR

spectroscopy. The reaction was then stopped by quenching the crude product with acidified methanol (5 mL). The polymer was isolated and dried at 40 °C for 24 h under reduced pressure. A similar procedure was applied for the production of PEB in a 500 g scale in a glass reactor.

Random- and block copolymer synthesis. cROP of cyclic esters using OH-functionalized macroinitiators is a proven technology to produce the corresponding block- or graft copolymers. cROP of cyclic ethylene brassylate (CEB) and caprolactone (CL), using PP–OH (1) or PP–*co*–C_{11}OH (2, 3) as macroinitiator, readily afforded the corresponding block and graft copolymers (see Figure 1, S1–S5). Most likely due to the combination of a relatively low concentration of OH groups in PP-OH (1) and lower reactivity of CEB compared to CL, the synthesis of PP–*block*–PEB by ROP using PP–OH (1) proved to be more complicated.

Typical polymerization procedure of PP–*graft*–PCL via catalytic ring-opening polymerization. In the glovebox, catalyst $(BHT)_2Mg(THF)_2$ (400 mg), an equimolar amount of PP–*g*–C_{11}OH (3, 9.462 g, 0.375 mmol, M_n = 25.4 kg/mol, Đ = 2.4) and toluene (100 g) were placed in a small reactor with a mechanical stirrer. The mixture was removed from the glovebox. Caprolactone (37.5 g, 0.329 mol) was added and the reaction was carried out for 5 h at 150 °C. The progress of the reaction was followed by ^{1}H NMR spectroscopy by taking aliquots at set time intervals. The synthesized copolymer was cooled to room temperature and quenched using acidified methanol, isolated and dried in vacuum at room temperature for 18 h.

Typical procedure for the synthesis of PP–*block*–PEB copolymers via transesterification reaction. Chain-end hydroxyl-functionalized isotactic PP (1, 6.0 g, M_n = 14.3 kg/mol, Đ = 1.9) and PEB (3.0 g, M_n = 40.9 kg/mol, Đ = 2.7) with antioxidant Irganox 1010 (2500 ppm) were fed into a corotating twin-screw mini-extruder at 160 °C with a screw rotation rate set at 100 rpm. The polymers were premixed for 5 minutes. After this time, tin (II) 2-ethylhexanoate (0.09 g, 0.22 mmol) as catalyst was added and the mixture was stirred for an additional 5 minutes. Afterwards the extruder chamber was cooled and evacuated. Similar methods were applied for the preparation of each type of the compatibilizer presented in Table 3.

Typical procedure for the preparation of PP/PC blends. Isotactic PP (PP500P, 8.0 g) and PC (PC105, 2.0 g) with antioxidant Irganox 1010 (2500 ppm) were fed into a corotating twin-screw mini-extruder at 240 °C with a screw rotation rate set at 100 rpm. The mixture was processed for 5 minutes. Afterwards the mixture was evacuated directly to a mini-injection molding machine and the obtained blends were tested in terms of their morphology and mechanical properties.

Typical procedure for the preparation of PP/PC blends compatibilized by PP–*block*–PEB copolymer. Isotactic PP (PP500P, 8.0 g), PC (PC105, 2.0 g), antioxidant Irganox 1010 (2500 ppm) and PP–block–PEB compatibilizer (0.5 g) were fed into a corotating twin-screw mini-extruder at 240 °C with a screw rotation rate set at 100 rpm. The mixture was processed for 5 minutes. Afterwards the mixture was evacuated directly to a mini-injection molding machine and the obtained blends were tested in terms of their morphology and mechanical properties. A similar procedure was applied for the preparation of PP/PC blends compatibilized by the copolymers presented in Table 3.

Measurements

Size exclusion chromatography (SEC). Measurements were performed at 150 °C on a Polymer Char GPC-IR® built around an Agilent GC oven model 7890, equipped with an autosampler and the Integrated Detector IR4. 1,2-Dichlorobenzene (o-DCB) was used as an eluent at a flow rate of 1 mL/min. The data were processed using Calculations Software GPC One®. The molecular weights were calculated with respect to polyethylene or polystyrene standards. The analysis of long chain branches in the copolymers was performed using Polymer Laboratories PL-GPC220 system equipped with the Polymer Laboratories PL BV-400 viscometer (refractive index detector). The analysis was performed at 160 °C. 1,3,5-Tichlorobenzene (TCB) was used as an eluent at a flow rate of 1 mL/min. For the analysis set of three Polymer Laboratories 13 μm PLgel Olexis 300 × 7.5 mm columns was used. PP molar mass analysis was performed using linear PE standards and conversion of the values using Mark-Houwink constants.

Liquid-state ^{1}H NMR. ^{1}H NMR and ^{13}C NMR spectra were recorded at room temperature or at 80 °C using a Varian Mercury Vx spectrometer operating at

Larmor frequencies of 400 MHz and 100.62 MHz for 1H and 13C, respectively. For ^{1}H NMR experiments, the spectral width was 6402.0 Hz, acquisition time 1.998 s and the number of recorded scans equal to 64. ^{13}C NMR spectra were recorded with a spectral width of 24154.6 Hz, an acquisition time of 1.3 s, and 256 scans. 2D NMR spectra were recorded on a Varian Unity 500 plus spectrometer. Correlation spectra (COSY) were acquired using standard programs provided by a Varian spectrometer library with the following parameters: spectral width SW1 = SW2 = 6075.3 Hz, acquisition time 0.221 s, relaxation delay 1.4 s, and number of scans 8 × 300 increments.

Differential scanning calorimetry (DSC). Melting (T_m) and crystallization (T_c) temperatures as well as enthalpies of the transitions were measured using a Differential Scanning Calorimeter Q1000 from TA Instruments. The measurements were carried out at a heating and cooling rate of 10 °C/min from −50 °C to 200 °C. The transitions were deduced from the second heating and cooling curves.

Scanning electron microscopy (SEM). The freeze fractured samples were analyzed using a Phenom Pro (Phenom-World) apparatus operating at an accelerating voltage of 5 kV. The samples were sputter-coated using Q150R Rotary-Pumped Sputter Coater (Quorum Technologies) with gold. The morphology of foam cell structures was characterized with a JEOL JSM 7800-F Field Emission Scanning Electron Microscopy (FE-SEM) at an operating voltage of 5 kV. A piece of foam sample was cryogenically fractured for the cross-sectional morphology characterization. The foam cross section was examined using the Large Depth of Focus (LDF) mode and the Lower Electron Detector (LED) detector in the FE-SEM. The LDF mode provides a larger depth of focus than conventional SEM mode and is suitable for imaging of rough samples with micron size features. All the samples were sputter-coated with gold-palladium before SEM imaging in order to reduce the surface charging during imaging. Density analysis were carried out using PLT-A01 set for density determination for KERN PLT. The foam samples were immersed in water to determine the volume and the mass by weighing it on the balance. The volume determination is based on the Law of Archimedes.

Transmission electron microscopy (TEM). Details of the samples' morphology were examined with a transmission electron microscope (Tesla BS 500, Tesla,

Czech Republic), operating at 90 kV. Samples for TEM examination, in the form of ultra-thin sections approx. 60 nm thick, were prepared by cryo- ultra-sectioning with an ultramicrotome (PowerTome PC, Boeckeler, USA) equipped with a 35 ° diamond knife (Diatome, Switzerland). Ultra-thin sections were placed on standard copper grids for TEM examination. Before cutting the analyzed samples were exposed to the vapor of RuO4 at room temperature for a 24 h. From TEM micrographs the structural information on PC dispersion was extracted using the image analysis software ImageJ (National Institutes of Health, USA). Size determinations were made by evaluating at least 300 domains of PC for each sample.

Atomic force microscopy (AFM). The injection molded parts of samples were analyzed using Nanoscope V Multimode 8 Bruker apparatus. Tapping mode was employed in air using an integrated tip/cantilever (125 mm in length with ca. 300 kHz resonant frequency). Typical scan rates during recording were 1 line/s using a scan head with a maximum range of 16 × 16 mm. Transversal cross-section surface of the polymer blends was prepared at by using an ultramicrotome Leica Ultracut R with a diamond knife.

Dynamic mechanical thermal analysis (DMTA) was performed using a TA Instruments Q800 DMA. Samples were tested by strain-controlled temperature ramp with the frequency of 1 Hz. The temperature profile was from −150 °C to 180 °C with the ramp 3 °C/min. The glass transition temperature was calculated as the peak of the tangent delta signal.

Thermogravimetric analysis was performed on a TGA Q500 from TA Instruments. The measurements were carried out in a nitrogen atmosphere. Samples were heated from 20 to 700 ºC with a scan rate 10 °C/min.

Tensile testing. Tensile tests were performed with a Zwick type Z020 tensile tester equipped with a 20 kN load cell. The tests were performed on injection molded samples having the dimensions of 75 mm × 4 mm × 2 mm and prepared using co-rotating micro compounder MC 15HT and micro injection moulder IM 12 from Xplore. A grip-to-grip separation of 50 mm was used. The samples were pre-stressed to 3 N, then loaded with a constant cross-head speed 50 mm/min. The reported values are an average of at least 5 measurements of each composition.

Compression-molding experiments. All the sample plaques were prepared via compression molding of the injection-molded bars using PP ISO settings on LabEcon 600 high-temperature press (Fontijne Presses, the Netherlands). Namely, the injection-molded bars were cut in pieces and loaded into a stainless-steel mold 5 × 5 × 0.16 cm with aluminum foil or Teflon covering on either side. Then, the compression-molding cycle was applied: heating to 210 °C, stabilizing for 5 min with no force applied, 5 min with 100 kN normal force and cooling down to 40 °C with 15 °C/min and 100 kN normal force.

Melt rheology experiments. TA Instruments DHR-2 rheometer was used with a plate−plate geometry, diameter of the plates of 25 mm and measuring gap 1 mm, for small-amplitude oscillatory shear measurements. The characteristic rheological properties (storage and loss modulus, G′ and G″, and loss angle, δ) were obtained from frequency sweeps at three different temperatures (190, 210 and 230 °C) and in a broad range of angular frequencies, ω (from 0.01 to 100 rad/s). To determine the rheological properties in the linear viscoelastic regime, the strain applied was determined from strain sweeps and set to 1 % for all measurements. The experiments were performed in a nitrogen environment to avoid degradation of the material. Time sweeps using an angular frequency of 0.5 rad/s were performed for 20 minutes before and after the frequency sweeps. The time-evolution of the storage modulus was monitored to check whether the systems had reached their equilibrium status during the measurement of the frequency sweeps.

Uniaxial extensional measurements were performed at 160 °C, with a Modular Compact Rheometer MCR 502 Anton Paar equipped with a CTD 620 oven. Measuring system: SER2. Shaft cooling: 1 m3N/h. Heating: 0.75 m3N/h and 0 LN/h. Samples prepared in reactive extrusion followed by injection molding were cut in rectangular shape (1.7 × 1.1 × 0.15 cm) with parallel razor blades. The elongational viscosity was evaluated under several Hencky strain rates between 0.05/s and 0.5/s. The Hencky strain was kept constant at 3.5 by adjusting the interval duration time.

Procedure of foams preparation using MCU (micro foaming line). Polymers and additives (Polybatch FPE50T Talcum in PE 50% MB (cell-nucleator) and Atmer 7300 (cell-stabilizer)) were fed into twin-screw extruder. Polymer were dosed using volumetric screw feeder in speed of 15 rpm, which gives a throughput 290 g/h. The

mixture was processed at 80-160-210-210-210-210- 210-210-200-200 °C, and then evacuated to the cooled. Isobutane was used as a blowing agent and was injected using a syringe pump at 0.85 ml/min, which correlates to a gas dosage of 10.3 wt.%. An adjustable die was connected at the exit of the cooler. The temperature of cooler at the starting point was 200 °C and then was lowered every 5 min in steps of 5 °C. The foamed mixture was collected and measured in terms of its morphology and density. The pressure was controlled during the process and set at 30 bars by adjustable die.

Table S1. Molecular characterization and thermal properties of synthesized OH-functionalized PP.

Entry	**Sample**	M_n **[kg/mol]**[a]	M_w **[kg/mol]**[a]	**Đ**[a]	**OH/ chain**	T_m **[°C]**[b]	ΔH_m **[J/g]**[b]	T_c **[°C]**[b]	ΔH_c **[J/g]**[b]
1	PP–OH (**1**)	14.3	27.4	1.9	0.8	150.5	64.0	115.4	106.0
2	PP–co–C_{11}OH (**2**)	12.3	23.8	1.9	1.8	146.4	92.6	112.7	94.6
3	PP–co–C_{11}OH (**3**)	25.4	60.9	2.4	4.6	146.6	94.1	113.0	96.2
4	PP–OH_{REX} (**4**)	28.5	101.9	3.6	1-2	155.1	79.3	115.0	88.4

[a] Molecular weight and polydispersity determined by HT-SEC in 1,2-dichlorobenzene at 150 °C, b thermal properties established by DSC.

Table S2. Molecular characterization and thermal properties of poly(ethylene brassylate) (PEB) and polycaprolactone (PCL).

Entry	Sample	M_n [kg/mol][a]	M_w [kg/mol][a]	$Đ^a$	T_m [°C][b]	ΔH_m [J/g][b]	T_c [°C][b]	ΔH_c [J/g][b]
1	PEB	40.9	110.6	2.7	67.0	81.5	53.0	69.3
2	PCL	68.0	142.8	2.1	54.2	58.1	23.4	52.2

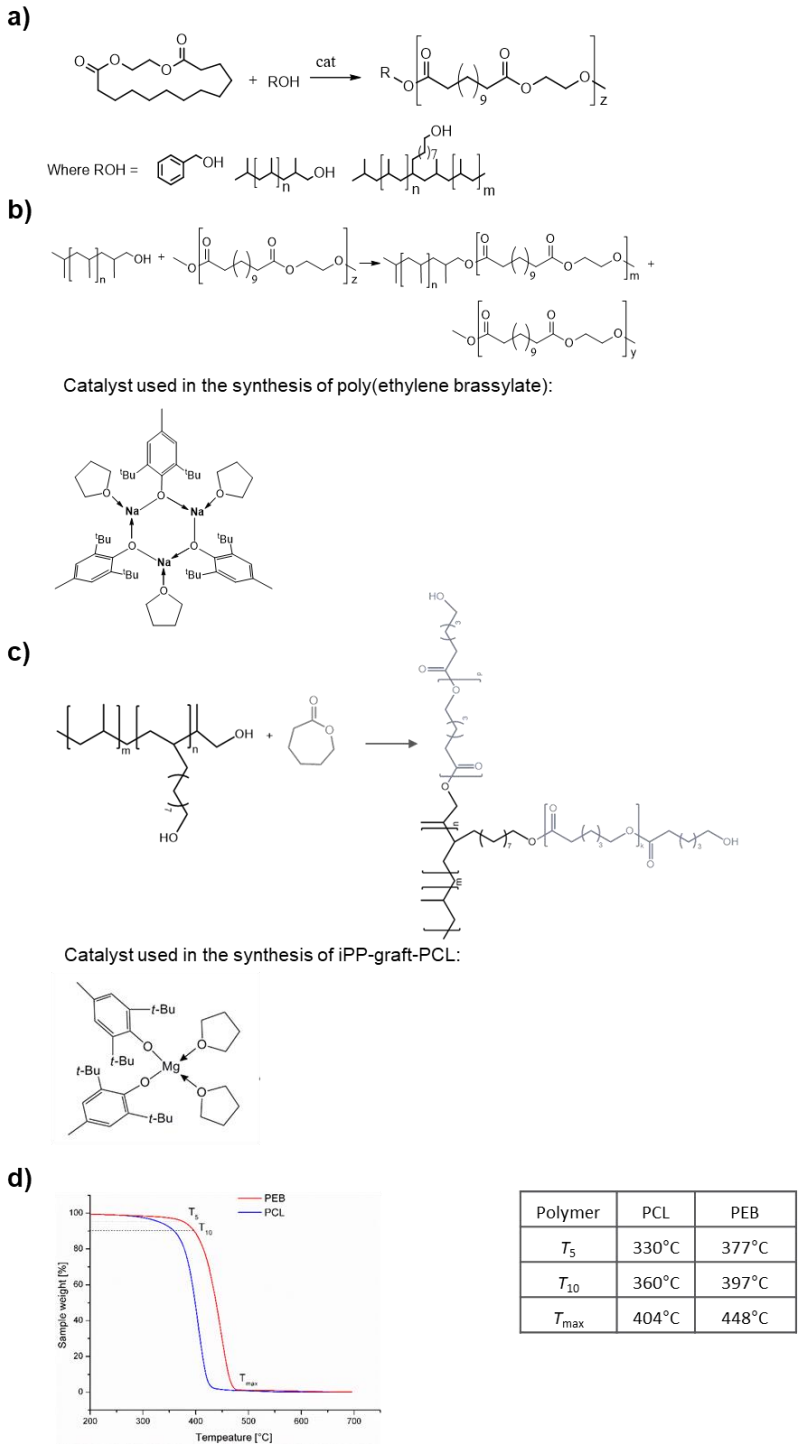

Polymer	PCL	PEB
T_5	330°C	377°C
T_{10}	360°C	397°C
T_{max}	404°C	448°C

Figure S1. a) cROP towards poly(ethylene brassylate), polypropylene–block–poly(ethylene brassylate b) transesterification of poly(ethylene brassylate) using OH–functionalized *i*PP by reactive extrusion, c) cROP towards polypropylene–graft–poly(caprolactone); d) thermogravimetric analysis of polycaprolactone (PCL) and poly(ethylene brassylate) (PEB) revealing higher thermal stability of PEB over PCL.

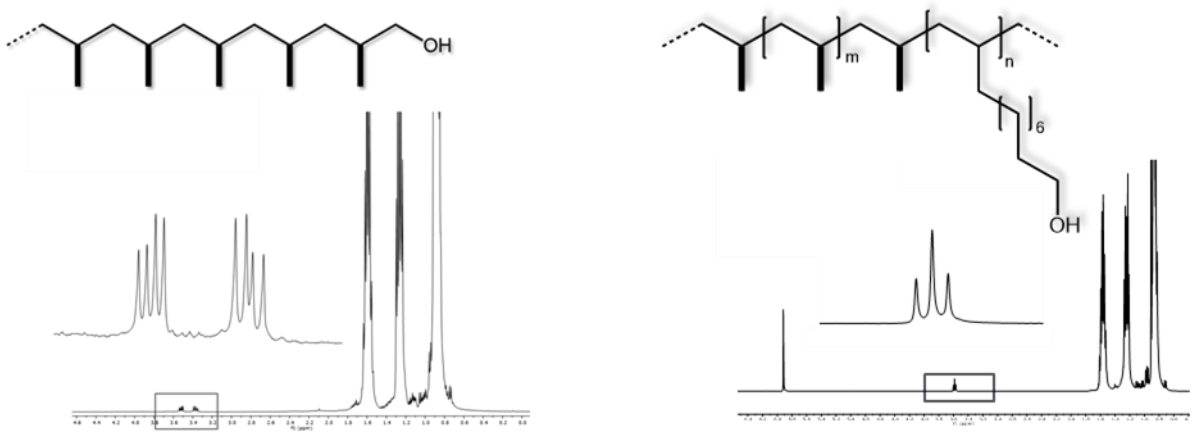

Figure S2. ^{1}H NMR spectra of OH-functionalized PP-OH SSC (left) and PP–co–C_{11}OH SSC (right)**.**

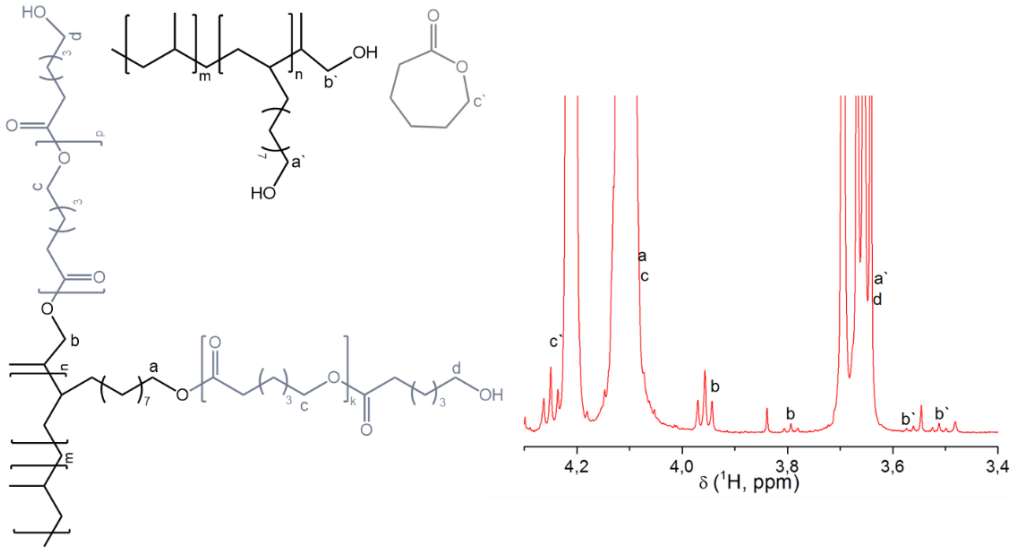

Figure S3. ^{1}H NMR spectra of PP–*graft*–PCL copolymer (entry 4, Table 3).

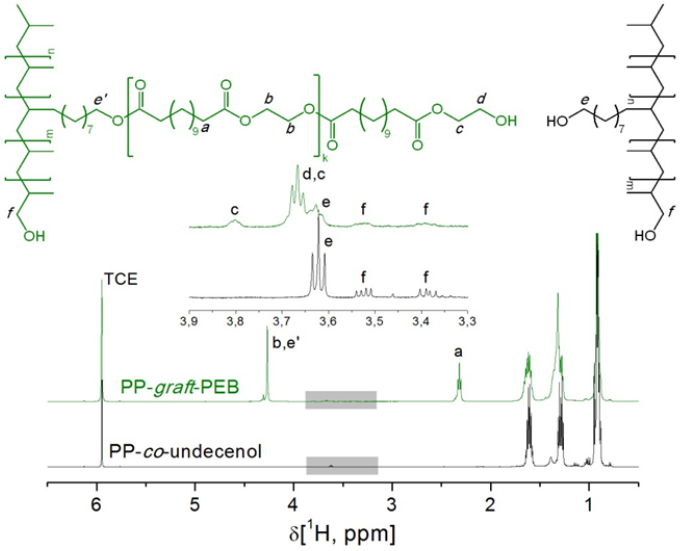

^{1}H NMR spectra of PP-*co*-C_{11}OH (entry 2, Table 1) and PP(2)-*graft*-PEB_{TE} copolymer

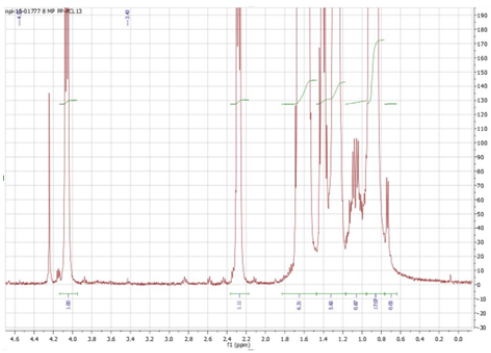

^{1}H NMR spectrum of *PP(3)-graft-PCLROP*

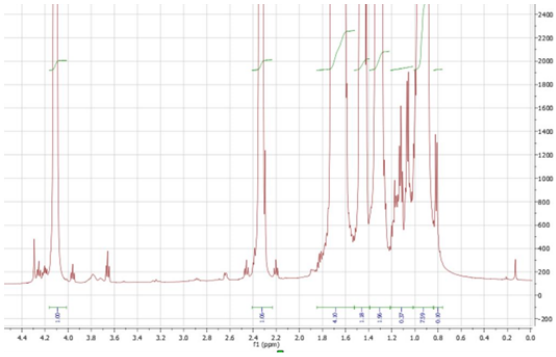

^{1}H NMR spectrum of PP(4)-*graft*-PCL_{TE}

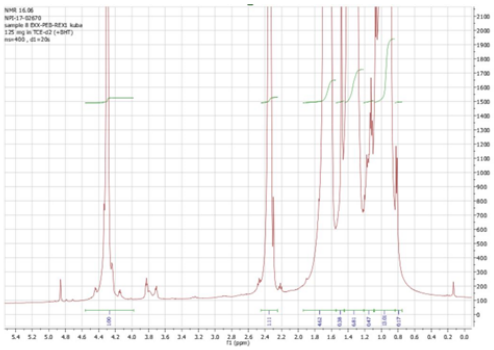

^{1}H NMR spectrum of PP(4)-*graft*-PEB_{TE}

Figure S4. ^{1}H NMR spectra of the synthesized copolymers (Table 3).

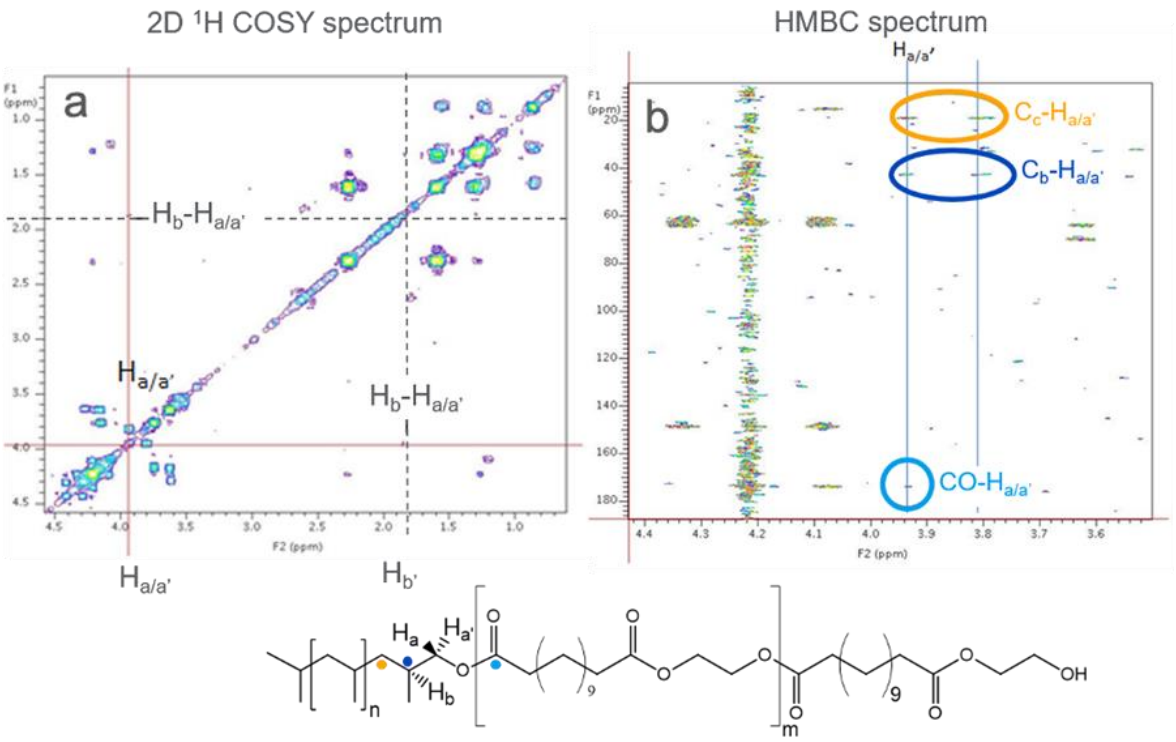

Figure S5. COSY (a) and HMBC (b) spectra of PP–block–PEB copolymer (entry 1, Table 1).

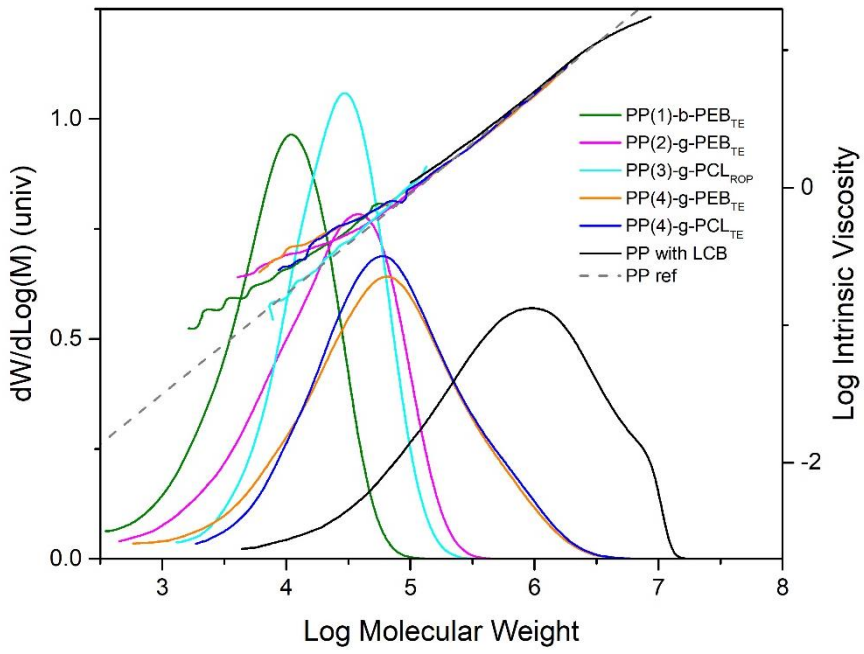

Figure S6. GPC with Differential Viscometer results of the synthesized copolymers

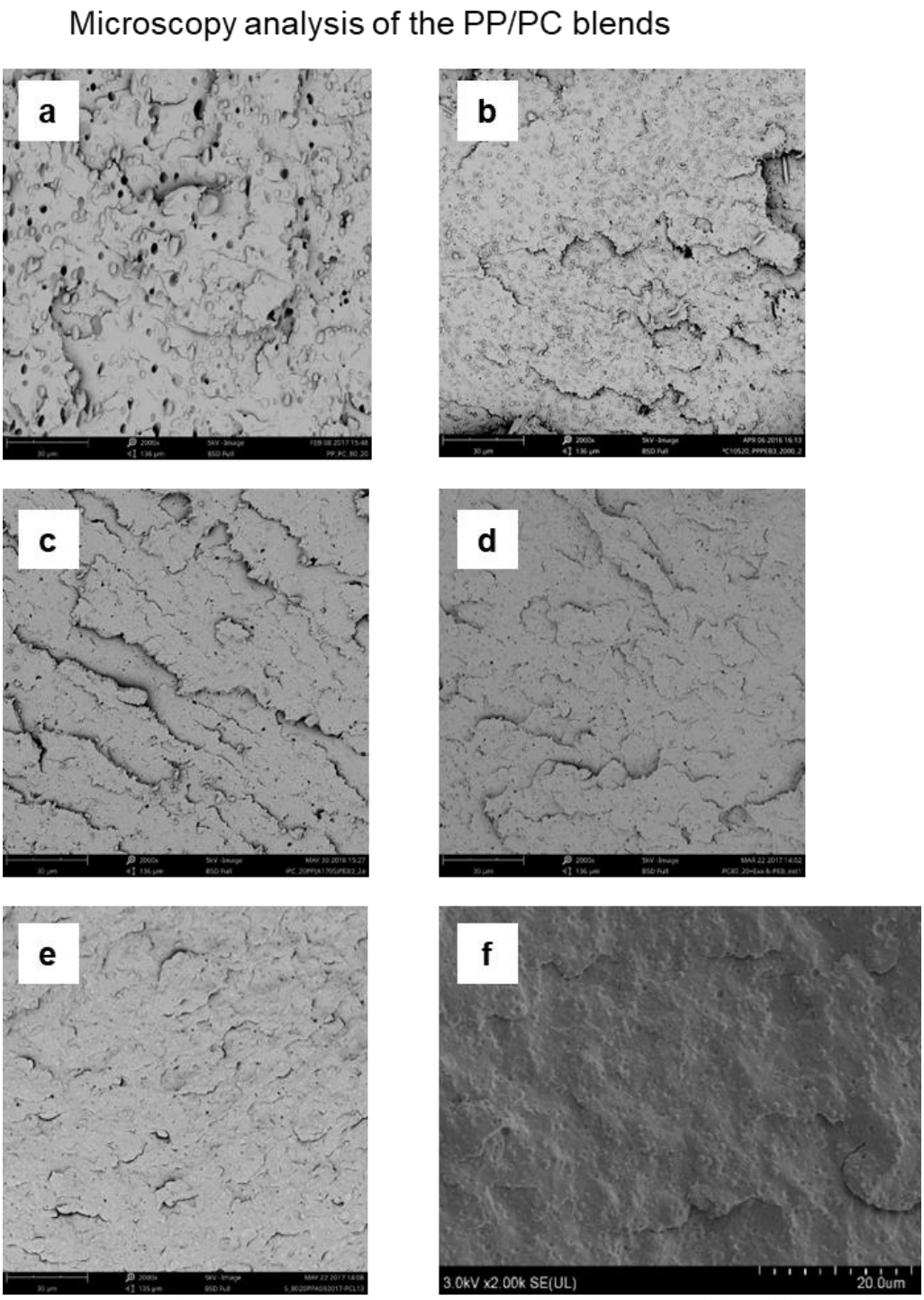

Figure S7. SEM micrographs of a) uncompatibilized PP/PC blend, b) PP/PC blend compatibilized by PP(1)–*block*–PEB_{TE}, c) PP/PC blend compatibilized by PP(2) –*graft*–PEB_{TE}, d) PP/PC blend compatibilized by PP(4)–*graft*–PEB_{TE}, e) PP/PC blend compatibilized by PP(3)–*graft*–PCL_{ROP}, f) PP/PC blend compatibilized by PP(4)–*graft*–PCL_{TE}.

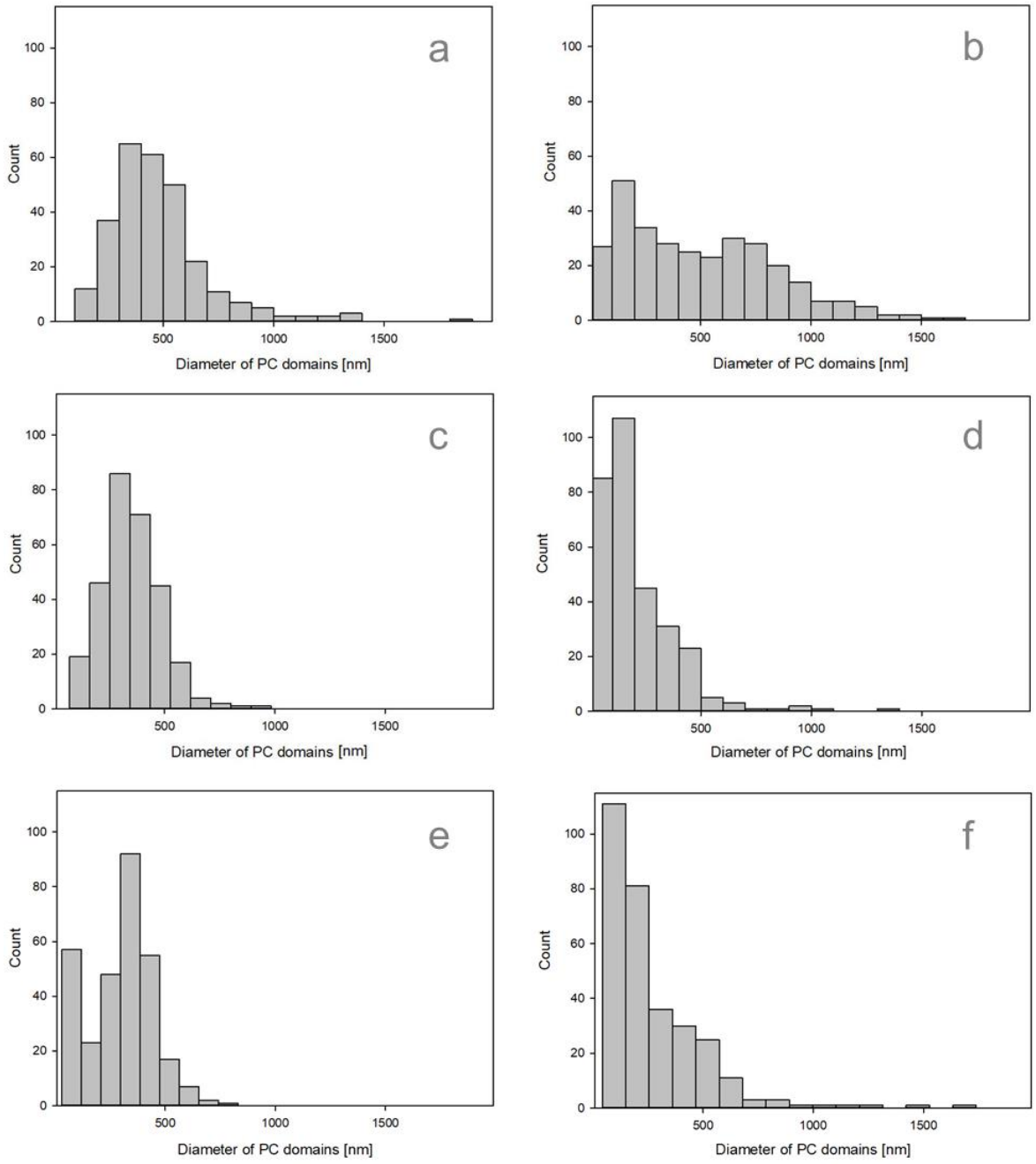

Figure S8. Size determinations of PC dispersed phase in a) uncompatibilized PP/PC blend, b) PP/PC blend compatibilized by PP(1)–*block*–PEB_{TE}, c) PP/PC blend compatibilized by PP(2)–*graft*–PEB_{TE}, d) PP/PC blend compatibilized by PP(4)–*graft*–PEB_{TE}, e) PP/PC blend compatibilized by PP(3)–*graft*–PCL_{ROP}, f) PP/PC blend compatibilized by PP(4)–*graft*–PCL_{TE}. The calculations are based on TEM analysis (Figure 1).

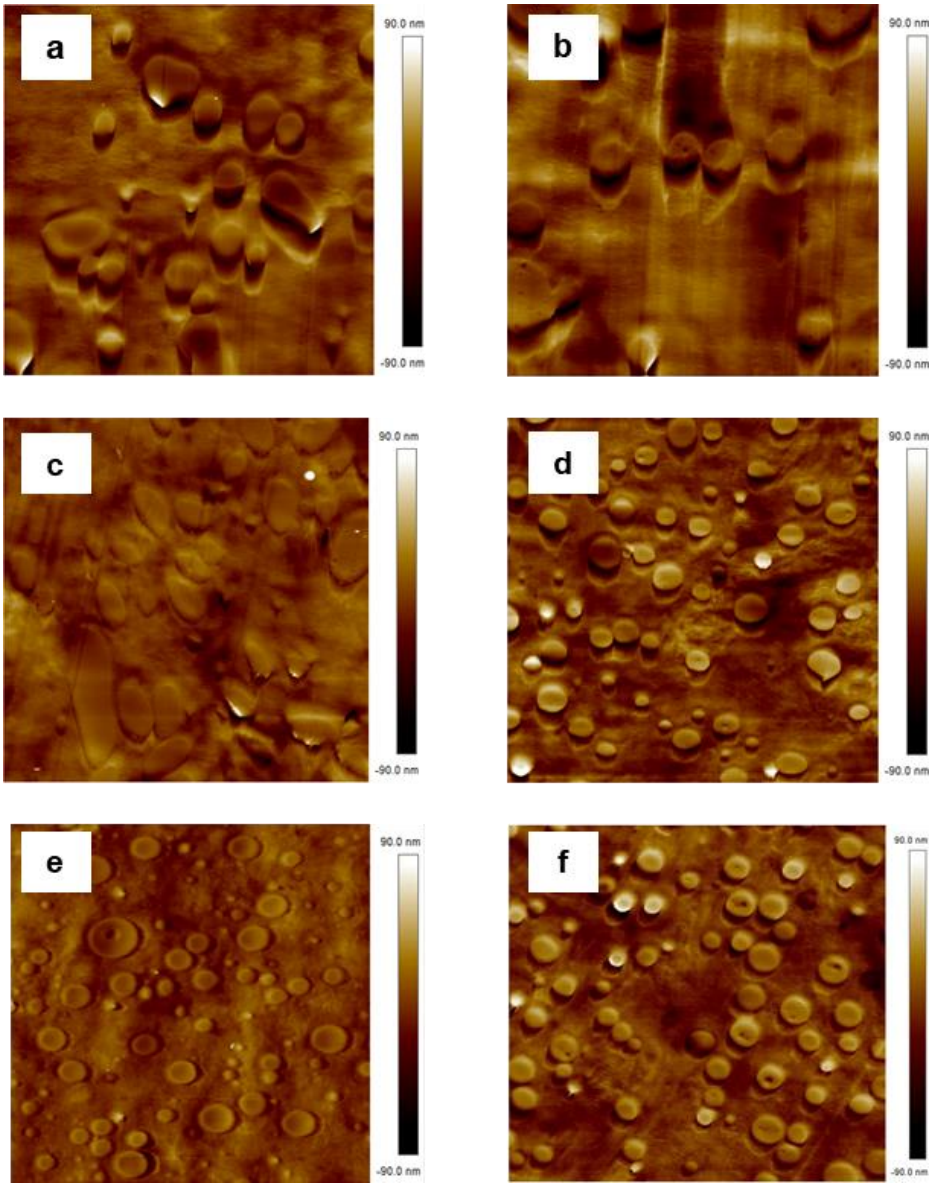

Figure S9. AFM height images (10 µm × 10 µm) of a) uncompatibilized PP/PC blend, b) PP/PC blend compatibilized by PP(1)–*block*–PEB_{TE}, c) PP/PC blend compatibilized by PP(2)–*graft*–PEB_{TE}, d) PP/PC blend compatibilized by PP(4)–*graft*–PEB_{TE}, e) PP/PC blend compatibilized by PP(3)–*graft*–PCL_{ROP}, f) PP/PC blend compatibilized by PP(4)–*graft*–PCL_{TE}.

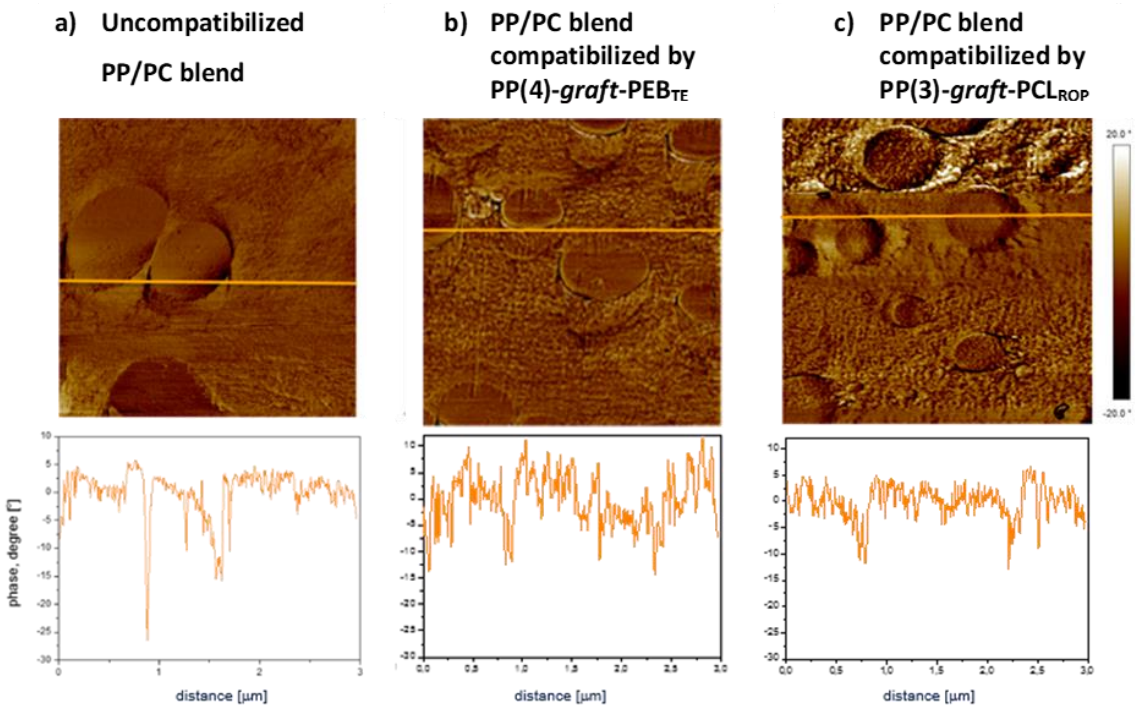

Figure S10. AFM phase images (3 μm × 3 μm) and phase diagrams of PP/PC uncompatibilized as well as compatibilized blends (for copolymers assignment see Table 1).

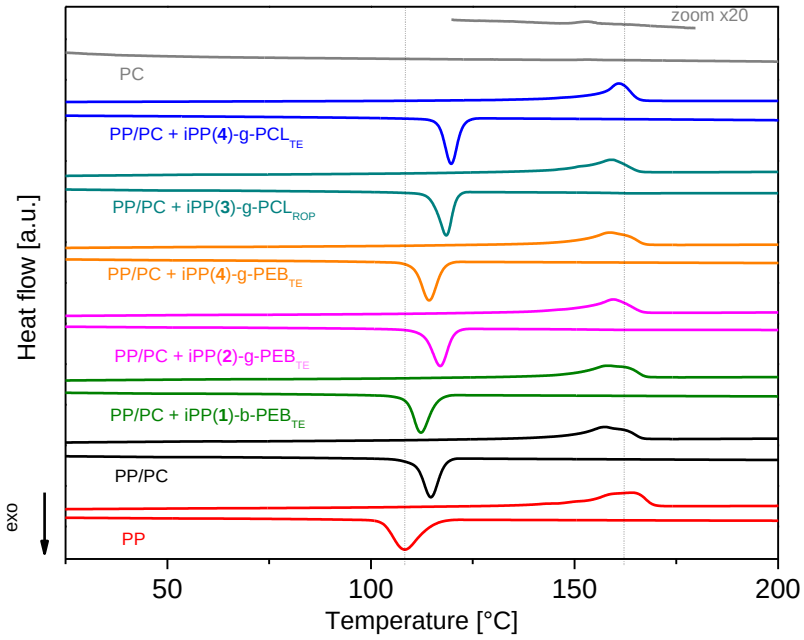

Figure S11. DSC analysis of PP, PC and PP/PC blends.

Table S3. Thermal properties of PP, PC and PP/PC blends.

Composition	compatibilizer	T_m [°C]	ΔH_m [J/g]	T_c [°C]	ΔH_c [J/g]
PP	-	164.6	98.3	108.3	91.7
PP/PC	-	157.9	77.5	114.7	75.0
PP/PC	PP(**1**)–*block*–PEB_{TE}	158.5	76.7	112.5	75.5
PP/PC	PP(**2**)–*graft*–PEB_{TE}	160.0	78.3	117.2	75.0
PP/PC	PP(**4**)–*graft*–PEB_{TE}	158.8	81.8	114.3	76.8
PP/PC	PP(**3**)–*graft*–PCL_{ROP}	159.2	74.5	118.5	76.0
PP/PC	PP(**4**)–*graft*–PCL_{TE}	157.6	75.3	115.2	81.3

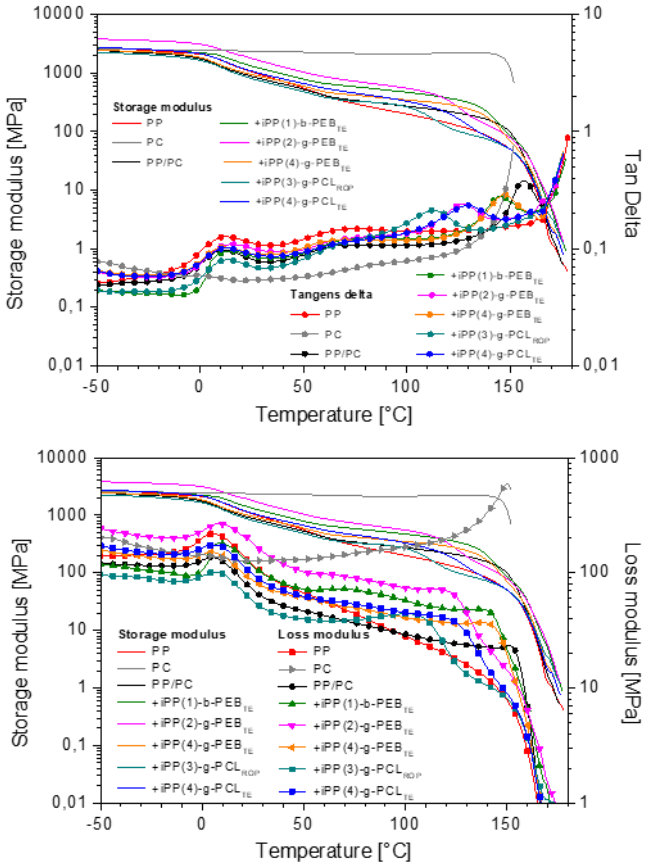

Figure S12. DMTA analysis of PP, PC and PP/PC blends

Table S4. DMTA results of PP, PC and PP/PC blends

Composition	Compatibilizer	Modulus [MPa]				T_g [°C]	
		Storage (E')		Loss (E'')			
		-20°C	100°C	-20°C	100°C	T_{g1}	T_{g2}
PP	-	2376.0	200.6	144.8	28.1	6.8	-
PC	-	2510.0	2139.0	155.7	167.9	-	150.3
PP/PC	-	2157.0	273.0	115.2	29.2	6.2	152.4
PP/PC	PP(**1**)–*block*–PEB_{TE}	2486.0	471.0	103.2	57.3	8.1	140.5
PP/PC	PP(**2**)–*graft*–PEB_{TE}	3532.0	552.2	201.9	74.1	9.1	120.7
PP/PC	PP(**4**)–*graft*–PEB_{TE}	2254.0	348.9	134.4	40.9	6.8	141.9
PP/PC	PP(**3**)–*graft*–PCL_{ROP}	2007.0	266.0	86.4	44.0	8.0	104.8
PP/PC	PP(**4**)–*graft*–PCL_{TE}	2491.0	331.2	144.9	45.1	6.8	122.6

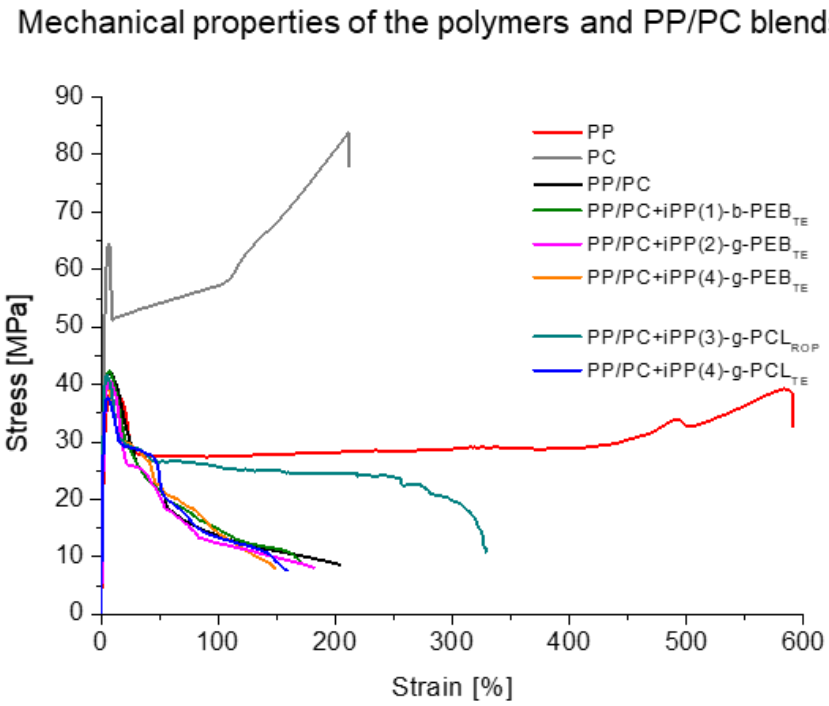

Figure S13. Tensile test curves of PP, PC and PP/PC blends

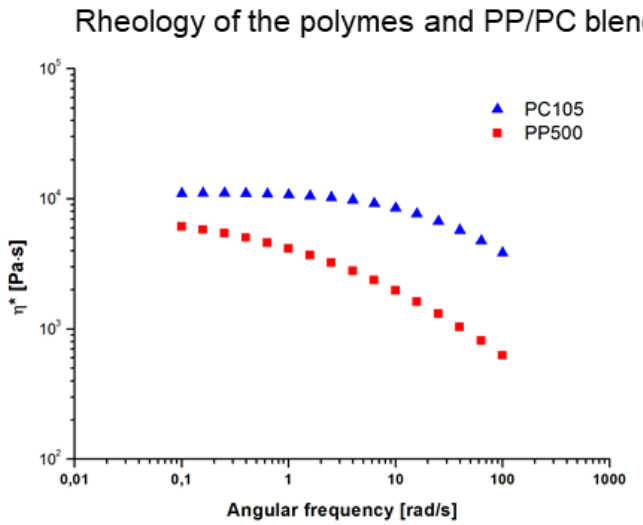

Figure S14. Changes of complex viscosity as a function of frequency for PP and PC.

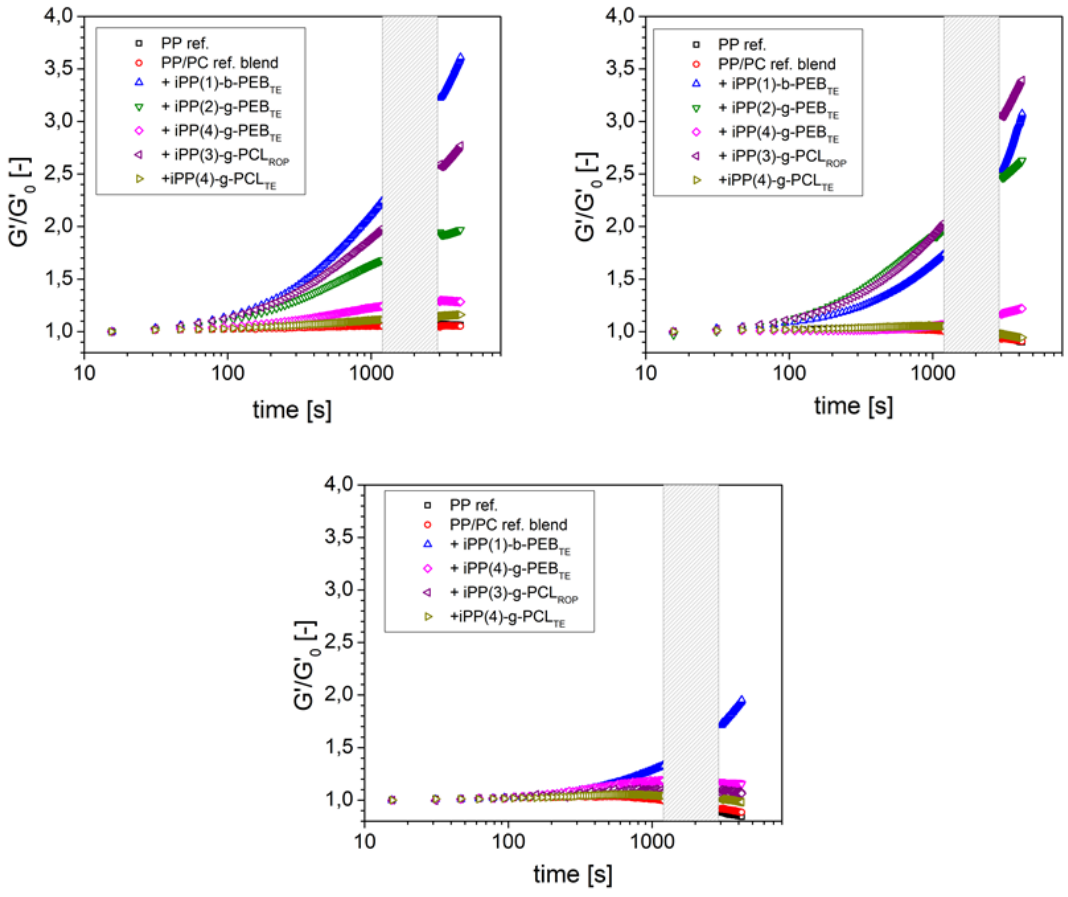

Figure S15. Time evolutions of the normalized storage modulus at 190 (a), 210 °C (b) and 230 °C (c) for all the materials analyzed in this work. The dashed area represents the time interval during which the frequency sweeps are performed.

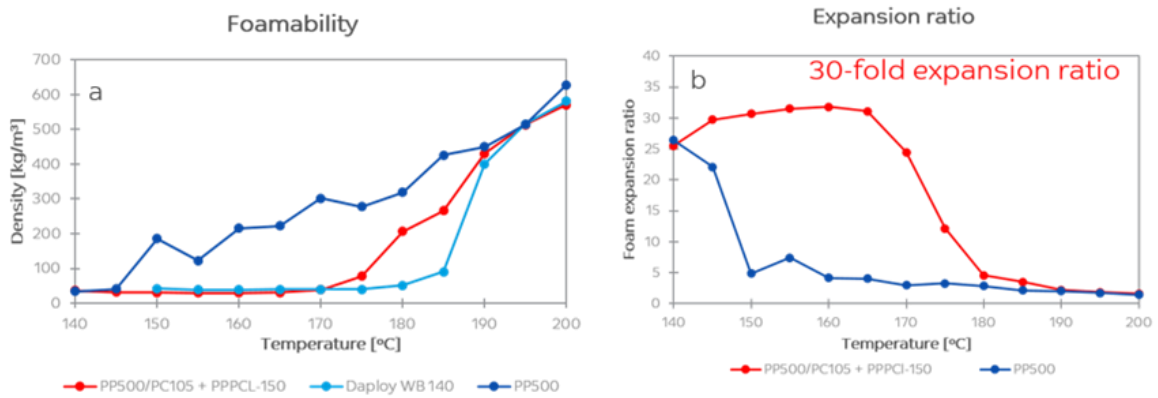

Figure S16. Foam densities of PP/PC blend compatibilized by PP(4)–*graft*–PCL_{TE} (Table 1, entry 5), LCBPP (Daploy™) and polypropylene (a); effect of temperature on the volume expansion ratio of the foamed PP/PC blend compatibilized by PP(4)–*graft*–PCL_{TE} (Table 1, entry 5) and polypropylene (b).

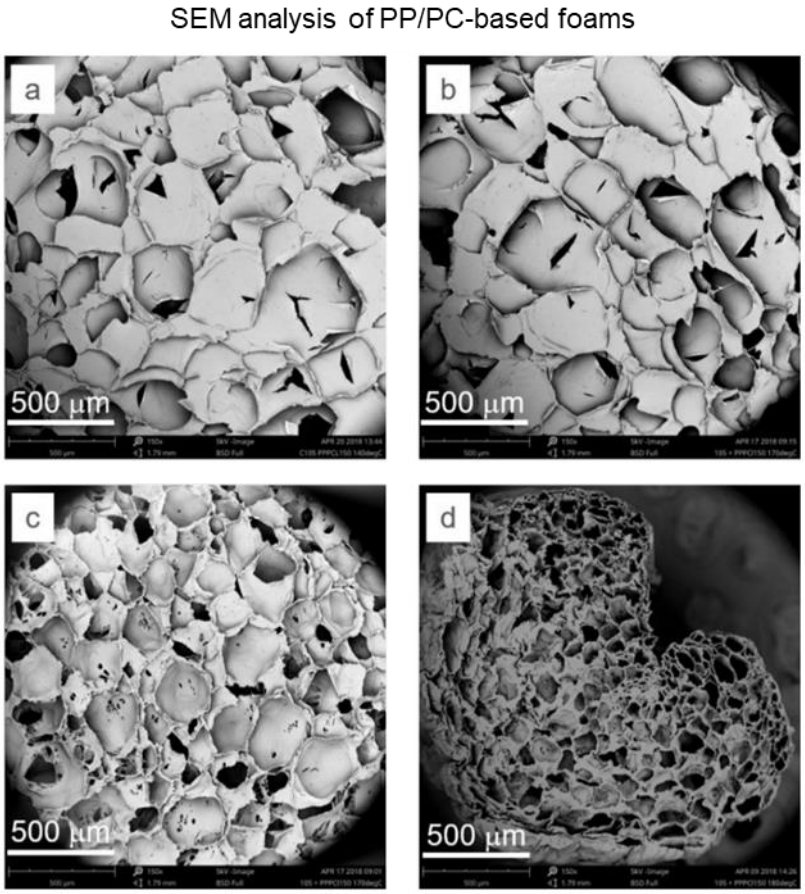

Figure S17. Technical SEM images of the PP/PC-based foams obtained at 140 °C (a), 155 °C (b), 170 °C (c), 180 °C (d). Please note that the irregular shape of the cells and the presence of several open cells originate from the samples preparation technique (freeze-fracturing).

4.6 Compatibilization of polypropylene / polyethylene blends

This subchapter has been published as:

_i_PP/HDPE blends compatibilized by a polyester: An unconventional concept to valuable products

Jakub Kruszynski, Weronika Nowicka, Artur Rozanski, Yingxin Liu, Daniele Parisi, Lanti Yang, Farhan Ahmad Pasha, Miloud Bouyahyi, Lidia Jasinska-Walc, and Rob Duchateau

Science Advances **2024** 10,eado1944

DOI: 10.1126/sciadv.ado1944

SCIENCE ADVANCES | RESEARCH ARTICLE

CHEMISTRY

_i_PP/HDPE blends compatibilized by a polyester: An unconventional concept to valuable products

Jakub Kruszynski[1,2]†, Weronika Nowicka[1,2]†, Artur Rozanski[3], Yingxin Liu[1], Daniele Parisi[4], Lanti Yang[5], Farhan Ahmad Pasha[6], Miloud Bouyahyi[1], Lidia Jasinska-Walc[1,2]*, Rob Duchateau[1,4]*

Polyolefins are the most widely used plastics accounting for a large fraction of the polymer waste stream. Although reusing polyolefins seems to be a logical choice, their recycling level remains disappointingly low. This is mainly due to the lack of large-scale availability of efficient and inexpensive compatibilizers for mixed polyolefin waste, typically consisting of high-density polyethylene (HDPE) and isotactic polypropylene (*i*PP) that, despite their similar chemical hydrocarbon structure, are immiscible. Here, we describe an unconventional approach of using polypentadecalactone, a straightforward and simple-to-produce aliphatic polyester, as a compatibilizer for *i*PP/HDPE blends, especially the brittle *i*PP-rich ones. The unexpectedly effective compatibilizer transforms brittle *i*PP/HDPE blends into unexpectedly tough materials that even outperform the reference HDPE and *i*PP materials. This simple approach creates opportunities for upcycling polymer waste into valuable products.

INTRODUCTION

With a market share of more than 60 % and having the lowest lifecycle environmental impact of all polymers, polyolefins play a crucial role in our daily life.[1-5] Polyolefins are lightweight, cheap and food contact approved, which makes them materials of choice for, often single use, packaging applications and other fast moving consumer goods. Consequently, vast amounts of polyolefin waste are produced annually. Driven by environmental awareness concerning the pollution of polymer waste and the carbon footprint of single use plastics, a growing amount of these polyolefins ends up in recycle streams rather than being landfilled or incinerated. Recycled polyolefin waste can be separated relatively easy from other polymers based on their density. However, separating polyolefins from each other is challenging.[6,7] The purity levels of current post consumer recycle (PCR) polyolefins, consisting of high density polyethylene (HDPE) and isotactic polypropylene (*i*PP), range between 80 and 90 % of either HDPE or *i*PP. Although this level of purity might seem adequate for mechanical recycling, the bulk properties of especially the *i*PP–rich blends are rather disappointing.[8] Despite both being simple aliphatic hydrocarbons, blends of HDPE and *i*PP are immiscible forming distinct phases.[9] To overcome the resulting poor mechanical properties, various compatibilizer strategies have been developed including miscibility and interfacial properties studies in ternary blends.[10-12] The most common compatibilizers are block- or graft copolymers consisting of HDPE- and *i*PP segments.[13-23] A major breakthrough in this field was achieved by Coates and coworkers, who demonstrated that small amounts of an HDPE- and *i*PP-based tetrablock copolymer ensures exceptional performance of HDPE/*i*PP blends and laminates.[24] Despite the promising results of using block- and graft copolymers as compatibilizers, their synthesis is challenging and often costly, which encumbers their large-scale production and widespread use. To accommodate the recycling of the vast and ever-growing amounts of mixed polyolefin waste produced yearly, cheap and easy to synthesize compatibilizers will be essential.

We envisioned an unconventional complementary strategy to compatibilize *i*PP/HDPE blends based on the concept of finding an inexpensive and easy to produce homopolymer that has a clear affinity for both HDPE and *i*PP. Although finding a homopolymer to effectively compatibilize HDPE/*i*PP blends seems very

unlikely, literature provides several interesting leads. Long chain aliphatic polyesters have shown remarkable PE–like properties.[25-27] Polypentadecalactone (PPDL), for example, has crystal structure, unit cell parameters and properties similar to those of HDPE (Fig. S1). Although still immiscible, PPDL and HDPE form blends with excellent mechanical properties, which finds its origin in epitaxial crystallization of PPDL onto HDPE, resulting in lamellae penetration through the interface of the two polymers.[28] The affinity of PPDL for *i*PP has thus far never been studied.

Pentadecalactone (PDL) is a renewable product that belongs to the class of naturally occurring macrocyclic musks used in the fragrance industry. Its eco-friendliness led to an increased demand and the development of improved synthetic routes, which makes PDL commercially available in larger quantities.[29] PDL can conveniently be polymerized using catalytic ring-opening polymerization to afford PPDL, a linear aliphatic polyester having 14 CH_2 moieties between each ester group.[30-32] The combination of an inexpensive catalyst and low polymerization temperature renders this chain growth polymerization process sustainable and scalable using standard melt polymerization reactors. For this study a PPDL with M_n = 99.5 kg·mol^{-1} and Đ = 2.2 was synthesized.

RESULTS AND DISCUSSION

To investigate whether PPDL also shows affinity to *i*PP and hence might function as a compatibilizer for blends consisting of HDPE and *i*PP, molecular dynamics simulations were performed. The miscibility of polymer blends is typically described by miscibility parameters such as the Binding Energy ($E_{binding}$), Mixing Energy (ΔE_{mix}) and the Flory-Huggins interaction parameter (χ). These parameters depend on the Hildebrand solubility parameter (δ) and cohesive energy densities (CED)[33–35], which can be obtained from Molecular Dynamics simulations.[36–40] For the simulations of the *i*PP/HDPE blends (with and without PPDL as compatibilizer), four models with different *i*PP and HDPE ratios were used (Fig. 1). The models PP' (PP82.3 wt%/HDPE9.7 wt%/PPDL8.0 wt%), and PP" (PP74.6 wt%/HDPE18.1 wt%/PPDL7.3 wt%), represent *i*PP–rich blends while PE' (PP12.4 wt%/HDPE73.1 wt%/PPDL14.5 wt%), and PE" (PP10.0 wt%/HDPE78.3 wt%/PPDL11.7 wt%), reflect the HDPE–rich compositions (Fig. 1E). To exclude crystallization-related phenomena, all the modeling was performed at 190 °C as the processing temperature of the blends.

First, the miscibility of binary *i*PP/PPDL, HDPE/PPDL and *i*PP/HDPE blends (~ 90:10 w/w) were investigated (Fig. 1C; Fig. S2–S4, Table S1). Furthermore, PPDL – like other long chain aliphatic polyesters, thoroughly studied by Mecking and coworkers[41] – and HDPE are structurally the most similar polymers, the $E_{binding}$ is the lowest of all three binary blends. Interestingly, the $E_{binding}$ for the *i*PP/PPDL blend is significantly higher than for the HDPE/PPDL blend, which based on the molecular structure of the polymers was not expected. The higher affinity of *i*PP to PPDL than to HDPE was underlined by the higher Ebinding for the *i*PP/PPDL as compared to the corresponding *i*PP/HDPE blend. The corresponding ΔE_{mix} and χ parameters show the same trend. These encouraging results incited us to study whether or not PPDL would have a compatibilizing effect on *i*PP/HDPE blends (Table S2; Fig. 1, S5, S6). As a fact, *i*PP/HDPE are immiscible at room temperature, leading to a positive Flory-Huggins interaction parameter (χ)[40, 42–44] at room temperature. However, these simulations were performed at 190 °C (processing temperature) and at this temperature the molten mixture of *i*PP/HDPE shows a negative Flory-Huggins interaction parameter (χ), as depicted in Figure 1C. Interestingly, the *i*PP/HDPE/PPDL ternary blends show a more negative (χ) value in all the cases in comparison to respective binary *i*PP/HDPE mixtures. This qualitatively trend demonstrates that the presence of PPDL increases the miscibility. Fig. 1B shows a strong increase (nearly doubling) of the $E_{binding}$ upon addition of PPDL to each of the blends, which demonstrates the compatibilizing capability of PPDL in all of these systems. Interestingly, the $E_{binding}$ is considerably higher for the *i*PP–rich blends compared to the HDPE–rich blends, being in agreement with the abovementioned higher affinity of PPDL for *i*PP than for HDPE. In order to understand the origin of difference in $E_{binding}$ *i*PP/PPDL and HDPE/PPDL, a detailed study on the complex relationships between chain, molecular and topological aspects, structure, morphology and properties will be required, which falls out of the scope of the current work. The best compatibilizing effect is found for the PP" blend (*i*PP/HDPE w/w ratio is 80/20; *i*PP/HDPE/PPDL w/w/w ratio is 75/18/7). The ΔE_{mix}, derived from the CED and fractional volume of the individual components, shows a very similar trend as the $E_{binding}$ and is the lowest for *i*PP–rich blends, especially for PP" (Fig. 1D). The Flory-Huggins interaction parameter also shows the most negative value for the compatibilized *i*PP–rich blend PP" (Fig. 1C). The literature on solubility

parameters such as $E_{binding}$, Mixing Energy (ΔE_{mix}) and the Flory-Huggins interaction parameter (χ) for HDPE/iPP is scattered and to our best knowledge, we could not find these values at 190 °C (processing temperature) for HDPE/*i*PP to adjudge the quantitative reliability. Nevertheless, the calculated values are good qualitative indications for these HDPE/*i*PP/PPDL mixtures, which encouraged us for experimental investigation of PPDL potential as compatibilizer for HDPE/*i*PP blends of different compositions.

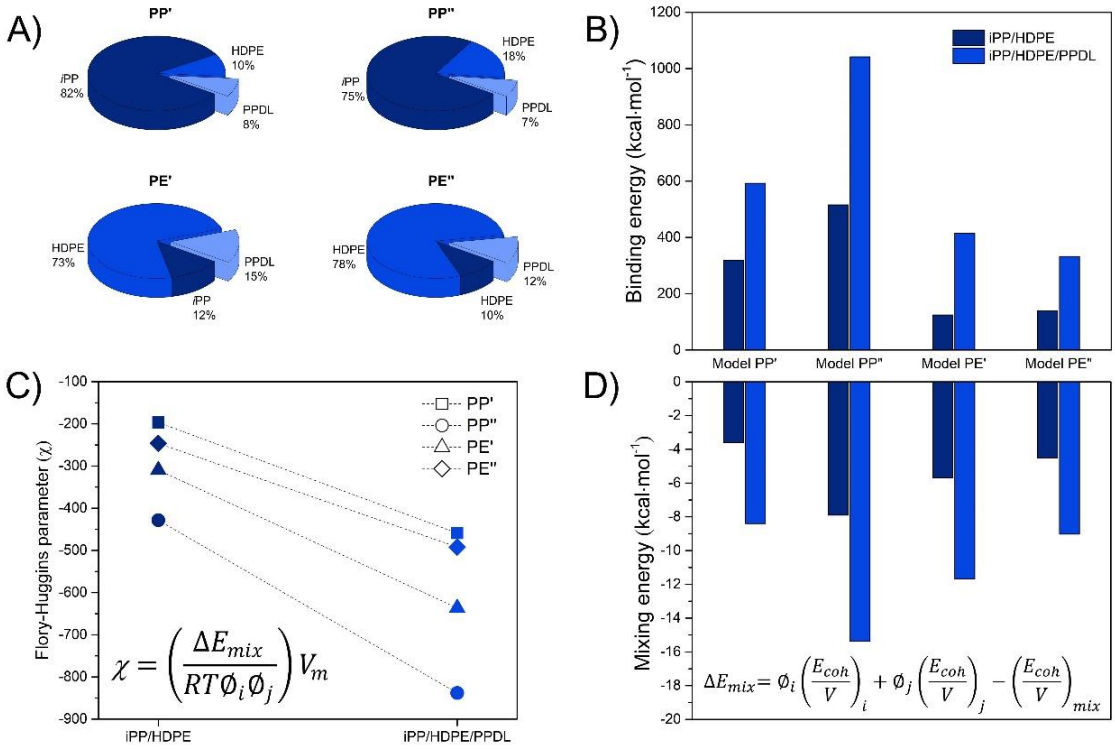

E)

Blend component	Model PP’	Model PP”	Model PE’
iPP (wt%)	82.3	74.6	12.4
HDPE (wt%)	9.7	18.1	73.1
PPDL (wt%)	8.0	7.3	14.5
HDPE/iPP ratio	11:89	20:80	85:15
iPP chains	12	12	1
HDPE chains	18	37	75
PPDL chains	2	2	2

Figure 1. Molecular Dynamics simulation of polymer miscibility. Blend compositions (A), binding energy $E_{binding}$ (B), Flory-Huggins interaction parameter χ (C) and mixing energy ΔE_{mix} (D) for non–compatibilized and compatibilized blends PP’, PP”, PE’ and PE” as well as input data for modeling (E).

To obtain more detailed insight into the interactions between PPDL, HDPE and *i*PP, wide angle x-ray scattering (WAXS) analysis of the individual blend components have been performed and thermal properties, as well as morphology of the binary blends, have been studied by differential scanning calorimetry (DSC) and transmission electron microscopy (TEM) analysis, respectively. The blends were prepared in a co-rotating twin screw extruder and analyzed by size exclusion chromatography (SEC) (Table S3; Fig. S7). The WAXS profiles show a clear resemblance of the orthorhombic crystal structures of PPDL and HDPE, whereas *i*PP crystallizes in the monoclinic α form (Fig. S1, Fig. 2 A–B).[45] The individual components in the blends crystalize independently and do not affect each other.[46] DSC analysis (Fig. 2C, S8) revealed that blending HDPE with PPDL leads to a significant increase in the crystallization temperature (T_c) of PPDL by 5 °C. This behavior can be explained by the aforementioned epitaxial crystal growth of PPDL onto HDPE lamellae, which function as nucleating agents[28]. Conversely, no increase in T_c of PPDL is observed upon blending with *i*PP, which is in agreement with the lack of epitaxy for this system. However, the T_c of *i*PP increased substantially from 113 °C to 121 °C when mixed with PPDL, which is likely a result of heterogeneous nucleation caused by spinodal decomposition leading to a reduced nucleation barrier.[47] TEM spectroscopy confirms that epitaxy, usually accompanied by clear lamellae penetration through the interface of immiscible components, is the origin of the affinity between HDPE and PPDL (Fig. 2 D-E).[28, 48] As a result, the HDPE/PPDL blend image does not reveal a clear interphase between PPDL and HDPE matrix. On the other hand, the morphological study of the *i*PP/PPDL blend exhibited a pronounced phase separation of the components with no indication of epitaxy for *i*PP/PPDL blends. Though, a rather rough interphase does suggest some partial mixing of the amorphous phase at the interface. Hence, both molecular dynamics simulations and experimental data demonstrate that PPDL has an affinity to both HDPE and to *i*PP, albeit different in nature. Whereas the resemblance in crystal structure of PPDL and HDPE results in epitaxy, PPDL and *i*PP show a better miscibility of the amorphous phases.

The next step was to experimentally test the efficiency of PPDL as a compatibilizer for *i*PP/HDPE blends. As mentioned earlier, most *i*PP and HDPE recycle streams contain more than 80 % of the main component. Whereas HDPE–rich recycled materials reveal good mechanical properties, the mechanical

performance of the *i*PP–rich congeners is unsatisfactory due to its brittle nature. We therefore focused on *i*PP–rich blends and used compositions with 80/20 and 90/10 *i*PP/HDPE w/w ratios.

First, the thermal properties (Fig. S9 and Table S4;) and morphologies (Fig. 3, S10–S12) of the ternary *i*PP/HDPE/PPDL blends were investigated. The *i*PP/HDPE/PPDL 90/10/5 and 80/20/5 w/w/w compositions show the same increase (5 °C) in the T_c of the PPDL as for the binary HDPE/PPDL blend. The T_c of *i*PP also increases for both blends, but less as compared to the *i*PP/PPDL blend (4 °C versus 8 °C). Most likely, the crystallization of HDPE results in heterogeneous nucleation of the *i*PP.[49, 50] The presence of distinct PPDL crystallization and melting peaks indicates that upon cooling even a small amount of PPDL forms a separated phase in the blends. Comparison of the TEM images of the *i*PP/HDPE 90/10 w/w and *i*PP/HDPE/PPDL 90/10/5 w/w/w compositions reveals a substantial decrease of the HDPE domain size from an average 400 nm to 200 nm upon addition of PPDL, indicative for the compatibilizing effect of the latter (Fig. 3 A–B, S10). Although the HDPE is well dispersed, slightly less pronounced reduction of the HDPE domain sizes has been observed for the *i*PP/HDPE/PPDL 80/20/5 w/w/w blend compared to the uncompatibilized *i*PP/HDPE 80/20 w/w blend (Fig. S11–S12). This might originate from an insufficient amount of the compatibilizer in respect to the contribution of HDPE in the final product. For both blends, the presence of PPDL leads to a significant change of the interphase between the blend components, which allows HDPE lamellae penetration into *i*PP matrix (Fig. S10, S11).

A)

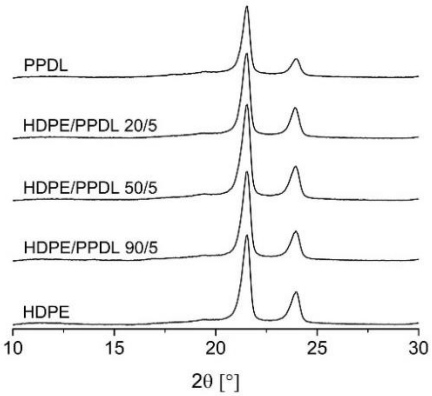

B)

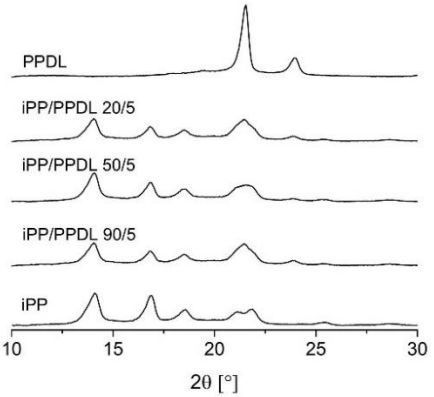

C)

Sample	T_m °C	T_c °C	ΔH_m J·g^{-1}
*i*PP	161.4	113.5	74.8
HDPE	131.1	118.5	180.5
PPDL	94.7	79.0/33.1	108.7
*i*PP/PPDL 90/5	162.8/93.0	121.0/79.7	90.4/4.0
*i*PP/PPDL 50/5	162.3/93.6	119.0/80.3	79.7/12.0
*i*PP/PPDL 20/5	162.3/93.8	120.3/80.6	84.3/16.9
HDPE/PPDL 90/5	129.7/93.2	117.9/84.5	149.4/3.4
HDPE/PPDL 50/5	130.5/93.7	117.2/84.2	151.4/5.5
HDPE/PPDL 20/5	129.5/93.6	117.5/84.5	127.3/14.4

D)

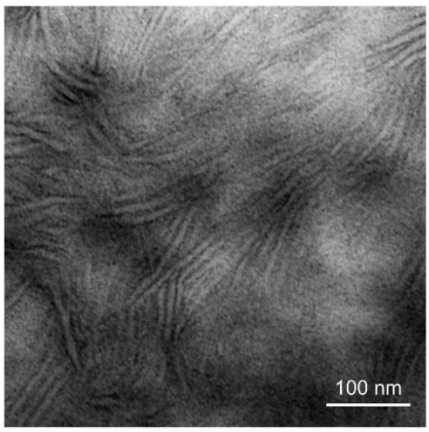

E)

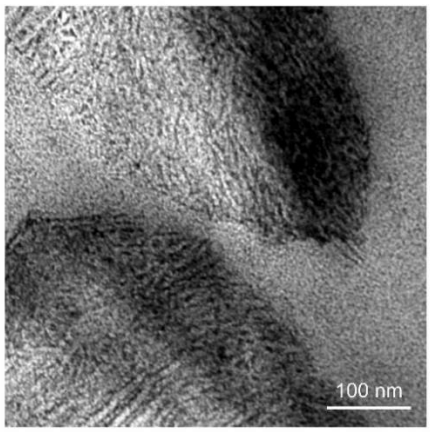

Figure 2. Morphology and thermal analysis of HDPE/PPDL and *i*PP/PPDL blends. WAXD analysis HDPE/PPDL, *i*PP/PPDL and individual polymers used for their preparation (A, B), thermal properties of the HDPE/PPDL, *i*PP/PPDL blends and individual polymers used for their preparation analyzed by DSC (C), TEM analysis of HDPE/PPDL (D) and *i*PP/PPDL (E) 90/10 w/w blends.

Atomic force microscopy (AFM) quantitative nano-mechanical mapping (QNM) was applied for a quantitative mapping of the blends' nano-mechanical properties (Fig. S13, S14). Peak-force QNM, used for the modulus mapping of the blends' components, revealed two well-defined *i*PP and HDPE phases for the uncompatibilized *i*PP/HDPE 90/10 w/w blend with an elastic modulus of 2.5 ± 0.2 GPa and 1.7 ± 0.2 GPa, respectively. It is important to underline that typically the viscoelastic responses of polymer samples are frequency dependent and an increase of the storage modulus and the glass transition temperature might be observed at higher frequencies.[51] Indeed, AFM-QNM analyses performed at frequency of 2000 Hz, which is 1000 time higher than the typical bulk mechanical testing by DMTA analysis, demonstrate slightly higher modulus values for both the *i*PP and the HDPE phase in the tested blend sample in comparison to the DMA results performed at orders lower frequency[52]. Addition of PPDL to the *i*PP/HDPE 90/10 w/w composition did not seem to have a significant effect on the *i*PP (2.5 ± 0.2 GPa to 2.2 ± 0.2 GPa) and HDPE (1.7 ± 0.2 GPa to 1.3 ± 0.2 GPa) moduli as the values are indistinguishable within the error on the measurement. A similar result was obtained for the *i*PP/HDPE/PPDL 80/20/5 w/w/w composition. Whereas no drop in glass transition temperature (T_g, determined using DMTA) was observed for the ternary blends *i*PP/HDPE/PPDL, the lower T_g values of binary *i*PP/PPDL and HDPE/PPDL blends suggest a plasticizing effect for these blends (Table S5; Fig. S15–S18). The incorporation of increasing quantities of PPDL into *i*PP resulted in a reduction of the T_g from 7 °C to 3 °C, being in agreement with the theoretical values calculated using Flory-Fox equation (see SI: Discussions concerning compatibilizer distribution in the blends). Additionally, above the glass transition temperatures, only a minor decrease in the *i*PP storage and loss moduli was observed, indicating a small impact of PPDL on the viscoelastic properties of the polypropylene, as also proven by AFM-QNM. Importantly, the storage and loss moduli of the *i*PP/HDPE blends compatibilized by PPDL maintain the desired performance characteristics, ensuring the suitability of the blends for high temperature applications designed for *i*PP.

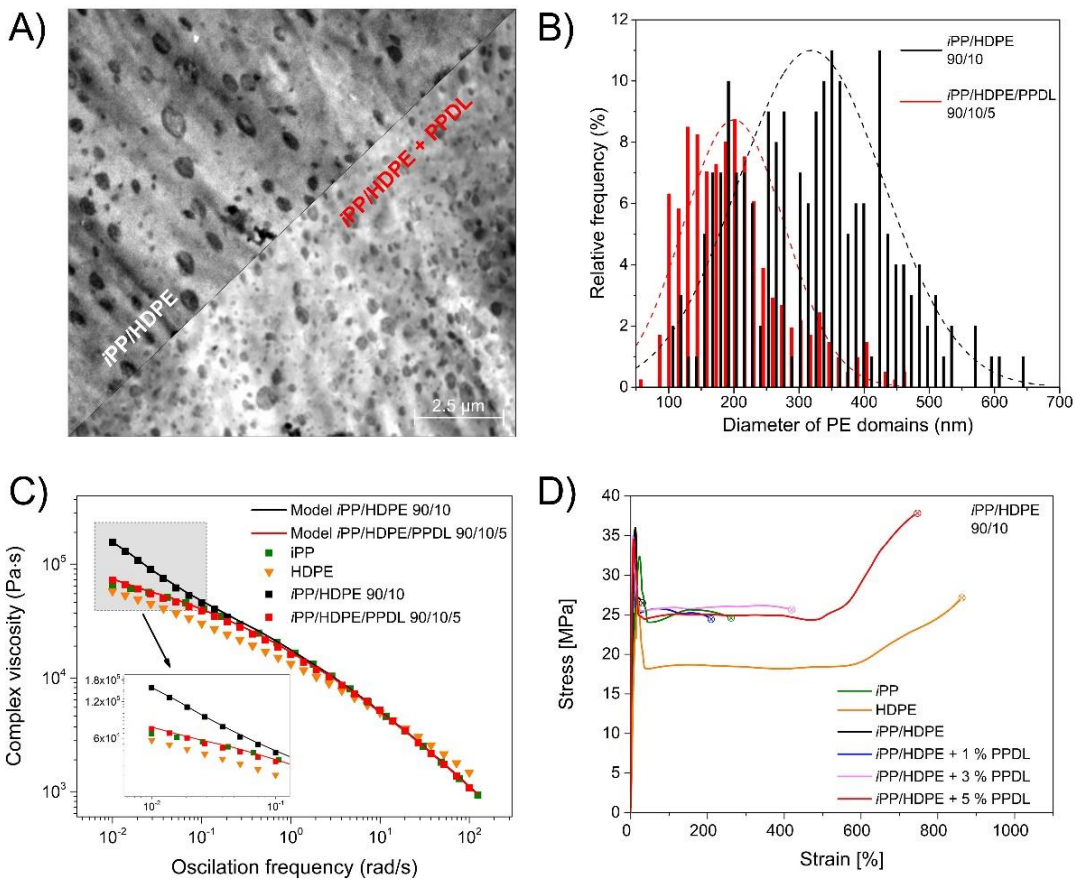

Figure 3. Morphology and performance analysis of *i*PP/HDPE 90/10 w/w blends. Transmission electron microscopy image of the *i*PP/HDPE 90/10 w/w blend and *i*PP/HDPE/PPDL 90/10/5 w/w/w blend (A). The compatibilizing effect of PPDL visualized by HDPE dispersed phase size determination in *i*PP/HDPE and *i*PP/HDPE/PPDL blends using TEM (B). Measured (symbols) and calculated (line) complex viscosity (η*) of *i*PP, HDPE, uncompatibilized *i*PP/HDPE 90/10 blend and compatible *i*PP/HDPE/PPDL 90/10/5 composition. Samples were tested under oscillation frequency (ω) in a constant temperature 190 °C (C). Static mechanical properties measurements of the compatibilized *i*PP/HDPE/PPDL blend, the uncompatibilized *i*PP/HDPE blend and *i*PP, HDPE and PPDL reference materials (D).

The effect of the PPDL compatibilizer on *i*PP/HDPE 90/10 w/w blends was also assessed by means of shear rheology in the linear viscoelastic regime (Fig. 3C). The two pure components, *i*PP and HDPE exhibit a quantitatively similar flow curve, characterized by the onset of a Newtonian regime, and a well-resolved shear thinning region with a slope between 0.7 and 0.8, in agreement with past works on

melts, and in particular polydisperse isotactic polypropylenes.[53] The uncompatibilized *i*PP/HDPE 90/10 w/w blend yielded a rheological spectrum that displays a low-frequency viscosity upturn, that sets the blend far from a Newtonian behavior, reflecting poor miscibility and the presence of agglomerates which prevents flow behavior. Conversely, the *i*PP/HDPE 90/10 blend compatibilized with 5 % PPDL shows Newtonian behavior at low-frequencies and a slightly higher viscosity compared to the reference *i*PP (see inset of Fig. 3C). That is, the presence of PPDL allowed for a blend, with intact shear thinning region, relevant for the processability of the polymers. The model of Gramespacher and Meissner (G–M) was adopted to capture the experimental rheological observations, and highlight the effect of the PPDL on the blends.[54] The G–M model is based on the additive contributions to the complex shear modulus of the continuous and dispersed phases, as well as the polymers interface. The latter is a function of the average domain size of the dispersed domains, and the interfacial energy. Note that the linear mixing rule works well when the blend constituents have Newtonian viscosities of the same order of magnitude, as in the present case.[54] For the non-compatibilized blend, an average domain size of 318.5 nm taken from Fig. 3B, and a typical interfacial energy for *i*PP/HDPE blends of 1.6 mN/m were adopted.[55] With such parameters, the model well-described the observed data (see black line in Fig. 3C). For the compatibilized blend, with an average domain size of 200 nm taken from Figure 3B, the best fit of the data was obtained with a lower interfacial energy equal to 0.1 mN/m. The result of this model corroborates the hypothesis that PPDL lowers the interfacial energy between the investigated polyolefins.

Although molecular dynamics simulations, physical properties analyses and morphological studies strongly indicate that PPDL functions as a compatibilizer for HDPE/*i*PP blends, the ultimate proof is provided by a static mechanical properties study (Table 1, Table S6, Fig. 3D, S19, S20). Pristine *i*PP and HDPE display ductile behavior when exposed to external uniaxial tension, which for the grades used in our study resulted in an average elongation at break of 290 % and 930 %, respectively. With a stress (273 MPa) and strain (1050 %) at break, the tensile behavior of PPDL strongly resembles that of HDPE. Conversely, the brittle failure with a maximum strain at break of only 32 % of the uncompatibilized *i*PP/HDPE blends is illustrative for their poor mechanical performance. Addition of a small amount of PPDL, miscible with *i*PP, epitaxially crystalizing onto HDPE and partially

localized at the interphase (Fig. S21, S22), indeed appeared to have a profound and unexpected effect on the mechanical properties of these blend. Surprisingly, the strain at the break values for both compatibilized *i*PP/HDPE/PPDL 90/10/5 and 80/20/5 w/w/w blends (726 % and 656 %, respectively) did not only approach that of pristine *i*PP, as was hoped, but they are even over 2 times higher than the value for *i*PP and are close to the strain at the break of HDPE. Additionally, a strain hardening comparable as for HDPE provides a significant enhancement of the stress at break from 23 MPa to 32 MPa. Importantly, the addition of 5 % of PPDL does not lead to a decrease of the yield stress or modulus. As a result, addition of a small amount of PPDL transforms the brittle uncompatibilized *i*PP/HDPE blend into a material with a considerably increased toughness than pristine *i*PP and HDPE. In the interest to optimize the compatibilizer amount, *i*PP/HDPE compositions containing 3 wt% and 1 wt% of PPDL were also tested (Table S6; Fig. S20). Lowering the amount of PPDL from 5 wt% to 3 wt% and finally to 1 wt% leads to a gradual drop of the stress and strain at break. But even with 1 wt% of PPDL in the blend, a strain at break similar to that of a neat *i*PP is obtained. It is worth mentioning that injection molded specimen revealed improved mechanical properties as the compression molded counterparts (Fig. S19, Table S6), clearly proving the potential for large scale industrial application of this approach to compatibilize *i*PP/HDPE blends with a simple polyester like PPDL.

Table 1. Static mechanical properties of the *i*PP/HDPE, *i*PP/HDPE/PPDL blends and polymers used for their preparation.

Sample	Yield Stress MPa	Yield Strain %	Stress at the break MPa	Strain at the break %
*i*PP	34.7±1.8	13.5±3.4	20.5±2.2	292±121
HDPE	28.9±1.4	11.1±2.8	23.2±5.5	934±123
PPDL	19.1±0.8	9.7±1.8	27.3±2.0	1050±116
*i*PP/HDPE 90/10	34.8±1.3	11.7±1.7	23.0±8.3	32±25
*i*PP/HDPE 80/20	33.9±0.8	9.1±1.8	21.8±9.9	26±18
iPP/HDPE/PPDL 90/10 + 1 % PPDL	34.3±0.5	6.6±0.3	19.2±10.5	289±238
iPP/HDPE/PPDL 90/10 + 3 % PPDL	34.9±0.6	6.0±0.2	28.2±10.9	464±191
*i*PP/HDPE/PPDL 90/10 + 5 % PPDL	34.5±0.4	8.3±0.5	31.7±8.6	726±127
*i*PP/HDPE/PPDL 80/20 + 5 % PPDL	34.5±0.8	7.6±0.6	24.0±10.4	656±146

We have demonstrated that a simple to produce aliphatic polyester can function as a highly effective compatibilizer for otherwise brittle, low value *i*PP/HDPE blends. The origin of the compatibilizing effect of PPDL for *i*PP/HDPE blends is twofold in nature. PPDL reveals epitaxial growth from HDPE lamellar crystals and miscibility with the amorphous phase of *i*PP. PPDL compatibilized *i*PP–rich blends are characterized by a decrease of the HDPE domain size from 400 to 200 nm, an increase of the T_c of PPDL due to epitaxy and a reduced T_g of the *i*PP phase due to the partial miscibility of the amorphous phases of PPDL and *i*PP. The static mechanical properties of the PPDL-compatibilized *i*PP/HDPE blends are exceptional showing a strong toughening effect of PPDL on the *i*PP/HDPE blend. The surprisingly effective compatibilizer transforms brittle *i*PP/HDPE blends into unexpectedly tough materials that even outperform the reference HDPE and *i*PP materials. Its simplicity makes this approach easily scalable and unlocks a potential route to convert large amounts of mixed polyolefin waste into high added value, high volume products.

MATERIALS AND METHODS

MATERIALS

Isotactic PP (PP531PH, SABIC), HDPE (HDPE B5429, SABIC), Irganox 1010 (BASF), ω-pentadecalactone (PDL, > 97 %, Merck), benzyl alcohol (99.8 %, Merck), calcium hydride (> 97 %, Merck), Al(CH3)3 (2 M solution in toluene) (Merck), N,N'-bis(salicylidene)-2,2-dimethyl-1,3-propanediamine (98 %, Sigma-Aldrich). Dry ethanol (Biosolve) was used as received. Tetrahydrofuran and toluene (Sigma-Aldrich) were dried using an MBraun-SPS-800 purification column system.

Synthesis of Salen aluminum methyl. In a nitrogen filled MBraun glove box, a toluene solution of N,N'-bis(salicylidene)-2,2-dimethyl-1,3-propanediamine (Salen ligand; 0.4 M, 20 mmol, 50 mL) was added to a toluene solution (0.5 M, 10 mmol, 20 mL) of trimethyl aluminum. After 1 hour, the Schlenk flask was taken out of the glove box and the pale yellow mixture was heated to 100 °C for 2 hours after which the solvent was removed in vacuo leaving Salen aluminum methyl as an off-white solid in quantitative yield.

Synthesis of polypentadecalactone (PPDL). In a nitrogen filled MBraun glove box, the Salen aluminum methyl precatalyst (97.2 mg, 0.28 mmol) was dissolved in toluene (4.0 g) and treated with benzyl alcohol (22.5 mg, 0.21 mmol). The glass crimp cap vial containing the clear catalyst solution was tightly closed and removed from the glovebox. The catalyst solution was introduced by syringe into a steel reactor charged with molten PDL (50 g, 0.208 mol). The reactor content was stirred (300 rpm) using a magnetic stirrer and heated (140 °C) using a heating plate for 24 h. Then the product was removed from the reactor, washed with methanol and dried in vacuum oven at 50 °C for 48 h.

Preparation of *i*PP/HDPE, *i*PP/HDPE/PPDL, *i*PP/PPDL and HDPE/PPDL blends

All blends were prepare using exactly the same procedure, only differing in the amounts of *i*PP, HDPE and PPDL. The appropriate amounts of blend components (approx. 40 g in total) were measured, mixed with antioxidant Irganox 1010 (2500 ppm) and fed into a co-rotating twin-screw extruder heated to 190 °C and a screw rotation rate set at 120 rpm resulting in a residence time of 1.5 min. To ensure good mixing, each mixture was passed 2 × through the extrusion.

Typical procedure for the preparation of an *i*PP/HDPE/PPDL blend *i*PP (PP531PH, 36 g) and HDPE (HDPE B5429, 4 g) and PPDL (2 g) with antioxidant Irganox 1010 (2500 ppm) were fed into a co-rotating twin-screw extruder. The extruder temperature was set at 190 °C and the screw rotation rate was set at 120 rpm. The mixture was extruded 2 × with an average residence time of 1.5 min.

Typical procedure for the samples preparation via injection molding. After blending in the extruder, the mixture was evacuated directly to a mini-injection molding machine with a stainless steel mold in accordance with ISO 527-3, type 5A. The injection temperature was set at 190 °C, and the process took place under a pressure of 15 MPa.

Typical procedure for the samples preparation via compression molding Compression molding of the polymer blends was performed using PP ISO settings on a LabEcon 600 high-temperature press (Fontijne Presses, The Netherlands). The materials were introduced into a Teflon mold to prepare samples with a thickness of 1 mm. The program for the compression molding involved the following steps: heating to 190 °C for 5 min under 100kN force followed by cooling to room temperature for 10 min under applied force.

METHODS

Molecular dynamics model preparation. To create a realistic model, we used the number average molecular weights of the HDPE (M_n = 13.0 kg·mol^{-1}), *i*PP (M_n = 166.9 kg·mol^{-1}) and PPDL (M_n = 99.5 kg·mol^{-1}) that were actually used in blending experiments in this study. The molecular weights needed to be normalized by a factor of 10 resulting in HDPE, *i*PP and PPDL chains consisting of 47, 400 and 40 monomeric units, respectively (Figure 1). All Molecular Dynamics Simulations have been performed at the process temperature at which the polymers were blended experimentally (190 °C). This temperature was also chosen to avoid problems due to the semi–crystalline nature of all three polymers. Based on calculations and experimental data, the density of 0.76 g·cm^{-3} was selected for the polymer mixtures.[56]

The simulations were performed using BIOVIA Materials Studio 2022.[57] The Amorphous Cell module was used to construct representative models of the different polymer mixtures.[58] The Forcite module was used for periodic boundary condition-based molecular dynamics calculations to predict key properties. The most advanced Condensed-phase Optimized Molecular Potentials for Atomistic Simulations Studies (COMPASSIII) was selected for the molecular dynamics simulations.[59-62] In COMPASSIII, the total energy (E_{total}) of the simulation system is represented by the summation and non-bonding interactions (eq. 1, 2).

$$E_{\mathrm{total}} = E_{\mathrm{b}} + E_{\mathrm{q}} + E_{\emptyset} + E_{\chi} + E_{\mathrm{cross}} + E_{\mathrm{vdw}} + E_{\mathrm{ele}} \quad (1)$$

$$E_{total} = E_{valence} + E_{cross} + E_{nonbond} \quad (2)$$

Four different models with different *i*PP and HDPE ratios were used. The models PP’ and PP” are *i*PP-rich while PE’ and PE” are HDPE-rich. Detailed description of these models is covered in Table S2 and the models are depicted in Fig. S5 and Fig. 1. Each set’s constructed 3D cubic cell was subjected to a series of geometry optimization and molecular dynamics simulations using a Forcite module as implemented in Materials Studio 2022. Firstly, the cell was annealed with a periodic boundary condition to 190 °C for 0.5 ps with a pressure of 10−3 GPa to eliminate internal stress. Subsequently, the cells were subjected to equilibration: First the geometry was optimized using the smart method (including steepest descent, conjugate gradient, and the Newton method) for more than 105 steps until a convergent value reached. Then the cubic cells were refined by ultra-short

molecular dynamics NVT (constant number of particles, N, volume, V, and temperature, T) simulation equilibrated at 190 °C with a time step of 0.5 fs for 5000 steps followed by a NPT ensemble run at 190 °C with a time step of 0.5 fs for 30000 steps. Minimum fluctuations in density and energy were two cut off criteria to determine the equilibrium of the system. Finally, the equilibrated cells were subjected to a production run of NPT (constant number of particles, pressure, and temperature) ensemble at 190 °C for 1000 ps. The miscibility parameters such as Binding Energy ($E_{binding}$), Mixing energy (ΔE_{mix}), and Flory-Huggins interaction parameter (χ) were calculated for all four models and respected values are reported in Table S2. The energy vs time maps of all four models are depicted in Fig. S6. From Fig. S6 it can be concluded that the energy of the system shows a minute fluctuation at approximately the average value, indicating that the systems are in an equilibrium state. Once the cubic cells of the ternary blends PP'(PP/HDPE/PPDL), PP" (PP/HDPE/PPDL), PE'(PP/HDPE/PPDL) and PE" (PP/HDPE/PPDL) were constructed, they were used to construct and analyze the corresponding binary blends PP'(PP/HDPE), PP'(PP/PPDL), PP'(HDPE/PPDL). To be consistent in sample volume, the third components of the original ternary blends were removed and the density of the remaining two components were taken as variable.

The conceptual basis of calculated properties

Hildebrand solubility parameter (δ): May be calculated by the square root of the cohesive energy density (CED) as shown in eq. 3 and describes the attractive strength between the molecules of the material eq. 4, exerting a huge influence on blend miscibility.

$$\delta = \sqrt{CED} \qquad (3)$$

$$\delta_{T^2} = \delta_{vdw^2} + \delta_{ele^2}, \delta_{ele^2} = \delta_{H^2} + \delta_{P^2} \qquad (4)$$

The cohesive energy densities (CED): are known to vary considerably with the molecular weight of the polymer. If all intramolecular forces are eliminated, CED is defined (eq. 5) as the increase in energy per mole of a material.[33,34]

$$CED = \left({}^{E_{coh}}/_{V}\right) \quad (5)$$

Mixing energy: The computational results of CED allow the calculation of the energy of mixing, ΔE_{mix}[38], of binary mixture of components I and j according to eq. 6.

$$\Delta E_{mix} = \emptyset_i \left(\frac{E_{coh}}{V}\right)_i + \emptyset_j \left(\frac{E_{coh}}{V}\right)_j - \left(\frac{E_{coh}}{V}\right)_{mix} \qquad (6)$$

The Hansen solubility parameters: a way of predicting if one material will dissolve in another and form a solution. They are based on the idea that like dissolves like where one molecule is defined as being 'like' another if it bonds to itself in a similar way. Specifically, each molecule is given three Hansen parameters, δd, δp, δh, each generally measured in MPa.

Flory-Huggins interaction parameter (χ): can be calculated from ΔE_{mix} using eq. 7. [42-44, 62] The smaller the Flory–Huggins parameter is, the better is the compatibility of the two components.

$$\chi = \left(\frac{\Delta E_{mix}}{RT\emptyset_i\emptyset_j}\right)V_m \quad (7)$$

Fractional volume: The volume fraction (ϕ_i) of a component i in the composite according to eq. 8, where ρ_c is the average density, ρ_i is the density of component i in the composite and C_i is its concentration in wt%.[40]

$$\phi_i = \left(\frac{C_i}{100}\right)\left(\frac{\rho_c}{\rho_i}\right) \quad (8)$$

Binding Energy: The binding energy ($E_{binding}$) , defined as the negative value of the interaction energy E_{inter}, is a measure of the compatibility between two components mixed with each other.[39] A negative $E_{binding}$ represents poor compatibility between two components while a large positive $E_{binding}$ represents good compatibility. The $E_{binding}$ between components j and i may be obtained by eq. 9.

$$E_{binding} = -E_{Inter} = -(E_{Complex} - E_i - E_j) \quad (9)$$

Samples analysis

Wide-angle X-ray scattering (WAXS**)** measurements were performed on a computer-controlled goniometer coupled with a CuKα radiation source (λ = 0.154 nm) at 30 kV and 50 mA (Panalytical B.V., Almelo, The Netherlands). The analyzed samples were prepared using compression molding procedure.

M_n, M_w and the polydispersity index were determined using Size Exclusion Chromatography (SEC). The measurements were performed at 150 °C on a Polymer Char GPC-IR® built around an Agilent GC oven model 7890, equipped with an autosampler and the Integrated Detector IR4. 1,2-dichlorobenzene (o-DCB) was used as an eluent at a flow rate of 1 mL·min−1. PS standards were selected to provide calibration points. The injection volume was 200 µL. The SEC data were processed using Calculations Software GPC One®.

Melting (T_m) and crystallization (T_c) temperatures as well as enthalpies of the transitions were measured by DSC using a DSC Q100 from TA Instruments. The measurements were carried out at a heating and cooling rate of 10 °C·min^{-1} from −40 °C to 230 °C under nitrogen flow (15 ml·min^{-1}). The transitions were deduced from the second heating and cooling curves.

Details of the samples' morphology were examined with a transmission electron microscope (Tesla BS 500, Tesla, Czech Republic), operating at 90 kV. Samples for TEM examination, in the form of ultra-thin sections approx. 60 nm thick, were prepared by cryo-ultra-sectioning with an ultramicrotome (PowerTome PC, Boeckeler, USA) equipped with a 35 ° diamond knife (Diatome, Switzerland). Ultra-thin sections were placed on standard copper grids for TEM examination. Before cutting the analyzed samples were exposed to the vapor of RuO4 at room temperature for a 24 h.[63] From TEM micrographs the structural information on HDPE dispersion was extracted using the image analysis software ImageJ (National Institutes of Health, USA).[64] Size determinations were made by evaluating at least 300 domains of HDPE for each sample.

Atomic Force Microscopy (AFM) was performed using Dimension FastScan AFM system from Bruker utilizing tapping mode AFM tips (Model TESPA-V2, k: 42 N·m−1, f: 320 kHz). The software Nanoscope Analysis 1.5 from Bruker was used as the computer interface for operation and analysis of AFM measurements. All AFM measurements were performed at ambient conditions. Samples were cryo-microtomed at −120 °C. Height and phase images were recorded simultaneously at a scan rate of 1 Hz with a resolution of 512 × 512 pixels. Optical imaging integrated in the AFM setup was first used before AFM measurement to select the area of interest for imaging. The nanomechanical properties of the samples were characterized by a high accuracy quantitative nanomechanical mapping mode (HA-QNM) at frequency of 0.7 Hz using TAP-150-30 silicon cantilever tips (Bruker AFM Probes, 5 N/m nominal spring constant) at ambient conditions. QNM mode enables the quantitative measurements of nano-scale material mechanical properties by performing pixel-wise force curves in the scanned area in a real time. Analysis of the individual force curve data by the AFM Nano-scope software provides a map of material properties with the same resolution as a topography image. Thereafter, the elastic modulus of the scanned surface was extracted from the force curve using

the Derjaguin-Muller-Toropov (DMT) model and presented in the modulus mapping images.

Dynamic mechanical thermal analysis (DMTA) was performed using a TA Instruments Q800 DMA. Samples were tested by strain-controlled temperature ramp with the frequency of 1 Hz. The measurements were performed using film-tension mode. The applied temperature profile was from −150 °C to the melting point of the sample with the ramp 2 °C·min^{-1}. The glass transition temperature was calculated as the maximum of the tangent delta signal.

Tensile tests were performed using a Zwick type Z020 tensile tester equipped with a 2.5 kN load cell according to ISO 527-3 standard (specimen type 1BA). A grip-to-grip separation of 40 mm was used. The samples were pre-stressed to 3 N, then loaded with a constant cross-head speed 40 mm·min^{-1}. Young Modulus was estimated with a constant cross-head speed of 1 mm·min^{-1} with external extensometer. The reported values are an average of at least 10 measurements of each composition.

A Discovery Hybrid Rheometer DHR-2 (TA instruments) equipped with a force rebalance transducer (FRT) was used for the shear rheological experiments. Stainless steel 25 mm diameter parallel plates were adopted for all the experiments. The temperature was controlled via a convection oven fed with nitrogen gas to minimize sample degradation. Samples were shaped into discotic specimen by means of hot-pressing, well above their glass transition temperature (typically at 180 °C), and then cooled to room temperature. After loading, all the samples were subjected to 30 minutes annealing at 180 °C to erase residual stresses, and to get rid of possible air bubbles, due to the hot pressing. After that, the following rheological protocol was adopted for each sample: i) dynamic strain amplitude sweep at ω= 100 rad·s^{-1} to detect the linear viscoelastic regime, ii) dynamic frequency sweep at strain amplitudes in the range of 1 – 5 % and frequency range between 100 and 0.01 rad·s^{-1}.

The Gramespacher and Meissner (G-M) model: According to the GM model, the frequency response of a polymer blend is given by two contributions[37]: 1) the viscoelastic response of the individual components that constitute the dispersed and the continuous phases, and 2) the interfacial tension. Hence, the total complex shear modulus writes as eq. 10.

$$G^*_{\text{blend}} = \emptyset\, G^*_{\text{PP}} + (1 - \emptyset) G^*_{\text{HDPE}} + G^*_{\text{interface}} \qquad (10)$$

with ϕ being the volume fraction of the dispersed phase (PP in our case), and G*PP, G*HDPE, G*interface the complex shear modulus of the PP, HDPE and the interfacial contribution, respectively. It is important to highlight the fact that the linear mixing rule may fail if the Newtonian viscosities of the two components are very different.

The effect of the interfacial tension on the moduli of Newtonian liquids was first addressed by Choi and Schowalter.[65] Subsequently, in 1989, Scholz et al.[66] reported a simplified version of the previous model, where the dynamic moduli, storage (G') and loss (G''), of a blend, can be calculated as:

$$G'(\omega) = \eta \frac{\omega^2(\tau_1-\tau_2)}{1+\omega^2\tau_1^2} = \frac{\eta}{\tau_1}\left(1-\frac{\tau_2}{\tau_1}\right)\frac{\omega^2\tau_1^2}{1+\omega^2\tau_1^2} \qquad (11)$$

$$G''(\omega) = \eta \frac{\omega^3\tau_1\tau_2-\omega)}{1+\omega^2\tau_1^2} = \frac{\eta}{\tau_1}\left(1-\frac{\tau_2}{\tau_1}\right)\frac{\omega\tau_1}{1+\omega^2\tau_1^2} + \omega\eta\frac{\tau_2}{\tau_1} \qquad (12)$$

The parameters of the above-reported equations are defined as:

$$\eta = \eta_{\text{matrix}}\left[1+\phi\frac{(5k+2)}{2(2k+1)}+\phi^2\frac{5(5k+2)^2}{8(k+1)^2}\right] \qquad (13)$$

$$\tau_1 = \tau_0\left[1+\phi\frac{5(19k+16)}{4(k+1)(2k+3)}\right] \qquad (14)$$

$$\tau_2 = \tau_0\left[1+\phi\frac{3(19k+16)}{4(k+1)(2k+3)}\right] \qquad (15)$$

$$\tau_0 = \frac{\eta_{\text{matrix}}R}{\alpha}\frac{(19k+16)(2k+3)}{40(k+1)} \qquad (16)$$

$$k = \frac{\eta_{\text{dispersed}}}{\eta_{\text{matrix}}} \qquad (17)$$

η_{matrix} and $\eta_{dispersed}$ are the Newtonian viscosities of the matrix and dispersed phase, respectively, R is the average radius of the dispersed domains, and α is the interfacial tension. It follows that the dynamic moduli of the blends write as follow:

$$G'_{\text{blend}} = \phi G'_{\text{PP}} + (1-\phi)G'_{\text{HDPE}} + \frac{\eta}{\tau_1}\left(1-\frac{\tau_2}{\tau_1}\right)\frac{\omega^2\tau_1^2}{1+\omega^2\tau_1^2} \qquad (18)$$

$$G^{"}_{\text{blend}} = \phi G^{"}_{\text{PP}} + (1-\phi) G^{"}_{\text{HDPE}} + \frac{\eta}{\tau_1}\left(1-\frac{\tau_2}{\tau_1}\right)\frac{\omega\tau_1}{1+\omega^2\tau_1^2} + \omega\eta\frac{\tau_2}{\tau_1} \quad (19)$$

Lastly, the complex viscosity of the resulting blend writes as:

$$\eta^*_{\text{blend}} = \frac{\sqrt{{G'_{\text{blend}}}^2 + {G^{"}_{\text{blend}}}^2}}{\omega} \quad (20)$$

REFERENCES

(1) M. D. Tabone, J. J. Cregg, E. J. Beckman, A. E. Landis, Sustainability Metrics: Life Cycle Assessment and Green Design in Polymers. *Environ. Sci. Technol.* **2010**, 44, 8264–8269.

(2) T. Hees, F. Zhong, M. Stürzel, R. Mülhaupt, Tailoring Hydrocarbon Polymers and All-Hydrocarbon Composites for Circular Economy. Macromol. *Rapid Commun.* **2019**, 40, 1800608.

(3) X. Wu, A. Tennakoon, R. Yappert, M. Esveld, M. S. Ferrandon, R. A. Hackler, A. M. LaPointe, A. Heyden, M. Delferro, B. Peters, A. D. Sadow, W. Huang, Size-Controlled Nanoparticles Embedded in a Mesoporous Architecture Leading to Efficient and Selective Hydrogenolysis of Polyolefins. *J. Am. Chem. Soc.* **2022**, 144, 5323–5334.

(4) N. M. Wang, G. Strong, V. DaSilva, L. Gao, R. Huacuja, I. A. Konstantinov, M. S. Rosen, A. J. Nett, S. Ewart, R. Geyer, S. L. Scott, D. Guironnet, Chemical Recycling of Polyethylene by Tandem Catalytic Conversion to Propylene. *J. Am. Chem. Soc.* **2022**, 144, 18526–18531.

(5) A. Arroyave, S. Cui, J. C. Lopez, A. L. Kocen, A. M. LaPointe, M. Delferro, G. W. Coates, Catalytic Chemical Recycling of Post-Consumer Polyethylene. *J. Am. Chem. Soc.* **2022**, 144, 23280–23285.

(6) K. M van Geem, Plastic waste recycling is gaining momentum. *Science* **2023**, 381, 607–608.

(7) Z. Xu, N.E Munyaneza, Q. Zhang, M. Sun, C. Posada, P. Venturo, N.A. Rorrer, J. Miscall, B.G. Sumpter, G. Liu, Chemical upcycling of polyethylene, polypropylene, and mixtures to high-value surfactants. *Science* **2023**, 381, 666-671.

(8) M. Xanthos, Recycling of the #5 Polymer. *Science* **2012**, 337, 700–702.

(9) K. A Chaffin, J. S. Knutsen, P. Brant, F.S Bates. High-Strength Welds in Metallocene Polypropylene/Polyethylene Laminates. *Science* **2000**, 288, 2187–2189.

(10) F. C. Stehling, T. Huff, C. S. Speed, G. Wissler, Structure and properties of rubber-modified polypropylene impact blends. *J. Appl. Polym. Sci.* **1981**, 26, 2693–2711.

(11) L. D'Orazio, R. Greco, E. Martuscelli, G. Ragosta, Effect of the addition of EPM copolymers on the properties of high density polyethylene/isotactic polypropylene blends: II. Morphology and mechanical properties of extruded samples. *Polym. Eng. Sci.* **1983**, 23, 489–497.

(12) C. Huang, M. Olvera de la Cruz, Analytic Interface Profile Approximation for Ternary Polymer Blends. *Macromolecules* **1996**, 29, 6068–6070.

(13) V. Busico, R. Cipullo, N. Friederichs, S. Ronca, M. Togrou, The First Molecularly Characterized Isotactic Polypropylene-block-polyethylene Obtained via "Quasi-Living" Insertion Polymerization. *Macromolecules* **2003**, 36, 3806–3808.

(14) V. Busico, R. Cipullo, N. Friederichs, S. Ronca, G. Talarico, M. Togrou, B. Wang, Block Copolymers of Highly Isotactic Polypropylene via Controlled Ziegler−Natta Polymerization. *Macromolecules* **2004**, 37, 8201–8203.

(15) D. J. Arriola, E. M. Carnahan, P. D. Hustad, R. L. Kuhlman, T. T. Wenzel, Catalytic Production of Olefin Block Copolymers via Chain Shuttling Polymerization. *Science* **2006**, 312, 714–719.

(16) G.W. Coates, G. J. Domski, Pyridlyamidohafnium catalyst precursors, active species from this and uses thereof to polymerize alkenes. WO2008112133A2, 2008.

(17) Y. Lin, V. Yakovleva, H. Chen, A. Hiltner, E. Baer, Comparison of olefin copolymers as compatibilizers for polypropylene and high-density polyethylene. *J. Appl. Polym. Sci.* **2009**, 113, 1945–1952.
(18) Y. Lin, G. R. Marchand, A. Hiltner, E. Baer, Adhesion of olefin block copolymers to polypropylene and high density polyethylene and their effectiveness as compatibilizers in blends. *Polymer (Guildf)* **2011**, 52, 1635–1644.
(19) F. S. Bates, M. A. Hillmyer, T. P. Lodge, C. M. Bates, K. T. Delaney, G. H. Fredrickson, Multiblock Polymers: Panacea or Pandora's Box? *Science* **2012**, 336, 434–440.
(20) Y. Hu, B. Conley, K. Walton, C. Shan, G. Marchand, R. Patel, Kupsch Eva, B. Walter, Multilayered polyolefin-based films, US 9,511,567 B2, **2016**.
(21) K. Klimovica, S. Pan, T. W. Lin, X. Peng, C. J. Ellison, A. M. Lapointe, F. S. Bates, G. W. Coates, Compatibilization of iPP/HDPE Blends with PE-g-iPP Graft Copolymers. *ACS Macro Lett.* **2020**, 9, 1161–1166.
(22) P. Wolff, A. Dickert, W. P. Kretschmer, R. Kempe, iPP/PE Multiblock Copolymers for Plastic Blend Recycling Synthesized by Coordinative Chain Transfer Polymerization. *Macromolecules* **2022**, 55, 6435–6442.
(23) H. Gao, X. Lu, S. Chen, B. Du, X. Yin, Y. Kang, K. Zhang, C. Liu, L. Pan, B. Wang, Z. Ma, Y. Li, Preparation of Well-Controlled Isotactic Polypropylene-Based Block Copolymers with Superior Physical Performance via Efficient Coordinative Chain Transfer Polymerization. *Macromolecules* **2022**, 55, 5038–5048.
(24) J. M. Eagan, J. Xu, R. Di Girolamo, C. M. Thurber, C. W. Macosko, A. M. LaPointe, F. S. Bates, G. W. Coates, Combining polyethylene and polypropylene: Enhanced performance with PE/iPP multiblock polymers. *Science* **2017**, 355, 814–816.
(25) M. Letizia Focarete, M. Scandola, A. Kumar, R. A. Gross, Physical characterization of poly(ω-pentadecalactone) synthesized by lipase-catalyzed ring-opening polymerization. *J. Polym. Sci. B Polym. Phys*. **2001**, 39, 1721–1729.
(26) M. De Geus, I. van der Meulen, B. Goderis, K. Van Hecke, M. Dorschu, H. van der Werff, C. E. Koning, A. Heise, Performance polymers from renewable monomers: high molecular weight poly (pentadecalactone) for fiber applications. *Polym. Chem.* **2010**, 1, 525–533.
(27) F. Stempfle, P. Ortmann, S. Mecking, Long-Chain Aliphatic Polymers To Bridge the Gap between Semicrystalline Polyolefins and Traditional Polycondensates. *Chem. Rev.* **2016**, 116, 4597–4641.
(28) M. P. F. Pepels, R. G. Kleijnen, J. G. P. Goossens, A. B. Spoelstra, R. Tandler, H. Martens, M. Soliman, R. Duchateau, Compatibility and epitaxial crystallization between Poly(ethylene) and Poly(ethylene)-like polyesters. Polymer (Guildf) **2016**, 88, 63–70.
(29) J. Panten, H. Surburg, B. Hölscher, New Oxa-Bridged Macrocycles. *Chem. Biodivers.* **2008**, 5, 1011–1022.
(30) M. P. F. Pepels, M. Bouyahyi, A. Heise, R. Duchateau, Kinetic Investigation on the Catalytic Ring-Opening (Co)Polymerization of (Macro)Lactones Using Aluminum Salen Catalysts. *Macromolecules* **2013**, 46, 4324–4334.

(31) L. Jasinska-Walc, M. R. Hansen, D. Dudenko, A. Rozanski, M. Bouyahyi, M. Wagner, R. Graf, R. Duchateau, Topological behavior mimicking ethylene–hexene copolymers using branched lactones and macrolactones. *Polym. Chem.* **2014**, 5, 3306–3310.

(32) L. Jasinska-Walc, M. Bouyahyi, A. Rozanski, R. Graf, M. R. Hansen, R. Duchateau, Synthetic Principles Determining Local Organization of Copolyesters Prepared from Lactones and Macrolactones. *Macromolecules* **2015**, 48, 502–510.

(33) P. Gestoso, J. Brisson, Orientation of uniaxially stretched poly(vinyl phenol)/poly(vinyl methyl ether) blends. *Polymer (Guildf)* **2001**, 42, 8415–8424.

(34) P. Gestoso, J. Brisson, Effect of hydrogen bonds on the amorphous phase of a polymer as determined by atomistic molecular modelling. Computational and Theoretical Polymer *Science* **2001**, 11, 263–271.

(35) M. Zhang, P. Choi, U. Sundararaj, Molecular dynamics and thermal analysis study of anomalous thermodynamic behavior of poly (ether imide)/polycarbonate blends. *Polymer (Guildf)* **2003**, 44, 1979–1986.

(36) M. Tambasco, J. E. G. Lipson, J. S. Higgins, Blend Miscibility and the Flory−Huggins Interaction Parameter: A Critical Examination. *Macromolecules* **2006**, 39, 4860–4868.

(37) J. Gupta, C. Nunes, S. Vyas, S. Jonnalagadda, Prediction of Solubility Parameters and Miscibility of Pharmaceutical Compounds by Molecular Dynamics Simulations. *J. Phys. Chem. B* **2011**, 115, 2014–2023.

(38) A. D. S. Gomes, Polymerization, IntechOpen, Rijeka, **2012**.

(39) Y. Guo, J. Liu, Y. Lu, D. Dong, W. Wang, L. Zhang, A combined molecular dynamics simulation and experimental method to study the compatibility between elastomers and resins. *RSC Adv.* **2018**, 8, 14401–14413.

(40) J. L. Lebga-Nebane, M. Sankarasubramanian, G. Chojecki, B. Ning, P. A. Yuya, J. C. Moosbrugger, D. H. Rasmussen, S. Krishnan, Polyetheretherketone, hexagonal boron nitride, and tungsten carbide cobalt chromium composite coatings: Mechanical and tribological properties. *J. Appl. Polym. Sci.* **2021**, 138, 50504.

(41) M. Häußler, M. Eck, D. Rothauer, S. Mecking, Closed-loop recycling of polyethylene-like materials. *Nature* **2021**, 590, 423–427.

(42) H. Abou-Rachid, L.-S. Lussier, S. Ringuette, X. Lafleur-Lambert, M. Jaidann, J. Brisson, On the Correlation between Miscibility and Solubility Properties of Energetic Plasticizers/Polymer Blends: Modeling and Simulation Studies. *Propellants, Explosives, Pyrotechnics* **2008**, 33, 301–310.

(43) A. Ahmadi, J. J. Freire, Molecular dynamics simulation study of compatibility for the polyvinylmethylether/polystyrene mixture. *Mol. Simul.* **2008**, 34, 1253–1258.

(44) X. W. Cui, L. Zhang, Amorphous State and Solubility Simulation of Poly(N-arylenebenzimidazole ketone). *Applied Mechanics and Materials* **2014**, 513–517, 295–298.

(45) G. Natta, P. Corradini, Structure and properties of isotactic polypropylene. *Il Nuovo Cimento* **1960**, 15, 40–51.

(46) M. Gazzano, V. Malta, M. L. Focarete, M. Scandola, R. A. Gross, Crystal structure of poly(ω-pentadecalactone). *J. Polym. Sci. B Polym. Phys.* **2003**, 41, 1009–1013.

(47) M. K. Mitra, M. Muthukumar, Theory of spinodal decomposition assisted crystallization in binary mixtures. *J. Chem. Phys.* **2010**, 132, 184908.

(48) C. Yan, H. Li, J. Zhang, Y. Ozaki, D. Shen, D. Yan, A.-C. Shi, S. Yan, Surface-Induced Anisotropic Chain Ordering of Polycarprolactone on Oriented Polyethylene Substrate: Epitaxy and Soft Epitaxy. *Macromolecules* **2006**, 39, 8041–8048.

(49) Z. Bartczak, A. Galeski, M. Pracella, Spherulite nucleation in blends of isotactic polypropylene with high-density polyethylene. *Polymer (Guildf)* **1986**, 27, 537–543.

(50) N . W. Volchko, G. C. Rutledge, Heterogeneous nucleation of high-density Polyethylene crystals on graphene within microdomains. *Macromolecules* **2023**, 56, 4123–4134.

(51) R. B. Blumstein, Thermal Characterization of Polymeric Materials. Second Edition Volumes 1 and 2 Edited by Edith A. Turi (Polytechnic University, New York). Academic Press: San Diego. 1997. xxiv + 2420 pp. ISBN 0-12-703783-7. *J. Am. Chem. Soc.* **1997**, 119, 9589–9590.

(52) M. E. Dokukin, I. Sokolov, Quantitative Mapping of the Elastic Modulus of Soft Materials with HarmoniX and PeakForce QNM AFM Modes. *Langmuir* **2012**, 28, 16060–16071.

(53) D. Parisi, A. Han, J. Seo, R. H. Colby, Rheological response of entangled isotactic polypropylene melts in strong shear flows: Edge fracture, flow curves, and normal stresses. *J. Rheol.* (N Y N Y) **2021**, 65, 605–616.

(54) H. Gramespacher, J. Meissner, Interfacial tension between polymer melts measured by shear oscillations of their blends. *J. Rheol.* (N Y N Y) **1992**, 36, 1127–1141.

(55) S. Jose, A. S. Aprem, B. Francis, M. C. Chandy, P. Werner, V. Alstaedt, S. Thomas, Phase morphology, crystallisation behaviour and mechanical properties of isotactic polypropylene/high density polyethylene blends. *Eur. Polym. J.* **2004**, 40, 2105–2115.

(56) J. E. Mark, Physical properties of polymers handbook. vol. 1076 (Springer, 2007).

(57) Dassault Systemes. BIOVIA MATERIALS: Studio Overview, **2017**.

(58) D. N. Theodorou, U. W. Suter, Detailed molecular structure of a vinyl polymer glass. *Macromolecules* **1985**, 18, 1467–1478.

(59) H. Sun, Ab initio characterizations of molecular structures, conformation energies, and hydrogen-bonding properties for polyurethane hard segments. *Macromolecules* **1993**, 26, 5924–5936.

(60) H. Sun, COMPASS: An ab Initio Force-Field Optimized for Condensed-Phase ApplicationsOverview with Details on Alkane and Benzene Compounds. *J. Phys. Chem. B* **1998**, 102, 7338–7364.

(61) M. J. McQuaid, H. Sun, D. Rigby, Development and validation of COMPASS force field parameters for molecules with aliphatic azide chains. *J. Comput. Chem.* **2004**, 25, 61–71.

(62) R. L. C. Akkermans, N. A. Spenley, S. H. Robertson, COMPASS III: automated fitting workflows and extension to ionic liquids. *Mol. Simul.* **2021**, 47, 540–551.

(63) D. Montezinos, B. G. Wells, J. L. Burns, The use of ruthenium in hypochlorite as a stain for polymeric materials. Journal of Polymer Science: Polymer Letters Edition **1985**, 23, 421–425.

(64) National Institute of Health USA, ImageJ.

(65) S. J. Choi, W. R. Schowalter, Rheological properties of nondilute suspensions of deformable particles. *Phys. Fluids* **1975**, 18, 420–427.

(66) P. Scholz, D. Froelich, R. Muller, Viscoelastic Properties and Morphology of Two-Phase Polypropylene/Polyamide 6 Blends in the Melt. Interpretation of Results with an Emulsion Model. *J. Rheol. (N Y N Y)* **1989**, 33, 481–499.

Supplementary Materials for

*i*PP/HDPE blends compatibilized by a polyester: An unconventional concept to valuable products

Jakub Kruszynski, Weronika Nowicka, Artur Rozanski, Yingxin Liu, Daniele Parisi, Lanti Yang, Farhan Ahmad Pasha, Miloud Bouyahyi, Lidia Jasinska-Walc, and Rob Duchateau

Science Advances **2024***,* 10, eado1944.
DOI: 10.1021/acsapm.3c00566

This subchapter contains all data needed to evaluate the conclusions demonstrated in the paper.

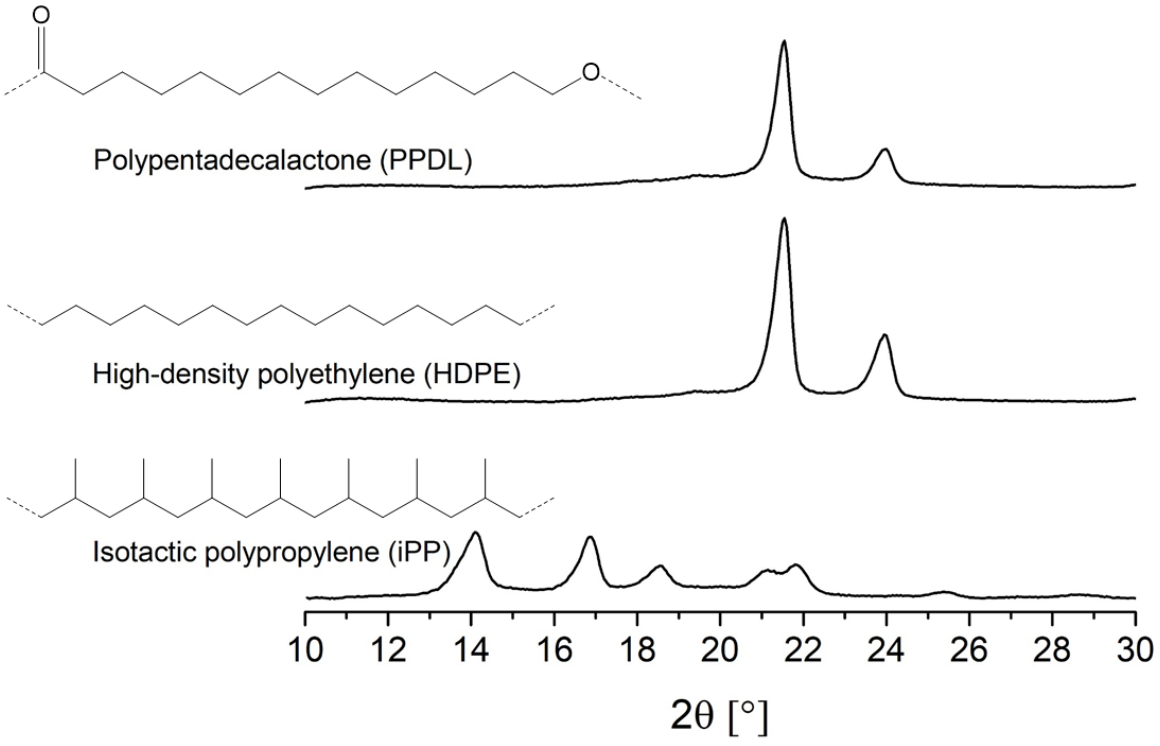

Figure S1. Chemical structure of polypentadecalactone synthesized by catalytic ring-opening polymerization, HDPE and *i*PP as well as WAXD profiles of the polymers.

Table S1. Composition and miscibility parameters for different binary blends.

Blend components	Composition	$E_{binding}$ kcal·mol^{-1}	ΔE_{mix} kcal·mol^{-1}	χ
HDPE/PPDL	87/13	211.30	−5.21	−283.77
*i*PP/PPDL	91/9	559.08	−9.74	−530.49
*i*PP/HDPE	89/11	318.97	−3.60	−196.63

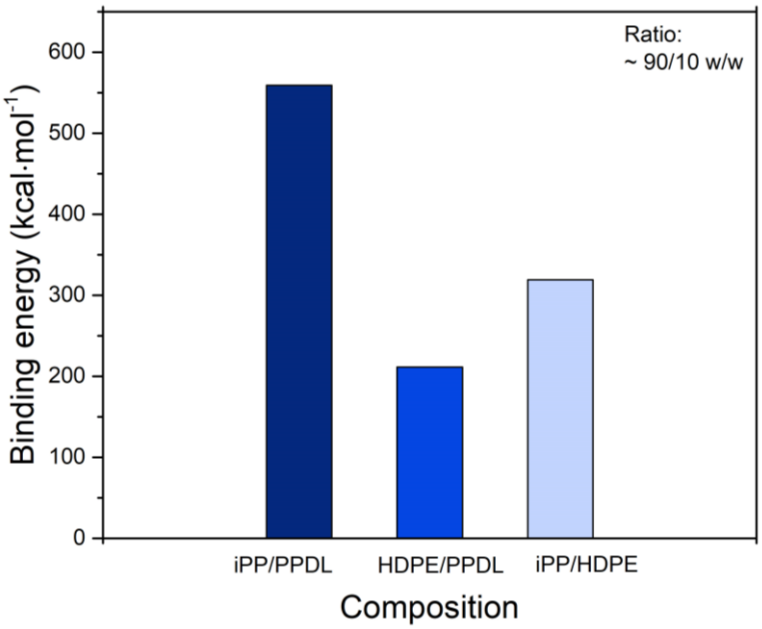

Figure. S2. Binding energy (E) calculated for *i*PP/PPDL (91/9 w/w%), HDPE/PPDL (87/13 w/w%) and *i*PP/HDPE (89/11 w/w%) binary blends.

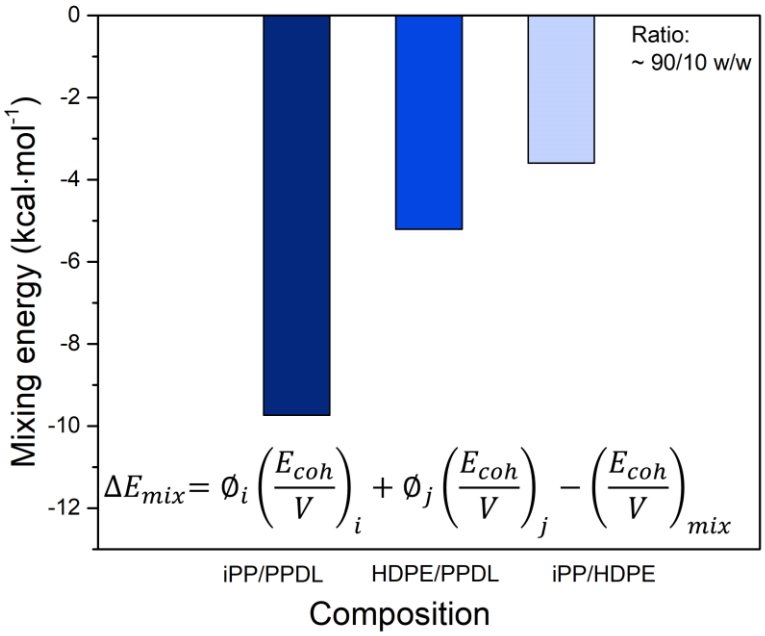

Figure S3. Mixing energy (ΔE_{mix}) calculated for *i*PP/PPDL (91/9 w/w%) HDPE/PPDL (87/13 w/w%), and *i*PP/HDPE (89/11 w/w%) binary blends.

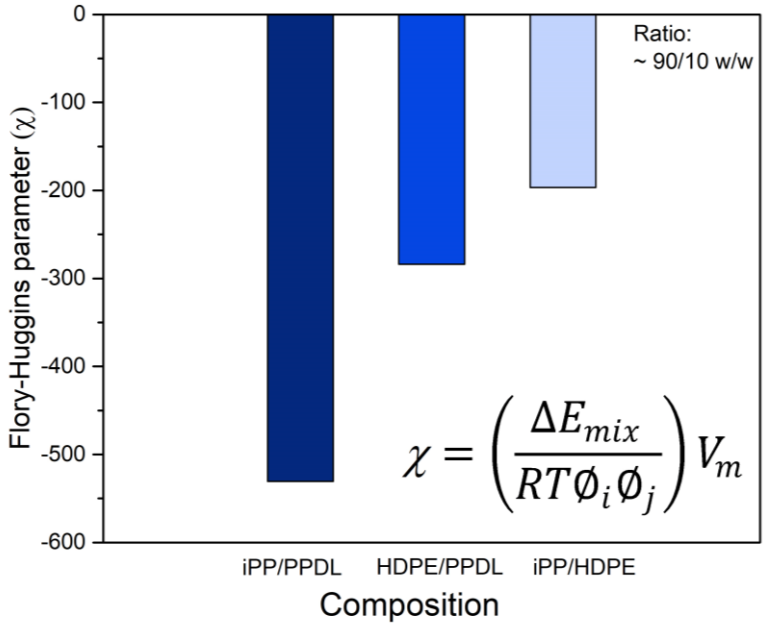

Figure S4. Flory-Huggins interaction parameter (χ) calculated for *i*PP/PPDL (91/9 w/w%), HDPE/PPDL (87/13 w/w%) and *i*PP/HDPE (89/11 w/w%) binary blends

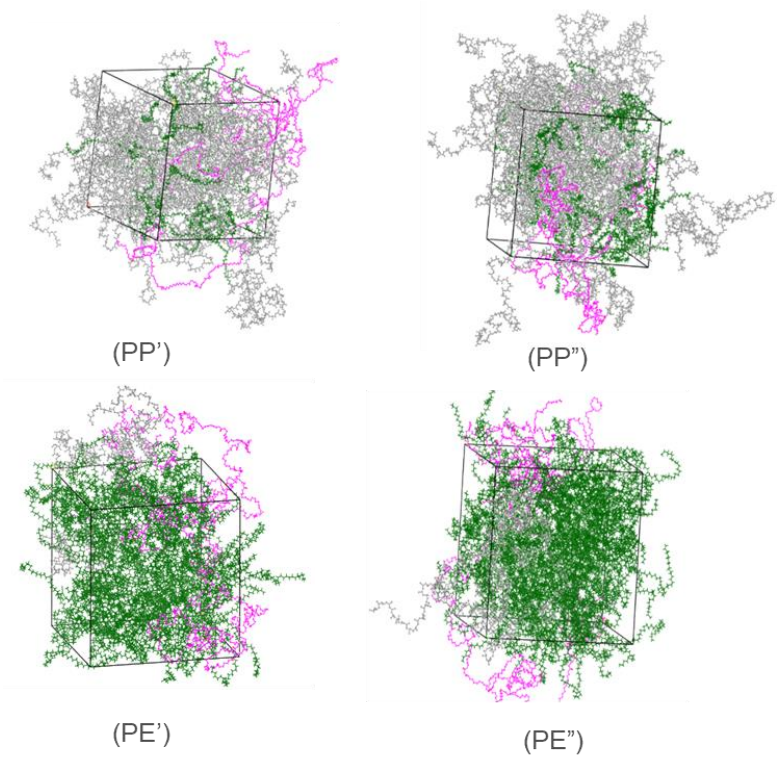

Figure S5. The snapshots of the interactive model PP'*i*PP$_{82.3\ wt\%}$/HDPE$_{9.7\ wt\%}$/PPDL$_{8.0\ wt\%}$), model PP" (*i*PP$_{74.6\ wt\%}$/HDPE$_{18.1\ wt\%}$/PPDL$_{7.3\ wt\%}$), model PE' (*i*PP$_{12.4\ wt\%}$/HDPE$_{73.1\ wt\%}$/ PPDL$_{14.5\ wt\%}$) and model PE" (*i*PP$_{10.0\ wt\%}$/HDPE$_{78.3\ wt\%}$/PPDL$_{11.7\ wt\%}$).

Table S2 The miscibility parameter values of the four different models.

Binding Energy ($E_{binding}$)		
	*i*PP/HDPE/PPDL	*i*PP/HDPE
PP'	592.43	318.97
PP''	1041.69	515.80
PE'	415.47	124.52
PE''	332.48	139.12
Mixing Energy (ΔE_{mix})		
	*i*PP/HDPE/PPDL	*i*PP/HDPE
PP'	−8.40	−3.60
PP''	−15.38	−7.90
PE'	−11.68	−5.68
PE''	−9.03	−4.52
Chi Parameter (χ)		
	*i*PP/HDPE/PPDL	*i*PP/HDPE
PP'	−459.04	−196.63
PP''	−837.96	−428.50
PE'	−636.41	−309.62
PE''	−492.00	−246.24

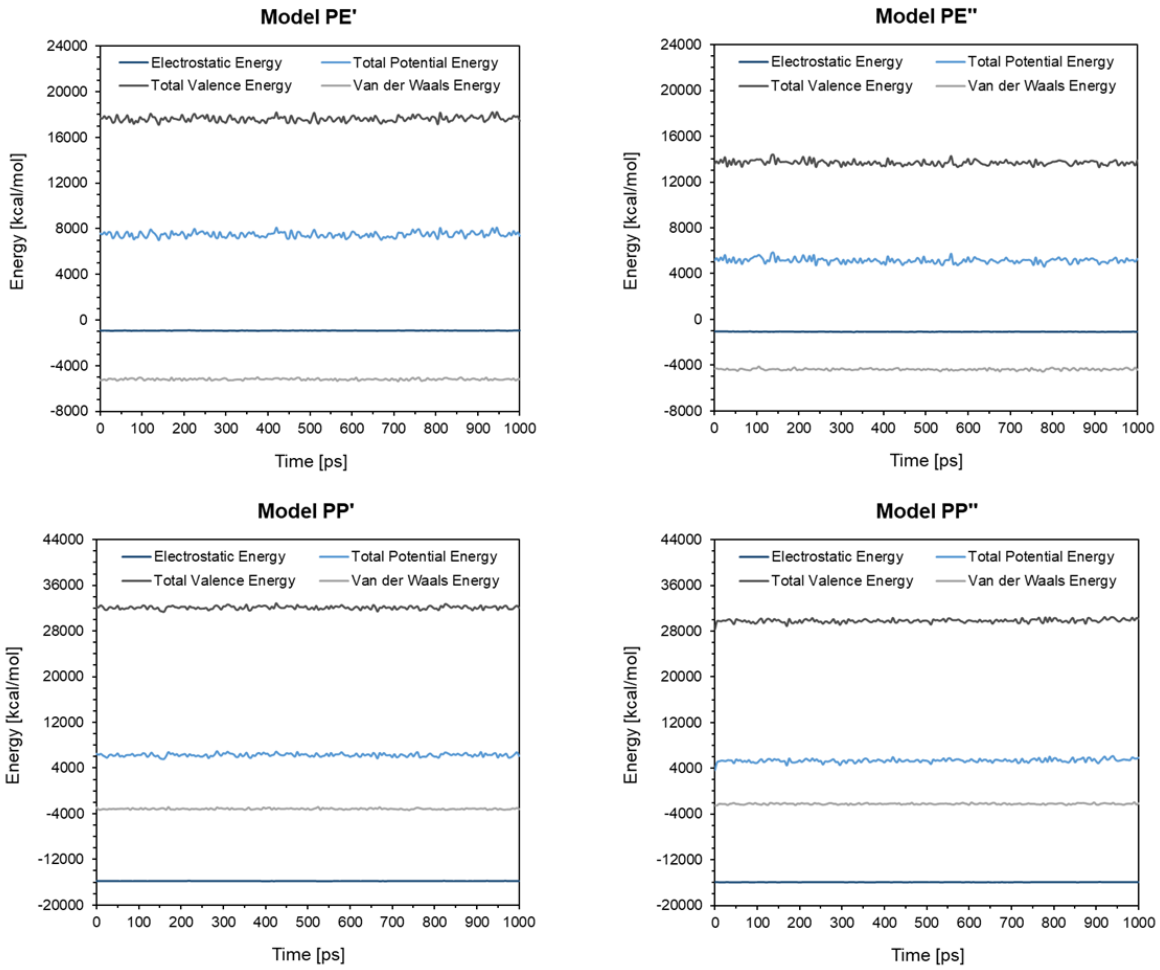

Figure S6. The energy of models PP', PP", PE' and PE" versus simulation time the last 1000 ps in NPT.

Table S3. SEC analysis of *i*PP, HDPE, PPDL used for blends preparation as well as *i*PP/HDPE and *i*PP/HDPE/PPDL blends.

Sample	M_n kg·mol^{-1}	M_w kg·mol^{-1}	$Đ$
*i*PP	166.9	871.7	5.2
HDPE	13.0	151.5	11.7
PPDL	99.5	215.1	2.2
*i*PP/HDPE 90/10	92.0	645.9	7.0
*i*PP/HDPE/PPDL 90/10/5	81.3	476.0	5.9
*i*PP/HDPE 80/20	56.6	608.0	10.7
*i*PP/HDPE/PPDL 80/20/5	59.6	609.3	10.2

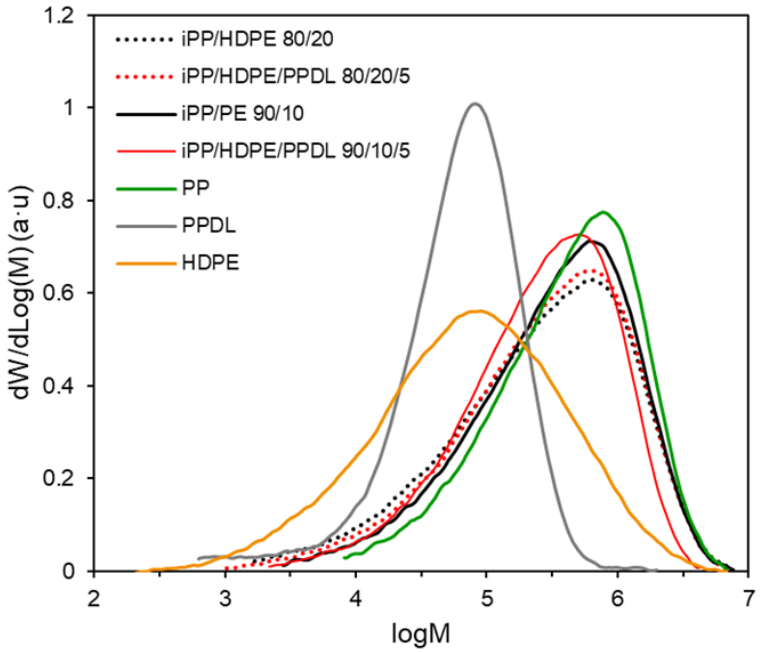

Figure S7. SEC analysis of the *i*PP/HDPE, *i*PP/HDPE/PPDL blends and polymers used for their preparation.

Table S4. Thermal properties of *i*PP/HDPE, *i*PP/HDPE/PPDL blends analyzed by DSC.

Sample	T_m °C	T_c °C	ΔH_m J·g^{-1}	ΔH_c J·g^{-1}
*i*PP/HDPE 90/10	164.3/128.2	117.6	70.8/3.1	98.0
*i*PP/HDPE/PPDL 90/10 + 1 % PPDL	160.7/127.2	117.4	67.6/14.4	105.4
*i*PP/HDPE/PPDL 90/10 + 3 % PPDL	162.3/127.7/92.9	117.6/83.7	64.1/14.4/2.6	100.9/2.6
*i*PP/HDPE/PPDL 90/10 + 5 % PPDL	161.6/127.4/93.1	117.2/83.9	59.8/12.7/4.4	91.3/4.2
*i*PP/HDPE 80/20	163.2/128.9	117.6	55.2/23.0	99.7
*i*PP/HDPE/PPDL 80/20 + 5 % PPDL	162.3/128.5/93.0	117.8/84.2	57.7/29.1/3.9	104.5/4.0

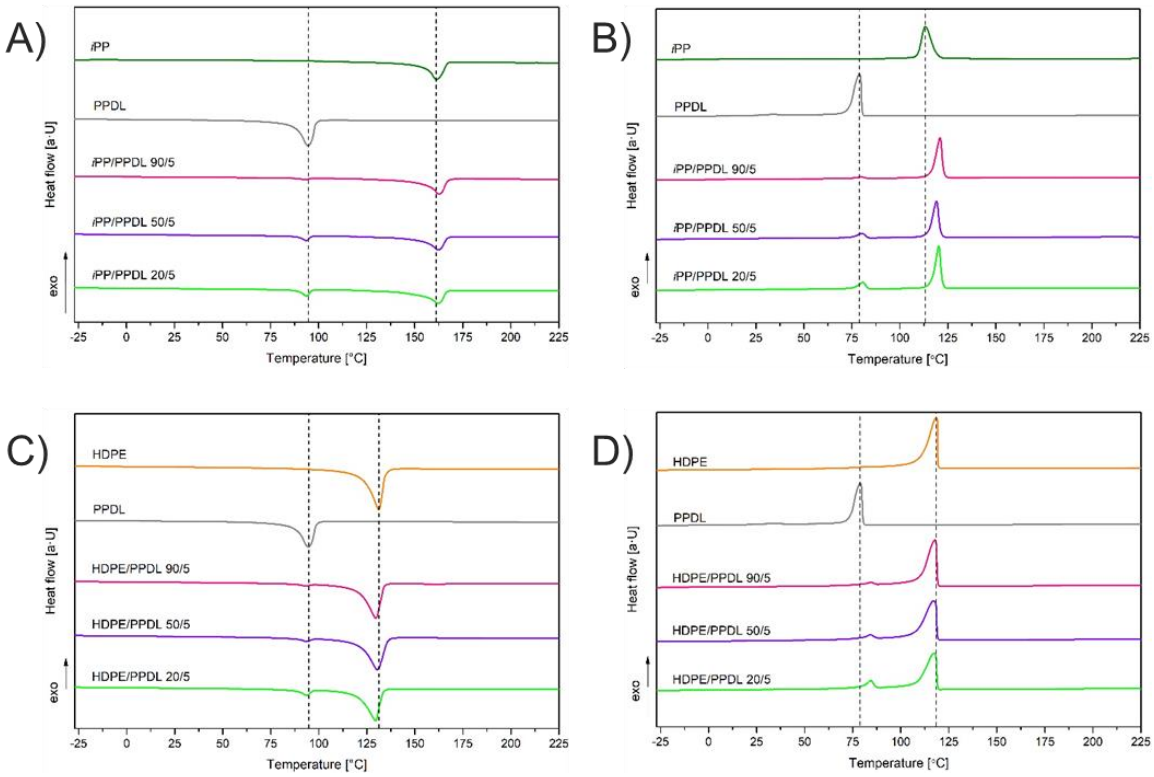

Figure S8. Melting and crystallization profiles of the *i*PP, HDPE, PPDL and blends of *i*PP/PPDL (A, B) as well as HDPE/PPDL (C, D) with different compositions.

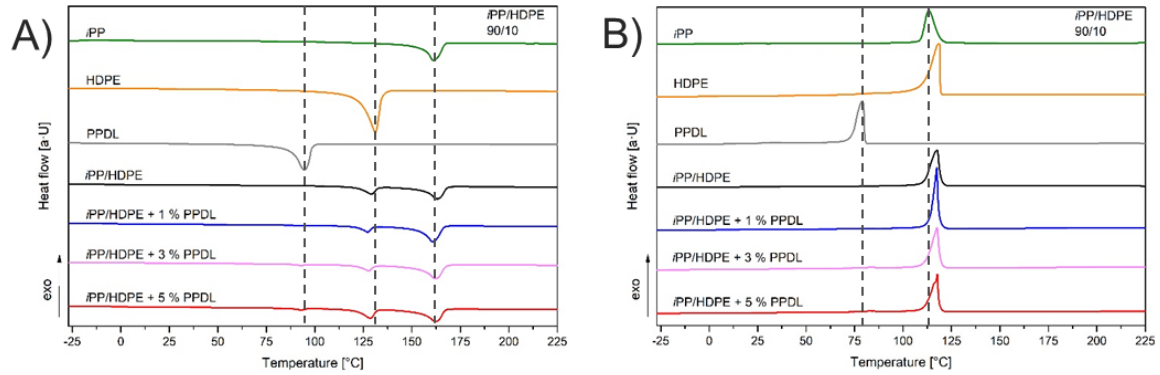

Figure S9. Melting (A) and crystallization (B) profiles of the uncompatibilized *i*PP/HDPE blends, products compatibilized by various amounts of PPDL as well as reference polymers used for blends preparation. DSC profiles were recorded for the *i*PP/HDPE 90/10 w/w and 80/20 w/w ratio.

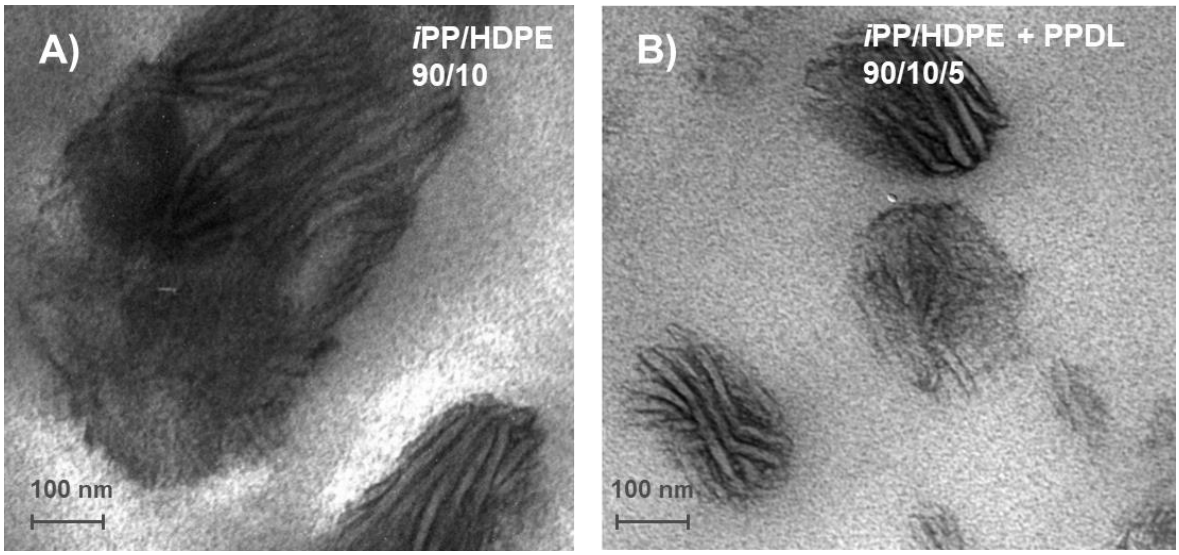

Figure S10. TEM analysis of the *i*PP/HDPE 90/10 w/w blend (A) and the composition consisting of *i*PP/HDPE/PPDL 90/10/5 w/w/w (B).

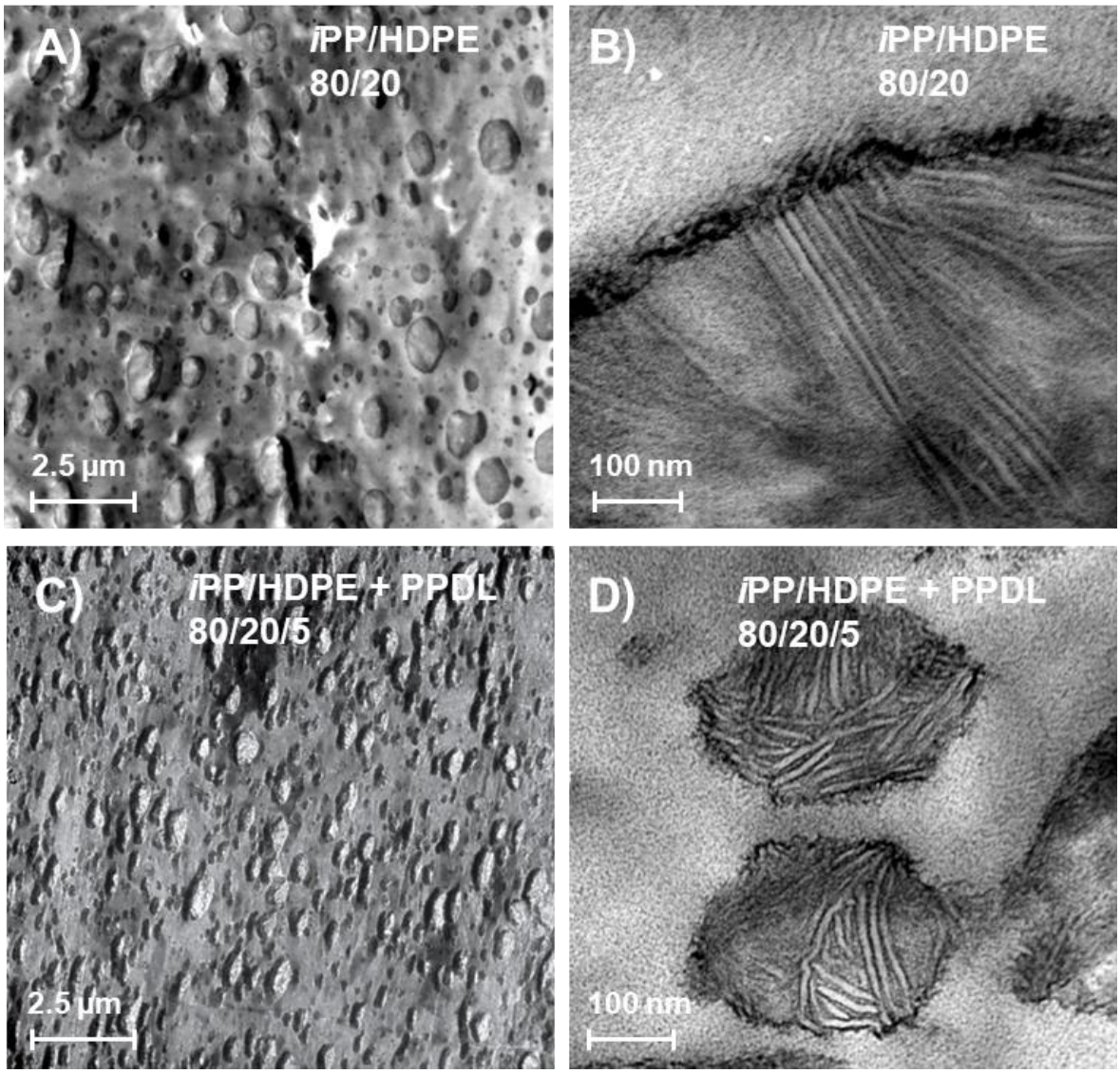

Figure S11. TEM analysis of the *i*PP/HDPE 80/20 w/w blend (A, B) and the corresponding compatibilized *i*PP/HDPE/PPDL 80/20/5 w/w/w sample (C, D).

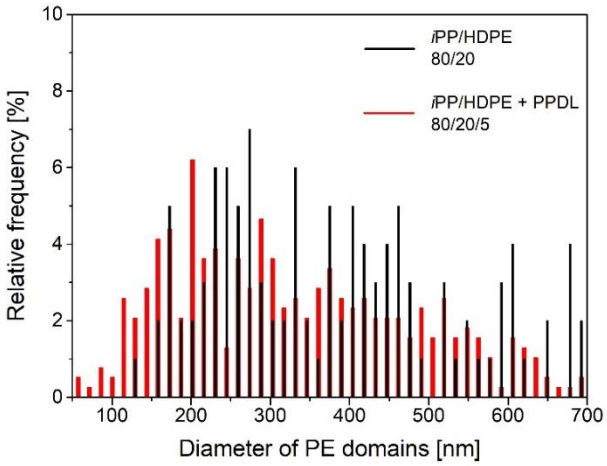

Figure S12. The compatibilizing effect of PPDL visualized by HDPE dispersed phase size determination in *i*PP/HDPE 80/20 w/w and *i*PP/HDPE/PPDL 80/20/5 w/w blends by TEM presented in Fig. S13.

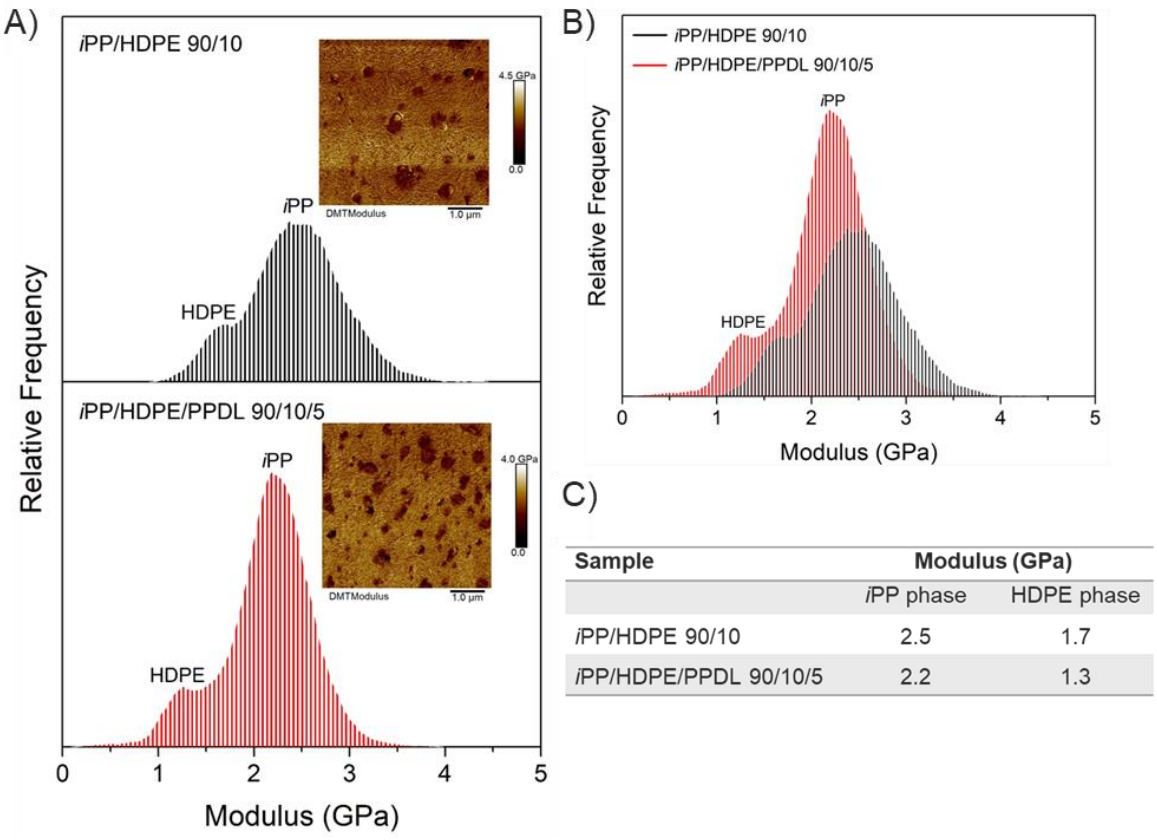

C)

Sample	Modulus (GPa)	
	*i*PP phase	HDPE phase
*i*PP/HDPE 90/10	2.5	1.7
*i*PP/HDPE/PPDL 90/10/5	2.2	1.3

Figure S13. AFM-QNM nano-mechanical properties of uncompatibilized *i*PP/HDPE and compatibilized *i*PP/HDPE/PPDL blends (A), comparison of the modulus mapping (B) and values of the blends elastic modulus (C) for the uncompatibilized *i*PP/HDPE 90/10 w/w and the compatibilized *i*PP/HDPE/PPDL 90/10/5 w/w/w blends.

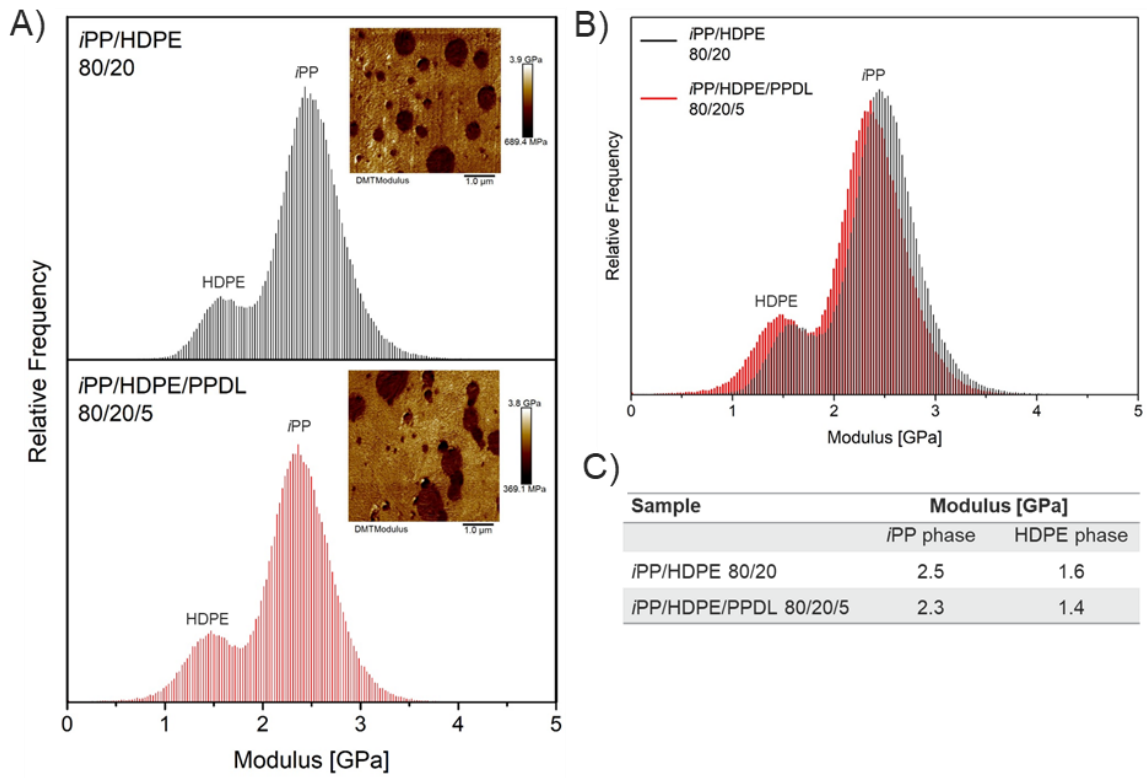

C)

Sample	Modulus [GPa]	
	*i*PP phase	HDPE phase
*i*PP/HDPE 80/20	2.5	1.6
*i*PP/HDPE/PPDL 80/20/5	2.3	1.4

Figure S14. AFM-QNM nano-mechanical properties of uncompatibilized *i*PP/HDPE and compatibilized *i*PP/HDPE/PPDL blends (A), comparison of the modulus mapping (B) and values of the blends elastic modulus (C) for the uncompatibilized *i*PP/HDPE 80/20 w/w and the compatibilized *i*PP/HDPE/PPDL 80/20/5 w/w/w blends.

Table S5. Dynamic Mechanical Thermal Analysis of the *i*PP/PPDL, HDPE/PPDL, *i*PP/HDPE, *i*PP/HDPE/PPDL blends and polymers used for their preparation. Samples were tested by strain-controlled temperature ramp with the frequency of 1 Hz.

Composition	T_g °C	*E*' at 25 °C GPa	*E*'' at 25 °C MPa	
*i*PP	7.2		1.49	86.3
HDPE	−103.4		1.80	121.9
PPDL	−24.3		0.68	35.3
*i*PP/PPDL 90/5	4.0		1.50	71.9
*i*PP/PPDL 50/5	2.7		1.54	77.1
*i*PP/PPDL 20/5	2.8		1.50	66.2
HDPE/PPDL 90/5	−104.5		1.49	132.4
HDPE/PPDL 50/5	−104.6		1.34	128.9
HDPE/PPDL 20/5	−109.0		1.30	118.2
*i*PP/HDPE 90/10	3.1	−109.9	1.42	68.0
*i*PP/HDPE 80/20	3.3	−107.6	1.59	85.5
*i*PP/HDPE/PPDL 90/10 + 1 % PPDL	3.5	−106.0	1.44	77.9
iPP/HDPE/PPDL 90/10 + 3 % PPDL	3.5	−104.9	1.51	76.5
*i*PP/HDPE/PPDL 90/10 + 5 % PPDL	5.2	−107.8	1.63	79.5
*i*PP/HDPE/PPDL 80/20 + 5 % PPDL	5.9	−106.6	1.57	83.1

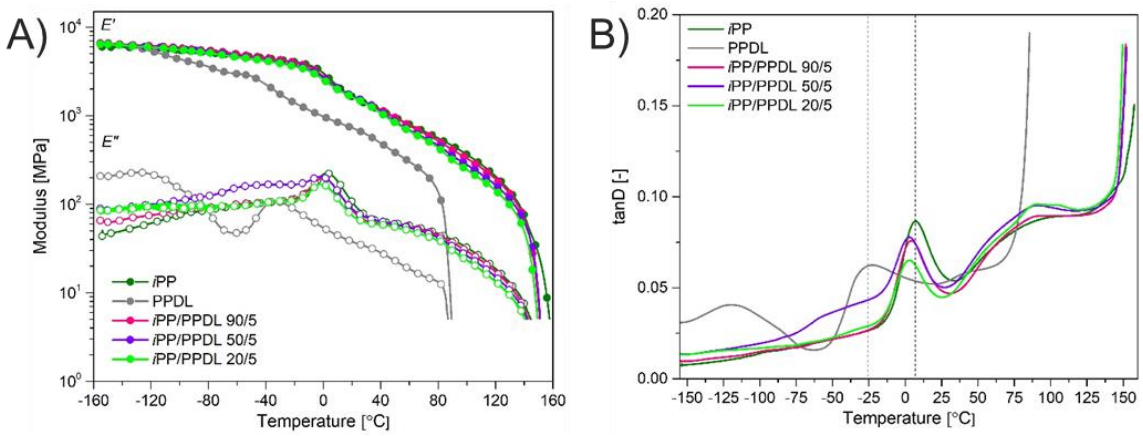

Figure S15. Storage (E') and loss (E'') moduli (A) as well as phase angle (B) of *i*PP, PPDL, *i*PP/PPDL blends analyzed by DMTA. Samples were tested by strain-controlled temperature ramp with the frequency of 1 Hz.

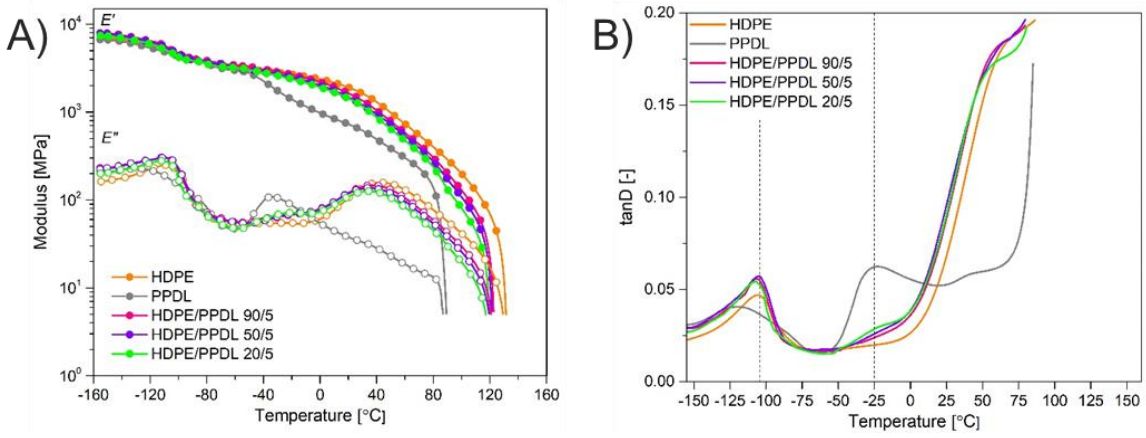

Figure S16. Storage (*E*') and loss (*E*'') moduli (A) and phase angle (B) of HDPE, PPDL, HDPE/PPDL blends analyzed by DMTA. Samples were tested by strain-controlled temperature ramp with the frequency of 1 Hz.

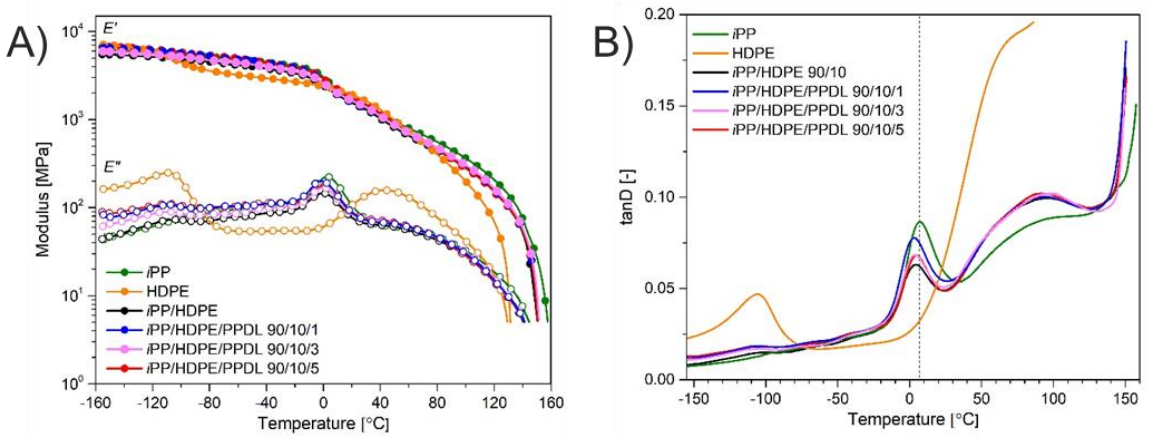

Figure S17. Storage (E') and loss (E'') moduli of *i*PP, HDPE, uncompatibilized *i*PP/HDPE 90/10 w/w reference and compatible *i*PP/HDPE/PPDL w/w/w compositions analyzed by DMTA. Figure (A) shows the performance of *i*PP/HDPE 90/10 w/w, *i*PP/HDPE/PPDL 90/10/1 w/w/w, *i*PP/HDPE/PPDL 90/10/3 w/w/w and *i*PP/HDPE/PPDL 90/10/5 w/w/w products. Figure (B) shows phase angle of these compositions. Samples were tested by strain-controlled temperature ramp with the frequency of 1 Hz.

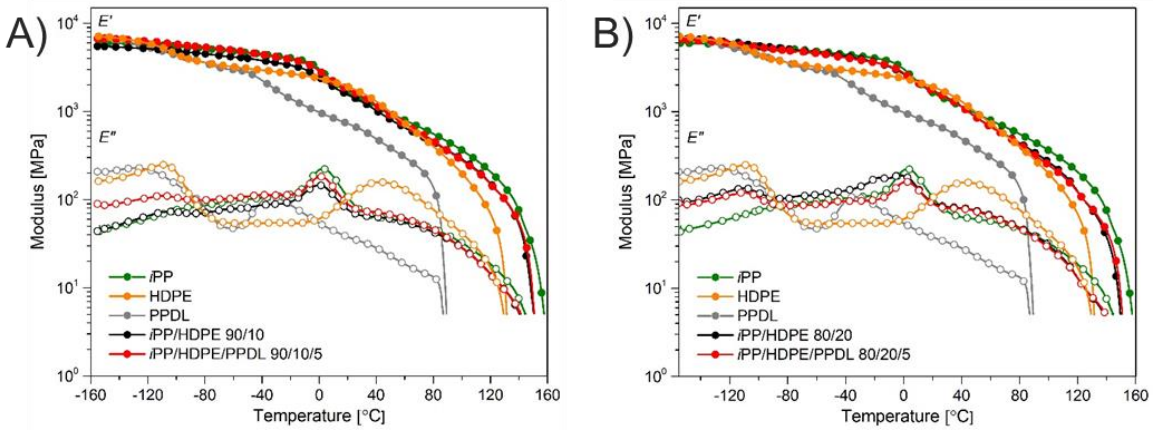

Figure S18. Storage (E') and loss (E'') moduli of *i*PP, HDPE, PPDL, uncompatibilized *i*PP/HDPE blends and compatible *i*PP/HDPE/PPDL compositions. Figure (A) shows the performance of the blends having *i*PP/HDPE w/w ratio equal to 90/10 while the Figure (B) reveals DMTA profiles of *i*PP/HDPE blends with the 80/20 w/w ratio. Samples were tested by strain-controlled temperature ramp with the frequency of 1 Hz.

Discussions concerning compatibilizer distribution in the blends

Using the Flory–Fox equation, the T_g values of the blend components have been calculated. For the *i*PP/PPDL 90/5, *i*PP/PPDL 50/5, *i*PP/PPDL 20/5 blends the calculated T_g is 5.3 °C, 4.0 °C, and 0.3 °C, respectively. On the other hand, the DMTA measurements indicate that the corresponding T_g of these compositions are 4.0 °C, 2.7 °C, 2.8 °C. The calculations clearly show that *i*PP (T_g = 7.2 °C) and PPDL (T_g = -24.3 °C) reveal miscibility. However, when higher amount of PPDL is introduced into the *i*PP/PPDL blend (*i*PP/PPDL 20/5) the T_g shift is lower than expected (2.8 °C versus 0.3 °C), meaning that not all PPDL mixes with the *i*PP matrix.

For the HDPE/PPDL blends, a lower T_g is observed in comparison to the HDPE (Tg = -103.4 °C) and PPDL (Tg = -24.3 °C) reference samples. This phenomena confirms lack of miscibility between these polymers. As illustrated by TEM, the interaction between HDPE and PPDL originates from the epitaxial crystal growth of PPDL onto HDPE lamellae and not from the miscibility of the amorphous phase.

Table S6. Static mechanical properties of the *i*PP/PPDL, HDPE/PPDL, *i*PP/HDPE, *i*PP/HDPE/PPDL blends.

Sample	Yield Stress MPa	Yield Strain %	Stress at the break MPa	Strain at the break %
*i*PP/PPDL 90/5	37.0±0.8	7.6±0.3	26.8±9.4	713±71
*i*PP/PPDL 50/5	35.0±0.3	7.9±0.2	36.2±3.9	725±93
*i*PP/PPDL 20/5	34.2±0.5	9.1±0.7	31.9±5.9	652±124
HDPE/PPDL 90/5	29.4±0.4	11.3±0.3	26.2±3.8	981±97
HDPE/PPDL 50/5	27.7±0.5	12.1±0.4	22.3±7.4	1071±96
HDPE/PPDL 20/5	26.6±0.4	12.5±0.4	21.1±1.6	848±72
*i*PP/HDPE/PPDL 90/10*	67.8±1.3	16.9±0.3	55.7±8.6	35±8
*i*PP/HDPE/PPDL 90/10 + 5 % PPDL*	58.2±4.0	13.6±1.8	54.7±8.4	254±37

*injection molded samples

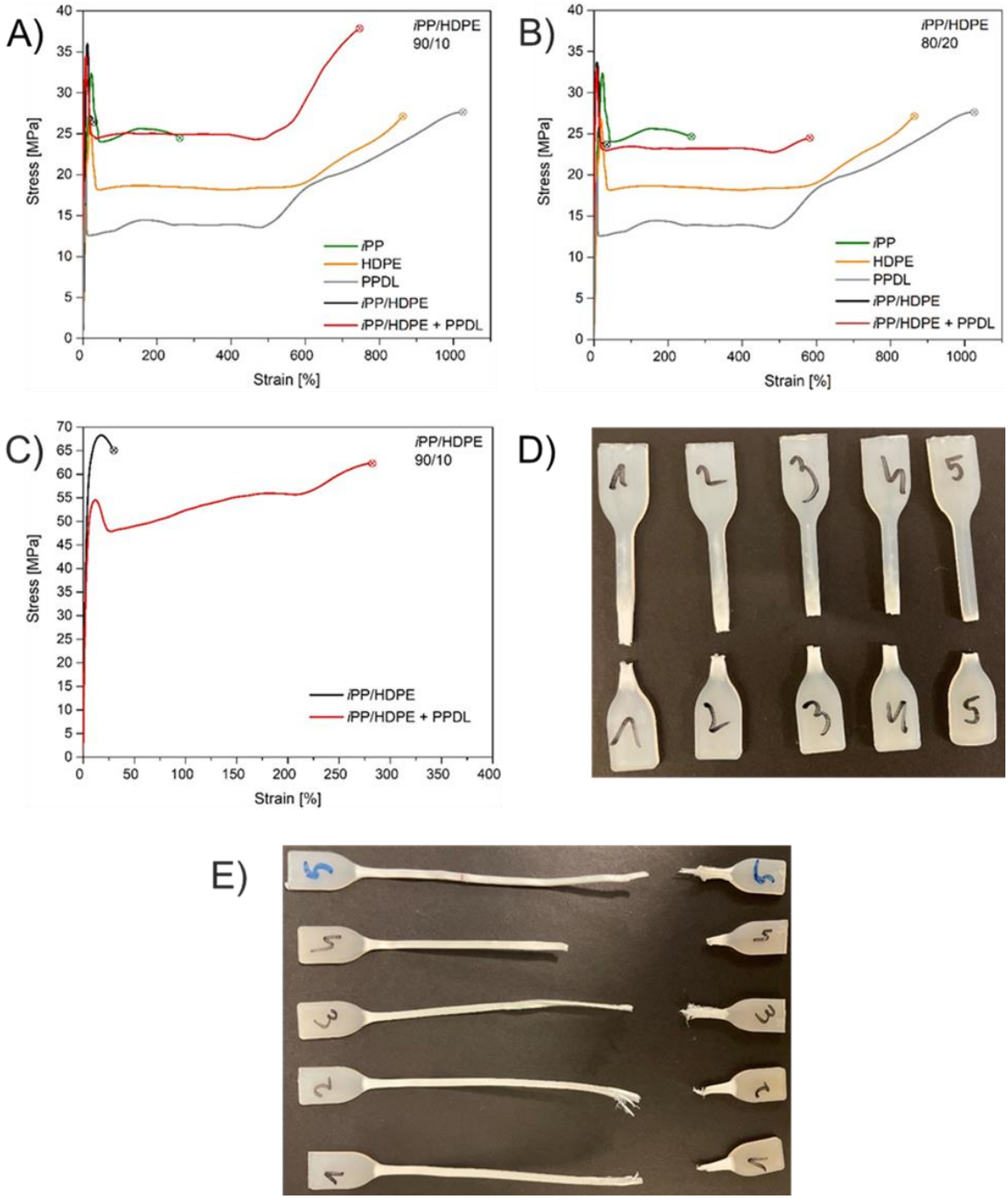

Figure S19. Representative stress-strain curves of *i*PP, HDPE, PPDL, uncompatibilized *i*PP/HDPE reference and compatible *i*PP/HDPE/PPDL blends. Figure (A) shows the performance of *i*PP/HDPE 90/10 w/w and iPP/HDPE/PPDL 90/10/5 w/w/w products. Figure (B) reveals the performance of *i*PP/HDPE 80/20 w/w and *i*PP/HDPE/PPDL 80/20/5 w/w/w samples. Figure (C) reveals the performance of *i*PP/HDPE 90/10 w/w and *i*PP/HDPE/PPDL 90/10/5 w/w/w samples prepared via injection molding. Figure (D) shows the image of the specimens *i*PP/HDPE prepared via injection molding after static mechanical properties measurements while (E) represents *i*PP/HDPE/PPDL blends.

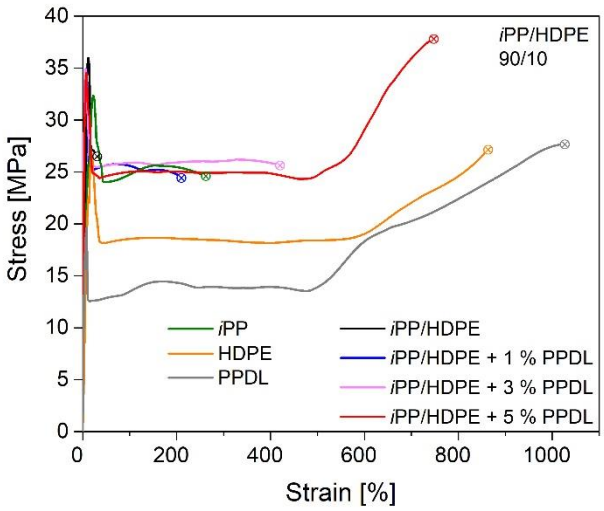

Figure S20. Representative stress-strain curves of *i*PP, HDPE, uncompatibilized *i*PP/HDPE reference blend and compatible *i*PP/HDPE/PPDL blends. The figure shows the performance of *i*PP/HDPE 90/10 w/w, *i*PP/HDPE/PPDL 90/10/1 w/w/w, *i*PP/HDPE/PPDL 90/10/3 w/w/w and *i*PP/HDPE/PPDL 90/10/5 w/w/w products plus reference samples HDPE and *i*PP.

Interphase analysis using AFM

The modulus mapping images of the uncompatibilized *i*PP/HDPE 80/20 w/w (Fig. S21a) and compatibilized *i*PP/HDPE 80/20/9 w/w/w blend (Fig. S21b) are presented using the same modulus scale range. Here, for a detailed interphase analysis in the blends a significant amount of PPDL was incorporated into the composition. The uncompatibilized *i*PP/HDPE blend shows homogenous/round shape PE domains (modulus around 1.5 GPa) dispersed in PP matrix (modulus of 2.3 GPa). For the compatibilized *i*PP/HDPE/PPDL blend, several additional domains at the HDPE and *i*PP interphase can be observed revealing modulus at the level of 1.2 GPa (red arrows in Fig. S21b and section analysis Fig. S22), which is clearly lower than the core of PE domains (around 1.5 GPa). As presented in Fig. S22, for the ternary blends three types of modulus area are observed, which are related to PP–rich, HDPE–rich and PPDL–rich phase where the last one is located mainly at the interphase.

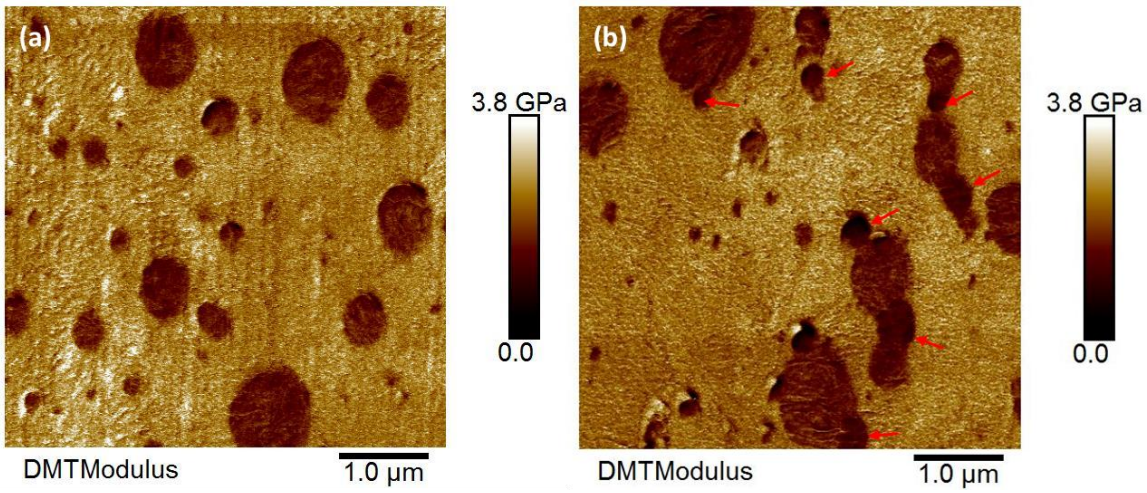

Figure S21. AFM–QNM nano-mechanical properties mapping of (a) uncompatibilized *i*PP/HDPE 80/20 w/w and (b) compatibilized *i*PP/HDPE/PPDL 80/20/9 w/w/w blends. Areas with lower modulus compared to average PE domains moduli are indicated with red arrows.

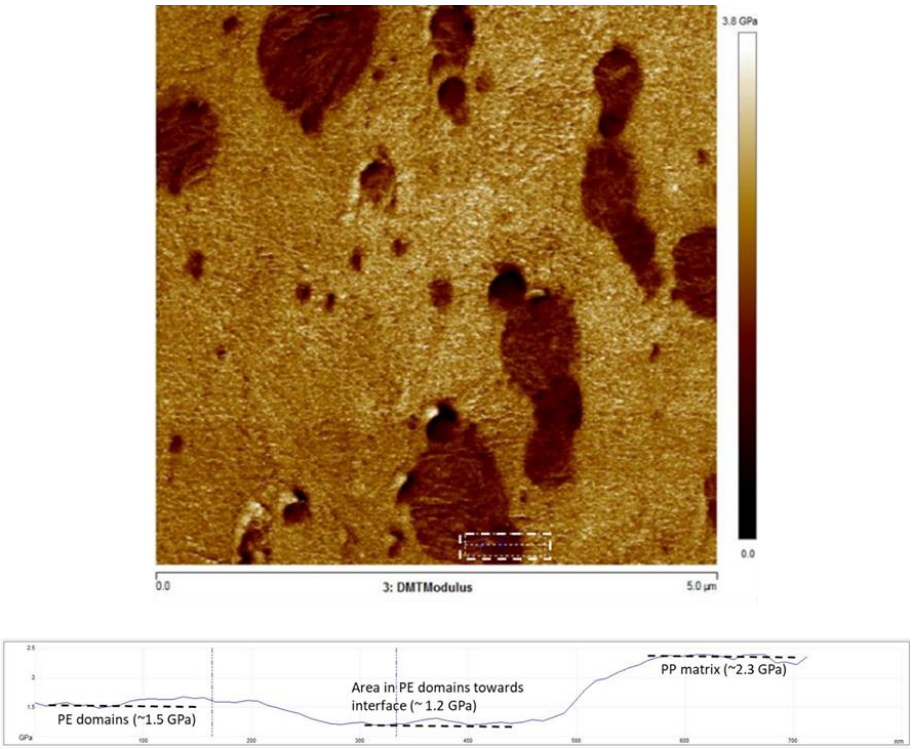

Figure S22. AFM–QNM section analysis of the *i*PP/HDPE/PPDL 80/20/9 w/w/w blend demonstrating modulus differences in the selected area (white square) of PP matrix, HDPE domains and area of the HDPE domains towards interface.

Summary

This thesis provides the characterization of randomly OH-functionalized polypropylene, as well as amphiphilic block and graft copolymers thereof. Special emphasis is placed on application of in reactor functionalized polyolefins (IRF-PO) as hot melt adhesives, particularly relevant in automotive applications and IRF-PO-based copolymers and PO-like polyesters in the compatibilization of polyolefin blends, which is essential for mechanical recycling. The understanding of the relationship between the chemical structure and properties of functionalized polyolefins is essential for their successful application. Parameters such as molecular weight, polydispersity, crystallinity, functionality level, concentration, and distribution of chain branches determine their properties.

Modern adhesives should simultaneously comply with ecological principles while utilizing cost-effective technology that ensures high product performance. In comprehensive evaluations, IRF-PO has proven its superiority over commercial polyolefin elastomer-based hot melt adhesives when bonding steel, aluminum and combinations of these metals with polyolefins. Research focuses on improving our understanding of the relationship between the chemical structure of functionalized polyolefins (FPOs) and its adhesion performance. It has been proven that, besides the fundamental role of polar moieties in the polyolefin chain, the removal of aluminum alkyl residues significantly improves adhesion strength, especially at lower application temperatures. This post-polymerization deashing step releases the hydroxyl groups, allowing them to bind more effectively. Additionally, the thermoplastic nature of IRF-PO enables easy debonding and rebonding, promoting reusability and recyclability of the adhesives—a fundamental aspect of the circular economy. Furthermore, this research explores a novel, patented approach (granted patent EP4484516B1) to enhance adhesive strength in functionalized polyolefins by blending them with non-functionalized counterparts. The study reveals that the crystallinity and miscibility of the polymers significantly influence adhesive performance. Remarkably, blends containing only 1% of poly(propylene-co-hex-1-ene-co-hex-5-en-1-ol) maintain initial adhesive strength. The presented outcomes demonstrate an efficient and cost-effective strategy to tune the properties of functional polyolefins, opening a wider range of applications, unavailable before for POs-based materials.

Considering that society struggles with enormous scale of plastic production and scant percentage of recycling, this thesis also seeks solutions for improved upcycling of polyolefins through an investigation of an efficient compatibilization strategy. The study focuses on widely used polymers such as PP, HDPE, and PC due to their significant contribution to global plastic production. Advanced microscopy techniques such as SEM, TEM, and AFM confirm that properly selected compatybilizers—PP-*graft*-PEB and PP-*graft*-PCL for PP/PC systems, and PPDL for PP/PE—reduce the size of dispersed domains in the matrix and enhance interfacial adhesion. This well-dispersed morphology results in significantly improved mechanical properties or surprisingly opens a possibility to produce foams from PP/PC blend. The approaches presented in this thesis provide promising opportunities for the upcycling of polymer waste streams into high-value products.

Abbreviations

^{1}H NMR	proton nuclear magnetic resonance spectroscopy
^{13}C NMR	carbon nuclear magnetic resonance spectroscopy
ICP-MS	inductively coupled plasma mass spectrometry
DSC	differential scanning calorimetry
DMA	dynamic mechanical analysis
GPC	gel permeation chromatography
TEM	transmission electron microscopy
SEM	scanning electron microscopy
AFM	atomic force microscopy
WAXS	wide-angle X-ray scattering
Z-N	Ziegler-Natta catalyst
SSC	single-site catalyst
MAO	methylaluminoxane
TEA	triethylaluminium
ADMET	acyclic diene metathesis
ROMP	ring-opening metathesis polymerization
OCT	olefins conversion technology
IRF	in-reactor functionalization
CTA	chain transfer agent
OBC	olefin block copolymer
CSP	chain-shuttling polymerization
*a*PP	atactic polypropylene
*i*PP	isotactic polypropylene
LDPE	low density Polyethylene
LLDPE	linear low-density polyethylene
HDPE	high-density polyethylene
FPO	functionalized polyolefin
POE	polyolefin elastomer
TPO	thermoplastic polyolefin
EPR	ethylene propylene rubber
EPDM	ethylene propylene diene monomer
PUR	polyurethane
TPU	thermoplastic polyurethane
EVA	ethylene vinyl acetate

PC	polycarbonate
HMA	hot melt adhesive
LSS	lap shear strength
M_w	weight average molar mass
M_n	number average molar mass
PDI	polydispersity index
T_m	melting temperature
T_c	crystallization temperature
T_g	glass-transition temperature
CSTR	continuous stirred-tank reactor
CAGR	compound annual growth rate

Acknowledgments

I would like to express my sincere gratitude to the many people who supported me during the last five years of that PhD journey.

First, to Professor Lidia Jasińska-Walc and Professor Rob Duchateau, I feel a great honor that I was able to meet you in 2016 and work with you during my master's internship and, later, during my doctoral studies. Your attention to my scientific and professional development, as well as your care during my time in the Netherlands—especially during the challenging years of the COVID-19 pandemic—has been invaluable. You taught me how to navigate the corporate world while maintaining scientific quality.

To Weronika Nowicka, there are no words to express how wonderful it was to collaborate with you. Thank you for your invaluable scientific insights, our brainstorming sessions about HMA and compatibilizers, and your constant, every day positive energy and support.

To my lovely wife, thank you! Your support, tolerance for my long stays in the Netherlands, and patience during my monologues about polypropylene have meant everything. And of course I would like to thanks to my new-born son, your expected coming into the world in August 2025 gave me extra motivation to finalize this PhD project.

I would also like to thank my parents and siblings. You encouraging and motivate me during tough moments.

Finally, I would like to thank everyone from Sabic and Gdansk University of Technology who supported me. Especially for: Miloud Bouyahyi, Mateusz Malus, Wojciech Szot, Yingxin Liu, Nydia Badillo, Emiel van der Boon, Bryan Marwi, Lanti Yang, Artur Rozanski, Artur le Layec and Daniele Parisi.

Words of thanks also towards people from Orlen S.A: Paweł Adamski, Marcin Konkol, Grzegorz Blonkowski, Robert Wysibirski and Marta Woźniak your support in the last year was very important for me. Thank you!

Curriculum Vitae

Jakub Kruszyński was born on August 21, 1992, in Wejherowo, Poland. He attended the Adam Mickiewicz High School (II LO) in Gdynia, where he passed the school-leaving exam. In 2012, he began further education at Gdańsk University of Technology in the Department of Chemical Technology. He obtained a bachelor's degree in 2016 in the polymer field of science. In the same year, he joined an international research group led by Rob Duchateau and Lidia Jasińska-Walc. In October 2016, he started a 9-month internship in SABIC Technology & Innovation Center in the Netherlands where he completed the experimental part of his master's thesis, focusing on the characterization and application of functionalized polyolefins. In 2018, he graduated from Chemical Technology at Gdańsk University of Technology.

In 2019, he joined the Research & Development Center of Synthos, a chemical company located in Oświęcim, Poland. His work primarily focused on conducting polymerization processes aimed at producing novel acrylic dispersions applied in the furniture and construction industry. After almost two years, he decided to continue research on polyolefins. He started PhD studies under the supervision of professor Lidia Jasińska-Walc. During this four year PhD journey, he spent two years at the SABIC Technology & Innovation Center in the Netherlands, where he investigated the properties and novel applications of functionalized polypropylene. The most promising results were published and are included in this thesis. After returning to Poland, he decided to join the Orlen Research & Development Center located in Płock, where he works up to now as a specialist in a Piloting and Modelling Team, Strategy and Innovation Area.